Designing Liquid Repellent Surfaces for Fabrics, Feathers and Fog

Shreerang S. Chhatre

B. Tech. + M. Tech., Indian Institute of Technology, Bombay, 2007
M. S. CEP, Massachusetts Institute of Technology, 2009

Submitted to the Department of Chemical Engineering in partial fulfillment of the requirements for the degree of

**DOCTOR OF PHILOSOPHY IN
CHEMICAL ENGINEERING PRACTICE**

AT THE
MASSACHUSETTS INSTITUTE OF TECHNOLOGY

December 2012

Author ………………………………………...
Shreerang S. Chhatre
Department of Chemical Engineering
December 2012

Certified by ………………………………………...
Robert E. Cohen
St. Laurent Professor of Chemical Engineering
Thesis Supervisor

………………………………………...
Gareth H. McKinley
SoE Professor of Teaching Innovation, Mechanical Engineering
Thesis Supervisor

Accepted by ………………………………………...
Patrick S. Doyle
Professor of Chemical Engineering
Chairman, Committee for Graduate Students

Designing Liquid Repellent Surfaces for Fabrics, Feathers and Fog

by

Shreerang S. Chhatre

Submitted to the Department of Chemical Engineering
in December 2012 in Partial Fulfillment of the
Requirements for the Degree of Doctor of Philosophy in Chemical Engineering Practice

ABSTRACT

Omniphobicity refers to a property of surfaces which are not wetted by water, oils, alcohols and other low surface tension liquids. Robust omniphobic surfaces can be applied in many areas including fabrics with chemical / biological protection and dirt / fingerprint resistant touch screens. The main aim of this thesis is to develop rules for the systematic design of omniphobic surfaces with a focus on textiles.

First, a design chart is developed to help us understand the impact of surface chemistry and surface topography on the wettability of a textured surface. A smaller characteristic length scale of a re-entrant surface topography, tighter weave and a coating with inherently low wettability are better for producing omniphobic surfaces that resist wetting by liquids with low surface tension. This framework is applied to textile fabrics and bird feathers to test their wettability. Using this framework, wettability of low surface tension liquids on a polyester fabric is tuned or switched using either thermal annealing or biaxial stretching. Army Combat Uniform fabrics are rendered oleophobic, thus opening the way to optimize omniphobic army uniforms.

The wettability of molecules similar to fluorodecyl POSS is investigated by measuring the contact angles with liquids of a broad range of surface tension and polarity. Of the molecules tested so far, fluorodecyl POSS has the lowest solid surface energy (9.3 mN/m) and the lowest increment in solid surface energy (7 mN/m). The wetting aspects of the hierarchical topography of bird feathers are captured using contact angle measurements in terms of a spacing ratio. Thermodynamics of the wetting of feathers and the robustness against wetting during the course of a dive are correlated to the wing spreading behavior. Our understanding of surface wettability of woven meshes is applied to optimize their fog collection ability. A business case for fog harvesting is developed and strategies to decrease asset and cash flow risks are proposed.

The contributions presented here provide means to better characterize surfaces with complex topography, tune and *a priori* predict their wettability and recommend a design strategy both at a molecular and a macroscopic level to maximize their non-wettability.

Thesis Supervisors: Prof. Robert E. Cohen, St. Laurent Professor of Chemical Engineering

Prof. Gareth H. McKinley, School of Engineering Professor of Teaching Innovation, Mechanical Engineering

ACKNOWLEDGEMENTS

Dedication

This thesis is dedicated to my mother (Aai).

Thanks a lot Aai for your unconditional love, the values you inculcated in me, and for always putting me and my education as your first and only priority.

ब्रह्मण्याधाय कर्माणि सङ्गं त्यक्त्वा करोति यः |
लिप्यते न स पापेन पद्मपत्रमिवाम्भसा ||

One who performs his duty without attachment, surrendering the results unto the Supreme God, is not affected by sinful action, as the lotus leaf is untouched by water (Shreemad Bhagwad Geeta, chapter 5, verse 10).

TABLE OF CONTENTS

LIST OF FIGURES

14

18

LIST OF TABLES

1 Introduction

Hazardous chemicals and liquid-borne biological pathogens present a threat to the life and well-being of a soldier. These dangers can be significantly reduced if the soldier's uniform is made out of a fabric which is not wetted by water, petroleum, oils, lubricants, and liquid chemicals. Such omniphobic fabrics will find further application in self-cleaning clothing. The US Army Natick Soldier Research Development Engineering Center (NSRDEC) is interested in designing omniphobic soldier uniforms, and they are the primary funding agency for this research.

Solid-liquid interactions are ubiquitous in nature and consequently understanding these interactions has been a research topic over the last couple of centuries. The first major contribution in interfacial phenomena is credited to Thomas Young (1805) and to honor his contribution, the equilibrium contact angle of a liquid droplet on a molecularly smooth solid surface is called Young's contact angle. Later Cassie-Baxter (1936) and Wenzel (1944) quantified the apparent contact angles on rough textured surfaces in terms of the topography of the roughness and chemistry of the solid-liquid interaction. Recently, there has been plenty of literature (summarized in Chapter 2) on developing surfaces which are not wetted by water, alcohols, oils and other liquids (and therefore termed "Omniphobic surface").

A design parameter approach to predict the apparent contact angle and breakthrough pressure for such non-wetting surfaces was developed in our group. The design chart framework to illustrate these design parameters is developed in Chapter 3. The design chart presented in this work can be used to *apriori* predict the state of a liquid droplet, its apparent contact angle and the pressure at which a non-wetting solid-liquid-air composite state irreversibly transitions into a fully-wetted state. The chart also deconvolutes the influence of solid surface chemistry, surface topography

and characteristic length scale on the wettability state of a liquid droplet. This framework can be generalized to any solid surface chemistry, probing liquid, and any solid with a periodic topography.

This thesis is an extension and application of the robustness framework to textured surfaces with a focus on commercially available textile fabrics. In Chapter 4, and Chapter 5, the theoretical framework is applied to a commercial polyester fabric (Anticon 100) to achieve stimuli responsive and tunable wettability for low surface tension liquids either using a thermal annealing treatment or a biaxial strain as stimulus.

In Chapter 6, the impact of chemical structure of the molecules used in the coating on their wettability is investigated. Fluorodecyl POSS and many analogous molecules were synthesized by Dr. Joseph Mabry and coworkers at the Edwards Air Force Base. In this work, we estimate the solid surface energy of these molecules based on frameworks developed by Zisman, Girifalco, Good coworkers. In Chapters 7, these design guidelines are applied to Army Combat Uniform fabrics to predict and enhance their non-wettability. These fabrics were supplied by Natick Soldier Research Development Engineering Center (NSRDEC).

The design principles that emerged from textile fabrics are applied to bird feather samples to quantify their wettability and to link the structure of the feather to its physiological behavior (Chapter 8). The bird feather samples were supplied by Dr. Andrew Parker from the Natural History Museum, London UK. Compared to microscopy, contact angle based characterization of the wetting aspects of hierarchically textured bird feathers is more objective. Using this technique of representing the bird feathers based on a simple cylindrical model, thermodynamics

of the wetting phenomena on a single feather can be better understood. Further, the influence of pressure perturbations on wetting of feathers during a dive can be quantified.

Finally, in Chapter 9, the understanding of solid-liquid interactions is applied to study and to improve the mechanism of fog harvesting using woven mesh surfaces. The surface topography and surface chemistry of woven wire mesh surfaces are varied and its impact on fog harvesting ability of the mesh is investigated. A business case for a fog collection based venture in Chile is presented by quantifying the uncertainty of the fog resource, suggesting strategies to alleviate some of this uncertainty and estimating the volatility of the cash flow.

2 Motivation and Background

2.1 Literature review

When a liquid in contact with a flat surface attains thermodynamic equilibrium, it exhibits a contact angle (θ_E), given by Young's relation $\cos \theta_E = (\gamma_{sv} - \gamma_{sl})/\gamma_{lv}$.[1] Here γ is the interfacial tension, and the subscripts s, l, and v denote the solid, liquid, and vapor phases, respectively. Altering the material chemistry of the solid surface changes the solid−liquid (γ_{sl}) and solid−vapor (γ_{sv}) interfacial tensions, thereby modifying the equilibrium contact angle (θ_E) for a given liquid on a solid surface.

When a liquid droplet contacts a textured solid surface, it can either form a fully wetted (Wenzel) interface with the liquid completely filling all the surface asperities,[2] or a composite solid−liquid−vapor (Cassie−Baxter) interface where numerous pockets of air are trapped underneath the contacting liquid.[3] Classically, the apparent contact angle (θ^*) for a liquid droplet on a composite interface has been computed by using the Cassie−Baxter (CB) relation [4-8]

$$\cos \theta^* = r_\phi \phi_s \cos \theta_E + \phi_s - 1 \qquad (2\text{-}1)$$

Here r_φ is the roughness (defined as the actual solid-liquid interfacial area divided by the projected area) of the wetted portion, φ_s is the area fraction of the liquid−air interface occluded by the solid texture, and θ_E is the equilibrium contact angle on a chemically identical smooth surface. The surface texture parameters r_φ and φ_s are schematically illustrated in Figure 2-1. If the liquid touches only the top of flat topped texture like an array of vertical pillars then $r_\varphi = 1$ (Figure 2-1A), and the CB relation simplifies to $\cos \theta^* = \phi_s \cos \theta_E + \phi_s - 1$. As a result of air entrapment in the composite state, it is possible to achieve high apparent contact angles ($\theta^* > 90°$) starting even with an inherently wetting surface (for which $\theta_E < 90°$), because as $r_\varphi \varphi_s \to 0$, $\theta^* \to 180°$.

28

The apparent contact angles obtained for a fully wetted interface are predicted by the Wenzel relation,

$$\cos\theta^* = r\cos\theta_E \qquad\qquad (2\text{-}2)$$

Here the roughness r is the ratio of the actual solid−liquid interfacial area to the projected solid−liquid interfacial area (shown in Figure 2-1). It should be noted that, in contrast to surfaces that can support a composite interface, surfaces that demonstrate large apparent contact angles in the Wenzel state require the smooth surface to be inherently nonwetting, i.e., $\theta_E > 90°$. On the other hand, for an inherently wetting surface, i.e., $\theta_E < 90°$, the Wenzel state leads to significantly lower apparent contact angles. Further, it is clear from the Wenzel relation that, as the roughness r becomes significantly greater than unity, the apparent contact angle $\theta^* \rightarrow 0°$ when $\theta_E < 90°$.
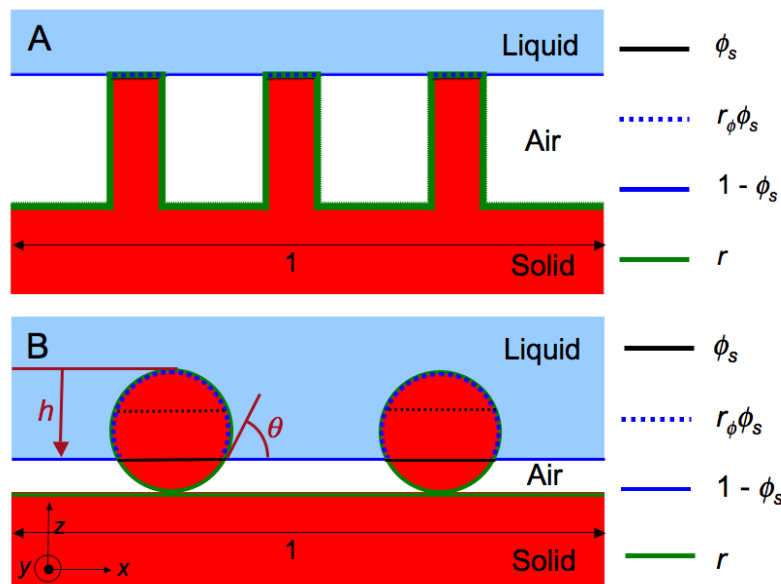
Figure 2-1. A schematic illustrating the various characteristic geometrical parameters used in the *Wenzel* and *Cassie-Baxter* relations for two different substrates (a) A flat-topped array of vertical pillars and (b) an array of cylinders possessing re-entrant texture. The gap between the features is significantly less than the liquids capillary length, an assumption that holds true for the various textures considered in this work. Thus, the liquid-vapor interface may be considered approximately flat, as shown in the figure.[7]

In addition, previous work has also shown that, as a consequence of the larger solid−liquid contact area in the fully wetted state, there is a higher chance of pinning of the

solid−liquid−vapor triple phase contact line, which results in significant contact angle hysteresis (*i.e.*, the difference between the apparent advancing and receding contact angles, $\Delta\theta = \theta^*_{adv} - \theta^*_{rec}$). The conditions for super non-wettability, *i.e.*, high apparent contact angles ($\theta^* > 150°$) and low contact angle hysteresis, can be realized only in the case of a composite interface where the solid−liquid contact area is low.[9]

2.2 Hydrophobic and oleophobic surfaces

There has been a lot of literature dedicated to the development of hydrophobic surfaces.[4, 10-24] In this section, I have provided a snapshot of some of the important contributions in the recent literature on surfaces with switchable and tunable wettability. Krupenkin and co-workers reported textured surfaces with a "Nanonail" like topography (shown in Figure 2-2(a)). Liquid droplets with a broad range of surface tensions form non-wetting composite interfaces on these nanonail surfaces (Figure 2-2(b)). Moreover, using electric voltage as a stimulus, wettability of theses surfaces could be tuned from a non-wetting composite state with high apparent contact angles to a fully-wetted state (Figure 2-2(c)). Apart from electric field (Figure 2-3(a)),[25] other stimuli like UV radiation (Figure 2-3(b)),[26, 27] heat (Figure 2-3(c)),[28] mechanical deformation (Figure 2-3(d)),[29] and pH[28] have been used to demonstrate switchable wettability on textured surfaces.

2.3 Hydrophobic and oleophobic textile surfaces

In this section, an overview of recent progress in the development of non-wettable textiles is presented. Please refer to various review articles for an exhaustive list of references.[20, 30] Ma and co-workers electrospun poly caprolactone (PCL) and coated the non-woven mat with poly alkyl ethyl methacrylate ($-CH_2=C(CH_3)COOCH_2CH_2(CF_2)_nCF_3$, n~7) using the iCVD technique to get a superhydrophobic surface.[31] They correlated various texture parameters like the radius of

30

an individual fiber and the spacing between fibers with the apparent contact angles. Their models

for bead-free and beed morphology, along with the predicted and measured values of apparent

contact angles are summarized in Figure 2-4.

Figure 2-2. (a) Nanonail geometry on a silicon wafer using reactive ion etching (b) Water and ethanol droplets bead up on this nanonail surface (c) The variation of apparent contact angle with applied voltage. A sharp wetting-dewetting transition is clearly seen for four alcohols.[25]
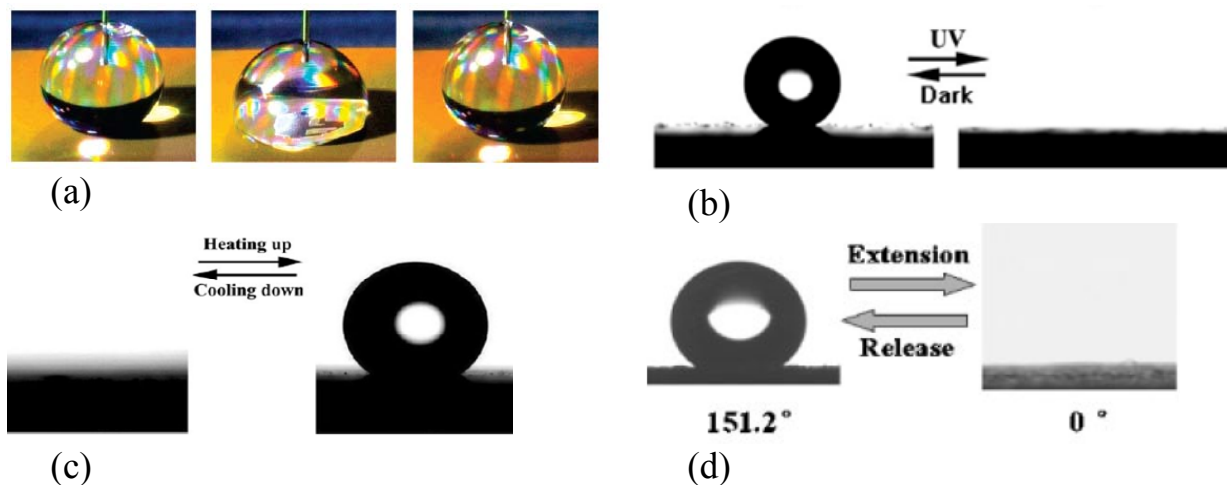
Figure 2-3. Stimuli-responsive superhydrophobic surfaces with (a) electrical voltage[25] (b) UV light[26] (c) temperature[28] and (d) mechanical strain[29] as a stimulus.

They correlated various texture parameters like the radius of an individual fiber and the spacing

between fibers with the apparent contact angles. Their models for bead-free and beed

morphology, along with the predicted and measured values of apparent contact angles are

summarized in Figure 2-4.
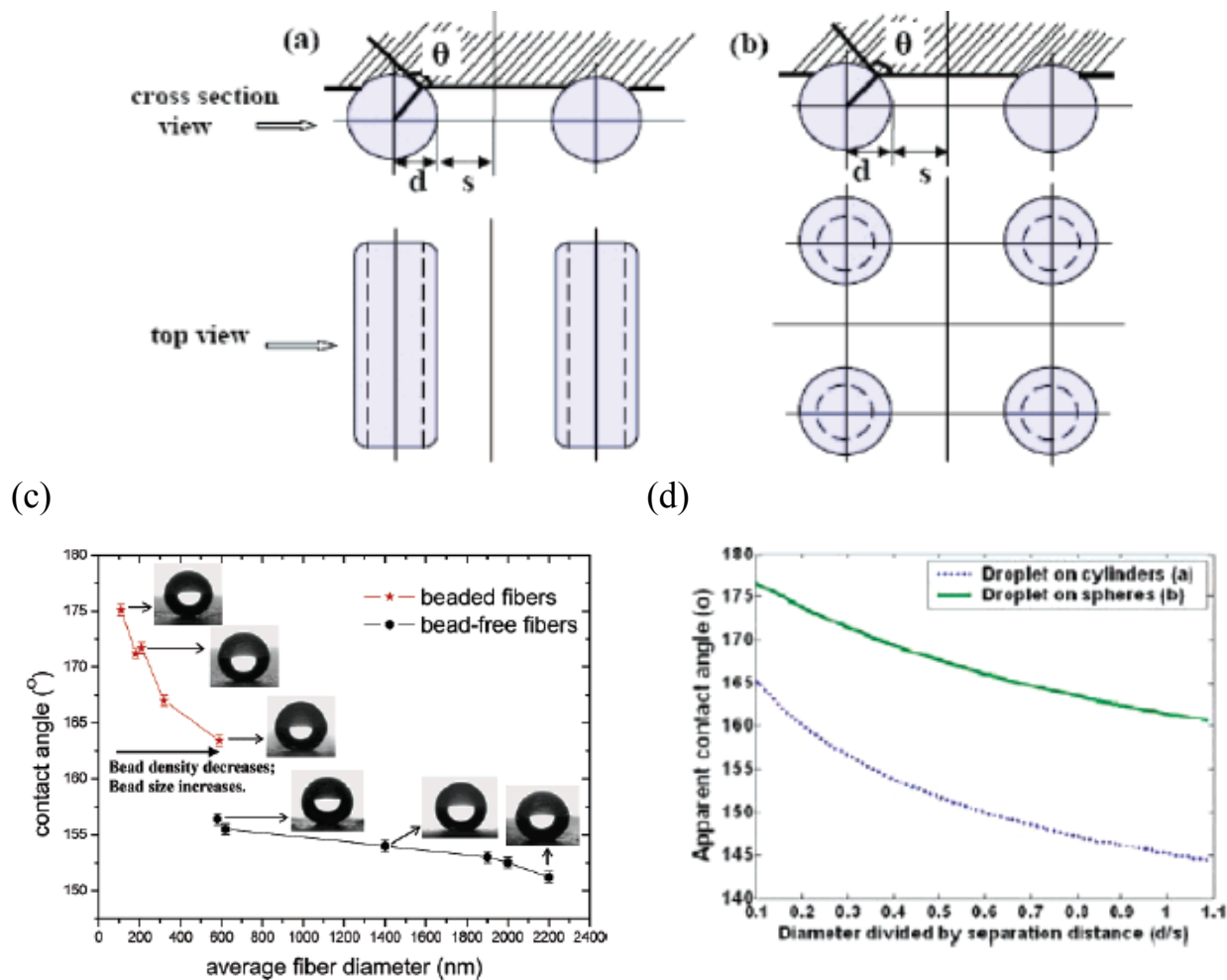
Figure 2-4. (a) and (b) Cartoons indicating the solid-liquid-air composite interface for bead-free and beaded fibers respectively. (c) Apparent contact angles (θ^*) of water droplets on perfluoroethyl methacrylate coated electrospun polycaprolactone fibers, and (d) theoretically expected values of the apparent contact angles are shown.[31]

Michielsen and Lee reported a superhydrophobic multifilament woven nylon fabric (SEM image shown in Figure 2-5(a)) coated with 1H, 1H–perfluorooctylamine grafted onto poly (acrylic acid). They measured contact angles on chemically equivalent smooth surfaces (θ_E) and coated textured fabrics (Figure 2-5(b), θ^*). Further, they modeled the fabric surface using monofilament or multifilament array of intertwined cylinders (as shown in Figure 2-5(c)).

(a)

(b)

(c)
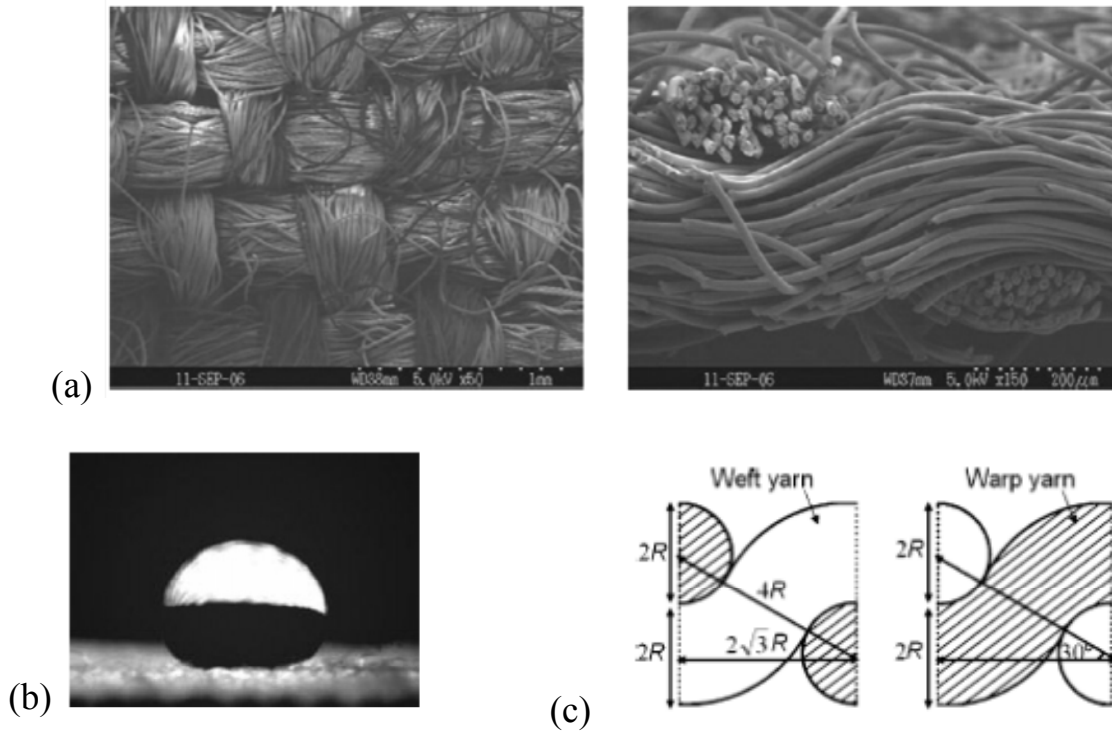
Figure 2-5. (a) SEM micrographs of a multifilament plain woven fabric, (b) a water droplet on the multifilament plain woven fabric with apparent contact angle $\theta^* = 168°$, and (c) cross-section views of a plain woven fabric at the warp and the weft yarn direction are shown.[5]

Brewer and Willis coated various textile fabrics using plasma polymerized perfluorodecyl acrylate (PFAC$_8$) to render those hydrophobic and oleophobic.[32] They recognized the individual role of a non-wettable surface coating and the underlying surface morphology of the textile fabric. Further they reported that hairy cotton provided the most non-wettable textured surface and even a mixture of hexane and pentane ($\gamma_{lv} = 17$ mN/m) did not wet the fabric.

Ming and co-workers reported superhydrophobic and oleophobic cotton textile fabric using an in-situ Stober process to modify the underlying texture of the cotton fabric.[33, 34] They reported that the underlying fabric texture was insufficient to provide non-wettability to low surface tension liquids like hexadecane ($\gamma_{lv} = 27.5$ mN/m). On the contrary, by introducing a micron-scale and a sub-micron scale texture, the fabric was rendered oleophobic.

33

(a)

(b)
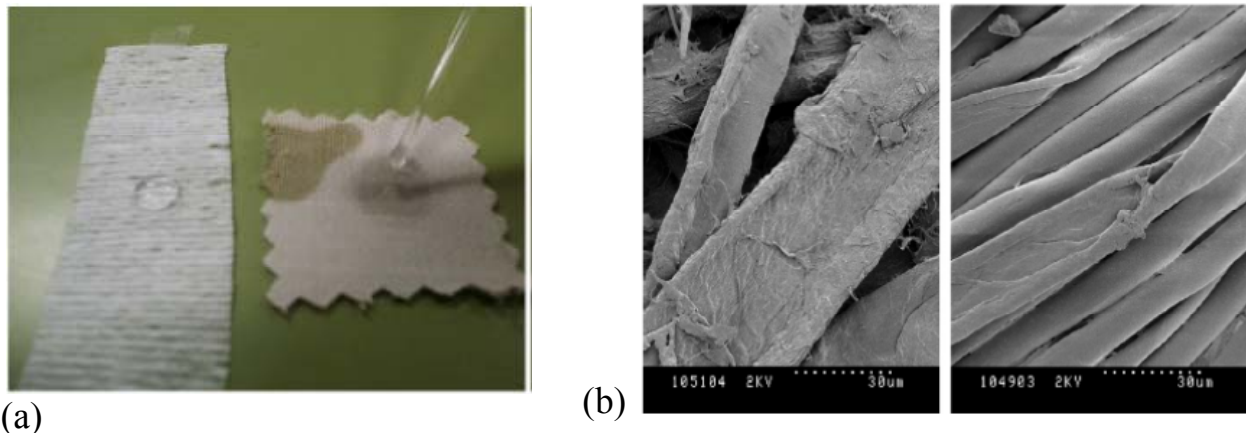
(c)

Textile material	Lowest surface tension liquid supported	Surface tension in mN/m
"Hairy" cotton material	Hexane / pentane	17.0
Cotton	n-heptane	20.1
Nylon	n-heptane	20.1
Polypropylene	n-heptane	20.1
Cotton arctic garbardine	n-octane	21.3
Polyester	n-octane	21.3
Polyester / cotton (67 / 33)	n-octane	21.3
Nomex	n-octane	21.3
Wood / polyester (45 / 55)	n-dodecane	25.1

Figure 2-6. (a) Both materials have been rendered liquid repellent by a PFAC8 coating. Unlike the material on the right, the left material can support a liquid drop of hexane. Images in (b) are SEMs for the respective materials. (c) Repellent properties of various textiles that have been rendered oleophobic are tabulated.[32]

(a)   (b)
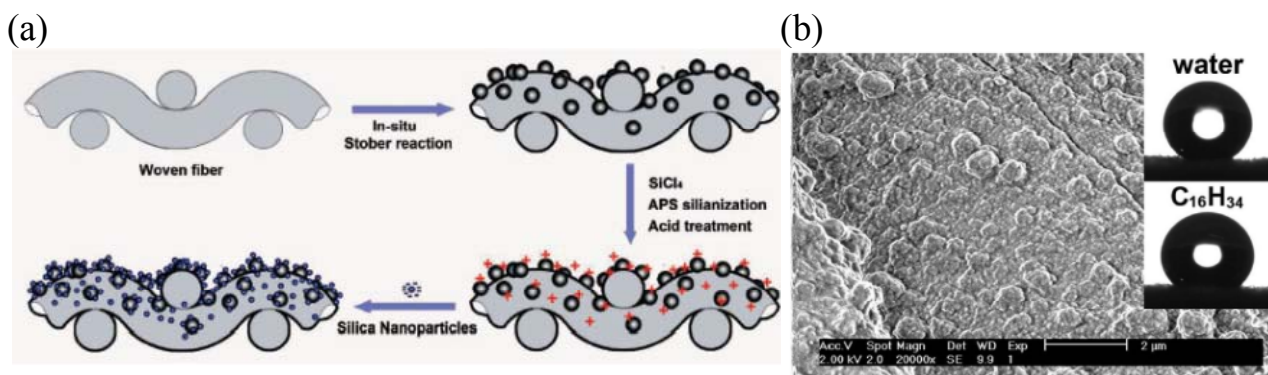
Figure 2-7. (a) Schematic Illustration of the Procedure for the Preparation of Dual-Size Structure onto the Surface of Woven Cotton Fibers, Combining an *In Situ* Stober Reaction with the Subsequent Adsorption of Silica Nanoparticles (b) Morphology of sample observed by SEM. Insets are profiles of water and hexadecane ($C_{16}H_{34}$) on the corresponding sample.[34]

2.4 Concept of re-entrance

Tuteja, Choi and co-workers postulated that the presence of re-entrant texture is a necessary condition to support a non-wetting composite interface for low surface tension liquids with low equilibrium contact angles ($\theta_E < 90°$).[6-8, 35] Re-entrant topography is defined as texture that bends back on itself, or a normal drawn to the horizontal intersects the texture in more than one point.
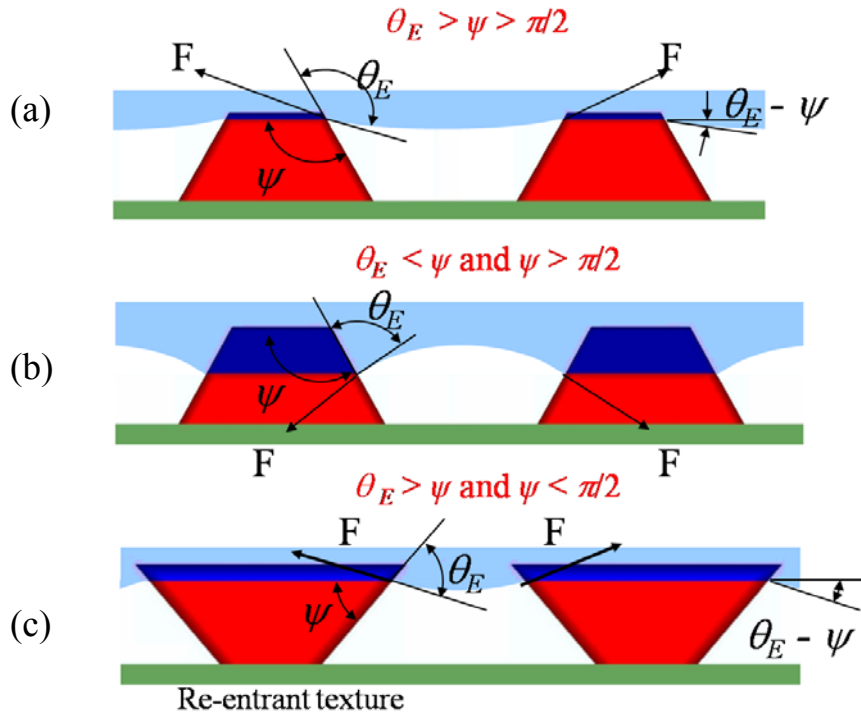
Figure 2-8. Liquid-vapor interface for a liquid with Young's contact angle θ_E on a rough solid with geometry angle ψ for the case (a) $\theta_E > \psi > 90°$, (b) $\theta_E < \psi$, $\psi > 90°$ and (c) $\psi < \theta_E < 90°$.[6, 7]

The texture is characterized using a texture angle ψ, which is the angle made by a local tangent to the texture with the horizontal measured inside the solid texture. Figure 2-8 represents model textures with a constant texture angle ψ. If $\psi > 90°$, then the texture is called as an entrant texture and it can support a composite interface only if the equilibrium contact angle (θ_E) of a liquid is larger than the texture angle ($\theta_E > \psi > 90°$, Figure 2-8(a)). On the contrary, if $\theta_E < \psi$, the net traction of the liquid-vapor interface is downwards and the texture promotes wetting (Figure 2-8(b)). Therefore surfaces with entrant texture can support composite interfaces only for high

surface tension liquids for which high equilibrium contact angles can be achieved by tuning the surface chemistry of the solid. For low surface tension liquids like methanol or octane, no surface chemistry exists for which $\theta_E > 90°$, therefore these liquids cannot form solid-liquid-air composite interfaces on surfaces with entrant texture.
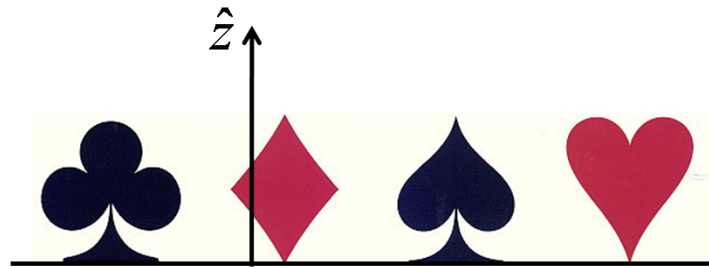
Figure 2-9. All the four card shapes are examples of re-entrant texture as a normal intersects the solid texture at more than one location. Club and spade shapes have $\psi_{min} < 0°$ whereas diamond and heart shapes have $\psi_{min} > 0°$.[7]

On the contrary for a re-entrant texture ($\psi < 90°$, Figure 2-8(c)), the net traction of liquid-vapor interface inhibits wetting if $\theta_E > \psi$. Therefore by reducing the magnitude of the texture angle ψ, it is possible (at least in theory) to achieve a composite interface for any liquid with a non-zero equilibrium contact angle, as long as $\theta_E > \psi$. For textures where the local texture angle changes at every point, a composite interface is possible if $\theta_E > \psi_{min}$. The minimum texture angle (ψ_{min}) is zero for spheres and cylinders, whereas $\psi_{min} < 0°$ for special texture like the club or spade card shapes (Figure 2-9). All the four card shapes are common examples of re-entrant texture, but the heart and diamond have $\psi_{min} > 0°$ whereas for club and spade, $\psi_{min} < 0°$. Note that the presence of re-entrant texture is **a necessary but not a sufficient condition** for the formation of non-wetting composite interfaces. The existence and robustness of these composite interfaces can be predicted by investigating the thermodynamic landscape, which is described in the next couple of sections.

2.5 Metastability of the composite interface

For low surface tension liquids with $\theta_E < 90°$, the fully wetted or Wenzel state represents the thermodynamic equilibrium state, whereas the composite interface or the Cassie−Baxter state is at best metastable, representing a local minimum in the overall free energy.[6, 7, 18, 22, 36-39] Thus, for low surface tension liquids, the transition from a composite interface to a fully wetted interface is irreversible, and typically this transition leads to a loss of super non-wettability. Tuteja and co-workers estimated the free energy of a solid-liquid-air composite interface for various model textures as a function of relative penetration depth (z/h_{max}) and apparent contact angle (θ_t^*).[7] In Figure 2-10, the free energy landscape for a model texture consisting of an array of cylinders is shown. For water ($\gamma_{lv} = 72.1$ mN/m) droplets on a hydrophobic surface (fluorodecyl POSS, $\theta_E \approx 120°$) the Cassie-Baxter state (composite interface) was found to be the global minimum whereas the Wenzel state (fully-wetted interface) represents a local energy minimum. For hexadecane droplets ($\gamma_{lv} = 27.5$ mN/m) on the same surface ($\theta_E \approx 80°$), the fully-wetted interface was the global minimum and the composite state was a local minimum.

From the free energy landscape, they estimated the breakthrough pressure (P_b) required for the disruption of a metastable composite interface and transition to a fully-wetted interface. Using this method, the breakthrough pressure was estimated to be infinity for re-entrant textured surface with $\psi_{min} \leq 0°$. This prediction was in stark contrast with the experimental observations of finite breakthrough pressure for such surfaces. In these simulations, the liquid-air interface was assumed to be flat even when there is a finite pressure difference across it. In reality, this assumption breaks down and the transition from a composite to a fully-wetted interface occurs via local sagging and distortion of the liquid-air interface and not by the displacement of a flat liquid-air interface down to the bottom of the surface topography. The robustness of a composite

37

interface against sagging of the air-liquid interface was quantified using a design parameter approach described in the following sections.

Water ($\theta_E = 120°$) on 44 wt% POSS e-spun surface
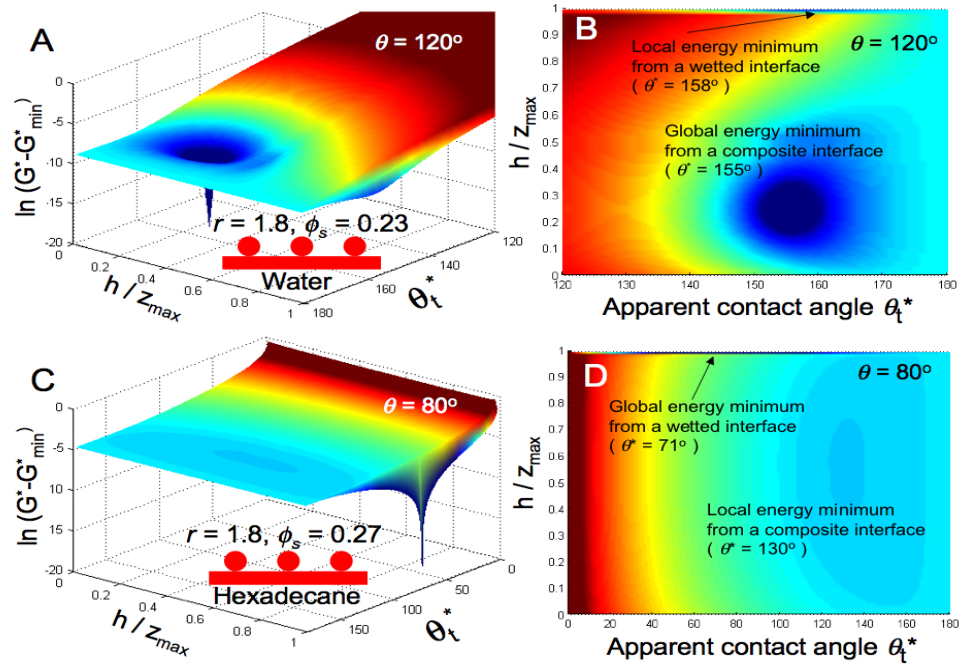
Hexadecane ($\theta_E = 80°$) on 44 wt% POSS e-spun surface

Figure 2-10. Variation in areal Gibbs free energy density as a function of contact angle and dimensionless height (h/z$_{max}$) is shown (a) for water (c) and hexadecane. The inset shows schematic of the surface geometry. (b) Contour plot (top view) of free energy plot for water (d) top view for hexadecane plot. The local and global equilibrium states are indicated.[7]

2.6 The robustness of a composite interface

Tuteja and co-workers introduced the concept of robustness factor (A^*), which is a dimensionless estimate of the breakthrough pressure (P_b), scaled with respect to a reference pressure ($P_{ref} = 2\gamma_{lv}/\ell_{cap}$), where $\ell_{cap} (= \sqrt{\gamma_{lv}/\rho g})$ is the capillary length, γ_{lv} is the surface tension and ρ is the density of the liquid. The reference pressure (P_{ref}) is chosen because it is close to a minimum pressure differential that can exist across a millimetric-scale curved air-liquid interface.

The equilibrium shape of a liquid droplet is governed by the balance between the gravity and surface tension forces acting on it. When the droplet is small ($R_{drop} << \ell_{cap}$, Figure 2-11(a)), gravity can be neglected in favor if surface tension and the droplet is nearly spherical.

38
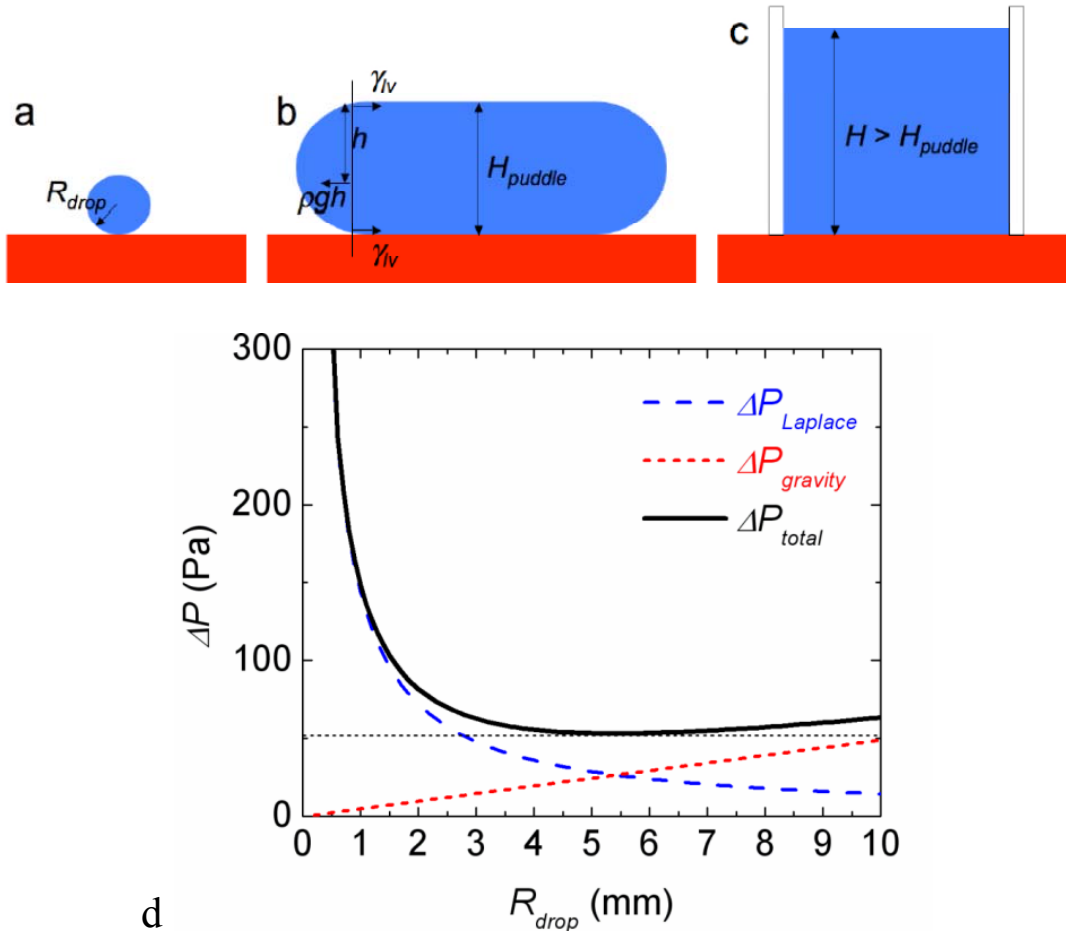
Figure 2-11. A schematic illustrating the various shapes of a liquid volume on an omniphobic surface. (a) A liquid droplet adopts the shape of perfect sphere when $R_{drop} << \ell_{cap}$ or $Bo << 1$. (b) A liquid volume forms a puddle when $Bo >> 1$. (c) A schematic of a large volume of liquid confined within a tube.[7] (d) The pressure difference across a curved air-liquid interface as a function of the radius of the water droplet ($\ell_{cap} = 2.7$ mm) is plotted.

The pressure differential across the droplet surface is given by the Laplace equation i.e.

$\Delta P \approx P_{Laplace} = 2\gamma_{lv}/R_{drop}$ (Figure 2-11(d)). As the droplet size increases ($R_{drop} \sim \ell_{cap}$, Figure

2-11(b)), the shape deviates from a sphere and flattens to a puddle. Now, the pressure at the

bottom of the puddle is the sum of a Laplace pressure and a hydrostatic head *i.e.*

$\Delta P = P_{Laplace} + P_{gravity}$. When more liquid volume is added, the liquid spreads on a higher area and

the height of the puddle never exceeds 2 ℓ_{cap}. Only if the liquid is constrained (ex. using vertical

walls like Figure 2-11(c)), the liquid level and consequently the pressure differential increases.

39

The variation of total pressure differential is schematically shown for a typical case with $\theta^* = 120°$ in Figure 2-11(d). It is very clear that P_{ref} is close to lowest pressure differential across a curved air-liquid interface and therefore it is a judicious choice of a pressure scale for the robustness parameter. Consequently, when $A^* < 1$, then the estimated breakthrough pressure (P_b) is lower than P_{ref}, and therefore such a curved air-liquid interface cannot exist. Therefore any combination of a textured surface and a probing liquid for which $A^* \leq 1$ is unable to support a composite interface and $A^* > 1$ becomes a necessary condition for the existence of a robust composite interface. Inspired from the concept of re-entrance and robustness factor, Tuteja *et. al*. reported micro-hoodoo like surfaces, which are not wetted by liquids with a broad range of surface tension (shown in Figure 2-12(a)), and therefore termed "Omniphobic."[7]
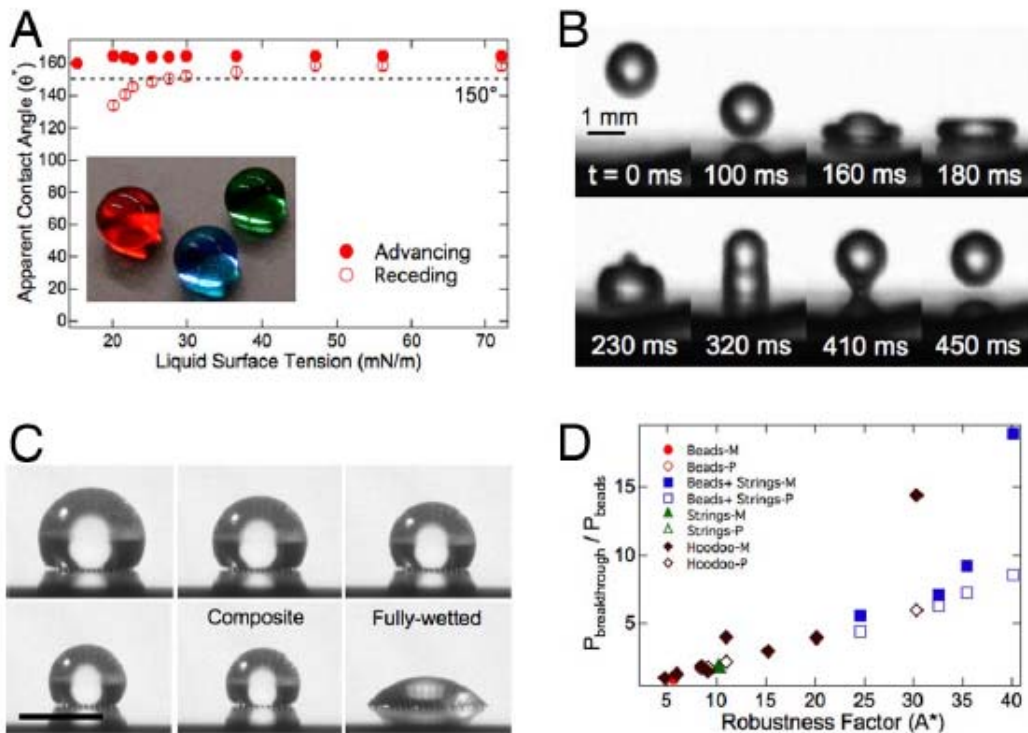
Figure 2-12. Omniphobicity of microhoodoo arrays. (A) The apparent advancing and receding contact angles on a silanized microhoodoo surface. The inset shows droplets of heptane (red), methanol (green), and water (blue) on the microhoodoo surface. (B) A series of images obtained using a high-speed digital video camera that illustrates the bouncing of a droplet of hexadecane on a silanized microhoodoo surface. (C) A series of images (obtained over a period of 5 min),

showing the evaporation of a droplet of methanol under ambient conditions, on a microhoodoo surface. (Scale bar, 1 mm). (*D*) A master curve showing the measured (filled symbols) breakthrough pressures for a number of microhoodoo and electrospun surfaces with various alkanes and alcohols, scaled with the breakthrough pressure of octane on the electrospun beads-only surface containing 44.4 wt% POSS, as a function of the robustness factor *A**. Predictions (hollow symbols) for the breakthrough pressures are also shown.[7]

These surfaces were not wetted by low surface tension liquids like hexadecane (γ_{lv} = 27.5 mN/m, Figure 2-12(b)) or methanol (γ_{lv} = 22.6 mN/m, Figure 2-12(c)). Methanol droplets are very volatile, and as the droplet size decreases, the Laplace pressure inside the droplet increases. Beyond a threshold the pressure differential becomes higher than P_b and the droplet transitions from a non-wetting composite state to a fully-wetted state (Figure 2-12(c)). Using the evaporating droplet test, the breakthrough pressure was measured for various microhoodoo surfaces and compared against theoretical prediction in Figure 2-12(d).

2.7 Main aims of the thesis

- A theoretical framework to predict the apparent contact angle (θ^*) and the breakthrough pressure (P_b) for the disruption of a composite interface has been developed previously in our research groups. The main aim of my thesis is to apply this robustness framework to commercially available textiles and predict the wettability of those fabrics.

- There is a considerable interest in developing oil, water and other chemical repellent (omniphobic) army combat uniform (ACU). The robustness framework will be used to quantify the impact of surface chemistry of the coating and the surface topography of the fabrics on its wettability. Based on the analysis, specific recommendations will be made to guide the design of omniphobic ACU fabric.

- The robustness parameter framework is currently in the form of a set of algebraic equations. One of the aims of this thesis is to express the framework in the form of a graphical design chart. These charts will serve as an engineering tool for designers to fabricate omniphobic

surfaces and *apriori* predict their wettability. Moreover, the impact of individual physico-chemical parameter on apparent contact angles (θ^*) and robustness (A^*, P_b) will be studied using these charts.

- Guided by the design parameters, oleophobic surfaces with tunable and switchable wettability will be designed based on biaxial mechanical strain, and tunable surface chemistry as a stimulus.

- Selection of the coating to provide high equilibrium contact angle (θ_E) is an important component of developing oleophobic surfaces. A structure / property analysis will be done on a series of fluoroalkylated silicon-containing compounds to analyze their wettability using Girifalco-Good method.

- The robustness parameter / design chart framework will be extended to predict wettability of bird feathers. The influence of feather texture on their wettability and consequently on the physiological behavior of the birds will be assessed.

- The understanding about wettability of textured surfaces will be extended to study the fog harvesting ability of coated wire mesh surfaces.

2.8 References

1. Young, T., An Essay on the Cohesion of Fluids. *Philosophical Transactions of the Royal Society of London* **1805,** 95, 65-87.
2. Wenzel, R. N., Resistance of solid surfaces to water by wetting. *Ind. Eng. Chem.* **1936,** 28, (8), 988-994.
3. Cassie, A.; Baxter, S., Wettability of porous surfaces. *Transactions of the Faraday Society* **1944,** 40, 546-551.
4. Marmur, A., Wetting on Hydrophobic Rough Surfaces: To Be Heterogeneous or Not To Be? *Langmuir* **2003,** 19, (20), 8343-8348.
5. Michielsen, S.; Lee, H. J., Design of a Superhydrophobic Surface Using Woven Structures. *Langmuir* **2007,** 23, (11), 6004-6010.
6. Tuteja, A.; Choi, W.; Ma, M.; Mabry, J. M.; Mazzella, S. A.; Rutledge, G. C.; McKinley, G. H.; Cohen, R. E., Designing Superoleophobic Surfaces. *Science* **2007,** 318, (5856), 1618-1622.

7.   Tuteja, A.; Choi, W.; Mabry, J. M.; McKinley, G. H.; Cohen, R. E., Robust omniphobic surfaces. *Proceedings of the National Academy of Sciences, USA* **2008**, 18200-18205.

8.   Tuteja, A.; Choi, W.; McKinley, G. H.; Cohen, R. E.; Rubner, M. F., Design parameters for superhydrophobicity and superoleophobicity. *MRS Bulletin* **2008,** 33, (8), 752-758.

9.   Johnson, R.; Dettre, R., *Contact angle hysteresis. In Contact Angle, Wettability and Adhesion*. American Chemical Society: Wahington, D.C., 1964.

10.   Patankar, N. A., Transition between Superhydrophobic States on Rough Surfaces. *Langmuir* **2004,** 20, (17), 7097-7102.

11.   Patankar, N. A., Mimicking the Lotus Effect: Influence of Double Roughness Structures and Slender Pillars. *Langmuir* **2004,** 20, (19), 8209-8213.

12.   Quéré, D., Rough ideas on wetting. *Physica A* **2002,** 313, 32-46.

13.   Quéré, D., Non-sticking drops. *Reports on Progress in Physics* **2005**, (11), 2495.

14.   Quéré, D., Wetting and Roughness. *Annual Review of Materials Research* **2008,** 38, (1), 71-99.

15.   Shibuichi, S.; Onda, T.; Satoh, N.; Tsujii, K., Super Water-Repellent Surfaces Resulting from Fractal Structure. *Journal of Physical Chemistry* **1996,** 100, (50), 19512-19517.

16.   Shibuichi, S.; Yamamoto, T.; Onda, T.; Tsujii, K., Super Water- and Oil-Repellent Surfaces Resulting from Fractal Structure. *Journal of Colloid and Interface Science* **1998,** 208, (1), 287-294.

17.   He, B.; Patankar, N. A.; Lee, J., Multiple Equilibrium Droplet Shapes and Design Criterion for Rough Hydrophobic Surfaces. *Langmuir* **2003,** 19, (12), 4999-5003.

18.   Herminghaus, S., Roughness-induced non-wetting. *Europhysics Letters* **2000,** 52, (2), 165.

19.   Marmur, A., From Hygrophilic to Superhygrophobic: Theoretical Conditions for Making High-Contact-Angle Surfaces from Low-Contact-Angle Materials. *Langmuir* **2008,** 24, (14), 7573-7579.

20.   Marmur, A., Solid-Surface Characterization by Wetting. *Annual Review of Materials Research* **2009,** 39, (1), 473-489.

21.   McHale, G.; Shirtcliffe, N. J.; Aqil, S.; Perry, C. C.; Newton, M. I., Topography Driven Spreading. *Physical Review Letters* **2004,** 93, (3), 036102.

22.   Nosonovsky, M., Multiscale Roughness and Stability of Superhydrophobic Biomimetic Interfaces. *Langmuir* **2007,** 23, (6), 3157-3161.

23.   Nosonovsky, M.; Bhushan, B., Patterned Nonadhesive Surfaces: Superhydrophobicity and Wetting Regime Transitionsâ€ *Langmuir* **2008,** 24, (4), 1525-1533.

24.   Onda, T.; Shibuichi, S.; Satoh, N.; Tsujii, K., Super-Water-Repellent Fractal Surfaces. *Langmuir* **1996,** 12, (9), 2125-2127.

25.   Ahuja, A.; Taylor, J. A.; Lifton, V.; Sidorenko, A. A.; Salamon, T. R.; Lobaton, E. J.; Kolodner, P.; Krupenkin, T. N., Nanonails: A Simple Geometrical Approach to Electrically Tunable Superlyophobic Surfaces. *Langmuir* **2008,** 24, (1), 9-14.

26.   Feng, X.; Feng, L.; Jin, M.; Zhai, J.; Jiang, L.; Zhu, D., Reversible Super-hydrophobicity to Super-hydrophilicity Transition of Aligned ZnO Nanorod Films. *Journal of the American Chemical Society* **2004,** 126, (1), 62-63.

27.   Feng, X. J.; Jiang, L., Design and Creation of Superwetting/Antiwetting Surfaces. *Advanced Materials* **2006,** 18, (23), 3063-3078.

28. Sun, T.; Wang, G.; Feng, L.; Liu, B.; Ma, Y.; Jiang, L.; Zhu, D., Reversible Switching between Superhydrophilicity and Superhydrophobicity. *Angewandte Chemie International Edition* **2004,** 43, (3), 357-360.

29. Zhang, J.; Lu, X.; Huang, W.; Han, Y., Reversible Superhydrophobicity to Superhydrophilicity Transition by Extending and Unloading an Elastic Polyamide Film. *Macromolecular Rapid Communications* **2005,** 26, (6), 477-480.

30. Ma, M.; Hill, R. M.; Rutledge, G. C., A Review of Recent Results on Superhydrophobic Materials Based on Micro- and Nanofibers. *Journal of Adhesion Science and Technology* **2008,** 22, 1799-1817.

31. Ma, M.; Mao, Y.; Gupta, M.; Gleason, K. K.; Rutledge, G. C., Superhydrophobic Fabrics Produced by Electrospinning and Chemical Vapor Deposition. *Macromolecules* **2005,** 38, (23), 9742-9748.

32. Brewer, S. A.; Willis, C. R., Structure and oil repellency: Textiles with liquid repellency to hexane. *Applied Surface Science* **2008,** 254, (20), 6450-6454.

33. Hoefnagels, H. F.; Wu, D.; deWith, G.; Ming, W., Biomimetic Superhydrophobic and Highly Oleophobic Cotton Textiles. *Langmuir* **2007,** 23, (26), 13158-13163.

34. Leng, B.; Shao, Z.; de With, G.; Ming, W., Superoleophobic Cotton Textiles. *Langmuir* **2009,** 25, (4), 2456-2460.

35. Choi, W.; Tuteja, A.; Chhatre, S.; Mabry, J. M.; Cohen, R. E.; McKinley, G. H., Fabrics with tunable oleophobicity. *Advanced Materials* **2009,** 21, (21), 2190-2195.

36. Cao, L.; Hu, H.; Gao, D., Design and Fabrication of Micro-textures for Inducing a Superhydrophobic Behavior on Hydrophilic Materials. *Langmuir* **2007,** 23, (8), 4310-4314.

37. Cao, L.; Price, T. P.; Weiss, M.; Gao, D., Super Water- and Oil-Repellent Surfaces on Intrinsically Hydrophilic and Oleophilic Porous Silicon Films. *Langmuir* **2008,** 24, (5), 1640-1643.

38. Jian-Lin, L.; Xi-Qiao, F.; Gangfeng, W.; Shou-Wen, Y., Mechanisms of superhydrophobicity on hydrophilic substrates. *Journal of Physics: Condensed Matter* **2007,** 19, (35), 356002.

39. Kurogi, K.; Yan, H.; Tsujii, K., Importance of pinning effect of wetting in super water-repellent surfaces. *Colloids and Surfaces A: Physicochemical and Engineering Aspects* **2008,** 317, (1-3), 592-597.

3 Design chart for liquid wettability of cylindrically textured surfaces

The main contribution of this thesis is the conceptualization of a design chart to predict the wettability of textured surfaces. The design chart is used to predict the apparent contact angle (θ^*) and robustness (A^*) of the solid-liquid-air composite interfaces. In the current chapter, development of the design chart is outlined and the chart is applied to successfully predict wettability of woven mesh surfaces.

3.1 Apparent contact angles on dip-coated carbon paper

To test the utility of the robustness factor framework, a commercially available cylindrically textured surface (carbon paper from Toray, Japan) was selected. It was dip-coated with a 50% POSS – 50% Tecnoflon solution and the apparent contact angle was measured using various test liquids. In our previous work,[1] we demonstrated that the effective spacing ratio (D^*) is readily obtained by fitting the CB relation (Equation 3.1) to the advancing contact angle data plotted as ($\cos\theta^*_{adv}$ vs $\cos\theta_{adv}$). The spacing ratio is given by $D^* = (R+D)/R$, where R is the radius of the cylindrical texture, $2D$ is the spacing between two cylinders and θ_E is the equilibrium contact angle. Using the value of the spacing ratio (D^*) determined from this fit, the dimensionless robustness factor (A^*, Equation 3.2) can also be plotted on the same non-wetting diagram, and the magnitude of the robustness factor helps to rationalize the transition from the composite to the fully-wetted interface.

$$\cos\theta^* = -1 + \frac{1}{D^*}\left[(\pi - \theta_E)\cos\theta_E + \sin\theta_E\right] \qquad (3\text{-}1)$$

$$A^* = \frac{\ell_{cap}}{R}\left(\frac{1}{D^* - 1}\right)\left(\frac{1 - \cos\theta_E}{D^* - 1 + 2\sin\theta_E}\right) \qquad (3\text{-}2)$$

For the carbon paper example in Figure 3-1, the spacing ratio was computed to be $D^* = 4.1 \pm 0.6$

from regression to the measured advancing contact angle data on the textured (θ^*_{adv}) and smooth

surface (θ_{adv}).[1] The coated carbon paper surface is superhydrophobic with $\theta^*_{adv} = 153 \pm 2°$ for

water droplets. Liquids like methanol ($\gamma_{lv} = 22.7$ mN/m, $\theta_{adv} = 55 \pm 3°$, $\theta^*_{adv} = 120 \pm 3°$, $A^* = 8.1$)

and octane ($\gamma_{lv} = 21.6$ mN/m, $\theta_{adv} = 51 \pm 3°$, $\theta^*_{adv} = 106 \pm 3°$, $A^* = 6.9$) also formed robust

composite interfaces on the dip-coated carbon paper ($R = 6$ μm, $D^* = 4.1 \pm 0.6$). On the contrary,

heptane ($\gamma_{lv} = 20.1$ mN/m, $\theta_{adv} = 45 \pm 3°$, $\theta^*_{adv} \approx 0°$, $A^* = 5.8$) wetted the textured surface. The

observed spontaneous wetting by heptane was not expected because according to the design

parameter framework, the solid-liquid-air composite interface is robust for all values of $A^* > 1$.

Although the trend of decreasing apparent contact angle and robustness measurements with

changes in γ_{lv} is qualitatively correct, it is clear that the criterion is not a quantitative predictor of

the crossover from a Cassie-Baxter[2] (composite interface) to a Wenzel[3] (fully wetted) state. From

the SEM micrograph of the carbon paper surface, it is clear that the individual fibers forming the

re-entrant texture are distributed randomly and there is a considerable local variation in the value

of D^*. Therefore the carbon paper surface or any other nonwoven fiber mat surface with a broad

variation in the surface topography is not suitable for quantitative analysis of the effect of

varying topographical and surface properties on liquid non-wettability and robustness.

Consequently, in the following sections we turn to a series of woven meshes, each with regular

periodic texture, as the model textured surfaces.

(a)
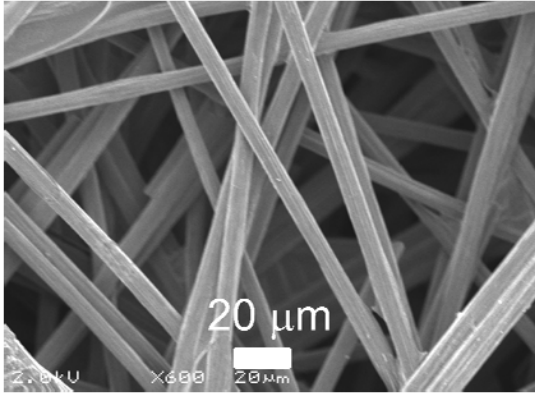
(b)
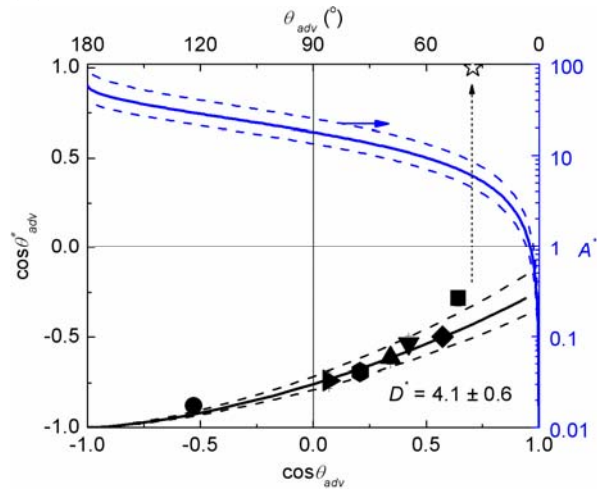
Figure 3-1(a) SEM image of the microfiber carbon paper (Toray, Japan) dip-coated with 50% POSS – 50% Tecnoflon. (b) Generalized wetting diagram for a 50 % POSS – 50% Tecnoflon (γ_{sv} = 10.7 mN/m) coated carbon paper. Apparent advancing contact angle data is plotted using water ($\bullet$, γ_{lv} = 72.1 mN/m), rapeseed oil ($\blacktriangleright$, γ_{lv} = 35.5 mN/m), hexadecane ($\blacklozenge$, γ_{lv} = 27.5 mN/m), dodecane ($\blacktriangle$, γ_{lv} = 25.3 mN/m), decane ($\blacktriangledown$, γ_{lv} = 23.8 mN/m), methanol ($\blacklozenge$, γ_{lv} = 22.7 mN/m), octane ($\blacksquare$, γ_{lv} = 21.6 mN/m), and heptane ($\star$, γ_{lv} = 20.1 mN/m). The spacing ratio is found to be $D^* = 4.1 \pm 0.6$ from the regression of the CB relation (Equation (3.1)) to the contact angle data and the robustness factor is computed using this value of the D^* (Equation (3.2)).

3.2 Contact angle measurements on dip-coated woven meshes

The woven meshes offer a set of periodic textured surfaces which are commercially available.

The mesh number refers to the number of openings per inch, therefore a smaller mesh number

indicates a coarse mesh and a larger mesh number indicates a finer mesh. The influence of

chemical interaction between various liquids and coating materials (θ_E), the characteristic

cylinder length scale (R), and the spacing between cylindrical fibers (D^*) on the wettability (θ^*)

and robustness (A^*) can be systematically evaluated by measuring the apparent contact angles on

woven meshes with a variety of coatings, wire radii, and spacing ratios respectively. In the first

set of experiments, three wire meshes (mesh 50 with R = 114 μm, mesh 100 with R = 57 μm and

mesh 325 with R = 18 μm) with identical spacing ratio (D^* = 2.2) were selected (Figure 3-2).
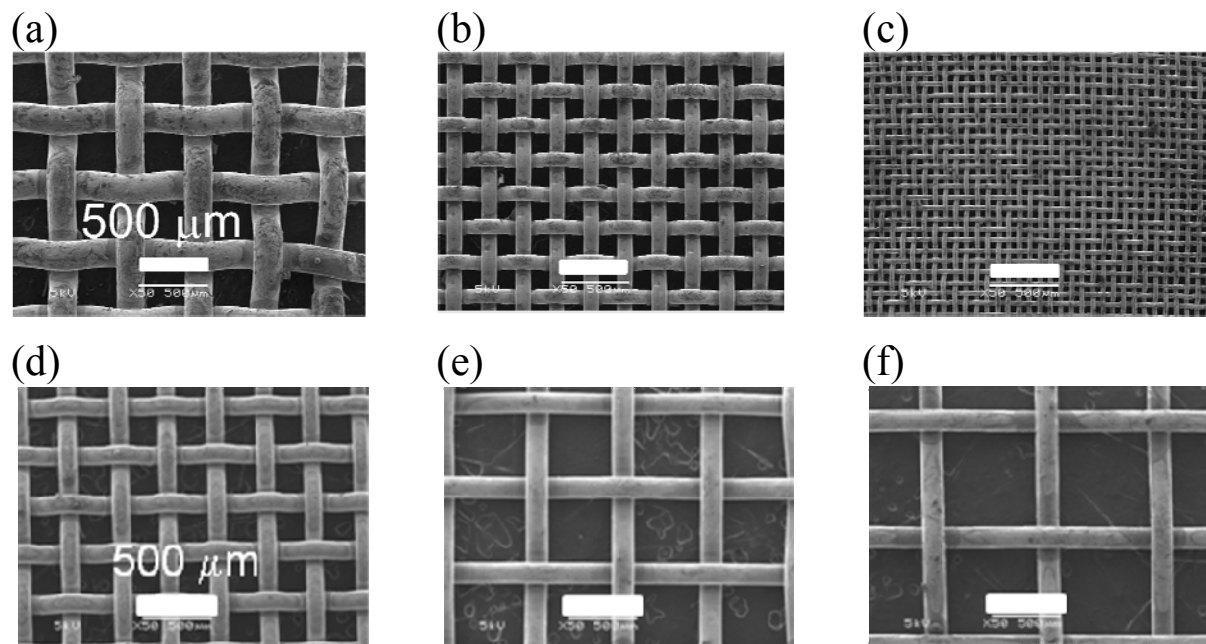
Figure 3-2. SEM micrographs of six woven meshes – (a) mesh 50 ($R = 114$ μm, $D^* = 2.2$), (b) mesh 100 ($R = 57$ μm, $D^* = 2.2$), (c) mesh 325 ($R = 18$ μm, $D^* = 2.2$), (d) mesh 30 ($R = 83$ μm, $D^* = 2.2$), (e) mesh 40 ($R = 83$ μm, $D^* = 3.9$), and (f) mesh 70 ($R = 83$ μm, $D^* = 5.1$) are shown. Due to the regularity of the mesh texture, the dimensionless spacing ratio (D^*) could be estimated from inspection of the SEM micrographs.

These wire meshes were each dip-coated using different solutions with a range of solid surface energies (γ_{sv}): (i) a 50/50 (by weight) mixture of fluorodecyl POSS and Tecnoflon (BR 9151, a fluoroelastomer from Solvay-Solexis), (ii) pure Tecnoflon and (iii) polyethyl methacrylate (PEMA). The solid surface energies (γ_{sv}) of (i) 10.7, (ii) 18.3 and (iii) 32.2 mN/m were estimated using the Owens-Wendt analysis with water and octane as the probing liquids.[4] Different polar liquids (water ($\gamma_{lv} = 72.1$ mN/m), ethylene glycol ($\gamma_{lv} = 47.7$ mN/m), and methanol ($\gamma_{lv} = 22.7$ mN/m)), non-polar liquids (methylene iodide ($\gamma_{lv} = 50.8$ mN/m) and rapeseed oil ($\gamma_{lv} = 35.5$ mN/m) in addition to a homologous series of n-alkanes starting from hexadecane ($\gamma_{lv} = 27.5$ mN/m) to pentane ($\gamma_{lv} = 15.5$ mN/m)) were used as contacting liquids for contact angle measurements. The advancing contact angle measurements on flat spin-coated silicon wafer

48

surfaces (θ_{adv}) and the textured dip-coated mesh surfaces (θ_{adv}^*) can all be displayed in a compact

manner on the generalized wetting diagram, as shown in Figure 3-3.
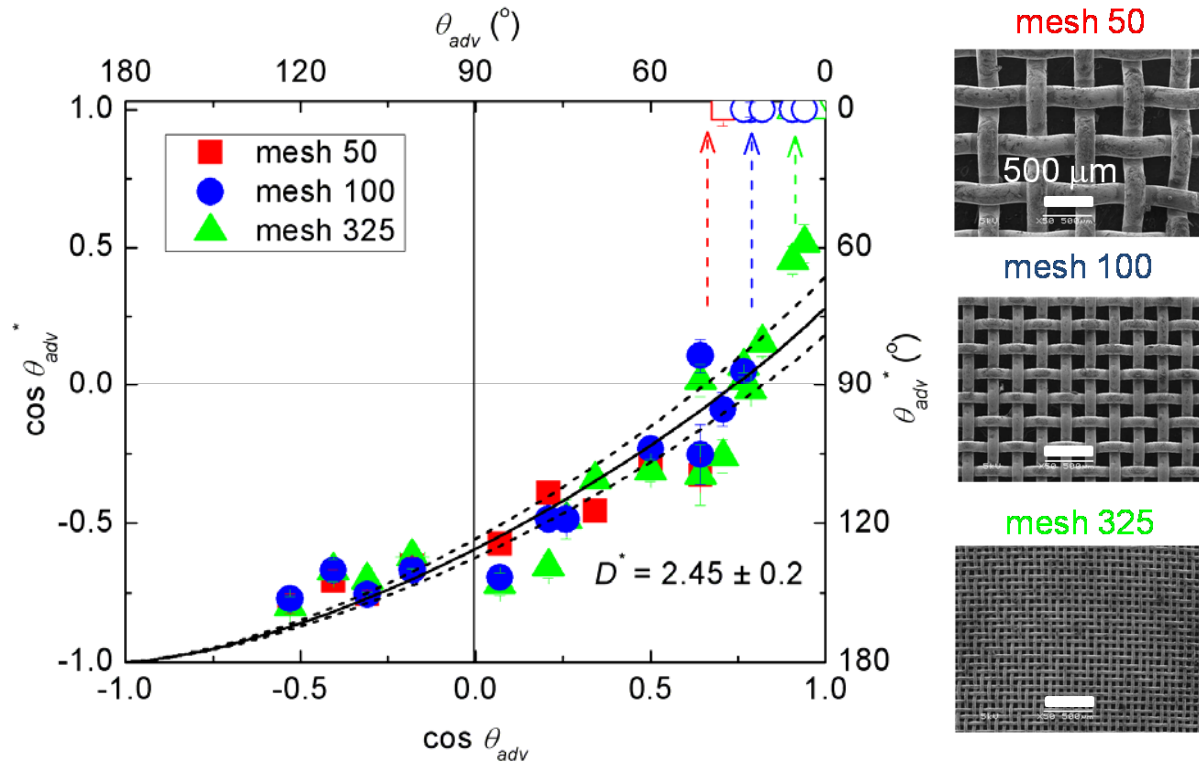
Figure 3-3. Generalized non-wetting diagram for the dip-coated woven meshes. The cosine of the advancing contact angle on the textured dip-coated mesh surfaces (θ_{adv}^*) is plotted against the cosine of the advancing contact angle on the flat spin-coated silicon wafer surfaces (θ_{adv}). The data plotted on the non-wetting diagram is for three mesh sizes (mesh 50 with $R = 114\ \mu m$ (■), mesh 100 with $R = 57\ \mu m$ (●), mesh 325 with $R = 18\ \mu m$ (▲)) with three different coatings ((i) 50% fluorodecyl POSS – 50% Tecnoflon ($\gamma_{sv} = 10.7$ mN/m), (ii) Tecnoflon ($\gamma_{sv} = 18.3$ mN/m) and (iii) polyethyl methacrylate (PEMA) ($\gamma_{sv} = 32.2$ mN/m)) and using various polar and non-polar liquids.

The spacing ratio (D^*) for the set of dip-coated meshes was estimated as 2.45 ± 0.2 by regression

of the contact angle data[1] and this value of D^* compared favorably with the estimated value of

the spacing ratio from the inspection of the SEM micrographs ($D^* = 2.2$, Figure 3-3). The CB

relation is independent of the length scale of the surface features, therefore the apparent

advancing contact angles (θ_{adv}^*) data on the dip-coated meshes (for $R = 18, 57$ and $114\ \mu m$)

collapse onto a single curve corresponding to $D^* = 2.45 \pm 0.2$ (Figure 3-3). The transition from a

robust composite interface to a fully-wetted interface occurs on all three meshes, but at different equilibrium contact angles. This mismatch in the equilibrium contact angle at which the failure of the composite interface occurs can be rationalized on the basis of the robustness factors for the dip-coated wire meshes. The robustness factor (A^*) varies inversely with the length-scale of the surface texture (R); the composite interface therefore fails at the highest equilibrium contact angle for the coarsest mesh ($\theta_{E,crit} \approx 42°$ for mesh 50, $R = 114$ μm) and at the lowest θ_E for the finest wire mesh ($\theta_{E,crit} \approx 14°$ for mesh 325, $R = 18$ μm). By implicitly solving the equation for robustness factor with $A^* = 1$, values of for $\theta_{E,crit}$ are predicted to be 42, 27 and 14° respectively for the mesh 50, 100 and 325 surfaces. The generalized wetting diagram depicted in Figure 3-3 has been popularized by numerous groups and it has become an established paradigm to represent changes to the apparent contact angle (θ^*) data on textured surfaces in comparison to the equilibrium contact angle (θ_E) on chemically identical flat surface. [5-8] This framework indeed provides a compact way to represent data on self-similar structures, but the impact of individual parameters, namely the spacing ratio (D^*) and the length scale of the texture (R) on the non-wettability cannot be deconvoluted readily.

3.3 Design chart

The two independent variables in the modified form of the CB relation are the equilibrium contact angle on a flat surface (θ_E) and the dimensionless spacing ratio (D^*). In order to mitigate the shortcomings of the generalized wetting diagram, a new design chart for understanding liquid wettability on omniphobic surfaces is proposed (Figure 3-4) in which the two independent variables are D^* and θ_E. The limiting values along the ordinate axis are chosen based on the accessible equilibrium contact angle values (θ_E) for water ($\gamma_{lv} = 72.1$ mN/m), from ~0° on a clean

glass surface to ~125° on a pure fluorodecyl POSS surface.[9] On this design chart, the ordinate (θ_E) is uniquely determined by the chemistry of the solid coating and the contacting liquid. This variation in the inherent solid-liquid interactions is independent of the surface topography of a textured surface which is the geometrical spacing ratio (D^*) on the abscissa. The lower limit of the spacing ratio is chosen as the smallest physically possible value of $D^* = 1$ and the upper limit is arbitrarily chosen to be $D^* = 2\pi$ corresponding to a very open weave texture. Four contours of fixed apparent contact angle ($\theta^* = 0$, 90, 120 and 150°) are calculated from the CB relation and are plotted on this (D^*, θ_E) design space.
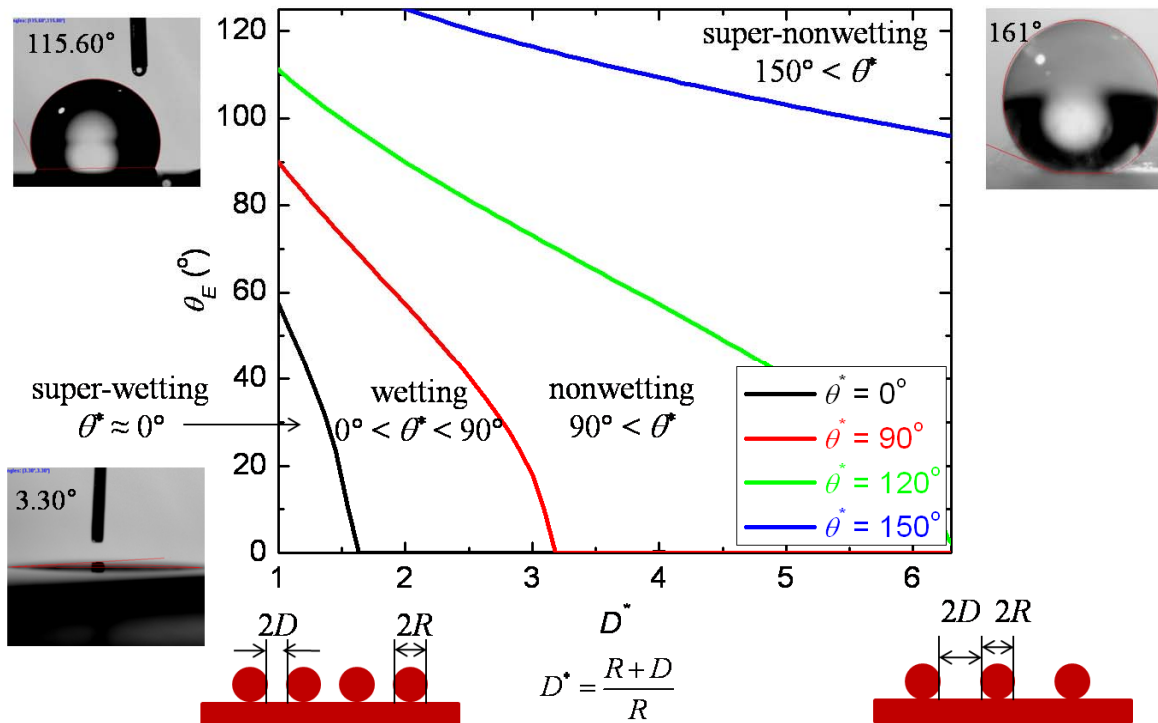
Figure 3-4. Design chart for liquid wettability on cylindrically textured surface. The contours of the apparent contact angle (θ^*) for ($\theta^* = 0$ (—), 90 (—), 120 (—) and 150° (—)) are plotted on the design chart with the equilibrium contact angle on a chemically identical smooth surface (θ_E) and the spacing ratio (D^*) as the two axes. Various regimes of wettability starting from super-wetting ($\theta^* \approx 0°$) to super-nonwetting ($\theta^* > 150°$) are shown on the design chart.

Cassie-Baxter used the apparent advancing (θ^*_{adv}) and receding contact angles (θ^*_{rec}) as the ordinate in their chart[2] whereas in the design chart presented here, the equilibrium contact angle on a chemically identical (θ_E) flat surface is plotted on the y-axis. The apparent advancing /receding contact angles are 'composite' variables that depend on chemistry, and the 'texture', (which consist of specific lithographic patterning, random roughness, weave/weft of woven structures etc). For this reason we argue that it is better to plot measured values of θ^* as a function of the two independent variables represented by the x and y axes. The important performance parameters (θ^* and A^*) of a coated fabric or other textured surfaces are then shown as contours of various constant value in our presentation, and they provide clear guidance for anticipating the efficacy of various designs that are based on selected values of D^* and θ_E. The equilibrium contact angle (θ^*) cannot be measured easily on textured surfaces, but it can be bracketed using the measured advancing and receding contact angles ($\theta^*_{adv} \geq \theta^* \geq \theta^*_{rec}$). Onda, Shibuichi and co-workers[5, 7, 8] report that the equilibrium contact angles are closer to the advancing contact angles than the receding contact angles. Therefore, in the design charts described below, we replace the equilibrium contact angle (θ_E) with the advancing contact angle on the flat surface (θ_{adv}) and the equilibrium contact angle on a textured surface (θ^*) with the apparent advancing contact angle (θ^*_{adv}).

As we have noted above, the apparent contact angle (θ^*) depends only on θ_E and D^* and it is independent of the length-scale (R) of the texture, which thus does not appear on the design chart. Consequently, while the design chart predicts the magnitude of the apparent contact angle (θ^*), it does not guarantee the existence or stability of the solid-liquid-air composite state. The graphical framework shown in Figure 3-4 does not recognize that the composite interface,

needed to achieve high values of θ^*, may be metastable or completely unstable, nor does it quantify the magnitude of the breakthrough pressure difference (P_b) required to disrupt a metastable composite (Cassie-Baxter) interface sufficiently to transition it to the fully-equilibrated wetted (Wenzel) state.

When represented on the design chart (Figure 3-4), the super-wetting region exists at the lower-left where the apparent contact angle predicted by the CB relation is nearly zero ($\theta^* \approx 0°$), even though the equilibrium contact angle on a chemically identical smooth surface is non-zero ($\theta_E > 0°$). This super-wetting region appears as a consequence of the cylindrical texture and in this region the additional energy released from the enhanced surface area provided by the texture coupled with the intrinsic partial wettability of the solid material results in complete wetting.[8, 10] From the design chart representation it is clear that the apparent contact angle (θ^*) can be increased by moving on the plot from left to right (by increasing D^*, the relative spacing of the topographical features) and/or by moving from bottom to top (by increasing θ_E which, for a selected liquid, is achieved through changes in the solid surface chemistry). The region bounded by the blue curve and the two axes (right top) is the region of super liquid non-wettability (*superhygrophobicity*)[11] characterized by a high value of apparent contact angle ($\theta^* > 150°$).

3.4 Impact of length scale on robustness and breakthrough pressure

Although this new design chart indicates the range of effective contact angles that can be achieved theoretically, it does not indicate if the resulting composite interface is stable. A modified form of the design chart for liquid wettability is presented in Figure 3-5. Here the shaded grey area represents combinations of the parameters θ_E, D^* and (ℓ_{cap}/R) for which the robustness factor is less than unity (Equation 3.2). The CB predictions are not extended into the

shaded area as the composite interface becomes unstable; a liquid drop placed on the texture will spontaneously transition to a fully-wetted interface in this grey shaded region. Important to note that the amount of (white) area on this design chart, corresponding to regions in which liquid drops can be supported on a composite air-solid interface, can be tuned by varying the ratio ℓ_{cap}/R. The capillary length is a material property of the contacting liquid (ℓ_{cap}) and practical values span an approximate range from 2.7 mm for water ($\gamma_{lv} = 72.1$ mN/m, $\rho = 1000$ kg/m^3) to 1.25 mm for methylene iodide ($\gamma_{lv} = 50.8$ mN/m, $\rho = 3325$ kg/m^3); that is the range of values over which the capillary length can be varied is quite limited. On the contrary, the radius of the cylindrical re-entrant features (R) on the surface can be varied by many orders of magnitude ($R \approx 100$ μm for commercial fabrics down to $R \approx 100$ nm for electrospun mats). When droplets of a given liquid (with fixed ℓ_{cap}) are placed on a textured surface with a particular spacing ratio (fixed D^*) and a specific coating (fixed θ_E), both the robustness factor (A^*) and the breakthrough pressure (P_b) are inversely proportional to the surface texture length scale R. In the case of smaller length-scale surface features (small R, or large ℓ_{cap}/R), a large fraction of the θ_E and D^* parameter space corresponds to a robust composite interface ($A^* > 1$) and is available for the design of robust non-wettable surfaces. The variation in the accessible area for designing non-wetting surfaces is schematically shown in Figure 3-5 with two different feature sizes. The line corresponding to $A^* = 1$ varies with D^* and θ_E for $0.2 \leq \ell_{cap}/R \leq 2000$. By keeping the surface chemistry of the solid, the composition of the contacting liquid and the geometric spacing ratio the same (*i.e.* fixed θ_E and D^*), and only reducing the length scale of the surface texture (R), the anticipated wetting behavior for a liquid droplet on a textured surface can be controlled from a super-wetting state to a robust composite non-wetting state.
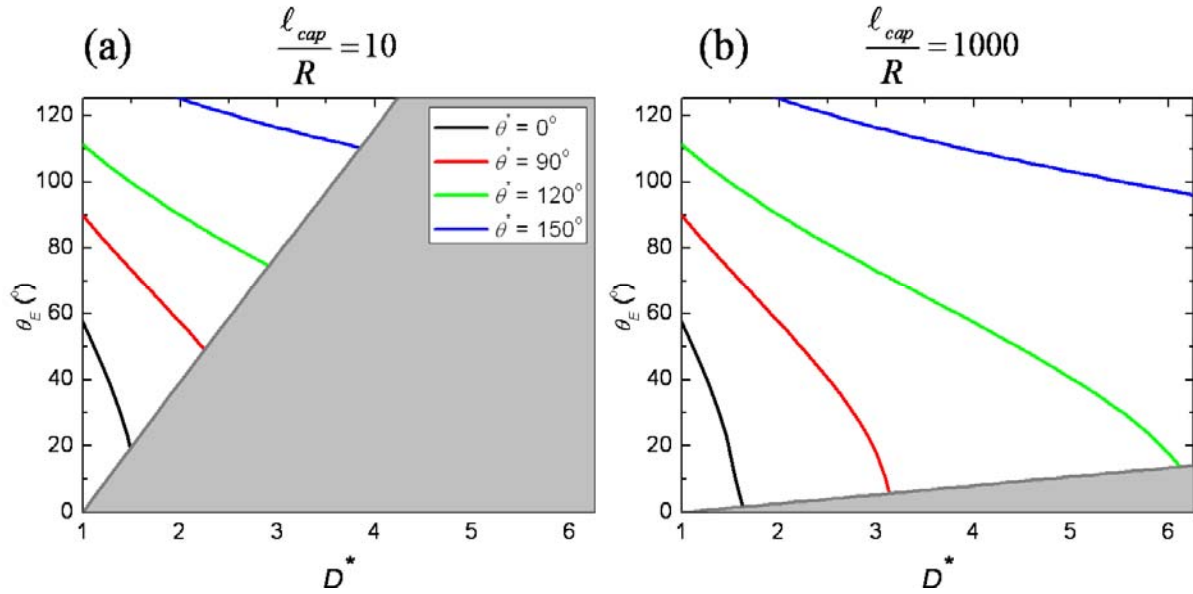
Figure 3-5. Modified form of the design chart for liquid wettability, which predicts the parameter space available for designing robust composite interfaces for two values of the ratio (ℓ_{cap} / R). Figure 4(a) represents a typical commercial textile surface with $\ell_{cap} \approx 2$ mm, $R \approx 200$ μm, and ℓ_{cap} / R = 10 and Figure 4(b) shows the modified design chart for a typical electrospun mat with $\ell_{cap} \approx 2$ mm, $R \approx 2$ μm, and ℓ_{cap} / R = 1000.

In the design chart framework presented here, the three main factors that govern the robustness of repellency to a selected liquid are completely decoupled: (i) the equilibrium contact angle exhibited by the liquid on a chemically identical smooth surface (θ_E), (ii) the spacing ratio of the textured surface (D^*), and (iii) the length scale of the features that produce the surface texture (R). It is straightforward to ascertain the effect of each one of these parameters on the robustness (A^*) and non-wettability (θ^*) of a textured surface, and it is clear that each of these parameters can be usefully manipulated during the design process. Similar design charts can be developed for surfaces with other texture geometries (e. g. spheres (section 3.11) micro-hoodoos,[9] nano-nails[12] etc.) by modifying the expression for A^* to account for the specific surface topography. The main focus of the present chapter is to elucidate the impact of the length scale (R), the spacing ratio D^* and surface chemistry (θ_E) on the apparent contact angle (θ^*) and the robustness

(A^*) of the solid-liquid-air composite interface. Cassie and Baxter worked with similar textured surfaces but they were concerned only with the apparent contact angles (θ^*) and focused exclusively on water (γ_{lv} = 72.1 mN/m) as the probing liquid. In this work, liquids with a broad range of surface tensions (from 72.1 mN/m for water to 15.5 mN/m for pentane) are used in order to explore non-wettability of woven and nonwoven structures to a wide range of liquids.

3.5 Varying the length scale (R) at constant coating chemistry (θ_E) and spacing ratio (D^*)

The effect of the microscopic length scale of the surface texture on the robustness of the composite interface is elucidated more clearly with the help of the design chart developed in this work. Figure 3-6 shows contact angle data measured on two 50% POSS – 50% Tecnoflon coated woven surfaces – mesh 325 (R = 18 µm, D^* = 2.45 ± 0.2, Figure 3-6(a)) and mesh 50 (R = 114 µm, D^* = 2.45 ± 0.2, Figure 3-6(b)).
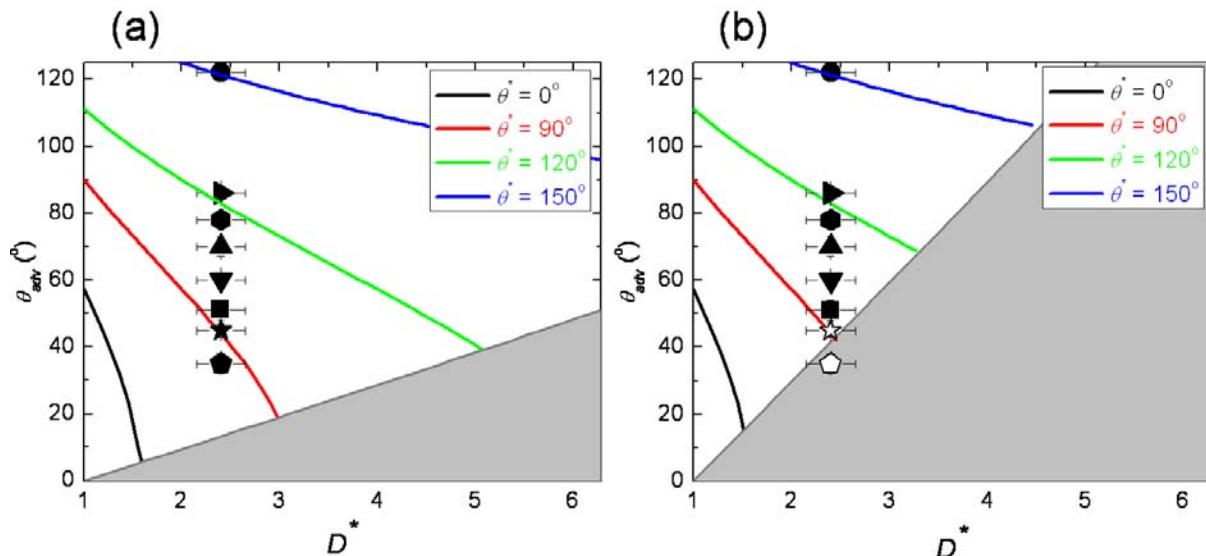
Figure 3-6. Contact angle data on wire meshes dip-coated with 50% POSS – 50% Tecnoflon (γ_{sv} = 10.7 mN/m) using water (●, γ_{lv} = 72.1 mN/m), ethylene glycol (◆, γ_{lv} = 47.7 mN/m) rapeseed oil (▶, γ_{lv} = 35.5 mN/m), hexadecane (●, γ_{lv} = 27.5 mN/m), dodecane (▲, γ_{lv} = 25.3 mN/m) decane (▼, γ_{lv} = 23.8 mN/m), octane (■, γ_{lv} = 21.6 mN/m), heptane (★, γ_{lv} = 20.1 mN/m), and pentane (⬟, γ_{lv} = 15.5 mN/m) are plotted on the design chart for liquid wettability. Figure 3-6(a) shows data for mesh 325 (R = 18 µm) and Figure 3-6(b) shows data for mesh 50

(R = 114 μm). The shaded area represents a set of (θ_E, D*, ℓ_{cap}/R) values for which the robustness factor for heptane is less than unity ($A^*_{heptane} < 1$). Filled symbols indicate a liquid droplet with a robust composite interface whereas open symbols ($\bigstar$, $\bigcirc$ etc.) indicate a liquid droplet which has transitioned into the fully-wetted Wenzel state.

Filled symbols on the design chart denote a robust composite interface whereas open symbols indicate a fully-wetted interface on the textured mesh surface. The liquid alkane with the lowest surface tension $i.e.$ pentane ($\pentagon$ in Figure 3-6(a), γ_{lv} = 15.5 mN/m) formed a robust composite non-wetting interface (with θ^*_{adv} = 91 ± 3°) on the finest mesh (325) dip-coated with 50% POSS – 50% Tecnoflon. On the contrary, even relatively higher tension liquids such as heptane ($\bigstar$ in Figure 3-6(b), γ_{lv} = 20.1 mN/m, θ_{adv} = 45 ± 2°) and pentane ($\bigcirc$ in Figure 3-6(b), γ_{lv} = 15.5 mN/m, θ_{adv} = 35 ± 3°) wet the identically coated textured surface (resulting in $\theta^*_{adv} \approx 0°$) of mesh 50. Although both the textured surfaces have identical coating chemistry, their different characteristic length scales result in different robustness factors. The value of A^* is reduced from high values at fine length scale $i.e.$ A^* = 5.8 and A^* = 9.1 on mesh 325 (R = 18 μm), to lower values at a coarser length scale $i.e.$ A^* = 0.9 and A^* = 1.4 (R = 114 μm). When the robustness factor reaches a value close to unity ($A^* \approx 1$), the composite interface sags severely and touches the next underlying layer of the solid texture, which results in a transition to the fully-wetted state. This transition is expected to take place at values of A^* order unity. In our idealized model ($i.e.$ a periodic array of parallel cylinders), we expect A^*_{crit} = 1 and indeed our observations suggest that the critical robustness factor is always $1 < A^* < 1.5$. For a comparatively higher surface tension liquid such as octane ($\blacksquare$, γ_{lv} = 21.6 mN/m, θ_{adv} = 51 ± 2°), the robustness factor decreases from A^*=11.2 on mesh 325 to A^*=1.7 on mesh 50. Because the robustness factor remains sufficiently greater than unity, a robust composite non-wetting interface is observed for

octane droplets on both the fine mesh 325 (θ^*_{adv}=109 ± 3°) and the coarse mesh 50 (θ^*_{adv}

=107 ± 4°) provided they are dip-coated with 50% POSS – 50% Tecnoflon.

The impact of length scale (R) on the robustness factor is depicted in Figure 3-7, where $\log_{10}A^*$ is

plotted for three different ratios ℓ_{cap} / R .

(a)

(b)

(c)
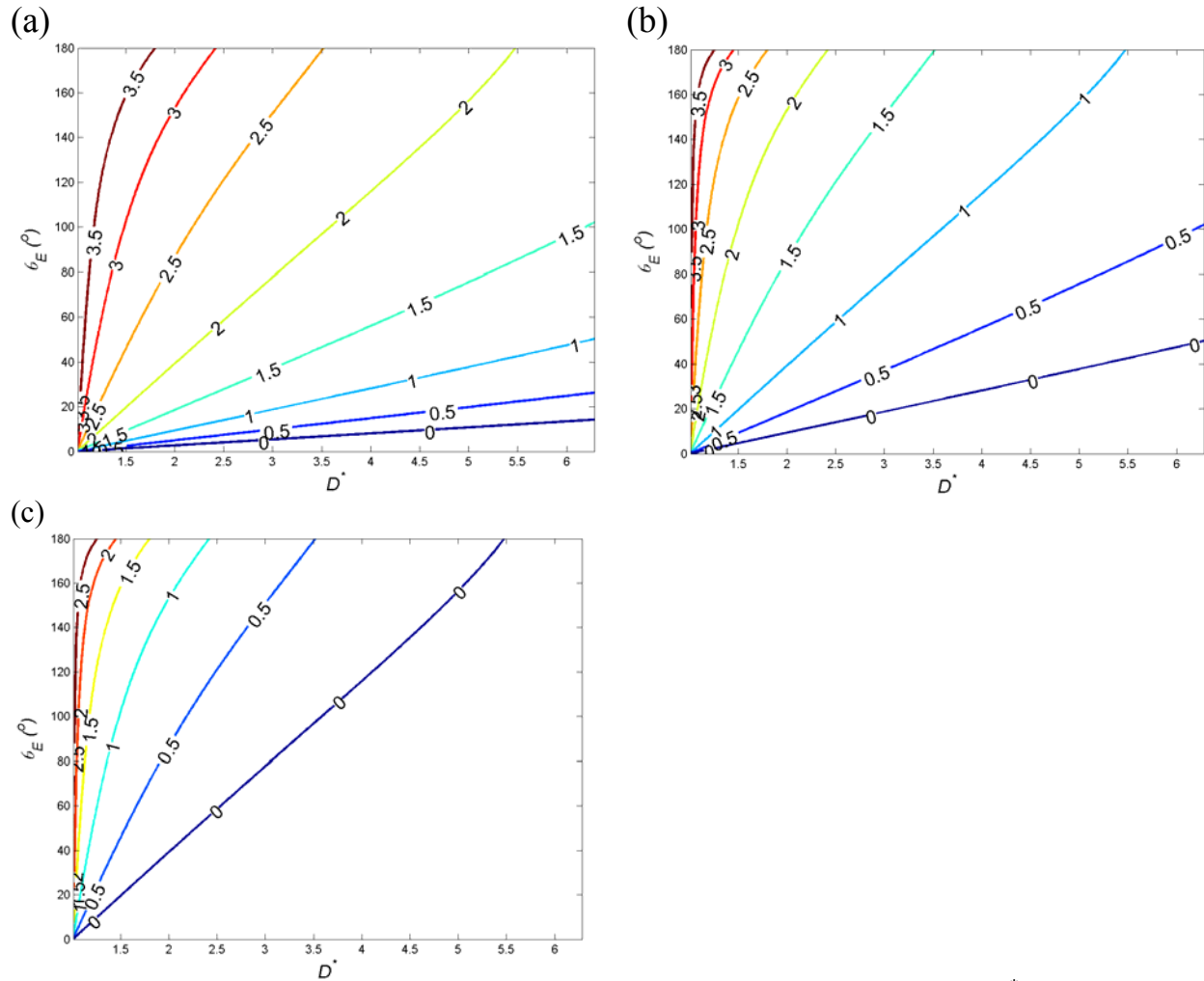
Figure 3-7. Contours of the logarithm (to the base 10) of the robustness factor (A^*) for
cylindrically textured surfaces with the radius of the cylindrical texture as R and the inter
cylinder spacing being 2D are shown on the (θ_E, D^*) design space. Here the ratio of the capillary
length and the texture length scale is chosen to be ℓ_{cap} / R = (a) 1000, (b) 100 and (c) 10. The
variation of the robustness factor by many orders of magnitude is depicted on this chart. The
same chart can be used to demarcate the A^* > 1 criterion for the existence of a robust composite
interface or to compute the breakthrough pressure (P_b) for a textured surface using $P_b = A^*P_{ref}$.

The portion of the design space to the right of the contour "0" represents a fully-wetted interface ($\log_{10}A^* < 0$ or $A^* < 1$). The magnitude of robustness factor is $\sqrt{10}$ times higher for every contour line as we move from the right bottom to the left top on the design chart. Note that consistent with the length scale independence of Equation 3.1, the measured apparent advancing contact angles are essentially unaffected by the significant changes in R at constant D^*.

3.6 Varying the coating chemistry (θ_E) at constant spacing ratio (D^*) and length scale (R)

In addition to the length-scale of the texture, the robustness factor (A^*, Equation 3.2) also depends upon the equilibrium contact angle on a chemically identical smooth surface (θ_E). The impact of the variation in θ_E on the robustness factor (A^*) was studied by dip-coating wire mesh 325 ($R = 18$ μm, $D^* = 2.45 \pm 0.2$) using either a 50% POSS – 50% Tecnoflon ($\gamma_{sv} = 10.7$ mN/m, Figure 3-8(a)) or a polyethyl methacrylate (PEMA, $\gamma_{sv} = 32.2$ mN/m, Figure 3-8(b)) coating.

For decane, the advancing contact angle on a smooth surfaces decreases from $\theta_{adv} = 60 \pm 2°$ on a flat 50% POSS – 50% Tecnoflon surface to $\theta_{adv} = 12 \pm 3°$ on a flat PEMA surface. The robustness factor decreases monotonically with θ_{adv}, from $A^* = 14.6$ on mesh 325 ($R = 18$ μm) dip-coated with 50% POSS – 50% Tecnoflon to $A^* = 0.8$ on the same woven surface coated with PEMA. As a result, decane forms a robust composite interface on mesh 325 ($\theta^* = 108 \pm 3°$, ▼ in Figure 3-8(a)) when it is coated with 50% POSS – 50% Tecnoflon but it fully wets the same underlying surface coated with PEMA ($\theta^* \approx 0°$, ▽ in Figure 3-8(b)). By contrast, the advancing contact angle for dodecane (▲, $\gamma_{lv} = 25.3$ mN/m) changes from $\theta_{adv} = 71 \pm 2°$ to $19 \pm 2°$, and the robustness factor on the surface diminishes from 19 to 2.6. The robustness factor remains sufficiently greater than unity and a robust composite interface ($\theta^*_{adv} = 59 \pm 3°$, ▲) is observed

even on a PEMA coated mesh 325 surface. Hexadecane (γ_{lv} = 27.5 mN/m, θ_{adv} = 25 ± 2°,

A^* = 4.1, = 64 ± 5°) and dodecane (γ_{lv} = 25.3 mN/m, θ_{adv} = 19 ± 2°, A^* = 2.6, θ^*_{adv} = 59 ± 3°) form

a robust metastable composite interface on a polyethyl methacrylate coated (PEMA, γ_{sv} = 32.2

mN/m) mesh 325 surface (R = 18 μm, D^* = 2.45 ± 0.2). From the magnitude of A^*, the

breakthrough pressure for hexadecane and dodecane droplets can be estimated to be about 118

and 71 Pa respectively. Also, the receding contact angles for hexadecane and dodecane droplets

on the mentioned wire mesh surface were found to be close to zero.
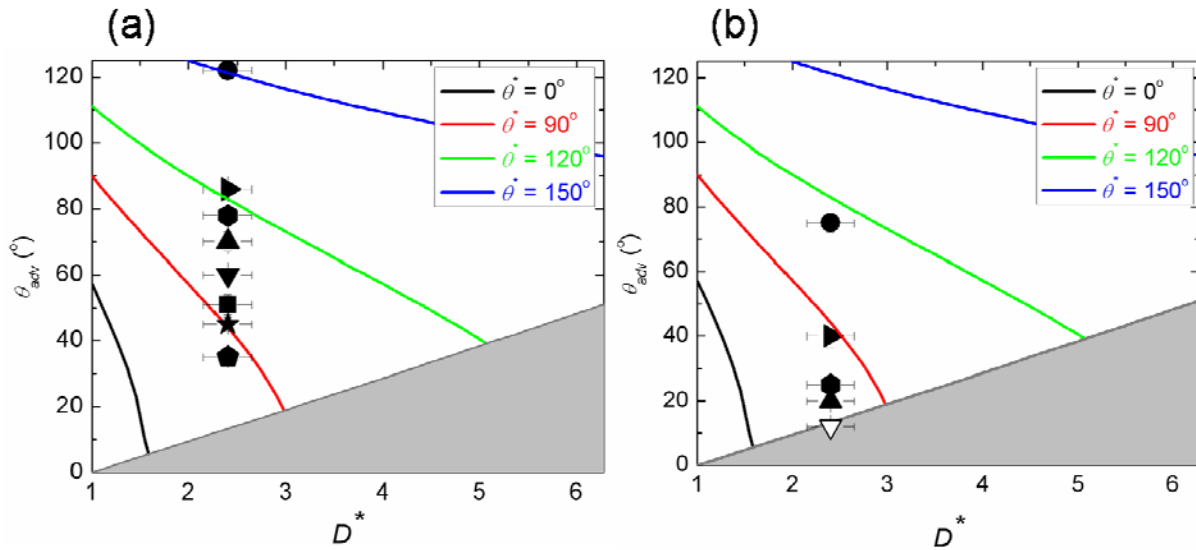
Figure 3-8. Contact angle data on the mesh 325 (R = 18 μm) using water (●, γ_{lv} = 72.1 mN/m), ethylene glycol (◆, γ_{lv} = 47.7 mN/m) rapeseed oil (▶, γ_{lv} = 35.5 mN/m), hexadecane (●, γ_{lv} = 27.5 mN/m), dodecane (▲, γ_{lv} = 25.3 mN/m) decane (▼, γ_{lv} = 23.8 mN/m), octane (■, γ_{lv} = 21.6 mN/m), heptane (★, γ_{lv} = 20.1 mN/m), and pentane (⬠, γ_{lv} = 15.5 mN/m) are plotted on the design chart for liquid wettability. Figure 3-8(a) shows data for the mesh dip-coated with 50% POSS – 50% Tecnoflon (γ_{sv} = 10.7 mN/m) and Figure 3-8(b) shows data for the dip-coated mesh with PEMA (γ_{sv} = 32.2 mN/m). The shaded area represents a set of (θ_E, D^*, ℓ_{cap} / R) values for which the robustness factor for heptane is less than unity ($A^*_{heptane}$ < 1). Because the characteristic length scale remains constant (R = 18 μm), the shaded area (A^* < 1, Equation (2)) remains the same in the two figures. Filled symbols indicate a liquid droplet with a robust composite interface whereas open symbols indicate a liquid droplet which has transitioned into the fully-wetted state.

These results illustrate that extremely low surface energy (γ_{sv}) coatings are not always necessary to obtain a robust composite interface provided the characteristic textural length scale is small enough. Even low surface tension liquids like hexadecane (⬡, $\gamma_{lv} = 27.5$ mN/m) and dodecane (▲, $\gamma_{lv} = 25.3$ mN/m) form robust and partially wetting composite interfaces ($\theta^*_{adv} = 64 \pm 5°$ for hexadecane and $\theta^*_{adv} = 59 \pm 3°$ for dodecane) on PEMA-coated stainless steel meshes with sufficiently small wire radii (R). The systematic understanding provided by the design chart and the data reported in this work show that by properly tailoring the surface topographical parameters (R, D^*) and surface chemistry (θ_E) appropriately, a robust composite interface can be achieved for a suitably designed surface and liquid pair.

3.7 Varying the spacing ratio (D^*) at constant coating chemistry (θ_E) and length scale (R)

From the observations in previous sections, we saw the impact of variation in (i) ℓ_{cap}/R or (ii) θ_E on the robustness factor (A^*). The third important factor that alters the robustness is the 'openness of the weave' or the spacing ratio (D^*) of the surface texture. The dependence of the robustness factor on D^* is explored by choosing a set of wire meshes which have identical radii ($R = 83$ μm) but different density weaves, and thus different spacing ratio ($D^* = 2.2$, 3.9 and 5.1). These wire meshes are dip-coated using the 50% POSS – 50% Tecnoflon solution and the contact angle measurement results are plotted in Figure 3-9. For the wire mesh with the tightest weave *i.e.* the smallest spacing ratio ($D^* = 2.2$, $R = 83$ μm, mesh 70), liquids such as octane (■, $\gamma_{lv} = 21.6$ mN/m, $A^* = 2.4$, $\theta^* = 110 \pm 3°$), and heptane (★, $\gamma_{lv} = 20.1$ mN/m, $A^* = 1.9$, $\theta^* = 104 \pm 4°$) form a robust composite interface. On the contrary, pentane (⬡, $\gamma_{lv} = 15.5$ mN/m) readily wets this surface because the robustness factor approaches unity ($A^* = 1.2$, $\theta^* \approx 0°$).
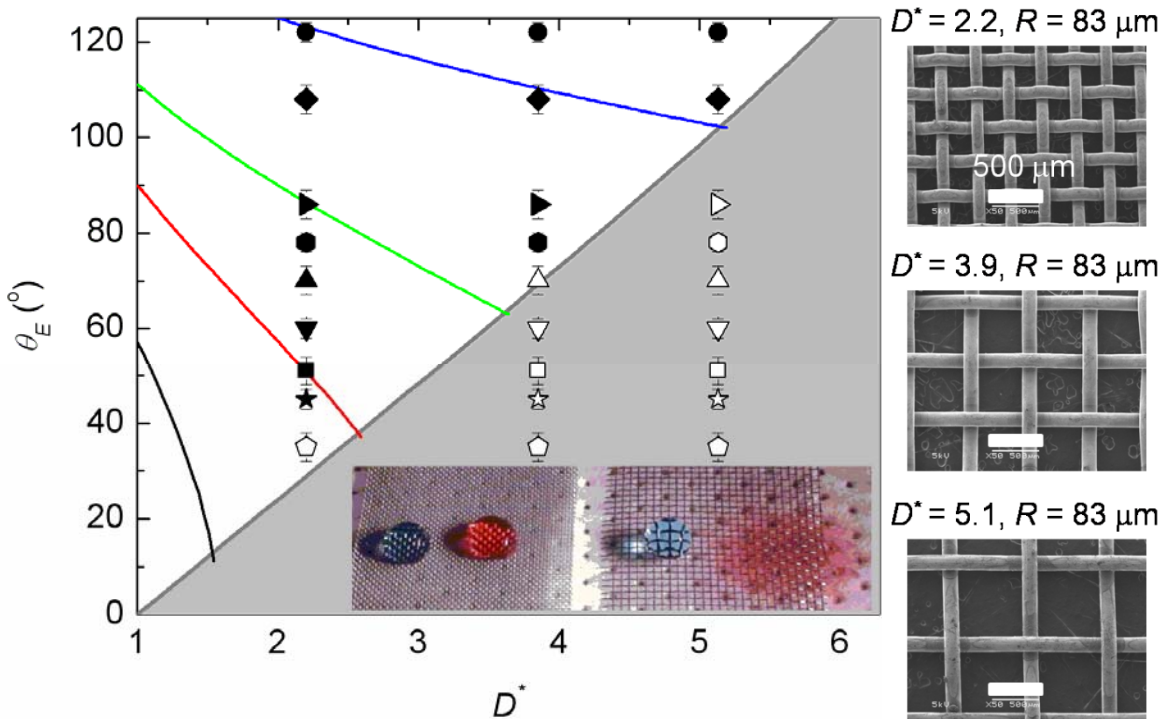
Figure 3-9. Contact angle data on mesh 70, 40, and 30 (all with $R = 83$ μm and $D^* = 2.2$, 3.9, and 5.1 respectively) dip-coated using 50% POSS – 50% Tecnoflon. Contacting liquids include water (●, $\gamma_{lv} = 72.1$ mN/m), ethylene glycol (◆, $\gamma_{lv} = 47.7$ mN/m) rapeseed oil (▶, $\gamma_{lv} = 35.5$ mN/m), hexadecane (⬢, $\gamma_{lv} = 27.5$ mN/m), dodecane (▲, $\gamma_{lv} = 25.3$ mN/m) decane (▼, $\gamma_{lv} = 23.8$ mN/m), octane (■, $\gamma_{lv} = 21.6$ mN/m), heptane (★, $\gamma_{lv} = 20.1$ mN/m), and pentane (⬠, $\gamma_{lv} = 15.5$ mN/m) are plotted on the design chart for liquid wettability. The shaded area represents a set of (θ_E, D^*, ℓ_{cap}/R) values for which the robustness factor for heptane is less than unity ($A^*_{heptane} < 1$). Filled symbols indicate a liquid droplet with a robust composite interface whereas open symbols indicate a liquid droplet which has transitioned into the fully-wetted interface. The left image in the inset shows nonwetting water (blue, $A^* = 14.5$) and rapeseed oil (red, $A^* = 5.8$) droplets with a robust composite interface on a mesh 70 surface ($R = 83$ μm; $D^* = 2.2$) coated with 50% POSS – 50% Tecnoflon. The right image shows a water droplet (blue, $A^* = 2.1$) in a robust composite interface on a mesh 30 ($R = 83$ μm and $D^* = 5.1$) surface with a similar coating. Rapeseed oil (red) wets the textured surface because the robustness factor drops to $A^* = 0.9$. The SEM micrographs of the three textured surfaces are shown on the right.

Dodecane (▲, $\gamma_{lv} = 25.3$ mN/m, $\theta^* = 123 \pm 3°$) forms a robust composite interface on the dip-coated mesh 70 surface ($R = 83$ μm, $D^* = 2.2$) whereas it wets an identically coated mesh 40 surface with a looser weave ($R = 83$ μm, $D^* = 3.9$, $\theta^* \approx 0°$, △). As feature spacing increases from 2.2 to 3.9, the spacing between the cylindrical texture increases (from $2D = 200$ to 470 μm) whereas the radius of the individual filament remains constant (at $R = 83$ μm). Consequently as

D^* increases, the air-liquid interface sags more severely and the robustness factor decreases. For dodecane the robustness factor decreases from $A^* = 4.0$ to $A^* = 1.1$ as D^* increases from 2.2 to 3.9 at constant $R = 83$ μm and $\theta_{adv} = 71 \pm 2°$. Similarly, the robustness factor continues to decline in magnitude as the spacing ratio increases from $D^* = 3.9$ to $D^* = 5.1$. In the case of rapeseed oil (▶, $\gamma_{lv} = 35.5$ mN/m), the robustness factor decreases from $A^* = 1.6$ on mesh 40 surface down to $A^* = 0.9$ on mesh 30 surface (with $R = 83$ μm and $D^* = 5.1$). Consequently, as expected rapeseed oil wets the 50% POSS – 50% Tecnoflon coated mesh 30 surface (▷ for $R = 83$ μm and $D^* = 5.1$, $\theta^* \approx 0°$). Droplets of water ($\gamma_{lv} = 72.1$ mN/m, blue) and rapeseed oil ($\gamma_{lv} = 35.5$ mN/m, red) on (i) mesh 70 surface with $D^* = 2.2$, $R = 83$ μm and (ii) mesh 30 surface with $D^* = 5.1$ and $R = 83$ μm are shown in the inset of Figure 3-9. The figure illustrates the importance of the mesh weave and spacing ratio (D^*) on the robustness of the composite interface. The apparent contact angle (θ^*) increases monotonically with increasing spacing ratio (D^*), as the wetted fraction of the solid ($r_\phi \phi_s$) diminishes. As a result, provided a robust composite interface is ensured ($A^* > 1$) then the apparent contact angle of water droplets ($\gamma_{lv} = 72.1$ mN/m, $\theta_{adv} = 122 \pm 2°$), increases from $\theta^* = 147 \pm 2°$ on mesh 70 ($R = 83$ μm, $D^* = 2.2$) to $\theta^* = 160 \pm 3°$ on mesh 30 (with $R = 83$ μm and $D^* = 5.1$). However if the robustness factor decreases below unity due to increasing spacing ratio (D^*), then the liquid droplets transition from a robust composite interface with high apparent contact angles to a fully wetted interface with very low apparent contact angles ($\theta^* \approx 0°$),[13] as in the case for decane droplets.

3.8 Thermodynamic criterion for the stability of a composite interface

All the data presented above demonstrate the influence of the surface texture (R, D^*), the liquid parameters (ℓ_{cap}), and the solid surface chemistry (θ_E) on the robustness factor (A^*) for liquid

droplets with metastable composite interface.[14] So far the data and the design chart provide no information about the boundary between metastable states and the thermodynamically equilibrated states.[11, 14-16] The apparent contact angle (θ^*) for a liquid droplet in a composite (or Cassie-Baxter) state on a cylindrically textured surface is given by the CB relation (Equation 3.1). On the other hand, the apparent contact angle (θ^*) for a fully-wetted (Wenzel) liquid droplet is given by the Wenzel relation[3] $\cos\theta^* = r\cos\theta_E$, where r is the Wenzel roughness given by the actual solid-liquid interfacial area divided by the projected solid-liquid interfacial area. For a parallel array of cylinders of radius R and spacing $2D$, the Wenzel roughness is $r = 1 + \left(\pi/D^*\right)$ where D^* is the spacing ratio. The condition for crossover from one thermodynamic equilibrium state to another can be obtained by solving both the CB and the Wenzel relation simultaneously for the critical angle θ_c (Equation 3.3).[11, 17, 18] This condition is plotted as the black dashed line on the design chart in Figure 3-10.

$$D^* = \frac{\sin\theta_c - \theta_c\cos\theta_c}{1 + \cos\theta_c} \tag{3-3}$$

From Figure 3-10, it is clear that $\theta_E > 90°$ is a necessary condition for the existence of a truly thermodynamically stable composite interface. Because there is no natural or artificial surface with $\theta_E > 90°$ for liquids with low surface tension, the composite interfaces for such liquids are at best metastable. Within the design chart represented by Figure 3-10, the region above the black dashed line corresponds to non-wetting droplets where the composite interface is the global minimum in free energy. This region is accessible essentially only with water ($\gamma_{lv} = 72.1$ mN/m) and other high surface tension liquids like glycerol ($\gamma_{lv} = 64$ mN/m), ethylene glycol ($\gamma_{lv} = 47.7$ mN/m) and methylene iodide ($\gamma_{lv} = 50.8$ mN/m). On the other hand, below the dashed line the fully-wetted or Wenzel state is the thermodynamic equilibrium and a composite interface

64

(Cassie-Baxter) is, at best, metastable.[9, 17-25] The cross-over condition from the Cassie-Baxter to Wenzel state is analogous to the binodal or the coexistence curve on a phase diagram.[26] Below this binodal curve, the composite interface is metastable but can still be realized under carefully controlled conditions until the necessary breakthrough pressure for the transition is applied (analogous to a nucleation event and the growth of the nucleus to reach the critical size). It is important to remember that the thermodynamic crossover condition is independent of the length scale of the texture (R), as Equation (3) is scale invariant.
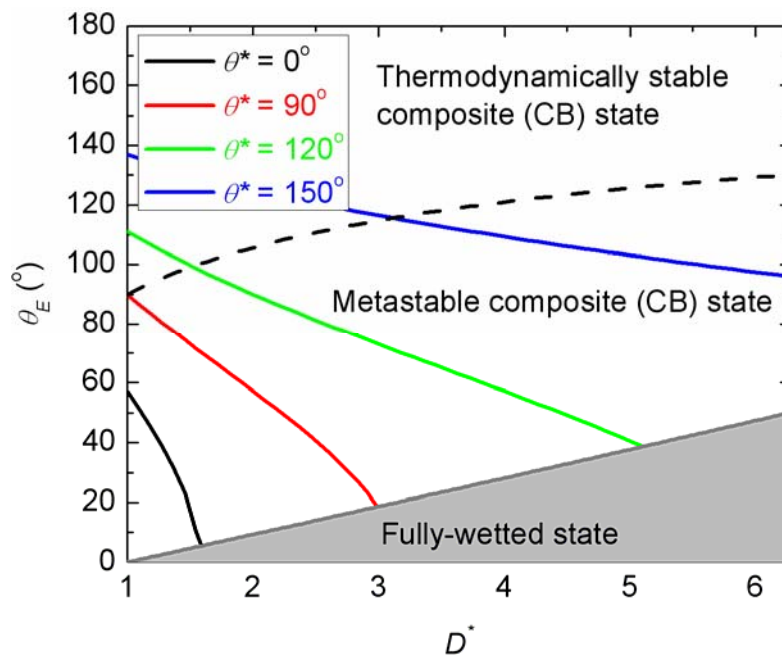
Figure 3-10. The thermodynamic condition for cross-over from the composite to the fully-wetted interface is shown as the black dashed line on the design chart for liquid wettability. The shaded region indicates parameter space inaccessible for designing non-wetting surfaces with cylindrical textures of length scale R such that $\ell_{cap} / R = 100$.

The metastable region extends from the crossover condition (black dashed line) to the edge of the shaded region, where the composite interface is thermodynamically unstable ($A^* < 1$) and it spontaneously transitions into the fully-wetted interface. This transformation of the sagging liquid-air composite interface to a fully-wetted interface is analogous to a pseudo-spinodal on the phase diagram. At the pseudo-spinodal, an infinitesimally small external perturbation results in

65

the spontaneous transformation (analogous to a spinodal decomposition which is spontaneous and has no nucleation events.) The pseudo-spinodal curve for the robust metastable regime found by setting $A^* = 1$ is a strong function of the length scale (R) (Figure 3-10).

3.9 Representation of a fully-wetted droplet on the design chart

The apparent contact angle of a liquid droplet in a fully-wetted state (θ^*) is given by the Wenzel relation, in terms of the equilibrium contact angle (θ_E) and relative roughness (r). Roughness (r) can be written in terms of the spacing ratio (D^*) as $r = 1 + \pi/D^*$, and therefore the variation of θ^* in terms of θ_E and D^* can be predicted (Figure 3-11).
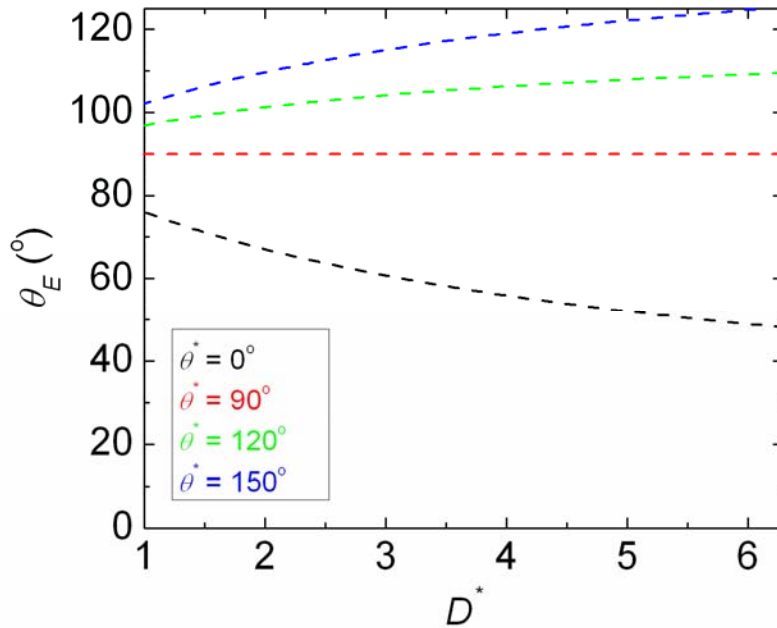
Figure 3-11. Design chart for the wettability of a liquid droplet in the fully-wetted state on cylindrically textured surface. The contours of the apparent contact angle (θ^*) for ($\theta^* = 0$ (— —), 90 (— —), 120 (— —) and 150° (— —)) are plotted on the design chart with the equilibrium contact angle on a chemically identical smooth surface (θ_E) and the spacing ratio (D^*) as the two axes.

This variation of apparent contact angle in the fully-wetted regime is combined with the variation of apparent contact angle with a solid-liquid-air composite interface, to predict the apparent contact angle as a function of surface chemistry (θ_E) and dimensionless spacing ratio (D^*) at

equilibrium. As shown in Figure 3-12, at equilibrium, all points above the binodal (_._._) are in a Cassie-Baxter state at equilibrium and all points below the binodal are in a Wenzel state at equilibrium. The apparent contact angles (θ^*) in both the Cassie-Baxter and Wenzel states are equal for all points on the binodal. Also, it is clear from the plot that for any $\theta_E < 90°$, a thermodynamically stable Cassie-Baxter state cannot exist. Whenever $\theta_E < 90°$, a fully-wetted state is always the global equilibrium state and a composite interface might be metastable at best.
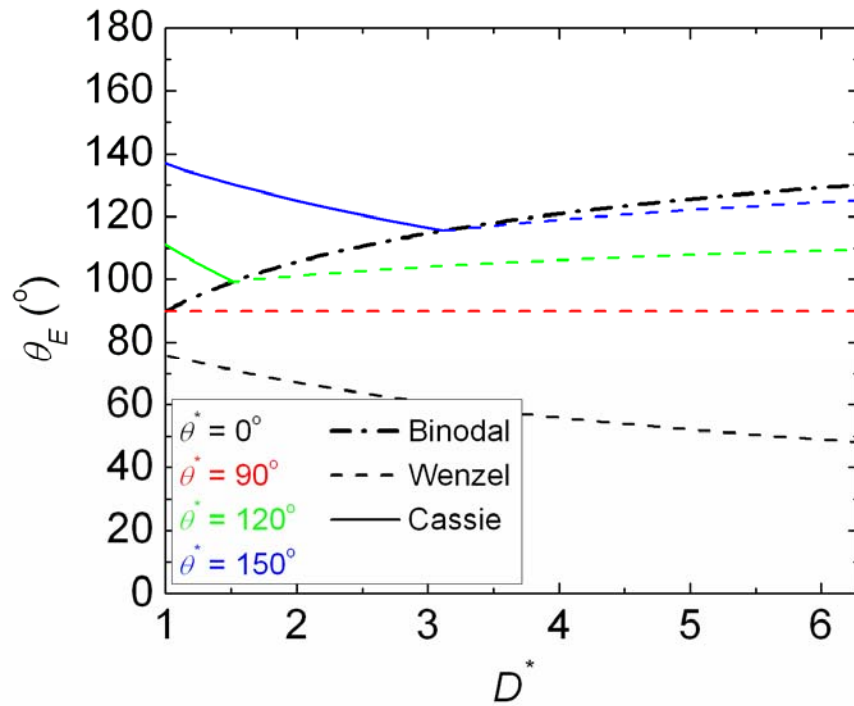
Figure 3-12. The variation in the apparent contact angle of a liquid droplet at equilibrium on a cylindrically textured surface is shown in this figure. Droplets in a fully-wetted state are depicted using a dashed line whereas droplets in a solid-liquid-air composite state are shown with a solid line. The binodal (_._._) is the locus of points for which the apparent contact angle in the Cassie-Baxter and Wenzel state are equal. For all points above and to the left of the binodal, the Cassie-Baxter state represents the thermodynamic equilibrium whereas all points below and to the right of the binodal are in the Wenzel state at equilibrium.

3.10   Importance of the capillary length scale

Capillary length is a material property of a given liquid and it is defined as $\ell_{cap} = \sqrt{\gamma_{lv}/\rho g}$, where γ_{lv} is the liquid surface tension, and ρ is the density of the liquid. Capillary length is used

as length scale while comparing a surface force and a body force (like gravity). Capillary length

varies over a small range for liquids with practical limits being 2.7 mm for water and 1.25 mm

for methylene iodide.

The advancing contact angle on a smooth Tecnoflon film for methylene iodide (γ_{lv} = 50.8 mN/m,

ℓ_{cap} = 1.25 mm) is θ_{adv} = 72 ± 2° and for rapeseed oil (γ_{lv} = 35.5 mN/m, ℓ_{cap} = 1.98 mm) is

θ_{adv} = 68 ± 2°. The advancing contact angle and surface tension for methylene iodide are larger

than the corresponding value for rapeseed oil. Consequently, it is expected that for a given

textured surface, methylene iodide will be more non-wetting compared to rapeseed oil, but on a

mesh 35 surface (R = 127 μm, D^* = 2.9) dip-coated with Tecnoflon (γ_{sv} = 18.3 mN/m), rapeseed

oil forms a robust composite interface (▶, θ^* = 115 ± 3°, Figure 3-13) whereas methylene iodide

fully wets the identical surface (☆, $\theta^* \approx 0°$). This apparent discrepancy can be explained by

considering the magnitude of the corresponding robustness factors. As the capillary length of

rapeseed oil is much larger as compared to methylene iodide, the robustness factor is

correspondingly higher for rapeseed oil. Therefore rapeseed oil (A^* = 1.5 > 1) forms a robust

composite interface whereas methylene iodide (A^* = 0.9 < 1) wets the textured surface. In Figure

3-13, the shaded area represents a set of θ_E, D^*, and R parameters for which $A^* < 1$ for methylene

iodide (ℓ_{cap} = 1.25 mm) whereas the grey line represents the area for which $A^* < 1$ for rapeseed

oil (ℓ_{cap} = 1.98 mm). In the area between the two grey lines in Figure 3-13, rapeseed oil is

expected to be in the robust metastable composite state whereas methylene iodide will wet the

textured surface. Therefore, the capillary length which is the square root of the ratio of surface

forces (γ_{lv}) and body forces (ρg) provides the appropriate scaling to determine the robustness

factor.

68
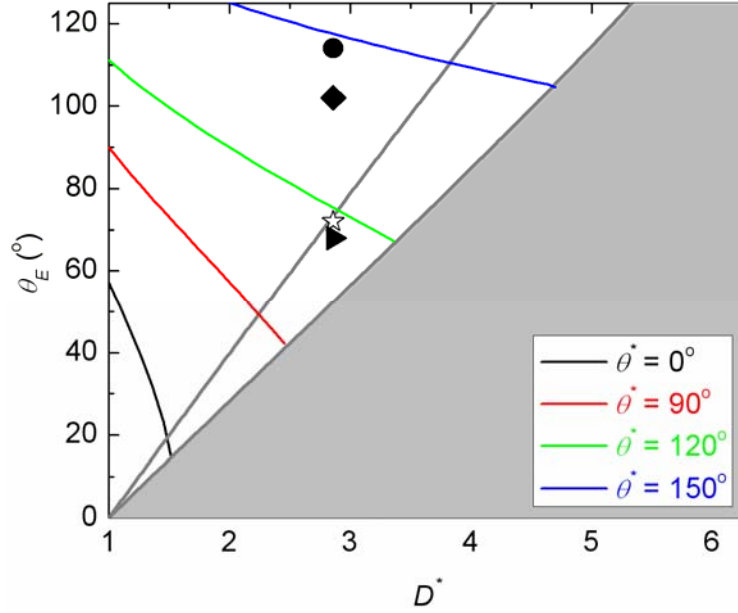
Figure 3-13. Design chart for liquid wettability for cylindrically textured surfaces with radius $R = 127$ μm. The contours of the of the apparent contact angle (θ^*) for ($\theta^* = 0$ (—), 90 (—), 120 (—) and 150° (—)) are plotted on the design chart with the equilibrium contact angle on a chemically identical smooth surface (θ_E) and the spacing ratio (D^*) as the two axes. In the shaded area, the robustness factor for rapeseed oil ($\ell_{cap} = 1.98$ mm) is less than unity. Below the grey line, the robustness factor for methylene iodide ($\ell_{cap} = 1.25$ mm) is less than unity.

3.11 Design chart for a surface textured with spheres of radius R and spacing $2D$

For a textured surface which is decorated by a hexagonally placed array of spheres with radius R and spacing $2D$ (Figure 3-14), the apparent contact angle can be computed using the CB relation.

Note that for a liquid droplet with equilibrium contact angle θ_E, we have $r_\phi = \dfrac{2(1+\cos\theta_E)}{\sin^2\theta_E}$,

$\phi_s = \dfrac{\pi \sin^2\theta_E}{2\sqrt{3}D^*}$, and $D^* = \left(\dfrac{R+D}{R}\right)^2$ therefore,

$$\cos\theta^* = -1 + \frac{1}{D^*}\left[\frac{\pi}{2\sqrt{3}}(1+\cos\theta_E)^2\right] \tag{3-4}$$

The contours of the apparent contact angle are plotted in Figure 3-14(c).
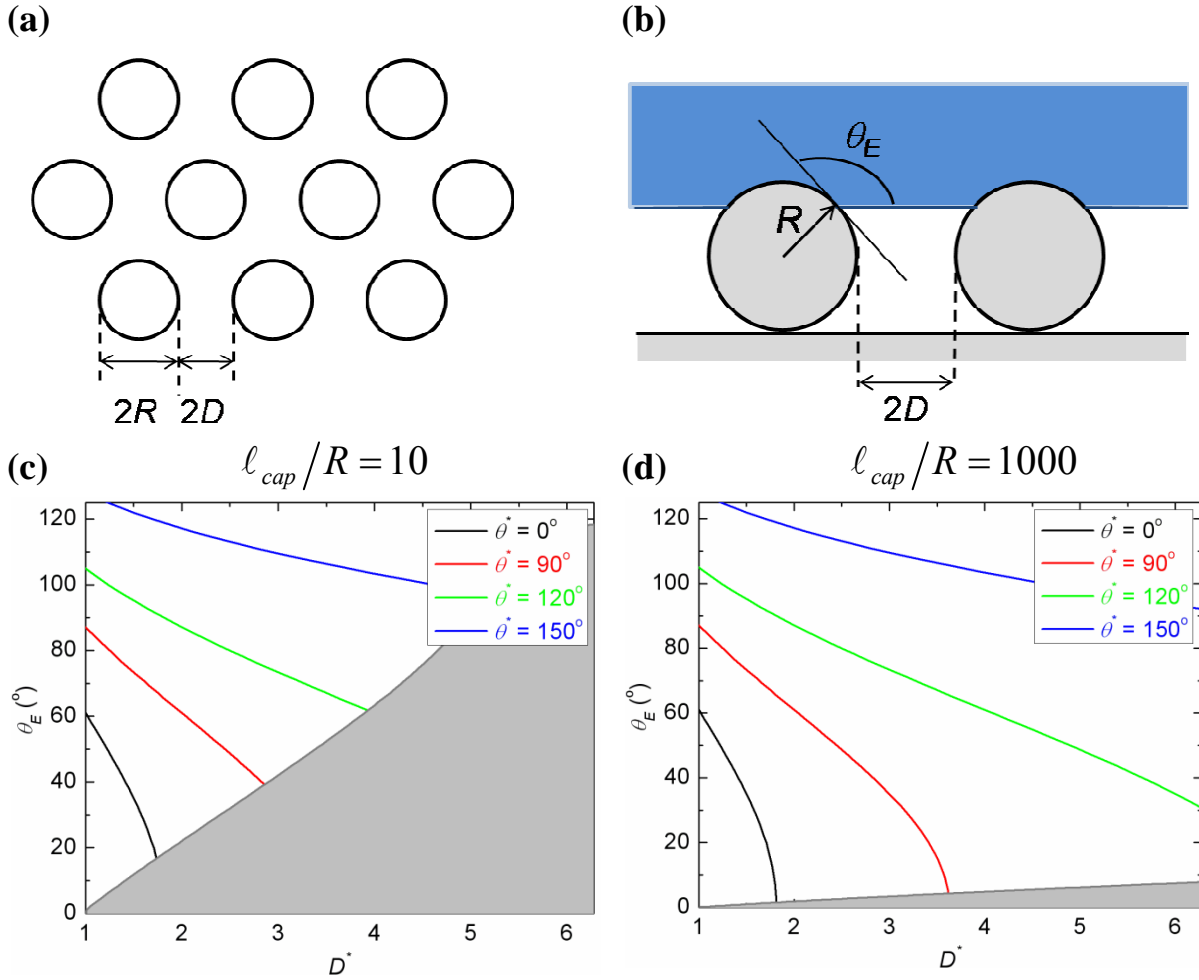
Figure 3-14 (a) Top view and (b) front view of a hexagonally packed regular array of spheres with radius R and spacing 2D. Design chart for liquid wettability of spherically textured surfaces. The contours of the apparent contact angle (θ^*) for ($\theta^* = 0$ (—), 90 (—), 120 (—) and 150° (—)) are plotted on the design chart with the equilibrium contact angle on a chemically identical smooth surface (θ_E) and the spacing ratio (D^*) as the two axes. Various regimes of wettability starting from super-wetting ($\theta^* \approx 0°$) to super-nonwetting ($\theta^* > 150°$) are shown on the design chart. This chart predicts the parameter space available for designing robust composite interfaces for two values of the ratio of the capillary length of the contacting liquid to the length scale of the surface texture (R). Figure (c) represents an hexagonal packed array of spheres with radius $R \approx 200$ μm, $\ell_{cap} = 2$ mm, and $\ell_{cap}/R = 10$ and Figure (d) shows the modified design chart for an array of spheres with $R \approx 2$ μm, and $\ell_{cap}/R = 1000$.

The robustness factor for the spherical texture (A^*) was computed by simplifying the expression for the robustness factor for hoodoo geometry.[25] By substituting the height of the hoodoo stem (H) and the minimum texture angle (ψ_{min}) to be zero, we obtain –

70

$$\frac{1}{A^*} \approx \frac{1}{H^*} + \frac{1}{T^*} \qquad (3\text{-}5)$$

where, $H^* = \dfrac{\ell_{cap}}{R}\left[\dfrac{\pi\left(1-\cos\theta_E\right)}{\left(2\sqrt{3}D^* - \pi\right)\left(\sqrt{D^*}-1\right)}\right]$, and $T^* = \dfrac{\ell_{cap}}{R}\left[\dfrac{\pi\sin\theta_E}{\left(2\sqrt{3}D^* - \pi\right)}\right]$

The impact of the pre-factor ℓ_{cap}/R on the robustness factor (A^*) is illustrated by plotting the

design chart in Figure 3-14 for (c) $\ell_{cap}/R = 10$ and (d) $\ell_{cap}/R = 1000$.

3.12   References

1.   Chhatre, S. S.; Tuteja, A.; Choi, W.; Revaux, A.; Smith, D.; Mabry, J. M.; McKinley, G. H.; Cohen, R. E., Thermal annealing treatment to achieve switchable and reversible oleophobicity on fabrics. *Langmuir* **2009,** In Press.
2.   Cassie, A.; Baxter, S., Wettability of porous surfaces. *Transactions of the Faraday Society* **1944,** 40, 546-551.
3.   Wenzel, R. N., Resistance of solid surfaces to water by wetting. *Ind. Eng. Chem.* **1936,** 28, (8), 988-994.
4.   Owens, D. K.; Wendt, R. C., Estimation of the surface free energy of polymers. *Journal of Applied Polymer Science* **1969,** 13, (8), 1741-1747.
5.   Onda, T.; Shibuichi, S.; Satoh, N.; Tsujii, K., Super-Water-Repellent Fractal Surfaces. *Langmuir* **1996,** 12, (9), 2125-2127.
6.   Quéré, D., Non-sticking drops. *Reports on Progress in Physics* **2005**, (11), 2495.
7.   Shibuichi, S.; Onda, T.; Satoh, N.; Tsujii, K., Super Water-Repellent Surfaces Resulting from Fractal Structure. *Journal of Physical Chemistry* **1996,** 100, (50), 19512-19517.
8.   Quéré, D., Wetting and Roughness. *Annual Review of Materials Research* **2008,** 38, (1), 71-99.
9.   Tuteja, A.; Choi, W.; Ma, M.; Mabry, J. M.; Mazzella, S. A.; Rutledge, G. C.; McKinley, G. H.; Cohen, R. E., Designing Superoleophobic Surfaces. *Science* **2007,** 318, (5856), 1618-1622.
10.   McHale, G.; Shirtcliffe, N. J.; Aqil, S.; Perry, C. C.; Newton, M. I., Topography Driven Spreading. *Physical Review Letters* **2004,** 93, (3), 036102.
11.   Marmur, A., From Hygrophilic to Superhygrophobic: Theoretical Conditions for Making High-Contact-Angle Surfaces from Low-Contact-Angle Materials. *Langmuir* **2008,** 24, (14), 7573-7579.
12.   Ahuja, A.; Taylor, J. A.; Lifton, V.; Sidorenko, A. A.; Salamon, T. R.; Lobaton, E. J.; Kolodner, P.; Krupenkin, T. N., Nanonails: A Simple Geometrical Approach to Electrically Tunable Superlyophobic Surfaces. *Langmuir* **2008,** 24, (1), 9-14.
13.   Choi, W.; Tuteja, A.; Chhatre, S.; Mabry, J. M.; Cohen, R. E.; McKinley, G. H., Fabrics with tunable oleophobicity. *Advanced Materials* **2009,** 21, (21), 2190-2195.
14.   Tuteja, A.; Choi, W.; McKinley, G. H.; Cohen, R. E.; Rubner, M. F., Design parameters for superhydrophobicity and superoleophobicity. *MRS Bulletin* **2008,** 33, (8), 752-758.

15. Marmur, A., Wetting on Hydrophobic Rough Surfaces: To Be Heterogeneous or Not To Be? *Langmuir* **2003,** 19, (20), 8343-8348.

16. Patankar, N. A., Transition between Superhydrophobic States on Rough Surfaces. *Langmuir* **2004,** 20, (17), 7097-7102.

17. Barbieri, L.; Wagner, E.; Hoffmann, P., Water Wetting Transition Parameters of Perfluorinated Substrates with Periodically Distributed Flat-Top Microscale Obstacles. *Langmuir* **2007,** 23, (4), 1723-1734.

18. Lafuma, A.; Quéré, D., Superhydrophobic states. *Nat Mater* **2003,** 2, (7), 457-460.

19. Cao, L.; Hu, H.; Gao, D., Design and Fabrication of Micro-textures for Inducing a Superhydrophobic Behavior on Hydrophilic Materials. *Langmuir* **2007,** 23, (8), 4310-4314.

20. Cao, L.; Price, T. P.; Weiss, M.; Gao, D., Super Water- and Oil-Repellent Surfaces on Intrinsically Hydrophilic and Oleophilic Porous Silicon Films. *Langmuir* **2008,** 24, (5), 1640-1643.

21. Herminghaus, S., Roughness-induced non-wetting. *Europhysics Letters* **2000,** 52, (2), 165.

22. Jian-Lin, L.; Xi-Qiao, F.; Gangfeng, W.; Shou-Wen, Y., Mechanisms of superhydrophobicity on hydrophilic substrates. *Journal of Physics: Condensed Matter* **2007,** 19, (35), 356002.

23. Kurogi, K.; Yan, H.; Tsujii, K., Importance of pinning effect of wetting in super water-repellent surfaces. *Colloids and Surfaces A: Physicochemical and Engineering Aspects* **2008,** 317, (1-3), 592-597.

24. Nosonovsky, M., Multiscale Roughness and Stability of Superhydrophobic Biomimetic Interfaces. *Langmuir* **2007,** 23, (6), 3157-3161.

25. Tuteja, A.; Choi, W.; Mabry, J. M.; McKinley, G. H.; Cohen, R. E., Robust omniphobic surfaces. *Proceedings of the National Academy of Sciences, USA* **2008**, 18200-18205.

26. Tester, J. W.; Modell, M., *Thermodynamics and Its Applications (3rd Edition)*. Prentice Hall PTR: 1996; p 201-220.

4 Thermal annealing treatment to achieve switchable and reversible oleophobicity on fabrics

[This chapter is partially reproduced from "S. S. Chhatre, A. Tuteja, W. Choi, A. Revaux, D. Smith, J. Mabry, G. H. McKinley, R. E. Cohen, *Langmuir* **2009**, 25 (23), 13625-13632" with permission from the American Chemical Society. Copyright 2009 American Chemical Society]

In previous chapters, a design chart for predicting wettability of liquids on textured surfaces was developed. In this chapter, the previously outlined robustness parameter framework and the design chart is applied to get a polyester fabric with switchable and reversible oleophobicity.

4.1 Coating methodology and conformality

A polyester fabric (Anticon 100) was dip-coated in a 10% POSS – 90% PEMA solution to generate a re-entrant textured surface with a conformal and low surface energy coating. Figure 4-1(a) shows an SEM micrograph for a piece of the dip-coated polyester fabric, while Figure 4-1(b) shows an EDAX elemental mapping for fluorine in an identical region of the sample. Figure 4-1(b) indicates that the fluorodecyl POSS (the only species with fluorine) has conformally coated individual fibers of the fabric.
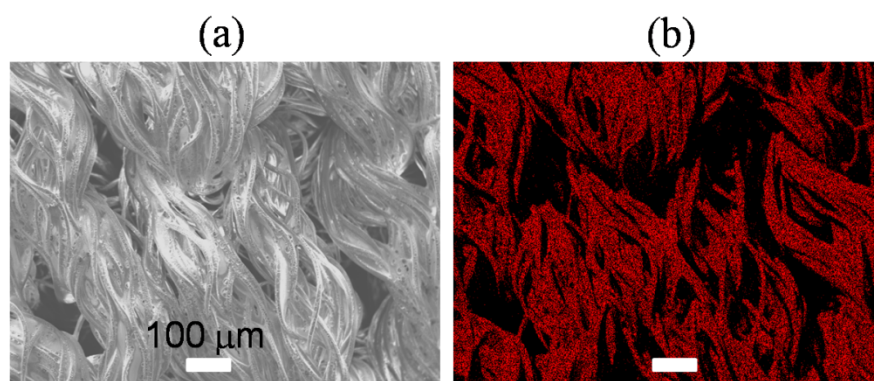
Figure 4-1 (a)An SEM micrograph of the polyester fabric Anticon 100 (b) EDAX fluorine elemental mapping of the identical area shown in Figure 3(a). The close correspondence between the two images confirms the conformal nature of the 10% POSS – 90% PEMA coating on the polyester fabric.

4.2 Tunable wettability on flat surfaces using thermal annealing treatment

In a blend of two or more components, selective migration of the low surface energy component at the solid-air interface has been observed in many polymeric systems.[1] Bousquet and co-workers tracked this variation of the air-solid interfacial composition in a polymeric blend of polystyrene (PS) with polystyrene-*block*-polyacrylic acid (PS-b-PAA).[2, 3] In the as-cast state, the polymeric surface was rich in low surface energy polymer PS and the surface was enriched further after heating the sample in dry air at 95 °C for 3 to 5 days. In contrast, a similar heat treatment in a humid environment resulted in the enrichment of the more hydrophilic PAA towards the air-solid interface.

In the present work, the interfacial energy between the solid surface and the annealing medium is used to control the surface composition and thereby to modulate the surface energy of a novel polymeric coating deposited on top of a commercially available polyester fabric. A thermal annealing treatment in dry air or water is used to tune the solid surface energy (γ_{sv}) and the resulting apparent contact angles (θ^*). This surface tunability, combined with the inherent re-entrant texture of the underlying fabric, leads to a switchable liquid wetting surface even for low surface tension liquids like hexadecane ($\gamma_{lv} = 27.5$ mN/m) and dodecane ($\gamma_{lv} = 25.3$ mN/m).

Contact angle measurements were performed on spin-coated silicon wafers in the original as-coated state (henceforth denoted by the notation - O) and also after consecutive annealing treatments of three hours at 90 °C, either in water followed by drying of the sample (denoted as - W) or in dry air (denoted as - A). The contact angles with water ($\gamma_{lv} = 72.1$ mN/m) displayed an oscillatory behavior for 2, 5, and 10 wt% POSS coating (Figure 4-2 (a), (b), and (c) respectively) for four cycles of the two different annealing treatments. Higher contact angles were consistently observed for the original as-coated or air-annealed samples, in comparison to the corresponding

water-annealed samples. Tapping mode AFM measurements showed that the rms roughness for all the samples considered range between approximately $4 - 5$ nm (Wenzel roughness, $r \approx 1.004$) and the roughness did not change appreciably after annealing. Therefore this variation in contact angles can be attributed to the variation of the surface chemical composition. The AFM phase images for air-annealed and water-annealed 10% POSS – 90% PEMA coatings on a silicon wafer are shown in Figure 4-2(d).
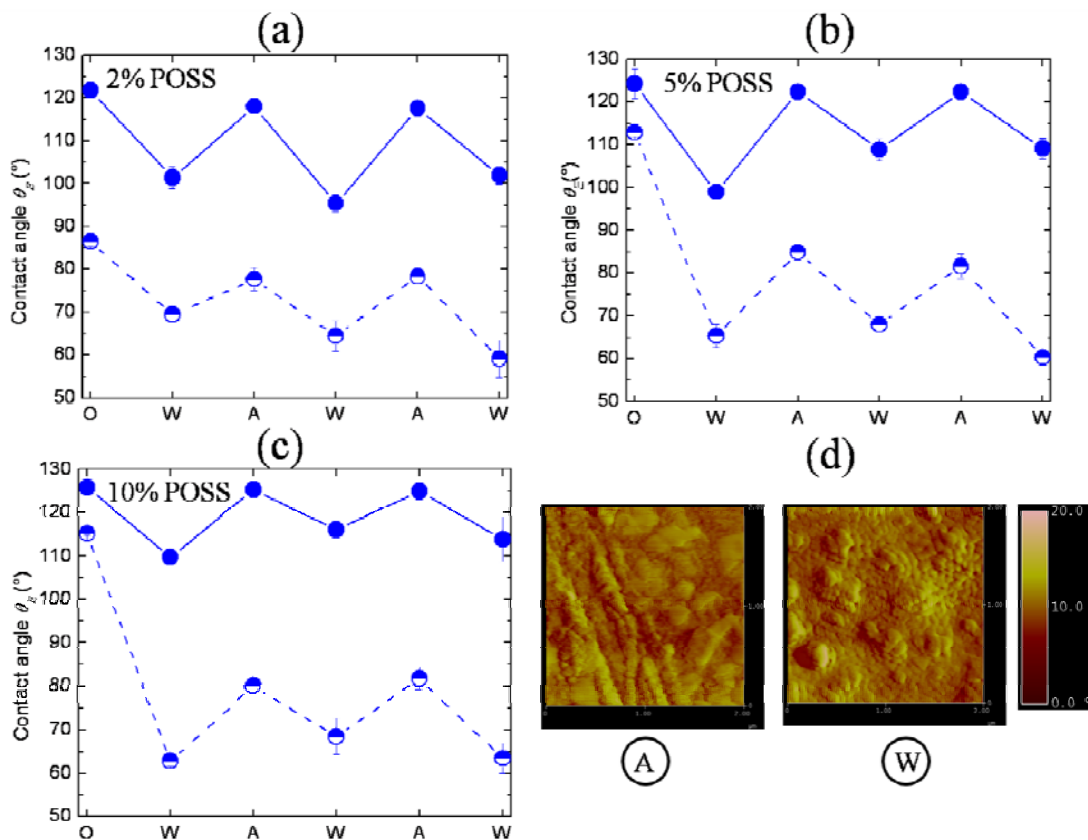
Figure 4-2. Contact angle measurements on flat spin-coated surfaces (rms roughness < 5 nm) (a) Advancing (filled symbols) and receding (half-filled symbols) contact angles for water on 2 wt%, (b) 5 wt% and (c) 10 wt% fluorodecyl POSS-coated flat surfaces. The contact angles were measured in the original state (denoted as - O), after annealing in water at 90 °C for three hours followed by drying at room temperature (denoted as - W), and after annealing in air at 90 °C for three hours (denoted as - A). (d) AFM phase images of 10 wt% fluorodecyl POSS-coated flat surface after annealing in air (A) and in water (W).

An identical sequence of annealing treatments resulted in a similar trend in the contact angle values for hexadecane ($\gamma_{lv} = 27.5$ mN/m) and other lower surface tension alkanes. The advancing

contact angle (θ_{adv}) with hexadecane varied from $80 \pm 2°$ on an air-annealed 10% POSS surface to $57 \pm 4°$ on the corresponding surface annealed in water. The corresponding receding contact angles (θ_{rec}) were $56 \pm 5°$ and $16 \pm 2°$ respectively. Using the measured values of the advancing contact angle with water and alkanes, the surface energy of the air-annealed and water-annealed 10% POSS – 90% PEMA flat surface was estimated independently using both Zisman[4] (Figure 4-3) and the Owens-Wendt analysis.[5] Extrapolation of advancing contact angle data obtained for spin-coated flat silicon wafers with the homologous series of alkanes, yields critical surface tension values of $\gamma_c^{(air)} = 3 \pm 1.5$ mN/m for the air-annealed and $\gamma_c^{(water)} = 15.3 \pm 0.4$ mN/m for the water-annealed surface respectively. Although the data for the air-annealed state in Figure 4-3 show a clear linear variation with γ_{lv}, the critical surface tension determined by extrapolation in the Zisman analysis is unphysically low. This is because we expect the surface tension to be greater than $\gamma_{sv} \approx 6.7$ mN/m, the accepted minimum corresponding to a surface comprised of a monolayer of $-CF_3$ moieties.[4, 6] Although the actual numerical value of the critical surface tension (γ_c) is likely to be an artifact of the extrapolation procedure, the comparison of the two sets of advancing contact angle data obtained from the same experimental protocol is still instructive. The data illustrates that the surface energy of the 10% POSS – 90% PEMA surface in the water-annealed state (W) is considerably higher than the surface energy in the air-annealed state (A).

The polar and dispersive contributions to the solid-vapor interfacial energy (γ_{sv}) were determined by the Owens-Wendt analysis using water and octane as the probing liquids. For the 10% POSS – 90% PEMA surface annealed in air, the polar component of the solid surface energy was $\gamma_{sv}^p = 0.3$ mN/m, with a dispersive component $\gamma_{sv}^d = 10.1$ mN/m, giving a total surface energy of $\gamma_{sv}^{(air)} =$

10.4 mN/m. Similarly, the polar component for the water-annealed surface was 1.3 mN/m and the dispersive component was 15.5 mN/m, leading to a total surface energy of $\gamma_{sv}^{(water)} = 16.8$ mN/m. The computed values of the estimated surface energy from Owens-Wendt analysis are more consistent with those expected for a fluorinated surface. These values again demonstrate that the surface energy is significantly higher after annealing in water (W) when compared to an identical surface annealed in air (A). For comparison, the estimated solid surface energy of a spin-coated PEMA surface is $\gamma_{sv} = 32$ mN/m ($\gamma_{sv}^{p} = 21$ mN/m and $\gamma_{sv}^{d} = 11$ mN/m). The low values of the solid surface energies estimated using the Owens-Wendt analysis also suggest a significant enrichment of the surface with the low surface energy fluorodecyl POSS species, for the air-annealed 10% POSS – 90% PEMA spin-coated surface.
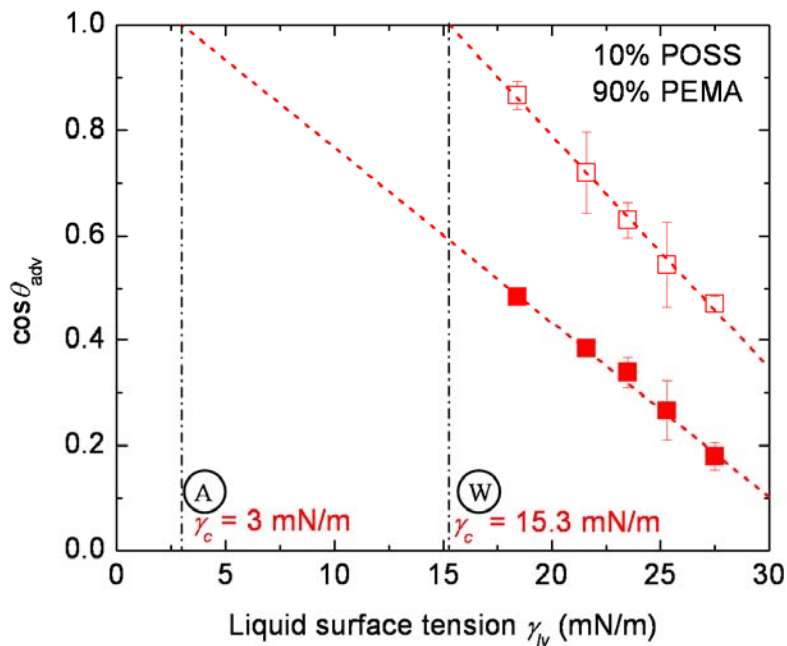
Figure 4-3. Zisman analysis for 10% POSS – 90% PEMA spin coated film annealed in air (A, red filled squares) and annealed in water (W, red open squares). The contact angle data are measured with alkanes *i.e.* hexadecane ($\gamma_{lv} = 27.5$ mN/m), dodecane ($\gamma_{lv} = 25.3$ mN/m), decane ($\gamma_{lv} = 23.8$ mN/m), octane ($\gamma_{lv} = 21.6$ mN/m), and hexane ($\gamma_{lv} = 18.5$ mN/m) as contacting liquids and the critical surface tension for the solid surface is obtained by linear extrapolation of the contact angle data.

4.3 Tunable wettability on a polyester fabric surface using thermal annealing treatment

This variation in the equilibrium contact angle on a flat surface can be amplified by combining the aforementioned annealing treatment with a re-entrant textured surface such as that of a commercially available fabric. The apparent contact angle (θ^*) measurements on the dip-coated fabric surface with water (γ_{lv} = 72.1 mN/m) are presented in Figure 4-4 (blue circles).
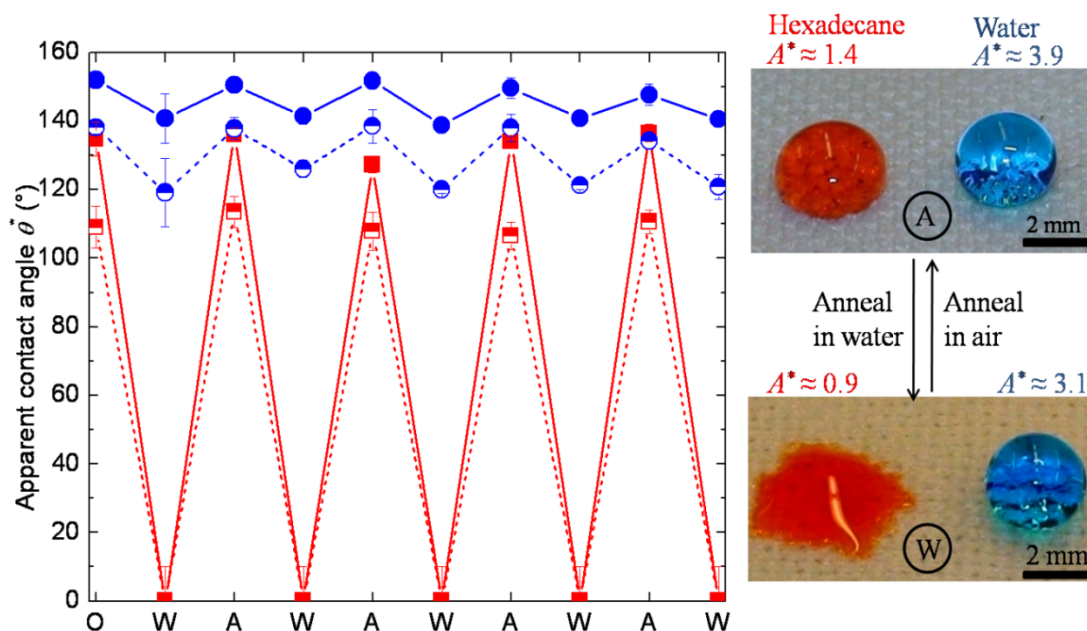
Figure 4-4. Switchable liquid wettability on a 10 wt% fluorodecyl POSS coated polyester fabric surface. (a) Apparent advancing (filled symbols) and receding (half-filled symbols) contact angle data with water (blue circles) and hexadecane (red squares) on 10 wt% fluorodecyl POSS-coated polyester fabric surface in the original as-made (O), water annealed (W), and air annealed (A) states. (b) Small droplets (V $\approx$ 50 μL) of water (γ_{lv} = 72.1 mN/m) and hexadecane (γ_{lv} = 27.5 mN/m) forming robust composite interfaces on the dip-coated fabric in the air annealed state (A). (c) Fully wetted hexadecane droplet along with a water droplet forming a robust composite interface on the dip-coated fabric in the water annealed state (W).

It is clear that the observed apparent contact angles (θ^*) show an oscillatory behavior when the dip-coated fabric is successively annealed in water and dry air. The apparent advancing contact angle (θ^*_{adv}) with water (filled blue circles in Figure 4-4(a)) varies from $150 \pm 2°$ in the air-annealed state, to $140 \pm 3°$ in the water-annealed state, whereas the corresponding apparent

receding angle (θ_{rec}^*) (open blue circles in Figure 4-4(a)) ranges from $137 \pm 3°$ to $121 \pm 4°$. The robustness of this solid-liquid-air composite interface was computed using Equation 2 by assuming that the size of the fabric bundles as the dominant surface texture (i.e. assuming $R = 100$ μm, Figure 4-1(a)). For the smallest value of advancing contact angle on a smooth surface ($\theta_{adv} \sim 95°$ i.e. the advancing contact angle on the surface annealed in water), the robustness factor is found to be significantly greater than unity ($A^* \sim 2.4$). As a consequence, water droplets form robust composite interfaces on both the air-annealed and water-annealed surfaces (Figure 4-4 (b) and (c) respectively).

It is clear from Equation 2 that the robustness of the composite interface established by a liquid drop in contact with a re-entrant texture varies with the surface tension of the contacting liquid. Hexadecane droplets ($\gamma_{lv} = 27.5$ mN/m) form a robust metastable composite solid-liquid-air interface (with $\theta_{adv}^* = 135°$, $\theta_{rec}^* = 115°$ and $A^* \sim 1.4$) on both the original as-made (O) and air-annealed surfaces (A, Figure 4-4(b)). However when annealed in water, the advancing contact angle for hexadecane droplets on a flat surface reduces from $\theta_{adv}^{(air)} = 80 \pm 2°$ to $\theta_{adv}^{(water)} = 57 \pm 4°$.

This reduction in the advancing contact angle on a flat surface (θ_{adv}) leads to a lowering of the robustness parameter to approximately unity ($A^* \approx 0.9$), consequently the solid-liquid-air composite interface on the fabric transitions to the fully-wetted or Wenzel state ($\theta_{adv}^* \sim 0°$, $\theta_{rec}^* \sim 0°$, as shown in Figure 4-4(c)). As a result, switchable liquid wettability for hexadecane can be achieved between the two states, corresponding to a robust (but metastable) composite interface and a fully wetted interface, by using simple annealing treatments in air and water respectively (red squares in Figure 4-4(a)). Moreover, this switchability in the wetting behavior is repeatable, and the reversibility is demonstrated over five cycles of air and water annealing treatments

(Figure 4-4(a)). The uncoated fabric and fabric coated with PEMA alone do not display any variation in the apparent contact angles with water and hexadecane after identical annealing treatments. Also, it is important to note that droplets of toluene or acetone which are good solvents for PEMA wet the polyester fabric surface after it has been dip-coated either with 10% POSS – 90% PEMA or with pure PEMA. If such liquids are used for annealing treatment or contact angle measurements, the PEMA in the coating progressively dissolves in the solvent and the oleophobicity of the fabric surface is subsequently destroyed. Such effects may be mitigated in applications by using alternate elastomeric binders that can be chemically crosslinked following dip-coating.

As a control experiment, contact angle measurements were performed on the polyester fabric in the as-received, uncoated state and also after dip-coating in 10 mg/ml pure PEMA in Asahiklin (AK 225). No significant variation was observed in the apparent contact angles (θ^*) on these samples after a couple of annealing cycles in DI water at 90 °C and in dry air at 90 °C for 3 hours (results shown in Figure 4-5).
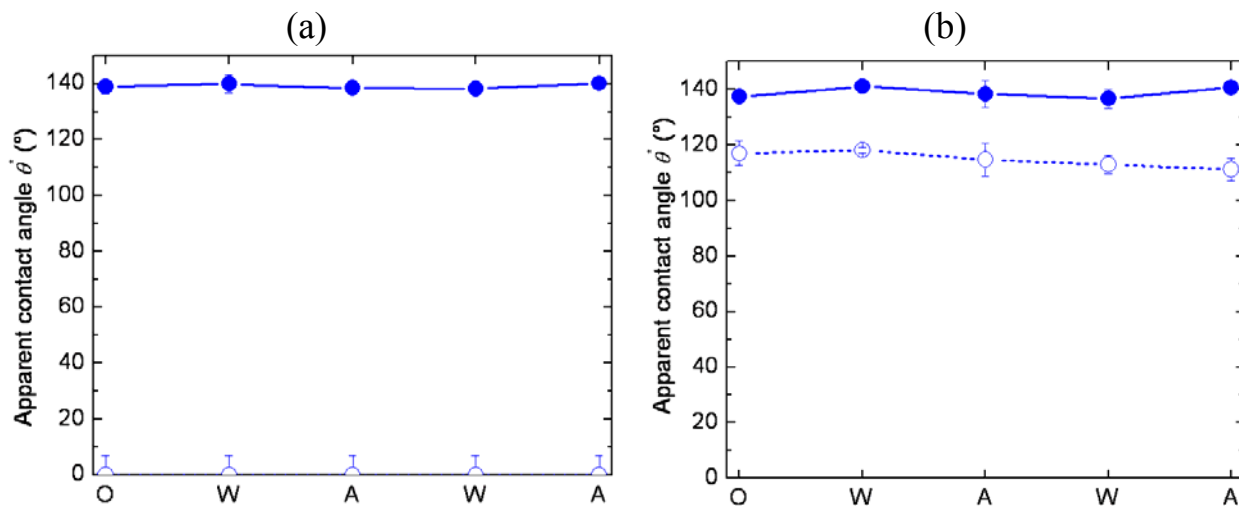
Figure 4-5. Variation in the apparent advancing (θ^*_{adv}) and receding (θ^*_{rec}) contact angles on polyester fabric (a) in the as-received uncoated state and (b) dip-coated with PEMA solution.

4.4 Generalized non-wetting diagram

The changes in the contact angles on flat (θ_E) and textured surfaces (θ^*) that result from annealing in air or water can be compactly represented in terms of a non-wetting diagram.[7-10] The variation in the cosine of the advancing apparent contact angle ($\cos\theta^*_{adv}$) on a dip-coated polyester fabric surface was plotted against the cosine of the advancing contact angle on a flat surface ($\cos\theta_{adv}$) as shown in Figure 4-6.
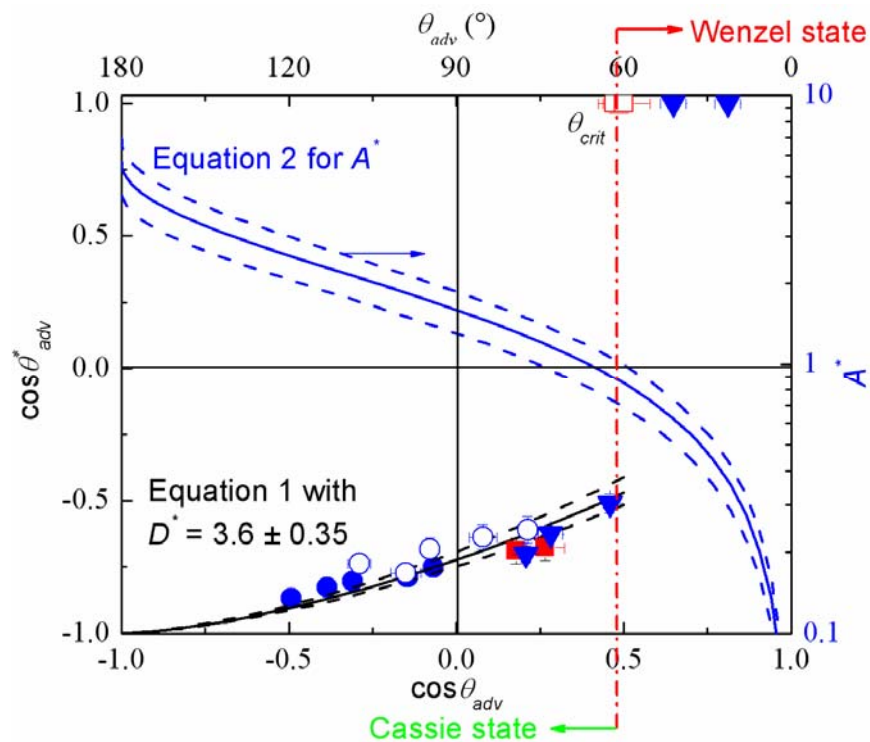
Figure 4-6. Generalized non-wetting diagram for the dip-coated oleophobic polyester fabrics. Cosine of the apparent advancing contact angle ($\cos\theta^*_{adv}$) is plotted against the cosine of the advancing contact angle on a flat surface ($\cos\theta_{adv}$). Advancing contact angle data is shown for water-methanol mixtures (blue circles), and alkanes hexadecane ($\gamma_{lv} = 27.5$ mN/m) and dodecane ($\gamma_{lv} = 25.3$ mN/m) (red squares) on air-annealed (A, filled symbols) and water-annealed (W, open symbols) 10% POSS – 90% PEMA dip-coated surfaces. Advancing contact angles with water-methanol mixtures on PEMA-coated surface are also plotted (blue filled triangles). The black dotted line is the Cassie-Baxter equation with $D^* = 3.6 \pm 0.35$ (Equation 1). The blue solid line is the robustness parameter (A^*) corresponding to $R = 100$ μm and $D^* = 3.6$ plotted against the cosine of the advancing contact angle on a flat surface (θ_{adv}). The transition from a composite to a fully wetted interface takes place around $\theta_{crit} \approx 60°$.

The existence of a robust oleophobic textured surface is demonstrated by the data in the lower right quadrant (where $\theta_{adv} < 90°$ but $\theta^*_{adv} > 90°$, and henceforth denoted as Quadrant IV). Figure 4-6 shows the observed advancing contact angle data for water-methanol mixtures (blue) and alkanes (red) on dip-coated polyester fabric. From the Zisman analysis (Figure 2) and Owens-Wendt analysis, it is clear that the air-annealed surface coating has a lower surface energy than the corresponding water-annealed 10% POSS – 90% PEMA coating. Therefore higher contact angles are observed for water-methanol mixtures (0 to 80% by volume methanol) on the air-annealed surface (A, blue filled circles in Quadrant III, where $\theta_{adv} > 90°$ and $\theta^*_{adv} > 90°$) compared to those on the water-annealed surface (W, blue open circles in Quadrants III and IV). Water-methanol mixtures up to 80% methanol by volume formed robust composite interfaces on fabric samples dip-coated in 10% POSS – 90% PEMA and subsequently annealed in either air (A) or water (W). On the contrary, lower surface tension liquids like hexadecane ($\gamma_{lv} = 27.5$ mN/m) and dodecane ($\gamma_{lv} = 25.3$ mN/m) switched from a robust metastable composite interface in the air-annealed state (A, red filled squares in Quadrant IV) to a fully wetted interface in the water-annealed state (W, red open squares in Quadrant I).

In order to explore the parameter space in Quadrant IV more effectively, the polyester fabric was dip-coated in pure PEMA solution ($\theta_{adv} = 78°$ with water) and contact angle measurements were performed on the textured PEMA surface. Water-methanol mixtures up to 40% methanol by volume formed a robust composite interface on the fabric dip-coated in PEMA alone (blue filled triangles in Quadrant IV). Mixtures with higher fractions of methanol wetted the PEMA-coated fabric spontaneously (blue filled triangles in Quadrant I). It is important to point out that once again the wetting behavior on PEMA coated fabric samples was independent of the annealing history.

The contact angle data on the three different coatings applied to the polyester fabric (*i.e.* (i) air annealed 10% POSS – 90% PEMA, (ii) water annealed 10% POSS – 90% PEMA, and (iii) pure PEMA), and with different polar (water-methanol mixtures) and non-polar liquids (various alkanes) were used to obtain the best fit value of the single geometric parameter D^* (see Equation 1) which characterizes the dip-coated polyester fabric. The black line shown in Figure 5 is the Cassie-Baxter equation for a surface composed of an aligned array of cylinders (Equation 1) with $D^* = 3.6 \pm 0.35$. This value of the spacing ratio (D^*) is obtained from the contact angle measurements alone and compares favorably with the value of the spacing ratio estimated by visual inspection of the SEM micrograph. Therefore, by measuring the variation in the apparent contact angles on a conformally coated textured surface, the fabric texture can be characterized in terms of the geometric spacing ratio D^*.

For the surfaces considered in Figure 4-6, the transition from a composite interface to a fully-wetted interface occurs at a critical contact angle on a flat surface $\theta_{crit} \sim 60°$. This sharp transition can be rationalized by considering the variation of the robustness factor A^*. The variation in the robustness factor A^* for hexadecane ($\gamma_{lv} = 27.5$ mN/m, $\ell_{cap} = 1.91$ mm) is plotted against the advancing contact angle on a flat surface (θ_{adv}) on the non-wetting diagram by using representative values of surface geometry parameters ($R = 100$ μm, $D^* = 3.6 \pm 0.35$). As the contact angle of the liquid on the flat surface decreases and $\cos\theta_E \rightarrow 1$, the robustness factor steadily decreases (Equation 2).[11, 12] When the robustness factor (A^*) decreases towards values close to unity ($A^*_{crit} \approx 0.9$ in this case) the composite interface transitions to a fully-wetted interface. Note that the capillary length values for hexadecane ($\ell_{cap} = 1.91$ mm) and 60% methanol – 40% water mixtures ($\ell_{cap} = 1.86$ mm) are similar. Thereby, the critical robustness

factor values for the water-methanol mixtures are similar to the values computed for hexadecane. The robustness parameter framework suggests that a metastable composite interface can be achieved only when $A^* > 1$, therefore the Cassie-Baxter prediction in Figure 5 is extended only up to a contact angle on a smooth surface at which $A^* \sim 1$.

From Equation 2 and Figure 4-6, it is clear that hexadecane droplets (γ_{lv} = 27.5 mN/m) will establish a robust metastable Cassie state on textures with $D^* \approx 3.6$ if the advancing contact angle on a flat surface is θ_{adv} > 60°, but will transition to a fully-wetted Wenzel state if the contact angle is below θ_{adv} < 60° ($A^* \approx 1$). Variations in the apparent contact angle (θ^*) and design parameters (D^*, A^*) are outlined here for a particular fabric (Anticon 100) and a particular contacting liquid (hexadecane). However a similar framework can be developed for any liquid on any textured surface. By coating the texture with materials of various surface energy and performing contact angle measurements with a range of liquids, the textural parameters describing the surface can be fully characterized in terms of the dimensionless spacing ratio (D^*). Moreover having determined D^*, and knowing the equilibrium contact angle on a flat surface (θ_E) plus other physical properties of the liquid, the ability of a textured surface to support a composite interface with a given contacting liquid can be anticipated by computing the value of the robustness factor (A^*).

4.5 XPS studies to investigate the mechanism of switchable wettability

The observed changes in the macroscopic equilibrium contact angles (θ_E) (as highlighted in Figure 4-2) and the computed surface energy values can be related to molecular level rearrangements in the coating. The low surface energy component within the coating, *i.e.* fluorodecyl POSS ($\gamma_{sv} \approx 10$ mJ/m^2)[11] experiences a thermodynamic driving force to move

towards the solid-air interface in order to minimize the solid-vapor interfacial free energy (γ_{sv}) of the POSS – PEMA coating. The presence of solvent at the beginning of the drying step ensures high mobility of POSS, which facilitates its initial surface segregation. The fluorine to carbon (F/C) ratio for pure fluorodecyl POSS is 1.7 while it is 0 for pure PEMA. Based on these values, the F/C atomic ratio in the bulk of the 10% POSS – 90% PEMA sample can be readily computed to be 0.002. X-ray photoelectron spectroscopy (XPS) was used to probe the local composition of the surface (~ 10 nm probing depth).[13-15] XPS analysis was performed on spin-coated films of pure PEMA, pure fluorodecyl POSS and 10% POSS – 90% PEMA on silicon wafers and the results are summarized in . The various atomic ratios computed from the XPS survey spectra match reasonably with the computed values of the atomic ratios for pure PEMA and pure fluorodecyl POSS samples ().

The F/C ratios obtained from the survey spectra for air-annealed and water- annealed surfaces (Figure 6(a)) are 1.69 and 0.83 respectively. The greatly enhanced value of the F/C ratio at the surface (compared to the bulk) confirms the surface segregation of the low surface energy fluorodecyl POSS species. For the 10% POSS – 90% PEMA air-annealed samples, the atomic ratios (F/C, O/C and Si/C) are nearly equal to the corresponding ratios in the pure fluorodecyl POSS sample. This similarity in chemical composition and solid surface energy ($\gamma_{sv}^{(air)}$ = 10.4 mJ/m^2) of the 10% POSS – 90% PEMA air-annealed samples to pure fluorodecyl POSS ($\gamma_{sv} \approx 10$ mJ/m^2)[11] indicates that the surface is mostly composed of fluorodecyl POSS. In contrast, significant lowering of the F/C ratio from 1.69 to 0.83, enhancement of the O/C ratio from 0.13 to 0.24, and increase in the solid surface energy from 10.4 to 16.8 mJ/m^2 indicate that the 10% POSS – 90% PEMA water-annealed surface has a higher PEMA content. Because the annealing treatment is carried out above the glass transition temperature ($T = 90\,°C > T_g$), the PEMA

chains at the surface have sufficient mobility to rearrange. This rearrangement of the PEMA chains can be tuned using the surface energy of the annealing media and is reversible over many cycles, as demonstrated through the variation of the equilibrium contact angles on a flat spin-coated surface (θ_E, Figure 4-2) and on polyester fabrics (θ^*, Figure 4-4). By lowering the take-off angle at which the photo-electrons are collected, even thinner sample interrogation volumes (sampling depth < 10 nm) can be probed using XPS. When the samples were probed at a take-off angle of 20°, the F/C ratio was found to be higher than the F/C ratio obtained with 90° take-off angle (data presented in Further information about the chemical composition of the surface can be generated by examining high resolution carbon 1s spectra for samples annealed in air and water, as shown in Figure 4-7(b) and (c) respectively. Various peaks in the high resolution spectra were indexed by comparing the binding energy at the peak maximum with standard spectra available for PEMA and poly (vinylidene fluoride).[16] The spectrum for the air-annealed sample (Figure 4-7(b)) has a larger peak associated with the $-CF_2-$ moiety as compared to the peak associated with the $-CH_2-$ moiety, which once again indicates a larger surface presence of fluorodecyl POSS (which is the lone contributor to the $-CF_2-$ peak). On the other hand, for the case of the water-annealed sample (Figure 4-6(c)), the greater intensity of the $-CH_2-$ peak relative to the $-CF_2-$ peak confirms the presence of PEMA at the surface. The survey spectra and high resolution carbon 1s spectra for pure PEMA and pure fluorodecyl POSS is shown in Figure 4-8 for reference.

Therefore, it can be concluded that the rearrangement of the PEMA chains at the surface is the main response to the annealing treatment. This subtle molecular response in the local chemical composition, when combined with a strongly re-entrant physical texture gives rise to non-wetting surfaces with switchable oleophobicity.

), for the corresponding air-annealed, as well as the water-annealed samples. This systematic variation in the F/C ratio indicates that the amount of fluorodecyl POSS is highest within the first few molecular layers from the surface, irrespective of the annealing condition. This observation suggests that the fluorodecyl POSS crystals as a whole are not migrating towards or away from the interface between the solid and the annealing medium (dry air or water), and PEMA rearrangement at the surface seems to be a more feasible explanation for our observations.

Further information about the chemical composition of the surface can be generated by examining high resolution carbon 1s spectra for samples annealed in air and water, as shown in Figure 4-7(b) and (c) respectively. Various peaks in the high resolution spectra were indexed by comparing the binding energy at the peak maximum with standard spectra available for PEMA and poly (vinylidene fluoride).[16] The spectrum for the air-annealed sample (Figure 4-7(b)) has a larger peak associated with the $-CF_2-$ moiety as compared to the peak associated with the $-CH_2-$ moiety, which once again indicates a larger surface presence of fluorodecyl POSS (which is the lone contributor to the $-CF_2-$ peak). On the other hand, for the case of the water-annealed sample (Figure 4-6(c)), the greater intensity of the $-CH_2-$ peak relative to the $-CF_2-$ peak confirms the presence of PEMA at the surface. The survey spectra and high resolution carbon 1s spectra for pure PEMA and pure fluorodecyl POSS is shown in Figure 4-8 for reference.

Therefore, it can be concluded that the rearrangement of the PEMA chains at the surface is the main response to the annealing treatment. This subtle molecular response in the local chemical composition, when combined with a strongly re-entrant physical texture gives rise to non-wetting surfaces with switchable oleophobicity.

Figure 4-7. XPS analysis of the 10 wt% fluorodecyl POSS – 90% PEMA dip-coated flat surface. (a) Survey spectra of the dip-coated surface annealed in water (W), showing major elemental peaks corresponding to F, O, C, and Si. (b) and (c) High resolution carbon 1s spectra for air-annealed (A) and water-annealed (W) dip-coated surfaces showing peaks corresponding to various carbon moieties present in the top layer (d ≤ 10 nm) of the POSS-PEMA coating.

Table 4-1. Computed atomic ratios and experimentally observed values from the XPS spectra for pure PEMA, pure fluorodecyl POSS and air-annealed (A) as well as water-annealed (W) 10% POSS – 90% PEMA spin-coated silicon wafer samples.

Sample description (take-off angle)		F / C	O / C	Si / C
PEMA	Computed	0	0.33	0
	Observed	0	0.27	0
POSS	Computed	1.7	0.15	0.1
	Observed	1.85	0.13	0.09
10% POSS – 90% PEMA	Computed	~0	~0.33	~0
	Air-annealed (90°)	1.69	0.13	0.07
	Water-annealed (90°)	0.83	0.24	0.05
	Air-annealed (20°)	1.91	0.14	0.08

	Water-annealed (20°)	1.41	0.20	0.07
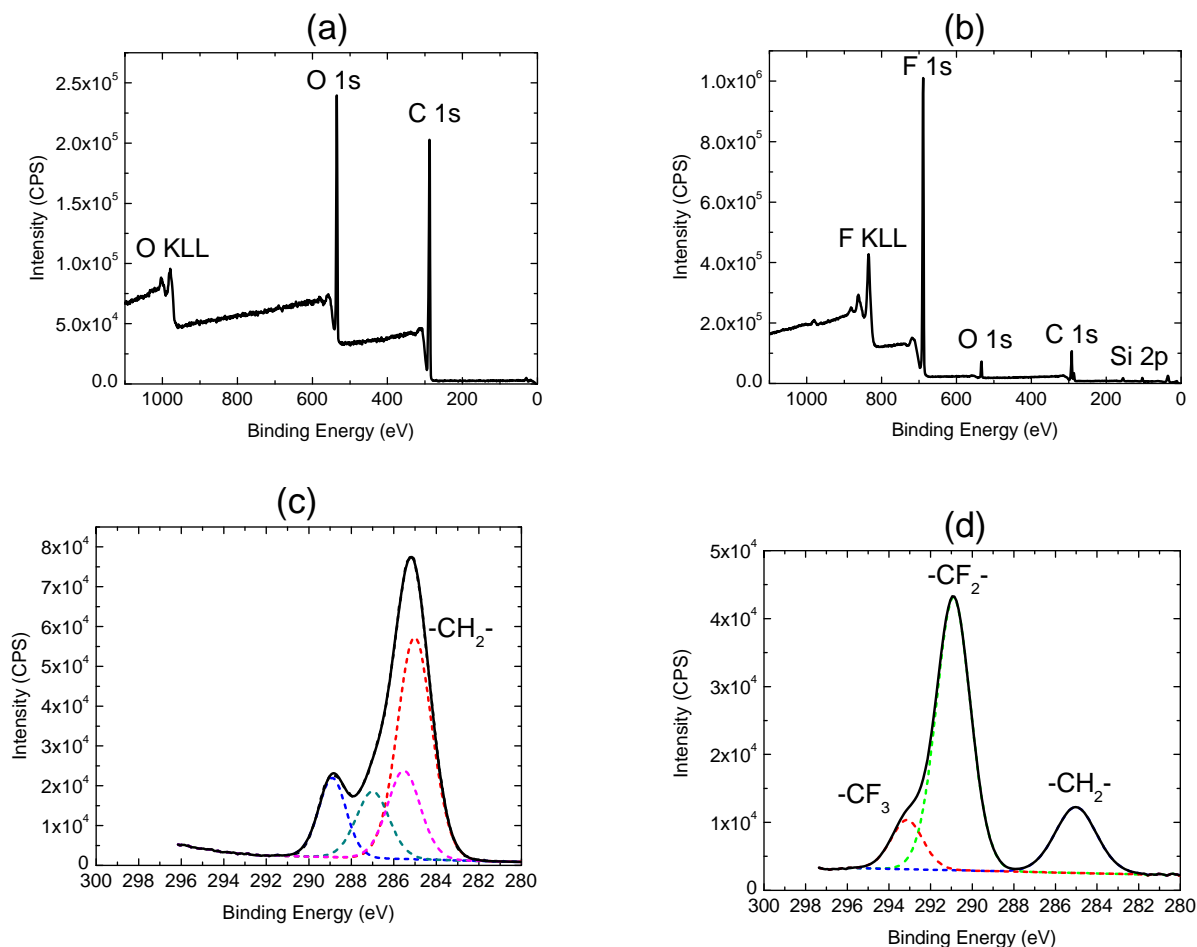
Figure 4-8. Survey spectra for (a) PEMA and (b) fluorodecyl POSS showing the characteristic peaks for carbon, oxygen, silicon, and fluorine and high resolution carbon 1s spectra for (c) PEMA and (d) fluorodecyl POSS are shown.

4.6 References

1. Luzinov, I.; Minko, S.; Tsukruk, V. V., Adaptive and responsive surfaces through controlled reorganization of interfacial polymer layers. *Progress in Polymer Science* **2004,** 29, (7), 635-698.
2. Bousquet, A.; Ibarboure, E.; Drummond, C.; Labrugere, C.; Papon, E.; Rodriguez-Hernandez, J., Design of Stimuli-Responsive Surfaces Prepared by Surface Segregation of Polypeptide-b-polystyrene Diblock Copolymers. *Macromolecules* **2008,** 41, (4), 1053-1056.
3. Bousquet, A.; Pannier, G.; Ibarboure, E.; Papon, E.; Rodriguez-Hernandez, J., Control of the Surface Properties in Polymer Blends. *Journal of Adhesion* **2007,** 83, (4), 335 - 349.
4. Zisman, W. A., *Relation of the equilibrium contact angle to liquid and solid construction.* American Chemical Society, Washington DC: 1964.

5.   Owens, D. K.; Wendt, R. C., Estimation of the surface free energy of polymers. *Journal of Applied Polymer Science* **1969,** 13, (8), 1741-1747.

6.   Nishino, T.; Meguro, M.; Nakamae, K.; Matsushita, M.; Ueda, Y., The Lowest Surface Free Energy Based on -CF3 Alignment. *Langmuir* **1999,** 15, (13), 4321-4323.

7.   Onda, T.; Shibuichi, S.; Satoh, N.; Tsujii, K., Super-Water-Repellent Fractal Surfaces. *Langmuir* **1996,** 12, (9), 2125-2127.

8.   Shibuichi, S.; Onda, T.; Satoh, N.; Tsujii, K., Super Water-Repellent Surfaces Resulting from Fractal Structure. *Journal of Physical Chemistry* **1996,** 100, (50), 19512-19517.

9.   Quéré, D., Non-sticking drops. *Reports on Progress in Physics* **2005**, (11), 2495.

10.   Quéré, D., Wetting and Roughness. *Annual Review of Materials Research* **2008,** 38, (1), 71-99.

11.   Tuteja, A.; Choi, W.; Mabry, J. M.; McKinley, G. H.; Cohen, R. E., Robust omniphobic surfaces. *Proceedings of the National Academy of Sciences, USA* **2008**, 18200-18205.

12.   Choi, W.; Tuteja, A.; Chhatre, S.; Mabry, J. M.; Cohen, R. E.; McKinley, G. H., Fabrics with tunable oleophobicity. *Advanced Materials* **2009,** 21, (21), 2190-2195.

13.   Schmidt, D. L.; Coburn, C. E.; DeKoven, B. M.; Potter, G. E.; Meyers, G. F.; Fischer, D. A., Water-based non-stick hydrophobic coatings. *Nature* **1994,** 368, (6466), 39-41.

14.   Ming, W.; van-de-Grampel, R. D.; Gildenpfennig, A.; Snijder, A.; Brongersma, H. H.; van-der-Linde, R.; de-With, G., Thermodynamically Controlled Surface Segregation of perfluoroalkyl-End-Capped PMMA as investigated by Low Energy Ion Scattering (LEIS). *Polymeric Materials Science and Engineering* **2003,** 88, 517.

15.   Mao, Y.; Gleason, K. K., Vapor-Deposited Fluorinated Glycidyl Copolymer Thin Films with Low Surface Energy and Improved Mechanical Properties. *Macromolecules* **2006,** 39, (11), 3895-3900.

16.   Beamson, G.; Briggs, D., *High resolution XPS of organic polymers: the Scientia ESCA300 database*. Wiley: New York, 1992.

5 Tunable wettability using biaxial stretching of fabrics

In this work, we analyze these design parameters more extensively to understand the combined effect of surface texture and material properties on the wetting characteristics of a given surface. Further, the design parameters predict that stretching fluorodecyl POSS dip-coated commercial fabrics can lead to a dramatic reduction in the robustness of the composite interface supported with a given contacting liquid. Indeed, beyond a critical imposed strain, the contacting liquid is completely imbibed into the fabric texture, leading to near zero contact angles. This allows us to develop for the first time surfaces that exhibit reversible, deformation-dependent, tunable wettability, including the capacity to switch their surface wetting properties (between super-repellent and super-wetting) against a wide range of polar and non-polar liquids.

5.1 Dip-coating and oleophobicity of the polyester fabric

When a liquid contacts a textured surface, such as the one shown in Figure 5-1, then, provided the pressure difference across the liquid-air interface is negligible, the liquid does not penetrate fully into the pores of the surface texture. Instead, the liquid fills the pores partially until the local angle (ψ) between the liquid and the textured substrate becomes equal to the equilibrium contact angle θ (given by Young's relation[1]) for the system.[2] The existence of a local texture angle ψ on the surface to enable the condition $\psi = \theta$ [3] to be fulfilled is a necessary, though not sufficient condition,[4] for the formation of a composite interface, such as the one shown in Figure 5-1.

The apparent contact angle θ^* for a composite interface is typically computed using the Cassie-Baxter relation given as:

$$\cos \theta^* = f_1 \cos \theta_E + f_2 \cos \pi = f_1 \cos \theta_E - f_2 \qquad (5\text{-}1)$$

where f_1 is the ratio of the total area of solid-liquid interface to a unit projected area of the textured substrate and f_2 is the corresponding ratio for the liquid-air interface.[5, 6] An example of a natural surface that is able to support a composite interface is shown in Fig. 1b which illustrates water (γ_{lv} = 72.1 mN/m) droplets beading up on top of a duck feather. A duck feather is composed of an array of micron scale cylindrical barbules (see an SEM in supporting information illustrating the details of the feather structure). The bright, reflective surface visible underneath the water droplet in Figure 5-1(b) is a signature of trapped air or the formation of a composite Cassie-Baxter interface. On the other hand, if the liquid fully penetrates into the texture to reach the bottom of the surface, the apparent contact angle θ^* is determined by the Wenzel relation:[5]

$$\cos \theta^* = r \cos \theta_E \qquad (5\text{-}2)$$

Here r is the surface roughness, defined as the ratio between the actual surface area and the projected area. Since r is necessarily greater than unity, roughness amplifies both the wetting ($\cos \theta^* \gg 0$ if $\cos \theta_E > 0$) and non-wetting ($\cos \theta^* \ll 0$ if $\cos \theta_E < 0$) behavior of materials in the Wenzel regime. Thus, it is possible to realize super-wetting on surfaces for which the equilibrium contact angle $\theta_E < 90°$, through the Wenzel regime, as $\theta^* \to 0$ when $r \gg 1$. Figure 5-1(c) illustrates the super-wetting of a duck feather by rapeseed oil (γ_{lv} = 35.7 mN/m), a liquid possessing a significantly lower surface tension and correspondingly lower equilibrium contact angle than water.

The formation of a composite interface typically enables super-repellency with both high apparent contact angle (θ^*) and low contact angle hysteresis (defined as the difference between the advancing and receding contact angles) when $f_1 \ll 1$.[5] Hence, the development of extremely

92

liquid-repellent surfaces requires the design of substrates that promote the formation of a composite interface with any liquid. Based on the condition $\psi = \theta_E$ for the existence of the composite interface defined earlier, we can anticipate that any surface that possesses a local texture angle (ψ) that is less than or equal to the equilibrium contact angle (θ_E) for the liquid, permits the formation of a composite interface.[5] This holds true even if the equilibrium contact angle $\theta_E < 90^o$.

There are numerous reports in the literature pertaining to the development of extremely low surface energy materials.[5] However, there have been no reports of untextured surfaces that exhibit an equilibrium contact angle $\theta > 90^o$ with various low surface tension liquids such as methanol ($\gamma_{lv} = 22.7$ mN/m) or octane ($\gamma_{lv} = 21.7$ mN/m). Thus, surfaces possessing 're-entrant' texture (i.e. $\psi < 90^o$) are necessary for supporting a composite interface with high apparent contact angles and low wetting hysteresis against these liquids. It should however be noted that when $\theta_E < 90^o$, the composite interface is necessarily metastable,[2] i.e. it corresponds to a local minimum in the overall Gibbs free energy for the system, while the fully-penetrated Wenzel state corresponds to the global minimum.[7]

Consider the surface texture shown in Figure 5-1(a). For such surfaces possessing re-entrant curvature,[8] ψ is multi-valued, varying between $\psi_{min} = 0^o$ and $\psi_{max} = 180^o$. Such a surface allows in principle for the possibility of supporting a composite interface with any liquid for which the equilibrium contact angle $\theta_E > 0^o$. However, the fact that $\psi \le \theta_E$ is a necessary but not sufficient condition is easily demonstrated by the observation that many natural and synthetic surfaces such as feathers, plant leaves or fabrics possess re-entrant curvature, but are still easily wetted by oils and other low surface tension liquids (Figure 5-1(c)).
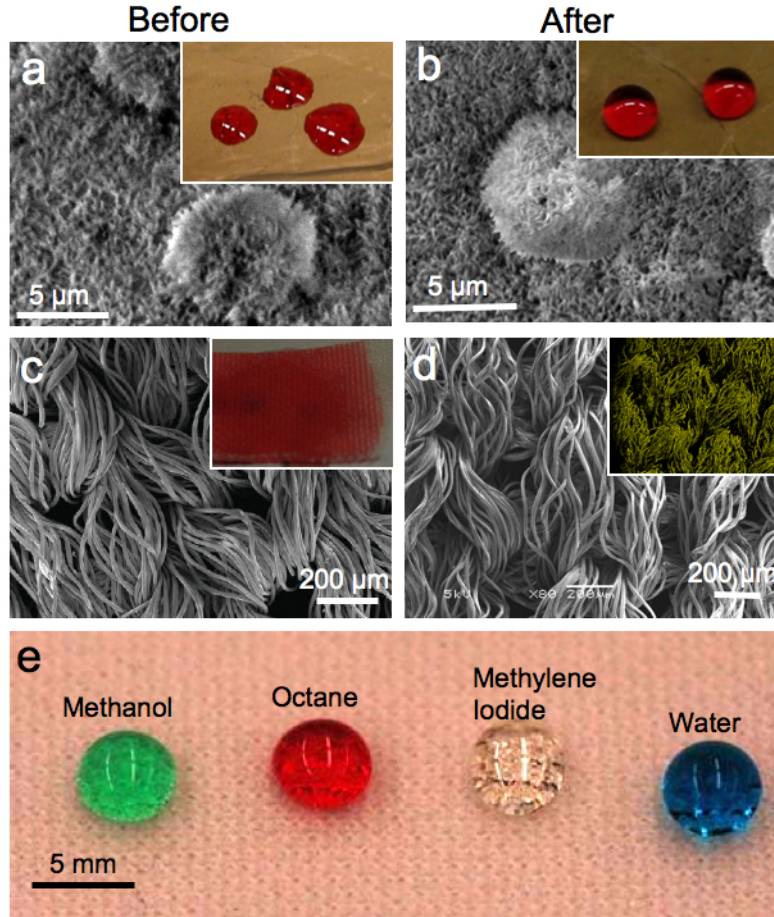
Figure 5-1 (a) A scanning electron microcopy (SEM) image of a lotus leaf illustrating its surface texture. The inset shows that droplets of rapeseed oil easily wet the surface of a lotus leaf. (b) An SEM image of a lotus leaf surface after the dip coating process. (c) An SEM image of the polyester fabric. In spite of the presence of re-entrant curvature, hexadecane can readily wet the fabric surface (inset). (d) An SEM image of the dip-coated polyester fabric. The inset shows the elemental mapping of fluorine obtained using energy dispersive X-ray scattering (EDAXS) (e) Super-repellency of a dip-coated polyester fabric against various polar and non-polar liquids.

The reason most natural or synthetic surfaces possessing re-entrant curvature fail to repel low surface tension liquids is because of the low robustness of the composite interface formed on such substrates. For such liquids, even small pressure differentials across the liquid-air interface can lead to significant sagging of the composite interface, as illustrated in Figure 5-1d. Any additional increase in the pressure differential across the interface, caused for example by the application of external pressure, leads to more severe sagging. Once the liquid-air interface is distorted enough to cause the sagging height (h_1) to become equal to the original clearance

between the liquid-air interface and the solid texture (h_2), the whole system rapidly transitions to a Wenzel state. Thus, if the breakthrough pressure required to force the sagging liquid-air interface to impinge on the solid substrate is small, even though the equilibrium condition $\psi = \theta_E$ indicates the existence of a composite interface, it would never be sufficiently stable to be observed in practice.[5]

The two important design characteristics for a composite Cassie-Baxter state on a textured surface with a particular contacting liquid are thus (i) the apparent contact angle θ^* and (ii) the robustness of the composite interface. The equilibrium apparent contact angles on the texture can be readily estimated using the Cassie-Baxter relation (Eq. 1), and various research groups have estimated the robustness of the composite interface by computing the overall free energy for the system.[9] Even though these free energy calculations can reliably predict whether or not a given surface texture provides the possibility of supporting a stable composite interface, it is unable to estimate the robustness of a composite interface to external perturbations.[5] The free energy analyses presented to date typically ignore the sagging of the liquid-air interface, leading to inaccurate predictions of breakthrough pressure for liquid droplets under external pressure, where the transition between the composite (Cassie) and the wetted (Wenzel) regimes is typically caused by the sagging of the liquid-air interface. Further, the assumption of a flat liquid-air interface in Gibbs free energy calculations leads to predictions of infinite breakthrough pressures for any surface having a local texture angle $\psi_{min} \leq 0^\mathrm{o}$, due to a singularity at $\psi = 0^\mathrm{o}$.

To provide a more accurate prediction of the robustness of a composite interface, we developed a dimensionless design parameter, A^*, which incorporates details of the sagging interface, the texture geometry and the equilibrium contact angle of the contacting liquid. This robustness factor represents the ratio between the breakthrough pressure required to disrupt a composite

interface, and the reference pressure P_{ref}, given as $P_{ref} = 2\gamma_{lv}/\ell_{cap}$, where $\ell_{cap} = \sqrt{\gamma_{lv}/\rho g}$ (here ρ is the fluid density and g is the acceleration due to gravity). As defined, P_{ref} is close to the minimum pressure across the composite interface for millimetric or larger liquid droplets or puddles. Thus, the breakthrough pressure for a given composite interface can be computed as

$P_{breakthrough} = A^* \times P_{ref}$.

For a texture with dominant cylindrical features, such as the duck feathers shown in Figure 5-1 and the fabric surface shown in Figure 5-3, A^* can be calculated to be:

$$A^* = \frac{P_{breakthrough}}{P_{ref}} = \frac{\ell_{cap}}{R}\left(\frac{1}{D^*-1}\right)\left(\frac{1-\cos\theta_E}{D^*-1+2\sin\theta_E}\right) \tag{5-3}$$

Here R is the fiber radius and D is half the inter-fiber gap, as shown in Figure 5-1(a). Eq. 3 shows that the robustness factor A^* allows one to correlate the breakthrough pressure with the characteristic properties of the surface texture (R, D), the liquid (ℓ_{cap}) and the solid-liquid interaction (θ_E). Large values of the robustness factor ($A^* \gg 1$) indicate the formation of a robust composite interface, with very high breakthrough pressures. On the other hand, as A^* approaches unity, $P_{breakthrough}$ approaches P_{ref}. Thus a composite interface on any surface for which $A^* < 1$ cannot maintain its stability against the smallest pressure differentials across the liquid-air interface, causing the liquid to spontaneously penetrate into the textured surface.

In addition to the robustness factor A^*, it is also useful to define another dimensionless parameter, D^*, that parameterizes the geometry of the re-entrant features. For a texture consisting of uniform cylindrical features as shown in Fig. 1a, Cassie and Baxter derived the ratios f_1 and f_2 in Eq. 1 to be $f_1 = R(\pi-\theta_E)/(R+D)$ and $f_2 = 1 - R\sin\theta_E/(R+D)$. Thus f_1 and f_2 are functions of both the material property θ and the surface geometry. We define the spacing ratio

96

$D^* = (R + D)/R$ to represent the dependence of these ratios on the details of surface texture alone. This allows us to re-write Eq. 1 as:

$$\cos\theta^* = -1 + \frac{1}{D^*}\left[\sin\theta_E + (\pi - \theta_E)\cos\theta_E\right] \tag{5-4}$$

Higher values of D^* correspond to a higher fraction of air in the composite interface (f_2 in Eq. 1), and consequently an increase in the apparent contact angle θ^* for a given liquid. Care must be taken in developing expressions for D^* and A^* for surfaces with variable surface texture parameters or multiple scales of roughness such as a duck feather and a lotus leaf (see supporting information for further details).

To achieve both high apparent contact angles with low contact angle hysteresis and a robust composite interface, we seek to maximize the two design parameters D^* and A^* simultaneously. However, for the cylindrical geometry, these two design factors are strongly coupled. Increasing the value of D^*, by increasing D or reducing R (with the other parameter fixed), leads to a decrease in the values of A^* (see Eq. 3).

Evaluating the magnitude of the robustness factor A^* also explains why rapeseed oil spontaneously penetrates the texture of many naturally re-entrant superhydrophobic surfaces such as a duck feather (see Fig. 1c, $D^* = 4$) and a lotus leaf (see inset of Figure 5-1a, $D^* = 58$). To enable these surfaces to support a composite interface with various low surface tension liquids, it is essential to increase the magnitude of the robustness factor A^*. For a fixed surface texture, such an enhancement can be induced most readily by markedly lowering the surface energy of the solid, leading to increased values of the equilibrium contact angle θ_E (based on the Young's relation).

97

In our recent work, we discussed the synthesis and application of a new class of polyhedral oligomeric silsesquioxane (POSS) molecules, in which the silsesquioxane cage is surrounded by 1H,1H,2H,2H-heptadecafluorodecyl groups. These molecules are referred to as fluorodecyl POSS. The high concentration of perfluorinated carbon atoms in the alkyl chains leads to an extremely low solid surface energy for these molecules ($\gamma_{sv} \approx 10$ mN/m). As a comparison, the surface energy of Teflon® is $\gamma_{sv} \approx 18$ mN/m.

To provide a conformal coating of fluorodecyl POSS molecules on any preformed substrate possessing re-entrant texture, we have developed a simple dip-coating procedure (see experimental methods). After the dip-coating process, the equilibrium contact angle for rapeseed oil on smooth glass slide increases to $\theta_E = 86^o$ compared to 5° on the uncoated slide. The dip-coating process also increases the value of the robustness factor for rapeseed oil on a duck feather and a lotus leaf to $A^* = 4.2$ (assuming $R = 1$ μm, $D = 20$ μm) and $A^* = 26$ (assuming $R_{nub} = 2.5$ μm, $D_{nub} = 5$ μm) respectively. As the lotus leaf does not possess a cylindrical surface texture, the robustness factor A^* for the lotus leaf cannot be computed using Eq. 3. Figure 5-1e shows that a dip-coated duck feather is able to support a composite interface with rapeseed oil, and thereby display high apparent contact angles ($\theta^* = 138°$). Further, Figure 5-1f shows an image of the back of a dip-coated duck feather. The top surface of the duck feather has multiple droplets of hexadecane ($\gamma_{lv} = 27.5$ mN/m; $A^* = 3.3$) on its surface (see inset). It is clear from the image that the dyed hexadecane droplets have not penetrated the texture of a dip-coated duck feather.

In Figure 5-1b we show an SEM micrograph highlighting the surface texture of a dip-coated lotus leaf. A comparison with the surface morphology of an uncoated lotus leaf (Figure 5-1a)

shows that all the surface details, even in the sub-micron range are preserved after the dip-coating process. The inset in Figure 5-1b shows that the dip-coating process turns the surface of the leaf oleophobic, allowing it to support a robust composite interface with rapeseed oil and display large apparent contact angles ($\theta^* = 145°$).

Another general class of textured substrates possessing re-entrant curvature is commercial fabrics. Figure 5-1c shows an electron micrograph of a commercial polyester fabric (Anticon 100 clean-room wipe). The inset in Figure 5-1c shows that a droplet of hexadecane completely wets the surface of the as-received polyester fabric. Figure 5-1d shows the surface morphology of a polyester fabric dip-coated with fluorodecyl POSS. All the surface details of the polyester fabric are preserved after the dip-coating process. The inset in Fig. 3d shows the elemental mapping of fluorine on the dip-coated fabric surface using energy dispersive X-ray scattering (EDAXS). This image confirms that the dip-coating process provides a conformal coating of fluorinated molecules on the fabric surface. The liquid repellency of the dip-coated fabric is highlighted in Fig. 3e which shows that this fabric is able to support a composite interface and display high apparent contact angles ($\theta^* \geq 140°$) even with octane ($\gamma_{lv} = 21.7$ mN/m). Taking the geometry of the bundle as the dominant texture ($R_{bundle} = D_{bundle} = 150$ μm, $R_{fiber} = 5$ μm, $D_{fiber} = 10$ μm, $D^* = 6$), the robustness factor $A^* = 2.5$. The reflective surface visible underneath all the droplets shown in the figure clearly indicates the formation of the composite interface.

5.2 Strain induced tunable wettability

To obtain even higher apparent contact angles with such low surface tension liquids, it is necessary to increase the value of the spacing ratio D^* (see Eq. 4). For polyester fabrics, this can be readily achieved by equal biaxial stretching such that the imposed strain ε is the same in both

directions. Strain ε is defined as $(L - L_0)/L_0$, where L and L_0 represent the stretched and non-stretched dimensions of the surface respectively. Stretching (such that the inter-fiber spacing D is increased for a fixed value of the fiber radius R) increases the spacing ratio to be $D^*_{stretched} = D^*_{non-stretched}(1 + \varepsilon)$, leading to an increase in the value of the apparent contact angles. Based on the CB relation, the apparent contact angles on the stretched fabric can then be computed as:

$$\cos\theta^*_{stretched} = -1 + \frac{1}{D^*_{stretched}}\left[\sin\theta + (\pi - \theta)\cos\theta\right] = -1 + \frac{1}{1+\varepsilon}(1 + \cos\theta^*_{non-stretched}) \qquad (5\text{-}5)$$

However, as mentioned earlier, for a cylindrical geometry the two design parameters D^* and A^* are strongly coupled (see Eq. 3). Another consequence of increasing the inter-fiber spacing D is more severe sagging of the liquid-air interface, leading to lower values of the robustness factor A^*. Thus, with increasing values of D^*, we expect to initially see an increase in the value of apparent contact angles θ^*. However, once A^* decreases to values close to unity, the system is expected to transition suddenly to the Wenzel state.

The changes in the apparent advancing and receding contact angles for dodecane (γ_{lv} = 25.3 mN/m, θ = 70°) on a dip-coated polyester fabric, as a function of the applied strain are shown in Figure 5-2. As expected from Eq. 5, initially there is an increase in both the apparent advancing and receding contact angles with increasing values of strain due to the increasing fraction of trapped air underneath the liquid droplet. Figure 5-2b shows the variation with applied strain in the values of both the robustness factor A^*, and the spacing ratio D^* for dodecane on the dip-coated fabric surface. Comparison between Figure 5-2a and Figure 5-2b shows that we see a rapid transition to a super-wetting regime with both $\theta^*_{adv} = \theta^*_{rec} = 0°$ when $A^* \to 1$. Threshold values of A^* for the transition from the composite regime to the Wenzel regime were measured to

be consistently close to unity (varying between $A^* = 1.0$ and $A^* = 1.7$) for various polar and non-polar liquids. Thus, biaxial stretching provides a simple mechanism for systematically adjusting the wetting properties of the dip-coated polyester fabric. To our knowledge, this is the first demonstration of tunable superoleophobicity on any surface.
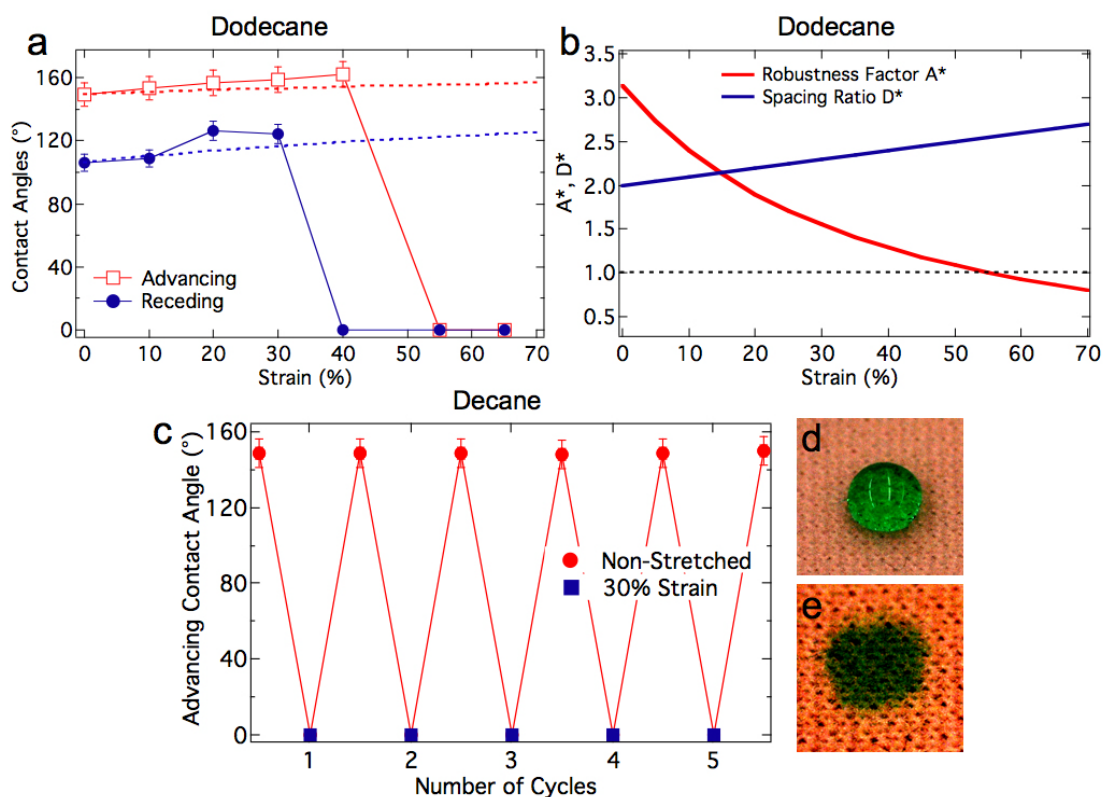
Figure 5-2. (a) The apparent advancing (red squares) and receding (blue dots) contact angles for dodecane ($\gamma_{lv} = 25.3$ mN/m) on a dip-coated polyester fabric, as a function of the applied bi-axial strain. The dashed red and blue lines are the apparent contact angles predicted by Eq. 5. (b) Predictions for A^* (red line) and D^* (blue line) as a function of the imposed bi-axial strain on the fabric. (c) Switchable oleophobicity of the dip-coated fabric with decane ($\gamma_{lv} = 23.8$ mN/m). (d) and (e) Decane droplets on a non-stretched and stretched (30% bi-axial strain) dip-coated polyester fabric respectively.

An example of switchable oleophobicity of the fabric surface is shown in Figure 5-2c. When a droplet of decane ($\gamma_{lv} = 23.8$ mN/m, $\theta = 60^{\circ}$) is placed on an unstretched ($D^* = 6$) dip-coated fabric, the relatively high value of the robustness factor ($A^* = 2.8$) enables the fabric to support a composite interface with decane and thereby display high advancing apparent contact angles

$\theta^* = 149° \pm 2°$ (Figure 5-2c). However, once the fabric is biaxially stretched to a strain of 30% ($D^* = 7.8$) to yield robustness factor values close to unity ($A^* \approx 1.4$), the fabric is fully wetted by decane, with $\theta^*_{adv} \to 0°$ (see Fig. 4e).

When the strain on the fabric is released, the initial surface texture is restored. Returning to the original value of inter-fiber spacing D leads once more to high values of the robustness factor A^*. This allows the fabric to support a composite interface and display high apparent contact angles with a new droplet of decane at any location on its surface, other than the spot where it was previously fully-wetted. The fabric is also able to regenerate its oleophobic properties, at the original wetted spot after a simple evaporative drying process. The data in Figure 5-2c shows the apparent contact angles with decane at a single fixed location on the dip-coated polyester fabric. The first contact angle measurement is performed on the unstretched fabric. Next, the fabric is stretched until D^* increases to a value of 7.8 and correspondingly A^* decreases to a value of 1.4, leading to complete wetting. The strain is then removed and the fabric is placed in a vacuum oven to dry at 100°C for 20 minutes. This is followed by another contact angle measurement at the same location. Next, the fabric is stretched again and the cycle is repeated. It is clear from Figure 5-2c that biaxial stretching enables the fabric to easily switch its wetting characteristics from perfectly oil-wetting to non-wetting, easily and reproducibly. Further, EDAXS elemental mapping (see supporting information) on the dip-coated fabrics after the sixth cycle shows that there is no apparent physical damage to the fabric coating after the entire process, such as cracking or delamination. Similar switchable wettability is also possible with ethanol ($\gamma_{lv} = 22.1$ mN/m), methanol ($\gamma_{lv} = 22.7$ mN/m) and dodecane ($\gamma_{lv} = 25.3$ mN/m) by stretching up to 20%, 30% and 60% strain respectively.

5.3 Strain induced sequential wetting of alkanes

From the definitions of the design parameters A^* and D^* in Equations 3 and 4, it is clear that for the same value of the spacing ratio D^*, different liquids possess different values of the robustness factor A^* due to the differing values of surface tension, capillary length and equilibrium contact angle for each liquid on the fluorodecyl POSS surface. Thus, while the dip-coated fabric may support a composite interface with a particular contacting liquid ($A^* \gg 1$), another liquid with a lower surface tension may fully wet the fabric ($A^* \approx 1$). In addition, as we have shown in Figure 5-2b, biaxial stretching of the fabric provides a simple mechanism to tune the robustness factor A^* and correspondingly adjust the conditions under which a liquid will wet and permeate through the fabric, or remain beaded up at the top of the surface.

Figure 5-3 highlights the strain-induced sequential wetting of a dip-coated polyester fabric with a series of drops by exploiting its sensitivity to the surface tension and equilibrium contact angle of the contacting liquid. The non-stretched ($D^* = 6$) dip-coated fabric shown in Figure 5-3a is able to support a composite interface with four different low surface tension alkanes, octane ($\gamma_{lv} = 21.7$ mN/m), decane ($\gamma_{lv} = 23.8$ mN/m), dodecane ($\gamma_{lv} = 25.3$ mN/m) and hexadecane ($\gamma_{lv} = 27.5$ mN/m). Starting from this initial state, we continuously increase the applied strain on the fabric. At a strain of 15% the spacing ratio reaches a value of $D^* = 6.9$, and the lowest surface tension oil octane ($A^*_{octane} \approx 1.7$) transitions to a fully wetted Wenzel state (Figure 5-3b), while the other three liquids maintain the Cassie-Baxter composite interface with the dip-coated fabric. Thus, the stretched fabric can demonstrate remarkably different wetting properties with liquids having a surface tension difference of $\Delta\gamma_{lv} \sim 2$ mN/m between them. On increasing the spacing ratio further, until the spacing ratio reaches a value of $D^* = 7.8$, decane ($A^*_{decane} \approx 1.4$) wets the fabric

surface (Figure 5-3c), while dodecane and hexadecane still maintain a non-wetting composite interface. Further stretching of the fabric (until $D^* = 9.6$) causes even dodecane ($A^*_{dodecane} \approx 1.0$) to transition to the fully-wetted interface (Figure 5-3d).
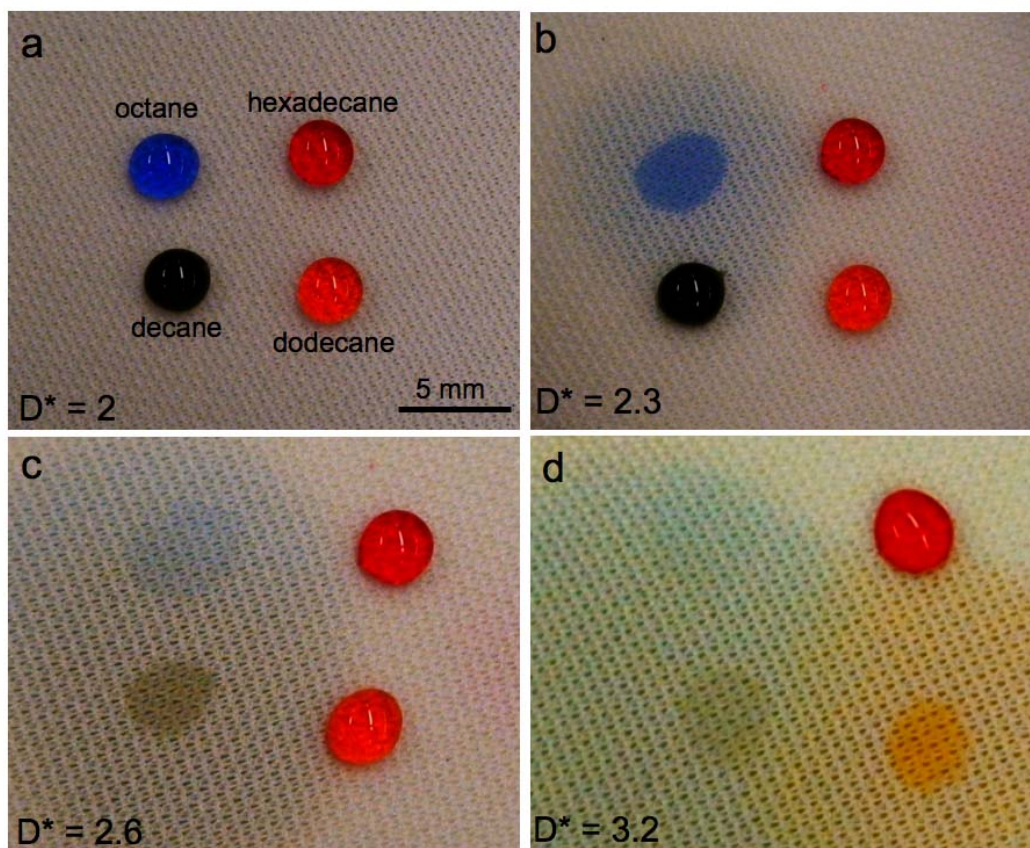
Figure 5-3. Sequential wetting of four alkane droplets on a dip-coated polyester fabric. (a) Super-repellency of the unstretched, dip-coated, fabric against octane (γ_{lv} = 21.7 mN/m), decane (γ_{lv} = 23.8 mN/m), dodecane(γ_{lv} = 25.3 mN/m) and hexadecane (γ_{lv} = 27.8 mN/m). (b) At 15% strain, octane droplet transitions to the Wenzel regime with $A^* = 1.7$. (c) At 30% strain, decane droplet transitions to the Wenzel regime with $A^* = 1.4$. (d) At 60% strain, dodecane droplet transitions to the Wenzel regime with $A^* = 1.0$. Hexadecane does not transition into the Wenzel regime until the fabric fibers start to tear apart at ~70% strain.

In conclusion, in this work we have developed a simple dip-coating process that enables us to provide a conformal coating of extremely low surface energy fluorodecyl POSS molecules on any surface, including those that inherently possess re-entrant texture, such as duck feathers, lotus leaves or commercially available fabrics. The synergistic effect of roughness, re-entrant texture of the preformed substrate, and the low surface energy of fluorodecyl POSS molecules,

enables the dip-coated texture to support a composite interface even with very low surface tension liquids. We have also used two design parameters A^* and D^* to provide an *a priori* estimate of both the apparent contact angles as well as the robustness of a composite interface. Biaxial stretching of a dip-coated, commercial polyester fabric can cause a significant enhancement in both the apparent advancing and receding contact angles as predicted by changes in the spacing ratio D^*. Further, due to the strong coupling between the two design parameters A^* and D^* for a typical fiber geometry, stretching the commercial fabrics can lead to a dramatic reduction in the robustness of the composite interface that is supported with a given contacting liquid. Indeed, beyond a critical strain at which A^* decreases to values close to unity, the contacting liquid spontaneously penetrates the fabric texture, leading to near zero contact angles. In the context of this design framework, we have developed suitably textured surfaces that can readily adjust their surface wettability and even switch their wettability behavior (between super-wetting and super-repellent) reversibly with a wide range of polar and non-polar liquids, in response to simple mechanical deformation.

5.4 References

1.	Nosonovsky[25] recently derived another important criterion for the creation of a local minimum in free energy, and thus for the creation of a stable heterogeneous interface: dAsldq < 0, where dAsl is the change in solid-liquid contact area with the advancing or receding of the liquid, and dq is the change in local contact angle. This criterion also emphasizes the importance of re-entrant surfaces.
2.	Cassie, A. B. D.; Baxter, S., Wettability of porous surfaces. *Trans. Faraday Soc.* **1944,** 40, 546–551.
3.	Wenzel, R. N., Resistance of solid surfaces to wetting by water. *Ind. & Eng. Chem.* **1936,** 28, 988–994.
4.	Tuteja, A.; Choi, W.; McKinley, G. H.; Cohen, R. E.; Rubner, M. F., Design parameters for superhydrophobicity and superoleophobicity. *MRS bull.* **2008,** 33, (8), 752-758.
5.	Tuteja, A.; Choi, W.; Mabry, J. M.; McKinley, G. H.; Cohen, R. E., Engineering robust omniphobic surfaces. *PNAS* **2008, In Press**.
6.	Nosonovsky, M.; Bhushan, B., Patterned Nonadhesive Surfaces: Superhydrophobicity and Wetting Regime Transitions. *Langmuir* **2008,** 24, (4), 1525-1533.

7.   Young, T., An Essay on the Cohesion of Fluids. *Philos. Trans. R. Soc. London* **1805,** 95, 65.

8.   Mabry, J. M.; Vij, A.; Iacono, S. T.; Viers, B. D., Fluorinated polyhedral oligomeric silsesquioxanes (F-POSS). *Angew. Chem. Int. Ed.* **2008,** 47, (22), 4137-4140.

9.   Zisman, W. A., *Relation of the equilibrium contact angle to liquid and solid construction. In Contact Angle, Wettability and Adhesion, ACS Advances in Chemistry Series.* American Chemical Society: Washington, DC. , 1964; Vol. 43, p 1–51.

6 Fluoroalkylated Silicon-Containing Surfaces – Estimation of Solid Surface Energy

6.1 Introduction

In the recent past, there have been a number of reports on surfaces that are not wetted by liquid droplets, *i. e.* superhydrophobic,[1-4] oleophobic,[5-15] hygrophobic,[16] omniphobic[7, 12] surfaces. These surfaces have potential applications in oil-water separation, non-wettable textiles,[2, 3, 6, 8, 9, 14, 15] and fingerprint/smudge resistant touch-screen devices. Here we use the term Omniphobicity to refer to surfaces that are not wetted by a broad set of liquids, including water, alkanes, alcohols, acids, bases and other organic liquids. The design of omniphobic surfaces involves selection of a suitable surface chemistry to minimize the solid surface energy and optimal choice of the surface texture.

In our previous work, we emphasized re-entrant topography as a necessary condition for the design of surfaces that are not wetted by low surface tension liquids.[7-9, 11-13] Liquids such as octane ($\gamma_{lv} = 21.6$ mN/m) and methanol ($\gamma_{lv} = 22.7$ mN/m) will partially wet a flat untextured surface (equilibrium contact angle, $\theta_E < 90°$) of any surface chemistry. Using a combination of surface chemistry and re-entrant texture, surfaces that exhibit substantially enhanced non-wettability to such liquids (apparent contact angle, $\theta^* > 90°$) can be created. On such non-wetting surfaces, liquid droplets sit partially on the solid texture and partially on the air trapped between the asperities of the solid texture. The Cassie-Baxter (CB) relation can be used to understand variations in the apparent contact angles (θ^*) for liquid droplets with solid-liquid-air composite
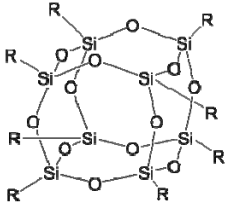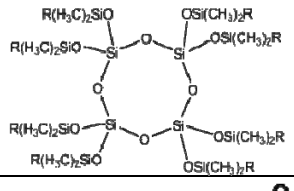
interfaces. The CB relation shows that the apparent contact angle (θ^*) increases as the equilibrium contact angle (θ_E) increases and as the relative amount of trapped air increases.[17] We have also developed an expression for the breakthrough pressure (P_b) required for the disruption of this solid-liquid-air composite interface (or 'CB state').[12] Both the apparent contact angle (θ^*) and the breakthrough pressure (P_b) increase monotonically with increasing equilibrium contact angle (θ_E).[7-9, 12] Therefore maximizing θ_E is one objective in the optimal design of omniphobic surfaces with robust composite interfaces.

We have used fluorodecyl POSS based coatings to design a range of robust non-wettable surfaces.[7-9, 11-13] A fluorodecyl POSS molecule consists of a silicon – oxygen cage surrounded by eight 1H,1H,2H,2H-heptadecafluorodecyl chains.[18] A flat silicon wafer spin-coated with a uniform coating of this molecule has one of the highest reported values of equilibrium contact angle for water droplets ($\theta_E \approx 122°$). Moreover, liquid droplets with a wide range of surface tension ($15.5 \leq \gamma_{lv} \leq 72.1$ mN/m) form high contact angles on a fluorodecyl POSS coated flat surface (as summarized in Figure 6-1). The contact angles (θ_{adv}, and θ_{rec}) are significantly higher on a fluorodecyl POSS surface than on a corresponding surface coated with a fluoropolymer such as Tecnoflon (BR 9151, a fluoro-elastomer from Solvay Solexis). In addition, it is apparent from Figure 6-1 that the difference between the corresponding contact angles on the two surfaces *increases* as the liquid surface tension (γ_{lv}) *decreases*. The molecular level origins of the unusually low wettability of fluorodecyl POSS remains unresolved.

In this study, we document the wettability of two sets of fluorinated silicon-containing molecules in an attempt to resolve some aspects of the unanswered questions regarding fluorodecyl POSS. In the first set, the length of the fluorinated chain is changed keeping the T_8 silicon/oxygen cage intact. [This cage is referred to generally as the T_8 cage because it has eight silicon atoms each

bonded to three oxygen atoms.] In the other set of molecules, the fluorodecyl chain is retained and the silicon/oxygen architecture is changed successively from a T_8 cage to a Q_4 ring [four Si atoms, each bonded to four oxygen atoms] or a M_2 straight chain [two Si atoms, each bonded to a single oxygen atom]. The structure and chemical formulae are summarized in Table 6-1.

Table 6-1. Structure of Fluorohexyl T_8, Fluoropropyl T_8, Hexafluoro-i-butyl T_8 is shown along with the structure of Fluorodecyl T_8 and Fluorooctyl T_8 , Fluorodecyl Q_4M_8 and Fluorodecyl M_2 for reference.

	Fluorodecyl T_8, R = -(CH$_2$)$_2$-(CF$_2$)$_7$-CF$_3$
	Fluorooctyl T_8, R = -(CH$_2$)$_2$-(CF$_2$)$_5$-CF$_3$
	Fluorohexyl T_8, R = -(CH$_2$)$_2$-(CF$_2$)$_3$-CF$_3$
	Fluoropropyl T_8, R = -(CH$_2$)$_2$-CF$_3$
	Hexafluoro-i-butyl T_8, R = -CH$_2$-CH(CF$_3$)$_2$
	Fluorodecyl Q_4M_8, R = -(CH$_2$)$_2$-(CF$_2$)$_7$-CF$_3$
	Fluorodecyl M2, R = -(CH$_2$)$_2$-(CF$_2$)$_7$-CF$_3$
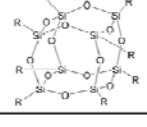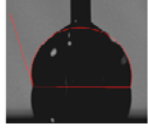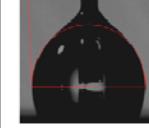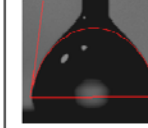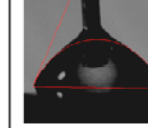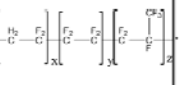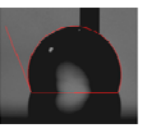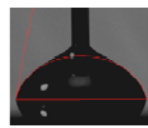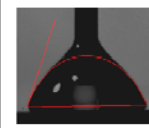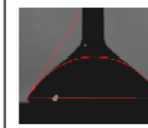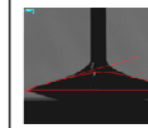
Apparent advancing contact angles (θ^*_{adv})	Water (γ_{lv} 72.1 mN/m)	Diiodomethane (γ_{lv} = 50.8 mN/m)	Rapeseed Oil (γ_{lv} = 35.5 mN/m)	Hexadecane (γ_{lv} = 27.5 mN/m)	Octane (γ_{lv} 21.6 mN/m)
Fluorodecyl POSS	$122 \pm 2°$	$100 \pm 2°$	$88 \pm 3°$	$80 \pm 1°$	$67 \pm 1°$
Tecnoflon	$110 \pm 2°$	$80 \pm 2°$	$71 \pm 2°$	$58 \pm 2°$	$16 \pm 3°$

Figure 6-1. Variation of advancing contact angles (θ_{adv}) on flat silicon wafers spin-coated with fluorodecyl T_8 and Tecnoflon is shown. The advancing contact angles decrease in magnitude as the surface tension of the contacting liquids decreases from γ_{lv} = 72.1 mN/m (for water) to γ_{lv} = 21.6 mN/m (for octane) and as the solid surface energy increases from fluorodecyl T_8 to Tecnoflon.

109

The wettability of these materials is assessed using contact angle measurements on smooth spin-coated Si wafers with a set of probing liquids. There are various methods described in the literature to estimate the solid surface energy from contact angle data: including the Zisman analysis,[19] Owens-Wendt method,[20] or Girifalco-Good method[21, 22]. In this work, we perform Zisman analysis with a set of n-alkanes, a standard framework for quantifying non-wettability of low energy solid surfaces. We also estimate the surface energies of our solid surfaces using the Girifalco-Good analysis, which additionally considers polar contributions in the wettability analysis.

6.2 Synthesis of fluoroalkylated silicon-containing molecules

Fluorodecyl, fluorooctyl and fluorohexyl POSS: A 94.3% yield of pure 1H,1H,2H,2H-heptadecafluorodecyl$_8$T$_8$ (Fluorodecyl POSS), a 95.1% yield of pure 1H,1H,2H,2H-tridecafluorooctyl$_8$T$_8$ (Fluorooctyl POSS), a 91.5% yield of pure 1H,1H,2H,2H-nonafluorohexyl$_8$T$_8$ (Fluorohexyl POSS)and was obtained using a previously reported method.[18]

Fluoropropyl POSS: Fluoropropyl POSS was synthesized using a modification of a previously reported method.[23] 3,3,3-Trifluoropropyltrichlorosilane (0.87 mL) was added to a stirred solution of heptakis(3,3,3-trifluoropropyl)tricycloheptasiloxane trisodium silanolate (4.00 g) in THF (70 mL) at room temperature. Triethylamine (0.49 mL) was then added drop wise to the mixture. The contents were stirred under nitrogen for 3 h in a 150 mL round bottom flask with a Teflon-coated magnetic stir bar. After filtering the precipitated salts, the filtrate was concentrated under reduced pressure. The fine white powder formed was rinsed with methanol and dried. A 76% yield of pure 3,3,3-trifluoropropyl$_8$T$_8$ (Fluoropropyl POSS) was obtained.

Hexafluoroisobutyl POSS: Hexafluoroisobutene (28.4 g, 173 mmole) was condensed into a 250 mL heavy walled reaction vessel with a Teflon-coated magnetic stir bar. HSiCl$_3$ (23.9 g, 176

mmol) was then added at -10 °C under nitrogen followed by a 0.2 M H_2PtCl_6 isopropanol catalyst solution (0.5 mL, 0.1 mmol). The flask was sealed, heated to 150 °C, and stirred for 40 h. The contents were then vacuum transferred at 0 °C to a collection flask, which was then cooled to -80 °C. While slowly warming to -40 °C, volatiles were removed under static vacuum to give an 85 % yield of hexafluoroisobutyltrichlorosilane (44.2 g, 148 mmol). ^{1}H NMR (δ, $CDCl_3$) 3.29 ppm (1H, nonet, $^{3}J_{H-F}$ and $^{3}J_{H-H}$ = 7.2 Hz, CH), 1.93 ppm (2H, d, $^{3}J_{H-H}$ = 7.2 Hz, CH_2); ^{19}F NMR (δ, $CDCl_3$) -68.23 ppm (d, $^{3}J_{H-F}$ = 7.2 Hz); ^{13}C{^{1}H} NMR (δ, $CDCl_3$) 123.28 ppm (quart, $^{1}J_{C-F}$ = 281 Hz, CF_3) 44.40 ppm (sept, $^{2}J_{C-F}$ = 30 Hz, CH), 18.49 (m, $^{3}J_{C-F}$ = 1.8 Hz, CH_2); ^{29}Si{^{1}H} NMR (δ, $CDCl_3$) 8.14 ppm (br, s).

Hexafluoroisobutyltrichlorosilane (44.19 g, 148 mmole) was placed into a 250 mL round bottom flask (rbf) with a Teflon-coated magnetic stir bar under nitrogen and heated to 100 °C. Trimethylorthoformate (145.3 mL, 1.33 mol) was added drop-wise over a period of 1.5 h and the reaction was refluxed overnight. 1H,1H,2H-Hexafluoroisobutyltrimethoxysilane was isolated by fractional distillation (bp = 102 °C) under full dynamic vacuum, in 63 % isolated yield (26.57g, 93 mmol). ^{1}H NMR (δ, $CDCl_3$) 3.52 ppm (9 H, s, OMe), 3.06 ppm (1H, nonet, $^{3}J_{H-F}$ and $^{3}J_{H-H}$ = 7.2 Hz, CH), 0.97 ppm (2H, d, $^{3}J_{H-H}$ = 7.2 Hz, CH_2); ^{19}F NMR (δ, $CDCl_3$) -69.25 ppm (d, $^{3}J_{H-F}$ = 7.2 Hz); ^{13}C{^{1}H} NMR (δ, $CDCl_3$) 123.75 ppm (quart, $^{1}J_{C-F}$ = 269 Hz, CF_3), 50.27 (s, OCH_3) 43.64 ppm (sept, $^{2}J_{C-F}$ = 29 Hz, CH), 3.20 (m, $^{3}J_{C-F}$ = 1.7 Hz, CH_2); ^{29}Si{^{1}H} NMR (δ, CDCl3) -48.7 ppm (s).

1H,1H,2H-Hexafluoroisobutyltrimethoxysilane (2.00 g, 7.00 mmole) and 205 mg of KOH solution (774 mg KOH in 100 mL H_2O) were added to 7 mL ethanol in a 25 mL rbf with a Teflon-coated magnetic stir bar and stirred overnight at room temperature, under nitrogen. The fine white powder formed was rinsed with ethanol and dried. An 85% yield of pure

Hexafluoroisobutyl POSS was obtained. ^{1}H NMR (δ, C_6F_6) 3.65 ppm (1H, nonet, $^{3}J_{H-F}$ and $^{3}J_{H-H}$ = 7 Hz, CH), 1.54 ppm (2H, d, $^{3}J_{H-H}$ = 7 Hz, CH_2); ^{19}F NMR (δ, C_6F_6) -70.4 ppm (d, $^{3}J_{H-F}$ = 7 Hz); ^{13}C{^{1}H} NMR (δ, C_6F_6) 123.47 ppm (quart, $^{1}J_{C-F}$ = 282 Hz, CF_3), 43.83 ppm (sept, $^{2}J_{C-F}$ = 30 Hz, CH), 5.18 (s, CH_2); ^{29}Si{^{1}H} NMR (δ, C_6F_6) -69.4 ppm (s).

1H,1H,2H,2H-Heptadecafluorodecyl$_8$M$_8$Q$_4$ **(Fluorodecyl$_8$M$_8$Q$_4$):** 1H,1H,2H,2H-Heptadecafluorodecyldimethylchlorosilane (25 g, 46.2 mmol), octakis[chloro calcium oxy]cyclotetrasilicate[24] (3.4 g, 3.7 mmol), acetone (50 mL), and AK225 (14 mL) were added to a 100 mL rbf and refluxed under nitrogen for three days.[25] The volatiles were then removed under vacuum. The product was dissolved in AK225 solvent (50 mL) and a water extraction was used to remove $CaCl_2$. Isopropanol (10 mL) and Amberlyst 15 (1 g) were added after reducing the solvent to 25 mL. After 3 h of stirring, the solution was filtered through silica gel (1.20 g, 60 Å pore size, 35-75 micron particle size). After re-dissolving the product in AK225 (11 mL), Amberlyst 15 (1.03 g) and silica gel were added,[26] and the mixture was stirred overnight at room temperature. The solution was filtered through silica gel and the volatiles were removed by dynamic vacuum. The fluorodecyl$_8$M$_8$Q$_4$ was dissolved in a minimal amount of AK225. A white precipitate formed upon sitting at room temperature. The AK225 was filtered off and the solid was washed with chloroform. A 9% yield (1.5 g) of fluorodecyl$_8$M$_8$Q$_4$ was obtained. ^{29}Si{^{1}H} NMR (AK225, ppm) 12.0 (s), -108.3 (s).

1,3-bis(1H,1H,2H,2H-Heptadecafluorodecyl)-1,3-tetramethyldisiloxane **(Fluorodecyl$_2$M$_2$ disiloxane)**: A distillation to isolate the fluorodecyl$_2$M$_2$ disiloxane was performed on the final distillate during the synthesis of Fluorodecyl$_8$M$_8$Q$_4$ at 118 °C, 0.2 mmHg. A 10% yield (4.7 g) of fluorodecyl$_2$M$_2$ disiloxane was obtained. ^{1}H NMR ($CDCl_3$, ppm) 0.12 (s), 0.75 (m), 2.03 (m). ^{29}Si{^{1}H} NMR ($CDCl_3$, ppm) 8.4 (s).

Surface characterization – The fluoroalkylated silicon-containing molecules were dissolved in Asahiklin solvent (AK 225, Asahi Glass Company) at a concentration of 10 mg/ml. Later, the solutions were spin-coated on a flat silicon wafer at 900 rpm for 30 seconds to achieve uniformly coated flat surfaces (AFM rms roughness < 10 nm) for contact angle measurements. Advancing and receding contact angles were measured using a VCA2000 goniometer (AST Inc.) with ~5 μL droplets of various liquids (purchased from Aldrich and used as received).

6.3 Zisman analysis on fluoroalylated silicon-containing surfaces

Zisman and co-workers introduced the concept of the critical surface tension for a solid surface (γ_c),[19, 27-38] and it has become the most commonly used parameter to rank order solid surface energy (γ_{sv}) and wettability of different substrates. In order to assess the impact of molecular structure on wettability, contact angle measurements were performed on the full set of fluoroalkylated silicon containing molecules shown in Table 6-1. n-alkanes [pentane $(\gamma_{lv} = 15.5$ mN/m) to hexadecane $(\gamma_{lv} = 27.5$ mN/m)] were used as contacting liquids, and the advancing contact angles (θ_{adv}) results are summarized in Figure 6-2. Strong linear correlations $(R^2 = 0.95$ to 0.99) were observed for plots of $\cos\theta_{adv}$ versus liquid surface tension (γ_{lv}). The critical surface tension (γ_c) for the spin-coated surfaces was obtained by a linear extrapolation of the best-fit line through the $\cos\theta_{adv}$ versus γ_{lv} data. The intercept of this extrapolation to the $\cos\theta_{adv} = 1$ line is the critical surface tension (γ_c). As the length of the perfluorinated chain decreased from fluorodecyl T_8 (■) to fluoropropyl T_8 (◄), the critical surface tension (γ_c) increased monotonically from 5.5 to 19.7 mN/m. This trend is consistent with Zisman's results on modified poly tetrafluoroethylene (PTFE),[37] chlorinated polymers,[31] fluorinated (meth)acrylate polymers,[35] and perfluorinated carboxylic acids.[29, 33, 34] Additionally, the critical surface tension (γ_c) increased as the size and complexity of the –Si/O– structure decreased; from

$\gamma_c = 5.5$ mN/m for the fluorodecyl T_8 (cage,■) to $\gamma_c = 14.5$ mN/m for the fluorodecyl Q_4 (ring,▲) and $\gamma_c = 19.6$ mN/m for the fluorodecyl M_2 (straight chain,▼).
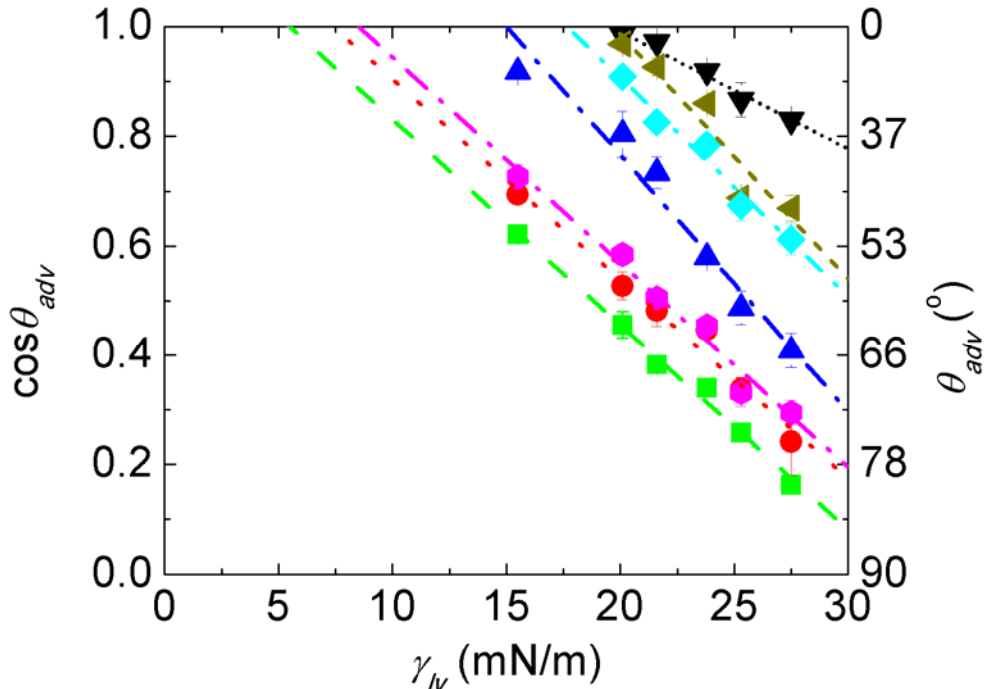
Figure 6-2. Zisman analysis for fluoroalkylated silicon-containing compounds. Cosine of advancing contact angles (θ_{adv}) for droplets of hexadecane ($\gamma_{lv} = 27.5$ mN/m), dodecane ($\gamma_{lv} = 25.3$ mN/m), decane ($\gamma_{lv} = 23.8$ mN/m), octane ($\gamma_{lv} = 21.6$ mN/m), heptane ($\gamma_{lv} = 20.1$ mN/m), and pentane ($\gamma_{lv} = 15.5$ mN/m) on a spin-coated film on a flat silicon wafer are plotted against the surface tension of contacting liquids (γ_{lv}). For fluorodecyl T_8 ($\gamma_c = 5.5$ mN/m, ■), fluorooctyl T_8 ($\gamma_c = 7.4$ mN/m, ●), fluorohexyl T_8 ($\gamma_c = 8.5$ mN/m, ⬣), fluoropropyl T_8 ($\gamma_c = 19.7$ mN/m, ◀), hexafluoroisobutyl T_8 ($\gamma_c = 17.7$ mN/m, ◆), fluorodecyl Q_4 ($\gamma_c = 14.5$ mN/m, ▲), and fluorodecyl M_2 ($\gamma_c = 19.6$ mN/m, ▼), the critical surface tension (γ_c) is obtained by a linear extrapolation of the corresponding best-fit line.

The critical surface tension (γ_c) is a qualitative indicator of the solid surface energy (γ_{sv}) but it is not equal to the solid surface energy ($\gamma_c \neq \gamma_{sv}$). Any liquid with a lower surface tension than the critical surface tension ($\gamma_{lv} < \gamma_c$) is expected to completely wet the solid surface ($\theta_E \approx 0$). Zisman noted that the critical surface tension (γ_c) can change if a different set of probing liquids is used on the same solid surface. When the solid surface and/or the contacting liquid is polar with a higher value of surface tension, the contact angle data deviates from the linear trend, as shown in Figure 6-3 for a flat silicon wafer spin-coated with fluorodecyl T_8. The advancing contact angle

data (θ_{adv}, ■) for liquids with a wider range of surface tensions ($15.5 \leq \gamma_{lv} \leq 72.1$ mN/m) are plotted along with the linear extrapolation of the Zisman line (——). The Zisman line fits the alkane data well ($R^2 = 0.99$ for fluorodecyl T_8, Figure 2, $\gamma_{lv} \leq 30$ mN/m), however it deviates significantly when other liquids are included ($R^2 = 0.04$ for fluorodecyl T_8, Figure 6-3). Alkanes are completely non-polar, while higher surface tension liquids like water, ethylene glycol or dimethyl sulfoxide have polar functional groups and the polarity of these probing liquids is considered to be the cause of deviation from the Zisman line.
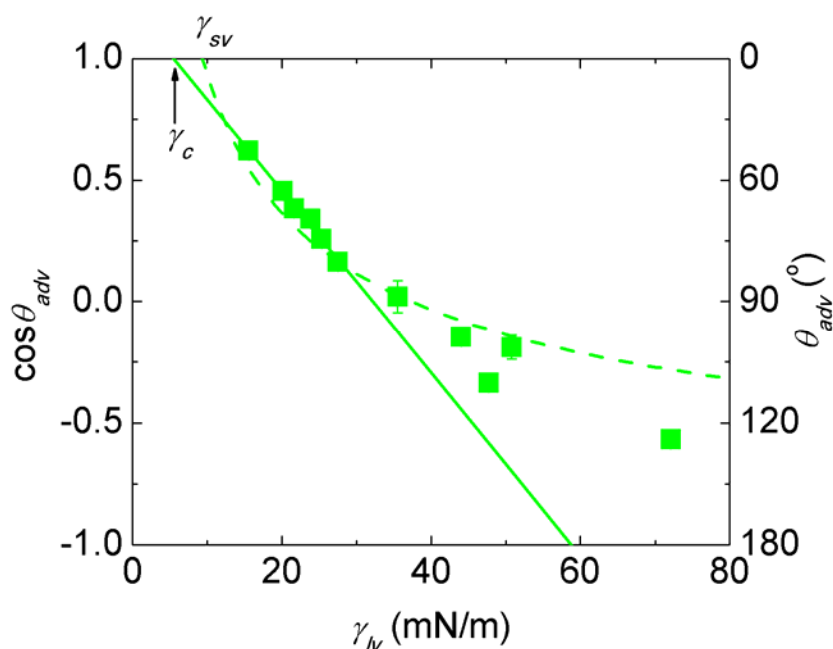
Figure 6-3. Variation of advancing contact angles (θ_{adv}) of liquid droplets with a wide range of surface tension on a fluorodecyl T_8 surfaces is shown in this figure. Cosine of advancing contact angles (θ_{adv}) for droplets of water ($\gamma_{lv} = 72.1$ mN/m), diiodomethane ($\gamma_{lv} = 50.8$ mN/m), ethylene glycol ($\gamma_{lv} = 47.7$ mN/m), dimethyl sulfoxide ($\gamma_{lv} = 44$ mN/m), rapeseed oil ($\gamma_{lv} = 35.5$ mN/m), hexadecane ($\gamma_{lv} = 27.5$ mN/m), dodecane ($\gamma_{lv} = 25.3$ mN/m), decane ($\gamma_{lv} = 23.8$ mN/m), octane ($\gamma_{lv} = 21.6$ mN/m), heptane ($\gamma_{lv} = 20.1$ mN/m), and pentane ($\gamma_{lv} = 15.5$ mN/m) on a spin-coated film on a flat silicon wafer are plotted against the surface tension of contacting liquids (γ_{lv}). The Zisman best fit line for the alkane data (——) and the best fit Girifalco-Good curve (– – ·) over the whole range of liquids is shown with the respective intercepts $\gamma_c = 5.5$ mN/m, and $\gamma_{sv} = 9.3$ mN/m respectively.

A better model which incorporates the polarity of the solid surface and/or the contacting liquid was proposed by Girifalco, Good and co-workers.[21, 22, 39-43] According to this framework, the

solid surface energy (γ_{sv}) is given by Equation 6.1, where θ_E is the equilibrium contact angle and φ_{sl} is a solid-liquid interaction parameter.

$$W_{sl}^a = \gamma_{lv}\left(1 + \cos\theta_E\right) = 2\phi_{sl}\sqrt{\gamma_{sv}\gamma_{lv}} \qquad (6\text{-}1)$$

Equation 6.1 has two unknowns, γ_{sv} and φ_{sl}. The parameter φ_{sl} equals the ratio of work of adhesion of the solid-liquid pair (W_{sl}^a) to the square roots of the works of cohesion of the solid ($W_{ss}^c = 2\gamma_{sv}$) and the liquid ($W_{ll}^c = 2\gamma_{lv}$), where $W_{ss}^c W_{ll}^c = 4\gamma_{sv}\gamma_{lv}$. The Berthelot geometric mean mixing rule suggests that the work of adhesion can be approximated as the product of the square roots of the two works of cohesion.[22] For non-polar liquid droplets on non-polar solids, this is indeed the case ($W_{sl}^a = \sqrt{W_{ss}^c W_{ll}^c}$), and the solid-liquid interactions are nearly ideal ($\varphi_{sl} = W_{sl}^a / \sqrt{W_{ss}^c W_{ll}^c} = 1$), e. g. alkane droplets on fluorodecyl POSS (Figure 6-2 and Figure 6-3). However, in general, the value of φ_{sl} for a solid/liquid pair is not known *a priori*. Contact angle measurements were performed over a broad range of liquids with differing polarities and the average value of φ_{sl} was assumed to be unity. The advancing contact angle measurement results, along with the ($\varphi_{sl} = 1$) best fit Girifalco-Good curve (— — .) are shown in Figure 6-3 for a fluorodecyl T_8 surface. Alkanes from pentane ($\gamma_{lv} = 15.5$ mN/m) to hexadecane ($\gamma_{lv} = 27.5$ mN/m), rapeseed oil ($\gamma_{lv} = 35.5$ mN/m), and diiodomethane ($\gamma_{lv} = 50.8$ mN/m) represent a set of non-polar liquids; whereas dimethyl sulfoxide ($\gamma_{lv} = 44$ mN/m), ethylene glycol ($\gamma_{lv} = 47.7$ mN/m) and water ($\gamma_{lv} = 72.1$ mN/m) have polar nature. When compared with the extrapolated Zisman line (——, $R^2 = 0.04$), the Girifalco-Good curve (— — .) is a much better fit ($R^2 = 0.88$) to the advancing contact angle data over the whole range of liquid surface tensions, barring the two outliers – water ($\gamma_{lv} = 72.1$ mN/m) and ethylene glycol ($\gamma_{lv} = 47.7$ mN/m), which lie significantly below the curve. Statistical analysis based on the

residuals between the best-fit predictions and measured values of $\cos\theta_{adv}$ are summarized in the Figure 6-4 and Figure 6-5.
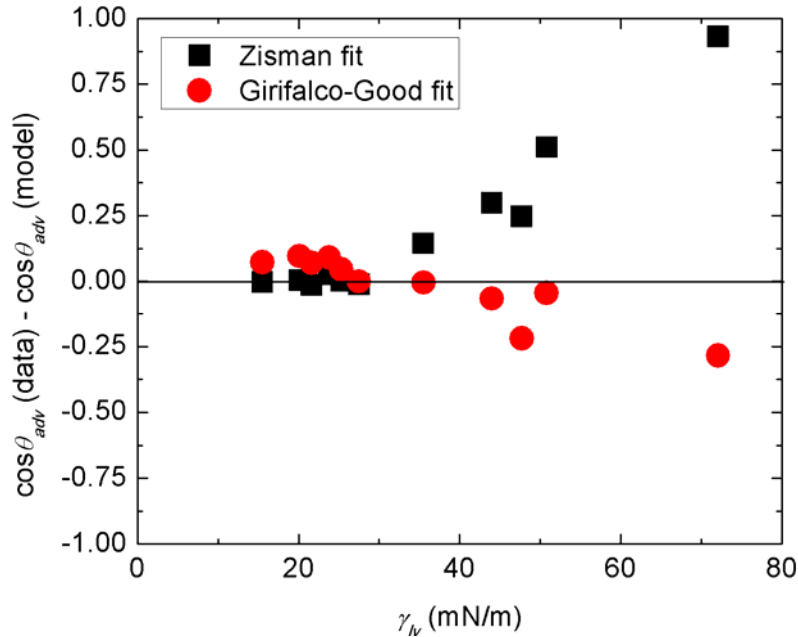
Figure 6-4. The difference (r) between measured value of the cosine of advancing contact angle ($\cos\theta_{adv}$) and the cosine of the expected contact angle from the Zisman as well as the Girifalco-Good relation is plotted against the liquid surface tension (γ_{lv}). The Girifalco-Good relation is a better fit to the data with a much smaller summation of the residual ($\sum r = -0.25$) compared to the Zisman analysis ($\sum r = 2.13$).

One of the main sources of uncertainty with Zisman analysis is the large extrapolation of the best-fit line to $\theta_{adv} \rightarrow 0$ that is typically required to estimate the value of γ_c. In the Girifalco-Good analysis, such an extrapolation is avoided. If a liquid (with surface tension γ_{lv}^*) is found such that it forms an equilibrium contact angle, $\theta_E \approx 90°$, then assuming that $\phi_{sl} = 1$, the solid surface energy can be found by solving Equation 1 which yields $\gamma_{sv} = \gamma_{lv}^*/4$. Even if such a liquid cannot be found, γ_{sv} can be estimated by interpolation using two liquids (say 1 and 2) if $\theta_{E,1} > 90°$ and $\theta_{E,2} < 90°$. The location, shape and curvature of the Girifalco-Good curve are an embodiment of the solid surface energy (γ_{sv}), and in Zisman analysis, it is γ_c. The solid surface energy (γ_{sv}) can also be represented as the intercept where the extrapolated Girifalco-Good curve intersects the $\cos\theta_{adv} = 1$ line [$\gamma_{sv} = 9.3$ mN/m in this case].
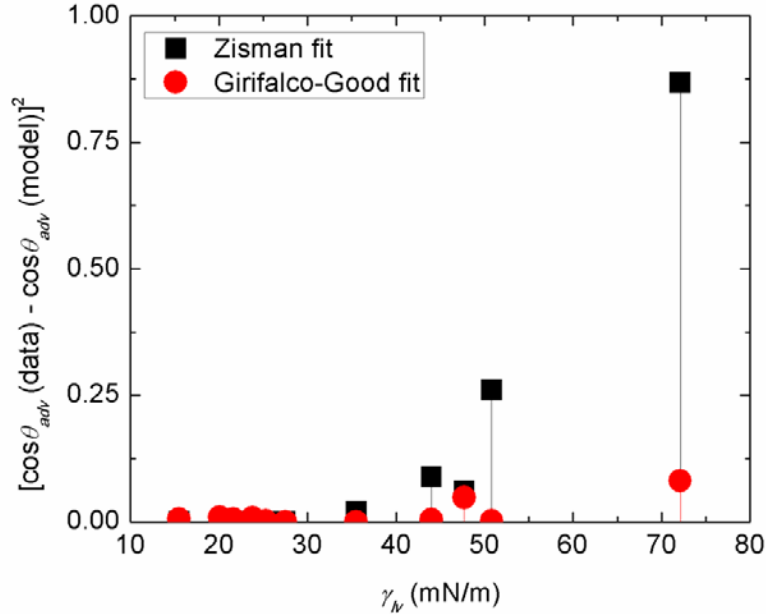
Figure 6-5. The square of the difference (r) between measured value of the cosine of advancing contact angle ($\cos\theta_{adv}$) and the cosine of the expected contact angle from the Zisman as well as the Girifalco-Good relation is plotted against the liquid surface tension (γ_{lv}). The Girifalco-Good relation is a better fit to the data with a much smaller summation of the squares of the residual ($\sum r^2 = 0.16$) compared to the Zisman analysis ($\sum r^2 = 1.30$).

Since the Girifalco-Good curve has positive curvature (*i.e.* it is concave 'upwards'), the Zisman critical surface tension always tends to underestimate the solid surface energy ($\gamma_c < \gamma_{sv}$) determined from Girifalco-Good analysis. The Girifalco-Good relation (Equation 1) can be re-written in the form $\cos\theta_E = -1 + 2\phi_{sl}\sqrt{\gamma_{sv}/\gamma_{lv}}$, which can be further expressed as a Taylor series when $\gamma_{lv}/\gamma_{sv} \to 1^+$ in terms of $(\gamma_{lv}/\gamma_{sv} - 1)$, as shown in Equation 6.2 (assuming $\varphi_{sl} = 1$, a good assumption for alkanes).[22]

$$\cos\theta_E = 1 - \left(\frac{\gamma_{lv}}{\gamma_{sv}} - 1\right) + \frac{3}{4}\left(\frac{\gamma_{lv}}{\gamma_{sv}} - 1\right)^2 - \frac{5}{8}\left(\frac{\gamma_{lv}}{\gamma_{sv}} - 1\right)^3 + \frac{35}{64}\left(\frac{\gamma_{lv}}{\gamma_{sv}} - 1\right)^4 - \dots \qquad (6\text{-}2)$$

This series converges only if $(\gamma_{lv}/\gamma_{sv} - 1) < 1$ *i.e.* $\gamma_{lv} < 2\gamma_{sv}$. The Taylor series can be truncated after the second term to get a linear relation between $\cos\theta_E$ and γ_{lv} (Equation 6.3), and absolute value of the slope of this line is expected to be the inverse of the solid surface energy (γ_{sv}).

$$\cos\theta_E \approx 1 - \left(\frac{\gamma_{lv}}{\gamma_{sv}} - 1\right) \qquad (6\text{-}3)$$

This linearization is valid only if the quadratic term is considerably smaller (ca 10%) compared to the linear term. This condition restricts the range of liquid surface tensions (γ_{lv}/γ_{sv}) < 1.13 for which the linearization is valid, therefore in general, this linearization should be avoided. Johnson and Dettre have reported the value of the Zisman slope along with the intercept (γ_c) as a more complete indicator of the solid surface energy.[44] The absolute value of the Zisman slope equals the reciprocal of the Zisman critical surface tension (*i.e.* $\partial\cos\theta_E/\partial\gamma_{lv} = -1/\gamma_{sv}$). Slopes in the range of -0.035 to -0.050 (mN/m)$^{-1}$ were reported and the absolute value of the slope tends to increase with increasing γ_c.[44] This trend is contradictory to the linear form of the truncated Taylor series expansion of the Giriflco-Good equation. Therefore, the slope of the Zisman line does not provide a complete description of the solid surface energy (γ_{sv}).

6.4 The Girifalco – Good analysis

The Girifalco-Good framework was also applied to smooth spin-coated surfaces prepared from the other T_8 molecules and the values of the solid surface energy (γ_{sv}) were computed from the advancing contact angle data (Figure 6-6). The calculated values of the solid surface energy monotonically increase from $\gamma_{sv} = 9.3$ to 18.7 mN/m as the length of the fluorinated side chain decreases from fluorodecyl T_8 (■) to fluoropropyl T_8 (◀). These values follow a similar trend to that of the critical surface tension (γ_c), but as expected, there is a lack of quantitative agreement between the two.

A close packed monolayer of –CF$_3$ moieties has the lowest known solid surface energy ($\gamma_{sv} \approx 6.7$ mN/m).[19, 45] The side-chains of the fluoroalkylated molecules under consideration terminate with –CF$_3$ groups which are backed by –CF$_2$– groups, with surface energies in the

range of $\gamma_{sv} \approx$ 18-20 mN/m.[36] As the length of the perfluorinated chain increases, close packing

of the chains becomes more favorable and consequently liquid-induced molecular reorganization

at the surface becomes restricted. For fluorodecyl T_8 with the longest perfluorinated chain (seven

–CF_2– groups), predominantly –CF_3 groups are presented at the surface and the surface energy

remains quite low (γ_{sv} = 9.3 mN/m). However, as the length of the fluorinated chain decreases,

the tendency to chain alignment and crystallization reduces and the chains at the solid-liquid

interface become more susceptible to liquid-induced reorganization.
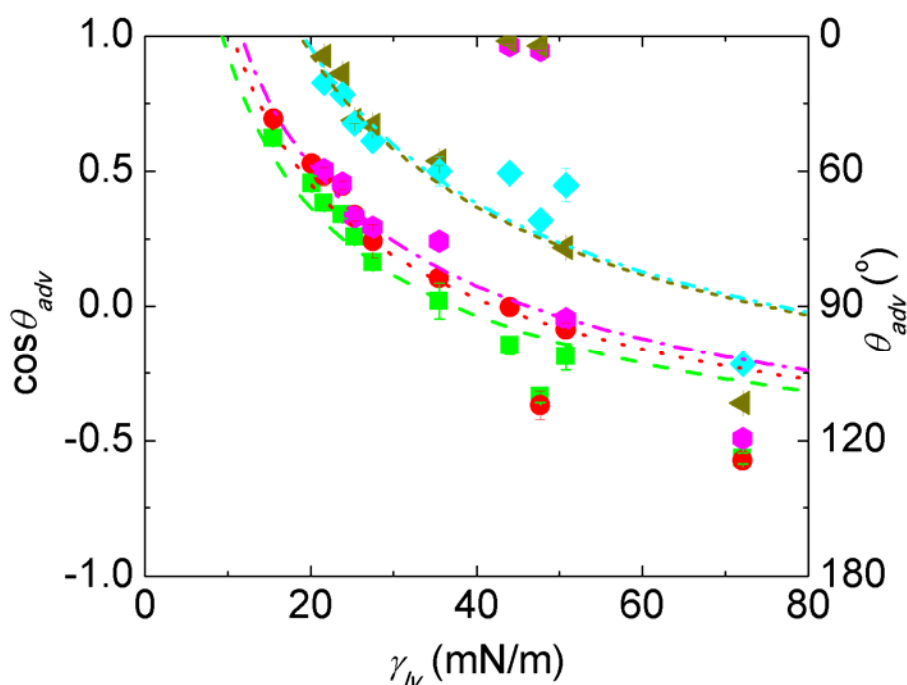
Figure 6-6. Variation of advancing contact angles (θ_{adv}) for T_8 cages surrounded by various fluorinated chains is summarized in this figure. Cosine of advancing contact angles (θ_{adv}) for droplets of water (γ_{lv} = 72.1 mN/m), diiodomethane (γ_{lv} = 50.8 mN/m), ethylene glycol (γ_{lv} = 47.7 mN/m), dimethyl sulfoxide (γ_{lv} = 44 mN/m), rapeseed oil (γ_{lv} = 35.5 mN/m), hexadecane (γ_{lv} = 27.5 mN/m), dodecane (γ_{lv} = 25.3 mN/m), decane (γ_{lv} = 23.8 mN/m), octane (γ_{lv} = 21.6 mN/m), heptane (γ_{lv} = 20.1 mN/m), and pentane (γ_{lv} = 15.5 mN/m) on a spin-coated film on a flat silicon wafer are plotted against the surface tension of contacting liquids (γ_{lv}). Solid surface energy for Fluorodecyl T_8 (γ_{sv} = 9.3 mN/m, ■), fluorooctyl T_8 (γ_{sv} = 10.6 mN/m, ●), fluorohexyl T_8 (γ_{sv} = 11.6 mN/m, ⬟), fluoropropyl T_8 (γ_{sv} = 18.7 mN/m, ◀), and hexafluoroisbutyl T_8 (γ_{sv} = 19.1 mN/m, ◆) is estimated by the extrapolation of the best fit Girifalco-Good curve.

Consequently, the underlying higher surface energy moieties (–CF_2– and –CH_2– groups) are exposed to the contacting liquid, and γ_{sv} increases significantly from the value γ_{sv} = 9.3 mN/m, which is close to that of a –CF_3 monolayer. It was also noted that some high surface tension liquids like dimethyl sulfoxide (γ_{lv} = 44 mN/m) or ethylene glycol (γ_{lv} = 47.7 mN/m) fully wet ($\theta_E \rightarrow 0°$) the fluorohexyl and fluoropropyl T_8 surfaces, even though $\gamma_{lv} >> \gamma_c$. This unexpected behavior is due to specific polar interactions across the solid-liquid interface and it can be understood by careful examination of the Girifalco-Good framework.

In one set of molecules, the T_8 cage structure was kept constant and the length of the perfluorinated side chain was changed (Figure 6-6). It was found that fluorodecyl T_8, with the longest perfluorinated side chain, had the lowest solid surface energy (γ_{sv}) among the T_8 molecules. Therefore, in a second set of molecules, the fluorodecyl side chain was kept constant but the –Si/O– architecture was changed from the T_8 cage (■) to a Q_4 ring (▲) as well as a linear chain molecule (▼, M_2). The solid surface energy (γ_{sv}) increased from 9.3 mN/m for the fluorodecyl T_8, to 14.3 mN/m for fluorodecyl Q_4, and finally to 26.8 mN/m for fluorodecyl M_2 (Figure 6-7). This trend is consistent with the variation in the corresponding critical surface tensions (γ_c) obtained from Zisman analysis. In this set of molecules, the perfluorinated side chain was held constant; therefore changes in the –Si/O– architecture are the only possible cause for the change in wettability. For the fluorodecyl M_2 molecules, the relative ease of access to the high surface energy –Si–O–Si– moiety is expected to be the reason for its high solid surface energy. The reason for the difference in wettability of the fluorodecyl T_8 and Q_4 molecules is currently unknown.
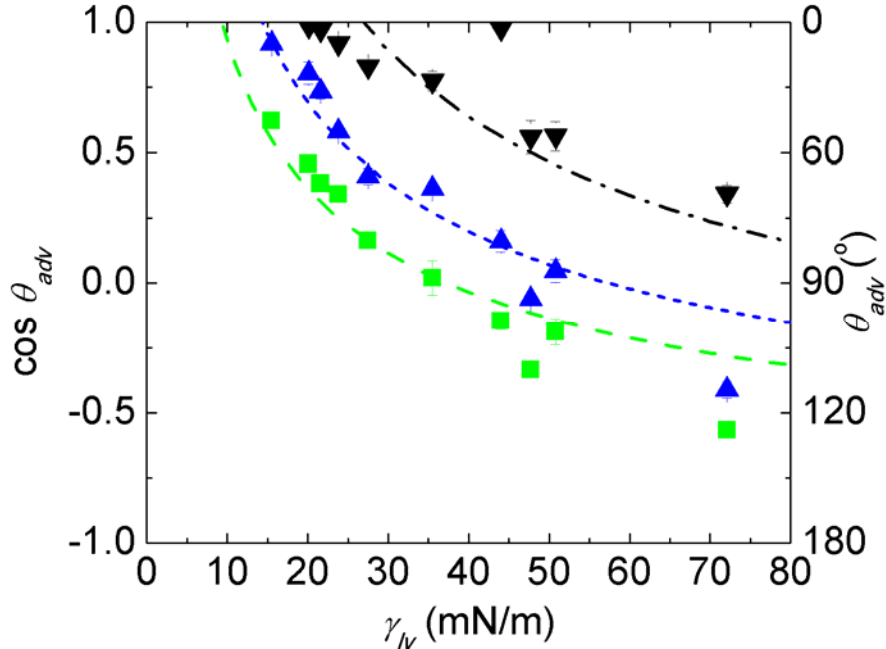
Figure 6-7. Variation of advancing contact angles (θ_{adv}) for various –Si/O– moieties surrounded by 1*H*,1*H*,2*H*,2*H*-heptadecafluorodecyl chains is summarized. Cosine of advancing contact angles (θ_{adv}) for droplets of water ($\gamma_{lv} = 72.1$ mN/m), diiodomethane ($\gamma_{lv} = 50.8$ mN/m), ethylene glycol ($\gamma_{lv} = 47.7$ mN/m), dimethyl sulfoxide ($\gamma_{lv} = 44$ mN/m), rapeseed oil ($\gamma_{lv} = 35.5$ mN/m), hexadecane ($\gamma_{lv} = 27.5$ mN/m), dodecane ($\gamma_{lv} = 25.3$ mN/m), decane ($\gamma_{lv} = 23.8$ mN/m), octane ($\gamma_{lv} = 21.6$ mN/m), heptane ($\gamma_{lv} = 20.1$ mN/m), and pentane ($\gamma_{lv} = 15.5$ mN/m) on a spin-coated film on a flat silicon wafer are plotted against the surface tension of contacting liquids (γ_{lv}). Solid surface energy for Fluorodecyl T_8 ($\gamma_{sv} = 9.3$ mN/m, ■), fluorodecyl Q_4 ($\gamma_{sv} = 14.3$ mN/m, ▲), and fluorodecyl M_2 ($\gamma_{sv} = 26.8$ mN/m, ▼) is estimated by the extrapolation of the best fit Girifalco-Good curve.

According to the Girifalco – Good framework, the total surface energy can be divided into a dispersion (or non-polar, γ^d) and a polar (γ^p) component. Subsequently, Girifalco, Good and co-workers expressed the polar component of a solid (γ_{sv}^p) or a liquid (γ_{lv}^p) in terms of hydrogen bond donating (or acidic, γ^+) and hydrogen bond accepting (or basic, γ^-) components (as shown in Equation 4).

$$\gamma_{lv} = \gamma_{lv}^d + \gamma_{lv}^p = \gamma_{lv}^d + 2\sqrt{\gamma_{lv}^+ \gamma_{lv}^-}$$
$$\gamma_{sv} = \gamma_{sv}^d + \gamma_{sv}^p = \gamma_{sv}^d + 2\sqrt{\gamma_{sv}^+ \gamma_{sv}^-}$$

(6-4)

Liquids such as acetone ($\gamma_{lv} = 25.2$ mN/m) or dimethyl sulfoxide ($\gamma_{lv} = 44$ mN/m) have an oxygen atom attached to an electropositive atom; therefore, the oxygen can donate its lone pair of

electrons or accept hydrogen bonds. These liquids do not have any acidic protons, and therefore have negligibly small values of hydrogen bond donating components of surface energy (γ_{lv}^+). Such liquids with one predominant polar component are said to be monopolar liquids. Liquids like ethylene glycol ($\gamma_{lv} = 47.7$ mN/m) and glycerol ($\gamma_{lv} = 66$ mN/m) have both (a) an electronegative atom like oxygen which can accept hydrogen bonds, and (b) a hydrogen atom bonded to electronegative oxygen atom, which can be easily donated. Therefore, such liquids have appreciable values of both the polar components ($\gamma_{lv}^+, \gamma_{lv}^-$), and they are commonly termed bipolar liquids. Values of the surface energy components are known (tabulated in the supporting information) based on water as a standard state with $\gamma_{lv}^+ = \gamma_{lv}^- = 25.5$ mN/m. Some researchers have recently argued that for water $\gamma_{lv}^+/\gamma_{lv}^- = 6.5$, based on the shifts in the absorption wavelengths of solvatochromic dyes,[46] but we have used the former standard state due to the availability of surface energy component data in this reference frame. Finally, it is important to note that the magnitude of acidic $\left(\gamma_{sv}^+\right)$ and basic components $\left(\gamma_{sv}^-\right)$ of the solid surface energy depends on the choice of the standard state, whereas the magnitude of the total polar $\left(\gamma_{sv}^p = 2\sqrt{\gamma_{sv}^+\gamma_{sv}^-}\right)$ and dispersion component $\left(\gamma_{sv}^d\right)$ is independent of the standard state.

Two molecules of a bipolar liquid can have dispersion (non-polar) as well as polar cohesive interactions with each other; and due to the presence of these additional polar interactions, the surface tension (γ_{lv}) and work of cohesion ($W_{ll}^c = 2\gamma_{lv}$) for bipolar liquids tends to be higher than for non-polar or monopolar liquids (Figure 6-8). A droplet of a bipolar liquid can interact with a non-polar solid only through dispersion adhesive interactions, and consequently the work of adhesion (W_{sl}^a) tends to be lower for a bipolar liquid on a non-polar solid. Therefore, for a droplet

of bipolar liquid (like water and ethylene glycol) on a non-polar solid, the parameter $\varphi_{sl} =$

$W_{sl}^a \big/ \sqrt{W_{ss}^c W_{ll}^c} < 1.$[47] In Figure 6-3, Figure 6-6 and Figure 6-7 we fitted Equation 1 to the

advancing contact angle data, assuming $\varphi_{sl} = 1$, but we now recognize that $\varphi_{sl} < 1$ for water and

ethylene glycol on non-polar surfaces. Therefore, these points corresponding to bipolar liquids

are not expected to lie on the best-fit curve (Equation 1).

(a) Bipolar liquid on a non-polar solid ($\varphi_{sl} < 1$)   (b) Monopolar or non-polar liquid on a non-polar solid ($\varphi_{sl} \approx 1$)
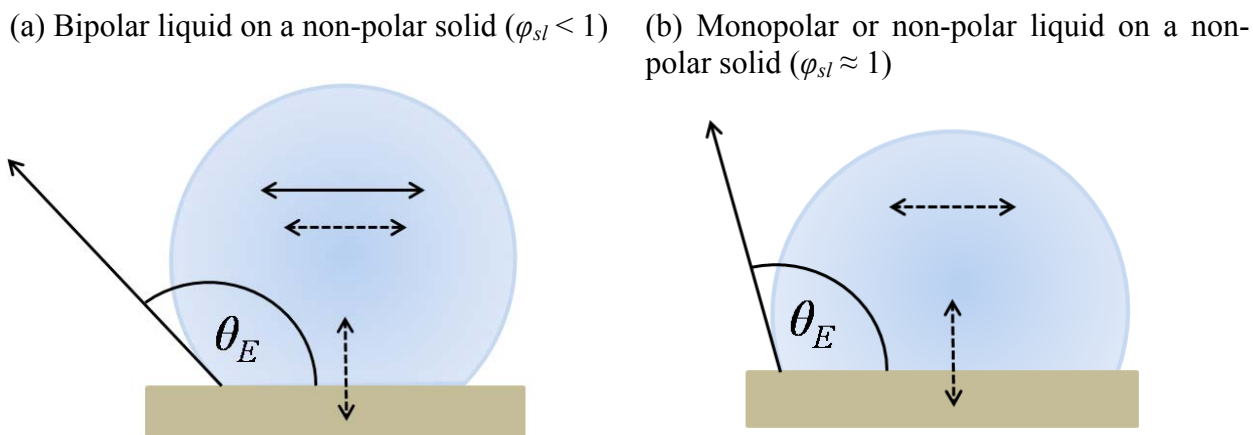
Figure 6-8. Schematic of (a) a bipolar and (b) a monopolar or a non-polar liquid droplet on a non-polar solid surface is shown. The dotted arrows (<– –>) indicate a non-polar (dispersion) interaction and the filled arrows (<—>) indicate a polar interaction. A bipolar liquid has both polar and non-polar cohesive interactions whereas a monopolar or a non-polar liquid has only non-polar cohesive interactions. Consequently, for the same values of liquid surface tension (γ_{lv}) and solid surface energy (γ_{sv}), a droplet of a bipolar liquid forms higher equilibrium contact angle (θ_E) compared to a droplet of either a monopolar or a non-polar liquid. (This figure is adapted from the book by Van Oss.[47])

The statistical Dixon Q-test was used to decide whether to use the water and/or ethylene glycol

data for fitting Equation 1. Based on the magnitude of the residuals and the Q-test tables, both

water and ethylene glycol data were rejected for fitting Equation 1 with a 95% confidence for the

fluorodecyl T_8 surface. A similar statistical exercise was carried out for all the solid surfaces and

the "best-fit" plots in Figure 6-6 and Figure 6-7 are based on the liquids which satisfy the Dixon

Q-test with 95% confidence (data shown in supporting information). Moreover from the value of

the best-fit predicted and experimentally measured contact angles, the parameter φ_{sl} can be

computed to be 0.60 for water and 0.75 for ethylene glycol on the fluorodecyl T_8 surface. For

monopolar or non-polar liquids on non-polar solids, both the cohesive and adhesive interactions are dispersive, therefore the parameter φ_{sl} is expected to be close to unity and it is found to be $0.95 \le \varphi_{sl} \le 1.05$ for such liquids on non-polar solids.

The advancing contact angles for dimethyl sulfoxide and ethylene glycol droplets were found to have surprisingly low contact angles ($\theta_{adv} < 15°$) on fluorohexyl T_8, fluoropropyl T_8, and fluorodecyl M_2 surfaces (Figure 6-6 and Figure 6-7). These low contact angles are believed to occur due to a strong specific polar interaction ($\varphi_{sl} \gg 1$) across the solid-liquid interface. These anomalously low contact angles were excluded from the fitting to obtain the solid surface energies. The solid-liquid work of adhesion (W_{sl}^a) can be written in terms of the individual components of the surface energy of the solid and contacting liquid [39, 42, 43]

$$W_{sl}^a = \gamma_{lv}\left(1+\cos\theta_E\right) = 2\left[\sqrt{\gamma_{sv}^d\gamma_{lv}^d} + \sqrt{\gamma_{sv}^+\gamma_{lv}^-} + \sqrt{\gamma_{sv}^-\gamma_{lv}^+}\right] \qquad (6\text{-}5)$$

Note that the first term on the right hand side of Equation 5 ($\sqrt{\gamma_{sv}^d\gamma_{lv}^d}$) has the same form as Equation 1, but the other two terms appear in the form of a cross product. The hydrogen bond donating component of the solid (γ_{sv}^+) interacts with the hydrogen bond accepting component of the liquid (γ_{lv}^-) and vice versa. If either the solid or the liquid is purely non-polar, then these polar interactions vanish and Equation 5 simplifies to Equation 1. The individual contributions to the liquid surface tension ($\gamma_{lv}^d, \gamma_{lv}^+, \gamma_{lv}^-$) are known for a few standard liquids (See supporting information). Therefore by measuring the equilibrium contact angles of (at least) three contacting liquid droplets, the three unknowns in Equation 5 ($\gamma_{sv}^d, \gamma_{sv}^+, \gamma_{sv}^-$) can be obtained by solving a linear system of three equations [A][x]=[b], given by Equation 6.

$$2 \begin{bmatrix} \sqrt{\gamma_{lv,1}^d} & \sqrt{\gamma_{lv,1}^-} & \sqrt{\gamma_{lv,1}^+} \\ \sqrt{\gamma_{lv,2}^d} & \sqrt{\gamma_{lv,2}^-} & \sqrt{\gamma_{lv,2}^+} \\ \sqrt{\gamma_{lv,3}^d} & \sqrt{\gamma_{lv,3}^-} & \sqrt{\gamma_{lv,3}^+} \end{bmatrix} \begin{bmatrix} \gamma_{sv}^d \\ \gamma_{sv}^+ \\ \gamma_{sv}^- \end{bmatrix} = \begin{bmatrix} \gamma_{lv,1}\left(1+\cos\theta_{E,1}\right) \\ \gamma_{lv,2}\left(1+\cos\theta_{E,2}\right) \\ \gamma_{lv,3}\left(1+\cos\theta_{E,3}\right) \end{bmatrix} \qquad (6\text{-}6)$$

The relative error in the contact angle measurements (the right hand side of Equation 6) is amplified by the condition number of matrix [A], therefore the contacting liquids are chosen such that the matrix [A] is not ill-conditioned or it has as low a condition number as possible.[46, 48] Dodecane (γ_{lv} = 25.3 mN/m), chloroform (γ_{lv} = 27.5 mN/m), and acetone (γ_{lv} = 25.2 mN/m) were chosen as a set of contacting liquids. All the three liquids have similar values of surface tensions but different polarities. Acetone has a strongly monopolar hydrogen bond accepting component ($\gamma_{lv}^+ = 0, \gamma_{lv}^- = 24\,\text{mN/m}$), and chloroform has a weekly monopolar hydrogen bond donating component ($\gamma_{lv}^+ = 3.8, \gamma_{lv}^- = 0\,\text{mN/m}$), whereas dodecane is completely non-polar ($\gamma_{lv}^+ = \gamma_{lv}^- = 0$). Even though both acetone and chloroform are polar, due to their monopolar nature, the polar component of surface energy is zero ($\gamma_{lv}^p = 2\sqrt{\gamma_{lv}^+ \gamma_{lv}^-} = 0$). The condition number of the pre-factor matrix [A] is reasonably small (7.2), therefore this set of liquids can be used successfully to evaluate the individual components of the solid surface energy. All three liquids are expected to have similar contact angles on non-polar solids (*i.e.* solids with $\gamma_{sv}^+ = \gamma_{sv}^- = 0$), as the last two terms of Equation 5 vanish and the interactions across solid-liquid are purely dispersive. Indeed, dodecane (θ_{adv} = 75 ± 2°, θ_{rec} = 60 ± 4°, ■), acetone (θ_{adv} = 71 ± 2°, θ_{rec} = 59 ± 4°, ■), and chloroform droplets (θ_{adv} = 73 ± 2°, θ_{rec} = 54 ± 4°, ■) all form similar contact angles on fluorodecyl T_8, which is a completely non-polar molecule (Figure 6-9(a)).

As the polarity of the surfaces increases from fluorodecyl T_8 to fluorooctyl T_8, and finally fluorodecyl Q_4, the acetone and chloroform droplets form much lower contact angles in

comparison with dodecane droplets. For example, on the fluorodecyl Q_4 surface (Figure 6-9(c)), the dodecane contact angles ($\theta_{adv} = 62 \pm 2°$, $\theta_{rec} = 17 \pm 2°$, ▲) are much larger than those measured for acetone ($\theta_{adv} = 30 \pm 1°$, $\theta_{rec} \approx 0°$, △) or chloroform ($\theta_{adv} = 29 \pm 4°$, $\theta_{rec} = 15 \pm 3°$, ◭). Therefore, it is vital to know about the polarity of the contacting liquids and solids when evaluating the equilibrium contact angles and solid surface energies (γ_{sv}).
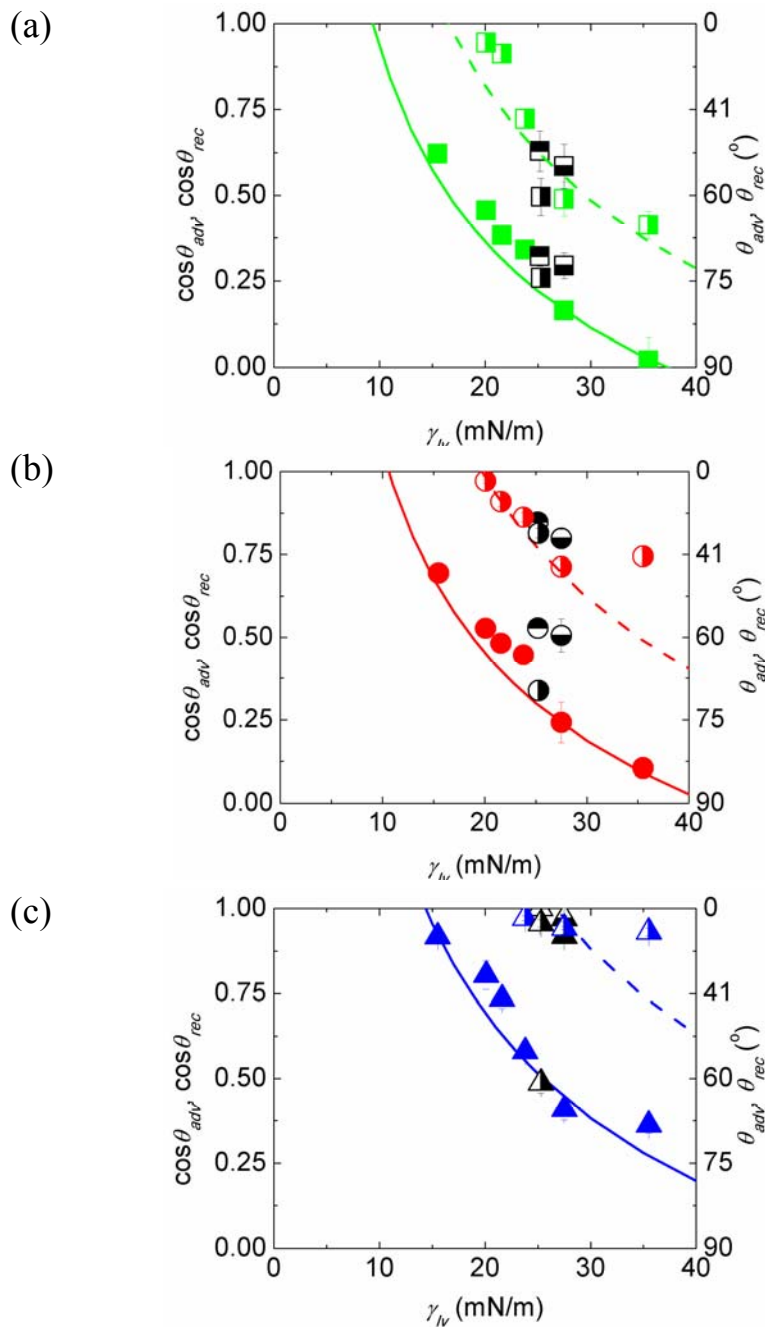
Figure 6-9. Variation of advancing and receding contact angles (θ_{adv}, θ_{rec}) is summarized for (a) fluorodecyl T_8 (■, ▢), (b) fluorooctyl T_8 (●, ◯), (c) fluorodecyl Q_4 (▲, △), and (d) _____. Cosine of advancing and receding contact angles (θ_{adv}, θ_{rec}) for droplets of hexadecane (γ_{lv} = 27.5 mN/m), dodecane (γ_{lv} = 25.3 mN/m), decane (γ_{lv} = 23.8 mN/m), octane (γ_{lv} = 21.6 mN/m), heptane (γ_{lv} = 20.1 mN/m), pentane (γ_{lv} = 15.5 mN/m), chloroform (γ_{lv} = 27.5 mN/m), and acetone (γ_{lv} = 25.2 mN/m) on a spin-coated film on a flat silicon wafer are plotted against the surface tension of contacting liquids (γ_{lv}). Solid surface energy is estimated by substituting the values of the contact angles with dodecane (■, ◯, △), chloroform (◼) and acetone droplets (▢) in the Girifalco – Good equation.

Fluorinated species have surfaces with relatively low polarity and low solid surface energy, and the reason for this can be understood by looking at the unusual characteristics of fluorine. Fluorine is the most electronegative element of the periodic table (3.98 on the Pauling scale). Carbon (2.55) is significantly less electronegative and consequently a C–F bond is polar ($C^{\delta^+} - F^{\delta^-}$) and acquires some ionic character. A carbon attached to three fluorine atoms (–CF$_3$) is significantly electron deficient; therefore the only way to reduce the dipole moment between this α carbon (–CF$_3$) and the adjacent β carbon is by fluorinating the β carbon as well. By perfluorinating a large number of successive carbon atoms, the –CF$_2$–CH$_2$– dipole is buried deep within the molecule. Therefore fluorodecyl T_8 and other molecules with long fluorinated side chains show negligible polar component of solid surface energy ($\gamma_{sv}^p \approx 0$). Furthermore, due to the small size (van der Waals radius, r = 1.47 Å), the polarizability of a fluorine atom is small, and it is difficult to create fluctuating dipoles involving fluorine atoms. The interaction energy arising from London forces varies as the square of the polarizability therefore the dispersion component of the solid surface energy (γ_{sv}^d) is also small for fluorinated species.[49] Intuitively, the high electronegativity of fluorine makes it an ideal candidate for accepting hydrogen bonds and therefore fluorinated species are expected to have a high value of γ_{sv}^-. However in practice, due to the small size and small polarizability, a fluorine atom holds its three lone pairs extremely tightly and therefore it is a poor hydrogen bond acceptor. The hydrogen bonds formed by

fluorinated species are weaker in strength (typically $1/4^{th}$ of the bond energy of a –C=O --- HOR bond).[50] On the contrary, hydrogen (2.20) and carbon (2.55) have similar electronegativities and they form non-polar bonds; due to the relatively higher polarizability of hydrogen, the dispersion component of the solid surface energy for hydrocarbons tends to be higher than corresponding fluorocarbons.

6.5 Solid surface energy estimation

Using the set of three liquids mentioned above (acetone, chloroform and dodecane) and using Equation 5, the solid surface energy was estimated for various fluoroalkylated silicon-containing molecules (summarized in Table 6-2).

Table 6-2. Computed values of solid surface energy (γ_{sv} mN/m) for various fluoroalkylated silicon containing moieties are summarized.

γ_{sv} (mN/m) based on contact angles (°) of the probing liquids	All liquids[*] (Equation 1 with $\varphi_{sl} = 1$)	Dodecane, acetone, and chloroform (Equation 5)	Diiodomethane, dimethyl sulfoxide and water (Equation 5)
Fluorodecyl T_8	9.3	10.2	8.8
Fluorooctyl T_8	10.6	13.6	10.9
Fluorohexyl T_8	11.6	26.8	47.4
Fluoropropyl T_8	18.7	21.4	38.4
Hexafluoro-i-butyl T_8	19.1	19.8	26.9
Fluorodecyl T_8	9.3	10.2	8.8
Fluorodecyl Q_4	14.3	20.1	14.9
Fluorodecyl M_2	26.8	--	39.7

*All liquids include a set of n-alkanes from pentane to hexadecane, rapeseed oil, dimethyl sulfoxide, ethylene glycol, diiodomethane, and water. Assuming a typical error in contact angle measurement ($\Delta\theta \approx 2°$), and from the condition number of the transformation matrix in the system of linear equations, a 15% relative error ($\delta\gamma_{sv}/\gamma_{sv}$) is expected in the computed values of the surface energies.

For the fluorodecyl T_8 POSS cages, this value of the surface energy agreed (within experimental error) with the value of surface energy estimated using Equation 1. However, these three probing liquids considered so far have low surface tensions ($\gamma_{lv} \approx 25$ to 27 mN/m) therefore they wet and

spread on most of the non-fluorinated surfaces that have $\gamma_{sv} > 25$ mN/m. Moreover, the relative error in the measurement of small contact angles is always large; therefore a set of probing liquids with higher surface tension is required to accurately probe higher energy surfaces. Water ($\gamma_{lv} = 72.1$ mN/m), diiodomethane ($\gamma_{lv} = 50.8$ mN/m), and dimethyl sulfoxide ($\gamma_{lv} = 44$ mN/m) constitute such a set with high values of liquid surface tension (and give rise to a small condition number for the matrix [A], cond(A) = 4.58). Using this set of liquids, a broader range of surfaces ($\gamma_{sv} < 40$ mN/m) can be analyzed using the Girifalco-Good method (see Table 6-2 and Table 6-3).

Table 6-3. Computed values of the dispersion (γ_{sv}^d), acidic (γ_{sv}^+), and basic (γ_{sv}^-) components of solid surface energy (mN/m) for various fluoroalkylated silicon containing moieties are summarized.

γ_{sv} (mN/m)	Alkanes (Zisman analysis)	All liquids* (Equation 1 with $\varphi_{sl} = 1$)	Diiodomethane, dimethyl sulfoxide and water (Equation 5)			
	γ_c	γ_{sv}	γ_{sv}	Dispersion (γ_{sv}^d)	Polar (γ_{sv}^p)	Acidic (γ_{sv}^+)	Basic (γ_{sv}^-)
Fluorodecyl T_8	5.5	9.3	8.8	8.7	0.1	0.04	0.1
Fluorooctyl T_8	7.4	10.6	10.9	10.6	0.3	0.2	0.1
Fluorohexyl T_8	8.5	11.6	47.4	11.4	36.0	20.8	15.6
Fluoropropyl T_8	19.7	18.7	38.4	19.1	19.3	11.8	7.9
Hexafluoro-i-butyl T_8	17.7	19.1	26.9	26.8	0.1	0.002	0.8
Fluorodecyl T_8	5.5	9.3	8.8	8.7	0.1	0.04	0.1
Fluorodecyl Q_4	14.5	14.3	14.9	14.5	0.8	0.0	0.2
Fluorodecyl M_2	19.6	26.8	39.7	30.9	8.8	2.0	9.7

For fluorohexyl, fluoropropyl and hexafluoro-i-butyl T_8 surfaces, solid surface energy values obtained using these three high surface tension liquids (column 4 of Table 6-3) did not match the previously obtained values (columns 2 and 3). In order to diagnose the reason for this mismatch,

the magnitudes of the individual components of the solid surface energy must be considered (as summarized in Table 6-4). The values of the dispersion component of the solid surface energy (γ_{sv}^{d} , given in column 5 of Table 6-3) match well with the solid surface energy (γ_{sv}, column 3 of Table 6-3) calculated using Equation 1.

The dispersion component of the solid surface energy (calculated in Table 6-3) increased monotonically from fluorodecyl T_8 (γ_{sv}^{d} = 8.7 mN/m) to hexafluoro-i-butyl T_8 (γ_{sv}^{d} = 26.8 mN/m), whereas the polar component (γ_{sv}^{p}) does not follow any clear trend. These fluoroalkylated T_8 molecules have two methylene groups connecting the –Si–O– cage with the fluoroalkyl chain (see structure in Table 1). Methylene groups are non-polar, but due to the higher polarizability of a –CH$_2$– moiety (as compared with a –CF$_2$– moiety), the dispersion component of the solid surface energy tends to be higher (γ_{sv}^{d} for polyethylene ≈ 30 – 32 mN/m, versus γ_{sv}^{d} = 18 – 20 mN/m for PTFE and 6.7 mN/m for a monolayer of –CF$_3$ groups). Therefore, this increase in γ_{sv}^{d} of the T_8 molecules is attributed to higher interaction of the contacting liquids with the underlying –CH$_2$–CH$_2$– and (–CF$_2$–)$_n$ groups. As the length of the perfluorinated chain decreases, the crystalline-like packing of the side chains becomes unfavorable and the underlying –CF$_2$– and –CH$_2$– groups start contributing to the total solid surface energy.

Similarly, when we compare the fluorodecyl T_8, Q_4 and M_2 molecules, we find that γ_{sv}^{d} increases monotonically from a T_8 cage (8.7) to a Q_4 ring (14.5) and finally to a M_2 straight chain (30.9 mN/m) and this increase in the dispersion component of the solid surface energy accounts for most of the increase in γ_{sv}. The T_8 cage structure seems to achieve an optimal packing of the eight fluorodecyl chains, which results in a very restricted ability to rearrange these chains when in contact with probing liquids. As a consequence, the fluorodecyl T_8 has the lowest solid surface

131

energy among all the molecules tested so far. The behavior of T_8 surfaces with fluorinated chains longer than the fluorodecyl (*i.e.* greater in length than $(-CF_2-)_7-CF_3$) is still an open question. Currently fluorododecyl and fluorotetradecyl T_8 synthesis is underway and the systematic analysis of their wettability will be the scope of a future investigation.

The main objective of this paper was to estimate the solid surface energy of the native solid surface. The discussion above is based on calculations of the solid surface energy obtained by substituting the advancing contact angles (θ_{adv}) in place of the equilibrium contact angle (θ_E) in the governing equations. The advancing contact angle (θ_{adv}) is the contact angle formed by a liquid droplet when it touches the solid surface for the first time, so the advancing contact angle (θ_{adv}) is the physically more relevant measurement to use rather than the receding contact angle (θ_{rec}) in the context of determining solid surface energies.

Although unintended chemical inhomogeneities and dust contamination can contribute to contact angle hysteresis, we believe that the most important factor is reorganization or reconstruction of the solid surface as a result of contact with the probing liquid. As a result, a finite contact angle hysteresis ($\Delta\theta = \theta_{adv} - \theta_{rec}$) was observed for all the molecules studied here. Substituting the advancing contact angles (θ_{adv}) on a flat surface in place of the equilibrium contact angle (θ_E), into the Girifalco-Good equation leads to a value of solid surface energy (say a), while substituting receding contact angles (θ_{rec}), yields a higher value of solid surface energy (say

$b > a$) *i.e.* $\cos\theta_{adv} = -1 + 2\phi_{sl}\sqrt{\dfrac{a}{\gamma_{lv}}}$ and $\cos\theta_{rec} = -1 + 2\phi_{sl}\sqrt{\dfrac{b}{\gamma_{lv}}}$. If the difference between b and a

is small, a low energy solid surface has the desirable attribute of being able to resist reorganization in the presence of the contacting liquid. As shown in Table 6-4, fluorodecyl T_8 exhibits lowest value of $b - a$ ($= 7$ mN/m). Fluorodecyl Q_4 and fluorodecyl M_2 molecules are

more susceptible to rearrangements in contact with probing liquids, as indicated by comparatively higher values of $b - a$, 12.2 and 9.0 mN/m respectively. In case of molecules with a T_8 cage, the fluoropropyl molecule has equally low value of $b - a$ as that of fluorodecyl T_8, though the inherent solid surface energy is much higher for the fluoropropyl T_8 molecule ($\gamma_{sv} = 18.7$ Vs 9.3 mN/m for fluorodecyl T_8).

Thus in summary we note that the special character of fluorodecyl POSS (lowest solid surface energy $\gamma_{sv} = 9.3$ mN/m along with maximum resistance to solid surface reconstruction) apparently arises from the favorable combination of the cage structure and the fluorodecyl side chains. The latter contribute to an unusually low value of dispersive contribution to the solid surface energy while simultaneously reducing polar contributions to nearly zero. The cage structure is relatively inflexible towards molecular reorganization compared to the ring or linear analogs. Whether or not fluorodecyl represents the optimal substituent remains an open question. A plot of solid surface energy (γ_{sv}) versus cage substituent chain length (Figure 6-10) suggests that a minimum may not yet have been achieved with the fluorodecyl substituent. Synthesis of the dodecyl and tetradecyl analogs is now underway to explore this unanswered question. We note, however, that very long fluoroalkyl chains on the POSS cage should eventually produce PTFE-like surface energies in the range of $\gamma_{sv} = 18$-20 mN/m, well above the value of $\gamma_{sv} = 9.3$ mN/m found here for the fluorodecyl cage molecule.
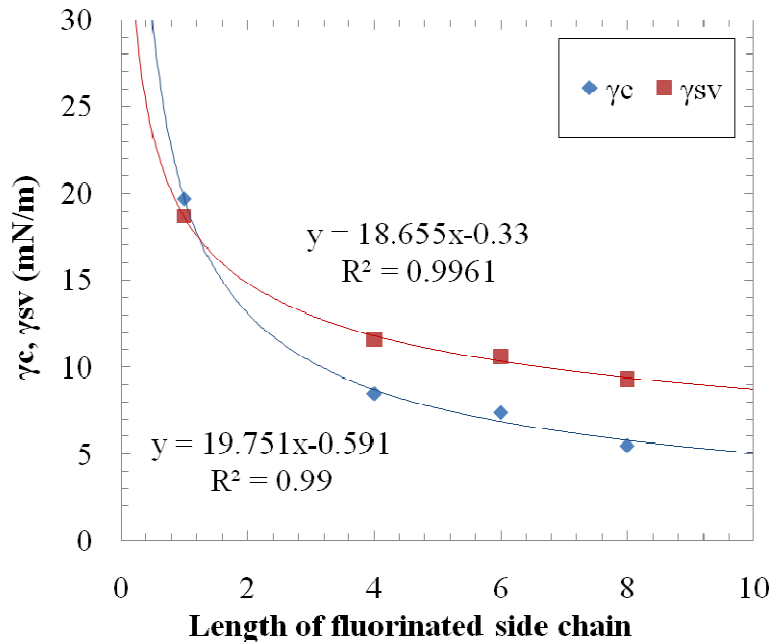
Figure 6-10. Solid surface energy (γ_{sv}) obtained by Girifalco-Good analysis and critical surface tension (γ_c) obtained by Zisman analysis is plotted against the length of fluorinated side chain for fluoroalylated T_8 molecules.
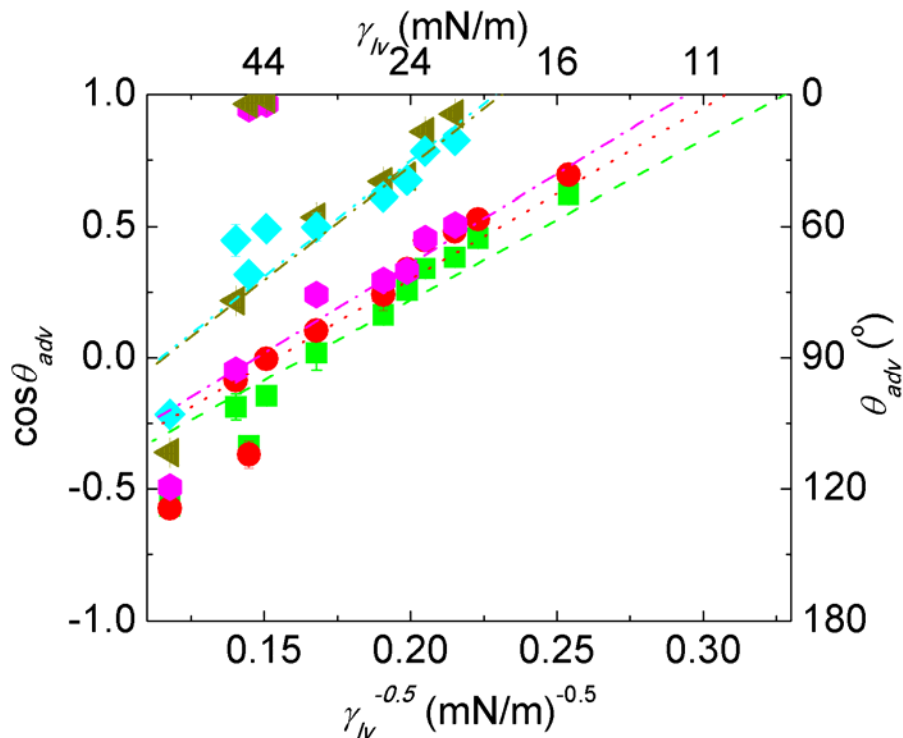
Figure 6-11. The data in Figure 3 (cosine of the advancing contact angle on various T_8 surfaces) are replotted against inverse square root of liquid surface tension. Best fit Girifalco-Good lines are plotted using Equation 1 with $\varphi_{sl} = 1$.

Table 6-4. Computed values of solid surface energy (γ_{sv} mN/m) for various fluoroalkylated silicon containing moieties are summarized.

γ_{sv} (mN/m) based on contact angles (°) of the probing liquids	All liquids[*] (Equation 1 with $\varphi_{sl} = 1$)	Dodecane, acetone, and chloroform (Equation 5)	Diiodomethane, dimethyl sulfoxide and water (Equation 5)	All liquids[*] (Equation 1 with $\varphi_{sl} = 1$)	Dodecane, acetone, and chloroform (Equation 5)	Diiodomethane, dimethyl sulfoxide and water (Equation 5)
		Advancing			Receding	
Fluorodecyl T_8	9.3	10.2	8.8	16.3	14.9	18.0
Fluorooctyl T_8	10.6	13.6	10.9	19.7	20.9	21.7
Fluorohexyl T_8	11.6	26.8	47.4	24.0	27.4	38.2
Fluoropropyl T_8	18.7	21.4	38.4	25.7	21.9	31.2
Hexafluoro-i-butyl T_8	19.1	19.8	26.9	28.5	21.6	42.5
Fluorodecyl T_8	9.3	10.2	8.8	16.5	14.9	18.0
Fluorodecyl Q_4	14.3	20.1	14.9	26.5	24.3	38.8
Fluorodecyl M_2	23.0	--	39.7	32.0	--	43.1

*All liquids include a set of n-alkanes from pentane to hexadecane, rapeseed oil, dimethyl sulfoxide, ethylene glycol, diiodomethane, and water. Assuming a typical error in contact angle measurement ($\Delta\theta \approx 2°$), and from the condition number of the transformation matrix in the system of linear equations, a 15% relative error ($\delta\gamma_{sv}/\gamma_{sv}$) is expected in the computed values of the surface energies.

Table 6-5. Values of hydrogen bond donating (γ_{lv}^+), hydrogen bond accepting (γ_{lv}^-), polar (γ_{lv}^p), dispersion (γ_{lv}^d), and total liquid surface tension (γ_{lv}) in mN/m used for the estimation of solid surface energy are summarized. [Taken from - Chaudhury, M. K. *Mat. Sci. Eng. R.* **1996**, 16, 97-159.]

Liquid	γ_{lv}	γ_{lv}^d	γ_{lv}^p	γ_{lv}^+	γ_{lv}^-
Acetone	25.2	25.2	0.0	0.0	24.0
Chloroform	27.5	27.5	0.0	3.8	0.0
Dimethyl sulfoxide	44.0	36.0	8.0	0.5	32
Water	72.1	21.1	51.0	25.5	25.5
Ethylene glycol	47.7	28.7	19.0	1.9	47.0
Diiodomethane	50.8	50.8	0.0	0.0	0.0
Rapeseed oil	35.5	35.5	0.0	0.0	0.0
Hexadecane	27.5	27.5	0.0	0.0	0.0
Dodecane	25.3	25.3	0.0	0.0	0.0
Decane	23.8	23.8	0.0	0.0	0.0
Octane	21.6	21.6	0.0	0.0	0.0
Heptane	20.1	20.1	0.0	0.0	0.0
Pentane	15.5	15.5	0.0	0.0	0.0

Table 6-6. Values of the advancing contact angles (θ_{adv}) for liquid droplets with a wide range of surface tensions on a flat silicon wafer spin-coated with fluoroalkylated silicon-containing compounds are summarized.

Solid / liquid	Fluorodecyl T_8	Fluorooctl T_8	Fluorohexyl T_8	Fluoropropyl T_8	Hexafluoro-i-butyl T_8	Fluorodecyl M_8Q_4	Fluorodecyl M_2
Water	$122 \pm 2°$	$122 \pm 2°$	$120 \pm 1°$	$111 \pm 1°$	$102 \pm 2°$	$114 \pm 2°$	$70 \pm 2°$
Diiodomethane	$100 \pm 2°$	$95 \pm 1°$	$93 \pm 1°$	$77 \pm 2°$	$63 \pm 4°$	$87 \pm 3°$	$56 \pm 4°$
Ethylene glycol	$111 \pm 2°$	$112 \pm 3°$	$19 \pm 2°$	$15 \pm 2°$	$71 \pm 2°$	$94 \pm 2°$	$56 \pm 5°$
Dimethyl sulfoxide	$98 \pm 2°$	$90 \pm 2°$	$15 \pm 2°$	$11 \pm 2°$	$63 \pm 2°$	$81 \pm 2°$	$12 \pm 3°$
Rapeseed oil	$88 \pm 3°$	$84 \pm 1°$	$76 \pm 1°$	$58 \pm 1°$	$60 \pm 4°$	$69 \pm 2°$	$39 \pm 3°$
Hexadecane	$80 \pm 1°$	$76 \pm 4°$	$73 \pm 1°$	$48 \pm 2°$	$52 \pm 2°$	$66 \pm 2°$	$34 \pm 2°$
Dodecane	$75 \pm 1°$	$70 \pm 1°$	$71 \pm 2°$	$47 \pm 1°$	$48 \pm 2°$	$62 \pm 2°$	$30 \pm 4°$
Decane	$70 \pm 2°$	$63 \pm 1°$	$63 \pm 1°$	$31 \pm 1°$	$38 \pm 2°$	$55 \pm 1°$	$23 \pm 1°$
Octane	$67 \pm 1°$	$61 \pm 2°$	$60 \pm 1°$	$22 \pm 3°$	$34 \pm 2°$	$43 \pm 2°$	$13 \pm 1°$
Heptane	$63 \pm 2°$	$58 \pm 2°$	$54 \pm 2°$	$17 \pm 1°$	$25 \pm 3°$	$32 \pm 4°$	$13 \pm 3°$
Pentane	$52 \pm 1°$	$46 \pm 2°$	$43 \pm 2°$	$14 \pm 1°$	$17 \pm 1°$	$23 \pm 1°$	$< 10°$

Table 6-7. Values of the receding contact angles (θ_{rec}) for liquid droplets with a wide range of surface tensions on a flat silicon wafer spin-coated with fluoroalkylated silicon-containing compounds are summarized.

Solid / liquid	Fluorodecyl T_8	Fluorooctl T_8	Fluorohexyl T_8	Fluoropropyl T_8	Hexafluoro-i-butyl T_8	Fluorodecyl M_8Q_4	Fluorodecyl M_2
Water	116 ± 2°	97 ± 2°	103 ± 4°	95 ± 2°	61 ± 2°	74 ± 3°	45 ± 3°
Diiodomethane	79 ± 3°	76 ± 3°	77 ± 1°	59 ± 2°	40 ± 2°	55 ± 2°	41 ± 1°
Ethylene glycol	87 ± 1°	82 ± 3°	< 10°	< 10°	24 ± 4°	60 ± 2°	40 ± 2°
Dimethyl sulfoxide	80 ± 5°	78 ± 2°	< 10°	< 10°	19 ± 2°	61 ± 7°	< 10°
Rapeseed oil	66 ± 3°	42 ± 2°	37 ± 4°	25 ± 3°	23 ± 6°	21 ± 2°	17 ± 2°
Hexadecane	61 ± 3°	45 ± 2°	39 ± 2°	39 ± 3°	37 ± 3°	20 ± 1°	18 ± 2°
Dodecane	60 ± 4°	35 ± 2°	36 ± 4°	34 ± 2°	40 ± 2°	17 ± 2°	14 ± 2°
Decane	44 ± 2°	30 ± 2°	30 ± 2°	25 ± 2°	26 ± 2°	14 ± 2°	< 10°
Octane	24 ± 2°	24 ± 2°	23 ± 3°	16 ± 1°	23 ± 2°	< 10°	< 10°
Heptane	19 ± 4°	14 ± 1°	15 ± 3°	12 ± 2°	18 ± 2°	< 10°	< 10°
Pentane	< 10°	< 10°	< 10°	< 10°	< 10°	< 10°	< 10°

Table 6-8. Computed values of solid surface energy (γ_{sv} mN/m) based on advancing and receding contact angles for various fluoroalkylated silicon containing moieties are summarized. From these values, various notions of contact angle hysteresis are computed.

γ_{sv} (mN/m) based on contact angles (°) of the probing liquids	All liquids* (Equation 1 with $\varphi_{sl} = 1$), based on –		b – a mN/m	$b^{0.5} - a^{0.5}$ $(mN/m)^{0.5}$	$\Delta = 2(1-(a/b)^{0.5})$
	advancing contact angles (a)	receding contact angles (b)			
Fluorodecyl T_8	9.3	16.3	7.0	0.99	0.49
Fluorooctyl T_8	10.6	19.7	9.2	1.19	0.54
Fluorohexyl T_8	11.6	24.0	12.5	1.51	0.61
Fluoropropyl T_8	18.7	25.7	7.0	0.74	0.29
Hexafluoro-i-butyl T_8	19.1	28.5	9.4	0.97	0.36
Fluorodecyl T_8	9.3	16.5	7.0	0.99	0.49
Fluorodecyl Q_4	14.3	26.5	12.2	1.36	0.53
Fluorodecyl M_2	23.0	32.0	9.0	0.86	0.30

6.6 References

1.   Lafuma, A.; Quéré, D., Superhydrophobic states. *Nat Mater* **2003,** 2, (7), 457-460.
2.   Ma, M.; Hill, R. M.; Rutledge, G. C., A Review of Recent Results on Superhydrophobic Materials Based on Micro- and Nanofibers. *Journal of Adhesion Science and Technology* **2008,** 22, 1799-1817.
3.   Ma, M.; Mao, Y.; Gupta, M.; Gleason, K. K.; Rutledge, G. C., Superhydrophobic Fabrics Produced by Electrospinning and Chemical Vapor Deposition. *Macromolecules* **2005,** 38, (23), 9742-9748.
4.   Michielsen, S.; Lee, H. J., Design of a Superhydrophobic Surface Using Woven Structures. *Langmuir* **2007,** 23, (11), 6004-6010.
5.   Ahuja, A.; Taylor, J. A.; Lifton, V.; Sidorenko, A. A.; Salamon, T. R.; Lobaton, E. J.; Kolodner, P.; Krupenkin, T. N., Nanonails: A Simple Geometrical Approach to Electrically Tunable Superlyophobic Surfaces. *Langmuir* **2008,** 24, (1), 9-14.
6.   Brewer, S. A.; Willis, C. R., Structure and oil repellency: Textiles with liquid repellency to hexane. *Applied Surface Science* **2008,** 254, (20), 6450-6454.
7.   Chhatre, S. S.; Choi, W.; Tuteja, A.; Park, K.-C.; Mabry, J. M.; McKinley, G. H.; Cohen, R. E., Scale Dependence of Omniphobic Mesh Surfaces. *Langmuir* **2010,** 26, (6), 4027-4035.
8.   Chhatre, S. S.; Tuteja, A.; Choi, W.; Revaux, A. l.; Smith, D.; Mabry, J. M.; McKinley, G. H.; Cohen, R. E., Thermal Annealing Treatment to Achieve Switchable and Reversible Oleophobicity on Fabrics. *Langmuir* **2009,** 25, (23), 13625-13632.
9.   Choi, W.; Tuteja, A.; Chhatre, S.; Mabry, J. M.; Cohen, R. E.; McKinley, G. H., Fabrics with tunable oleophobicity. *Advanced Materials* **2009,** 21, (21), 2190-2195.
10.   Choi, W.; Tuteja, A.; Mabry, J. M.; Cohen, R. E.; McKinley, G. H., A Modified Cassie-Baxter Relationship to Explain Contact Angle Hysteresis and Anisotropy on Non-Wetting Textured Surfaces. *Journal of Colloid and Interface Science* **2009,** 339, (1), 208-216.
11.   Tuteja, A.; Choi, W.; Ma, M.; Mabry, J. M.; Mazzella, S. A.; Rutledge, G. C.; McKinley, G. H.; Cohen, R. E., Designing Superoleophobic Surfaces. *Science* **2007,** 318, (5856), 1618-1622.
12.   Tuteja, A.; Choi, W.; Mabry, J. M.; McKinley, G. H.; Cohen, R. E., Robust omniphobic surfaces. *Proceedings of the National Academy of Sciences, USA* **2008**, 18200-18205.
13.   Tuteja, A.; Choi, W.; McKinley, G. H.; Cohen, R. E.; Rubner, M. F., Design parameters for superhydrophobicity and superoleophobicity. *MRS Bulletin* **2008,** 33, (8), 752-758.
14.   Hoefnagels, H. F.; Wu, D.; deWith, G.; Ming, W., Biomimetic Superhydrophobic and Highly Oleophobic Cotton Textiles. *Langmuir* **2007,** 23, (26), 13158-13163.
15.   Leng, B.; Shao, Z.; de With, G.; Ming, W., Superoleophobic Cotton Textiles. *Langmuir* **2009,** 25, (4), 2456-2460.
16.   Marmur, A., From Hygrophilic to Superhygrophobic: Theoretical Conditions for Making High-Contact-Angle Surfaces from Low-Contact-Angle Materials. *Langmuir* **2008,** 24, (14), 7573-7579.
17.   Cassie, A.; Baxter, S., Wettability of porous surfaces. *Transactions of the Faraday Society* **1944,** 40, 546-551.
18.   Mabry, J.; Vij, A.; Iacono, S.; Viers, B., Fluorinated Polyhedral Oligomeric Silsesquioxanes (F-POSS). *Angewandte Chemie International Edition* **2008,** 47, (22), 4137-4140.

19.   Zisman, W. A., *Relation of the equilibrium contact angle to liquid and solid construction*. American Chemical Society, Washington DC: 1964.

20.   Owens, D. K.; Wendt, R. C., Estimation of the surface free energy of polymers. *Journal of Applied Polymer Science* **1969,** 13, (8), 1741-1747.

21.   Good, R. J., Surface free energy of solids and liquids: Thermodynamics, molecular forces, and structure. *Journal of Colloid and Interface Science* **1977,** 59, (3), 398-419.

22.   Good, R. J., Contact angle, wetting, and adhesion: a critical review. *Journal of Adhesion Science and Technology* **1992,** 6, 1269-1302.

23.   Iacono, S. T.; Vij, A.; Grabow, W.; Smith, D. W.; Jr; Mabry, J. M., Facile synthesis of hydrophobic fluoroalkyl functionalized silsesquioxane nanostructures. *Chemical Communications* **2007**, (47), 4992-4994.

24.   Goodwin, G. B.; Kenney, M. E. Novel Route to Ca8Si4O12Cl8 Alkosycyclotetrasiloxanes, Aryloxycyclotetrasiloxanes, Alkylcyclotetrasiloxanes and Arylcyclotetrasiloxanes from Wollastonite (CaSiO3). 4824985, 1989.

25.   Teng, C. J.; Cai, G.; Weber, W. P., Synthesis and characterization of octakis(3,3,3-trifluoropropyldimethylsiloxy)cyclotetrasiloxane (I), octakis[tridecafluoro-2,2,5,5-tetramethyl-2,5-disilatridecanoxy]cyclotetrasiloxane (II) and octakis(7-pentafluorophenyl-2,2,5,5-tetramethyl-2,5-disilaheptanoxy)cyclotetrasiloxane (III). *Journal of Fluorine Chemistry* **2004,** 125, (10), 1451-1455.

26.   Lentz, C. W., Silicate Minerals as Sources of Trimethylsilyl Silicates and Silicate Structure Analysis of Sodium Silicate Solutions. *Inorganic Chemistry* **1964,** 3, (4), 574-579.

27.   Bernett, M. K.; Zisman, W. A., WETTING PROPERTIES OF TETRAFLUOROETHYLENE AND HEXAFLUOROPROPYLENE COPOLYMERS1. *The Journal of Physical Chemistry* **1960,** 64, (9), 1292-1294.

28.   Bernett, M. K.; Zisman, W. A., Surface-chemical properties of highly fluorinated compounds containing oxygen in the aliphatic chain. *The Journal of Physical Chemistry* **1973,** 77, (19), 2324-2328.

29.   Ellison, A. H.; Fox, H. W.; Zisman, W. A., Wetting of Fluorinated Solids by Hydrogen-Bonding Liquids. *The Journal of Physical Chemistry* **1953,** 57, (7), 622-627.

30.   Ellison, A. H.; Zisman, W. A., Wettability Studies on Nylon, Polyethylene Terephthalate and Polystyrene. *The Journal of Physical Chemistry* **1954,** 58, (6), 503-506.

31.   Ellison, A. H.; Zisman, W. A., Wettability of Halogenated Organic Solid Surfaces. *The Journal of Physical Chemistry* **1954,** 58, (3), 260-265.

32.   Fox, H. W.; Hare, E. F.; Zisman, W. A., The spreading of liquids on low-energy surfaces. VI. Branched-chain monolayers, aromatic surfaces, and thin liquid films. *Journal of Colloid Science* **1953,** 8, (2), 194-203.

33.   Schulman, F.; Zisman, W. A., The spreading of liquids on low-energy surfaces. V. Perfluorodecanoic acid monolayers. *Journal of Colloid Science* **1952,** 7, (5), 465-481.

34.   Shafrin, E. G.; Zisman, W. A., EFFECT OF PROGRESSIVE FLUORINATION OF A FATTY ACID ON THE WETTABILITY OF ITS ADSORBED MONOLAYER. *The Journal of Physical Chemistry* **1962,** 66, (4), 740-748.

35.   Bernett, M. K.; Zisman, W. A., WETTING PROPERTIES OF ACRYLIC AND METHACRYLIC POLYMERS CONTAINING FLUORINATED SIDE CHAINS. *The Journal of Physical Chemistry* **1962,** 66, (6), 1207-1208.

36.   Fox, H. W.; Zisman, W. A., The spreading of liquids on low energy surfaces. I. polytetrafluoroethylene. *Journal of Colloid Science* **1950,** 5, (6), 514-531.

37.   Fox, H. W.; Zisman, W. A., The spreading of liquids on low-energy surfaces. II. Modified tetrafluoroethylene polymers. *Journal of Colloid Science* **1952,** 7, (2), 109-121.

38.   Fox, H. W.; Zisman, W. A., The spreading of liquids on low-energy surfaces. III. Hydrocarbon surfaces. *Journal of Colloid Science* **1952,** 7, (4), 428-442.

39.   Chaudhury, M. K., Interfacial interaction between low-energy surfaces. *Materials Science and Engineering: R: Reports* **1996,** 16, (3), 97-159.

40.   Girifalco, L. A.; Good, R. J., A Theory for the Estimation of Surface and Interfacial Energies. I. Derivation and Application to Interfacial Tension. *The Journal of Physical Chemistry* **1957,** 61, (7), 904-909.

41.   Good, R. J.; Girifalco, L. A., A THEORY FOR ESTIMATION OF SURFACE AND INTERFACIAL ENERGIES. III. ESTIMATION OF SURFACE ENERGIES OF SOLIDS FROM CONTACT ANGLE DATA. *The Journal of Physical Chemistry* **1960,** 64, (5), 561-565.

42.   Van Oss, C. J.; Chaudhury, M. K.; Good, R. J., Interfacial Lifshitz-van der Waals and polar interactions in macroscopic systems. *Chemical Reviews* **1988,** 88, (6), 927-941.

43.   Van Oss, C. J.; Good, R. J.; Chaudhury, M. K., Additive and nonadditive surface tension components and the interpretation of contact angles. *Langmuir* **1988,** 4, (4), 884-891.

44.   Johnson, R. E.; Dettre, R. H., *Wetting of Low-Energy surfaces*. Marcel Dekker: New York, 1993; p 1-74.

45.   Nishino, T.; Meguro, M.; Nakamae, K.; Matsushita, M.; Ueda, Y., The Lowest Surface Free Energy Based on -CF3 Alignment. *Langmuir* **1999,** 15, (13), 4321-4323.

46.   Volpe, C. D.; Siboni, S., Some Reflections on Acid-Base Solid Surface Free Energy Theories. *Journal of Colloid and Interface Science* **1997,** 195, (1), 121-136.

47.   Van Oss, C. J., *Interfacial Forces in Aqueous Media*. Marcel Dekker, Inc.: New York, 1994; p 18-45.

48.   Shalel-Levanon, S.; Marmur, A., Validity and accuracy in evaluating surface tension of solids by additive approaches. *Journal of Colloid and Interface Science* **2003,** 262, (2), 489-499.

49.   Lemal, D. M., Perspective on Fluorocarbon Chemistry. *The Journal of Organic Chemistry* **2004,** 69, (1), 1-11.

50.   O'Hagan, D., Understanding organofluorine chemistry. An introduction to the C-F bond. *Chemical Society Reviews* **2008,** 37, (2), 308-319.

7 Oleophobic army fabrics

In this chapter, previously developed design parameter framework is used to a priori predict and enhance the non-wettability of army combat uniform fabrics. The chapter is divided in two parts – (a) applying the design framework to various textile fabrics supplied by the US Army Natick Soldier Research, Development, and Engineering Center (NSRDEC), (b) evaluating different periodic topographic models and to see whether these models can be applied to army fabrics.

The army fabrics were coated using the following protocol. Prepare a 50 – 50 fluorodecyl POSS (1*H*,1*H*,2*H*,2*H*-heptadecafluorodecyl silsesquioxane) – Tecnoflon (BR 9151, a fluoro-elastomer from Solvay Solexis) solution (total solids = 10 mg/ml) in Asahiklin solvent. Dip the fabric in the solution for about 10 minutes. Air-dry the fabric to remove solvent. Then keep it in a vacuum oven for 30 minutes at 60° C to ensure that all the solvent has evaporated.

7.1 Oleophobic ECWCS fabric

The ECWCS fabric (SEM image shown in Figure 7-1(b)) was dip-coated with 50% POSS – 50% Tecnoflon solution and then contact angle measurements were performed for a series of liquids from water (γ_{lv} = 72.1 mN/m), ethylene glycol (γ_{lv} = 47.7) rapeseed oil (γ_{lv} = 35.5), hexadecane (γ_{lv} = 27.5), dodecane (γ_{lv} = 25.3) and decane (γ_{lv} = 23.8) (results summarized in Table 7-1). A piece of dip-coated oleophobic ECWCS fabric with various liquid droplets (colored using food dyes) is shown in Figure 7-1(a). Water droplets formed high apparent contact angles (θ_{adv}^* = 142 ± 4° and θ_{rec}^* = 117 ± 7°) on the ECWCS fabric dip-coated with 50% POSS – 50% Tecnoflon. For an idealized cylindrical texture, the spacing ratio is given by $D^* = (R + D)/R$, where R is the radius of the cylindrical texture and $2D$ is the inter-cylinder spacing. The apparent

contact angle for a liquid droplet in solid-liquid-air composite interface is given by the Cassie-Baxter (CB) relation. For 1D cylindrical texture, the CB relation can be written as[1-6] –

$$\cos \theta^* = -1 + \frac{1}{D^*}\left[(\pi - \theta_E)\cos \theta_E + \sin \theta_E\right] \qquad (7\text{-}1)$$
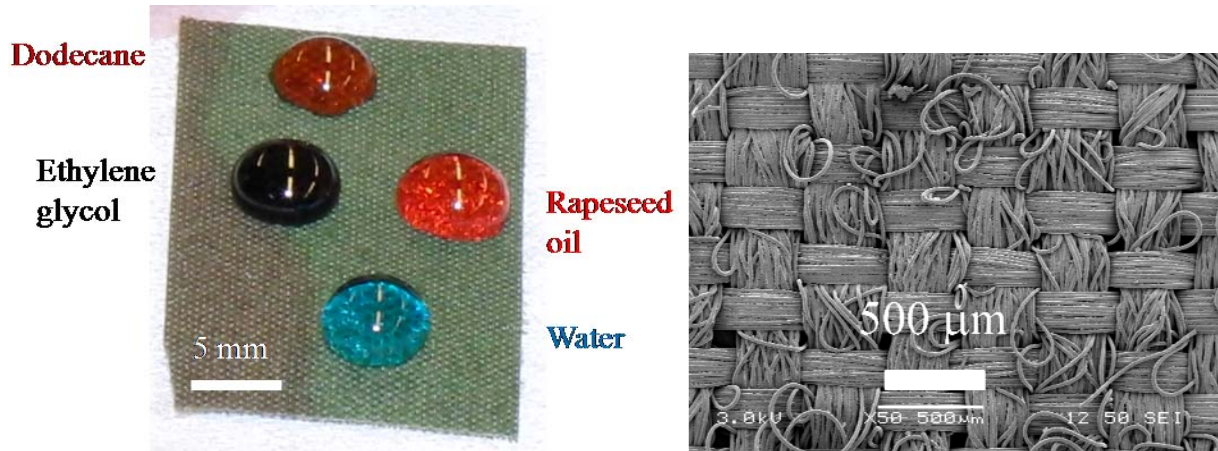
Figure 7-1(a) Droplets of water ($\gamma_{lv} = 72.1$ mN/m), ethylene glycol ($\gamma_{lv} = 47.7$ mN/m), rapeseed oil ($\gamma_{lv} = 35.5$ mN/m), and dodecane ($\gamma_{lv} = 25.3$ mN/m) form robust composite interfaces on the ECWCS fabric dip-coated with 50% POSS – 50% Tecnoflon. (b) SEM micrograph of the uncoated ECWCS fabric showing the bundles and individual fibers of the fabric.
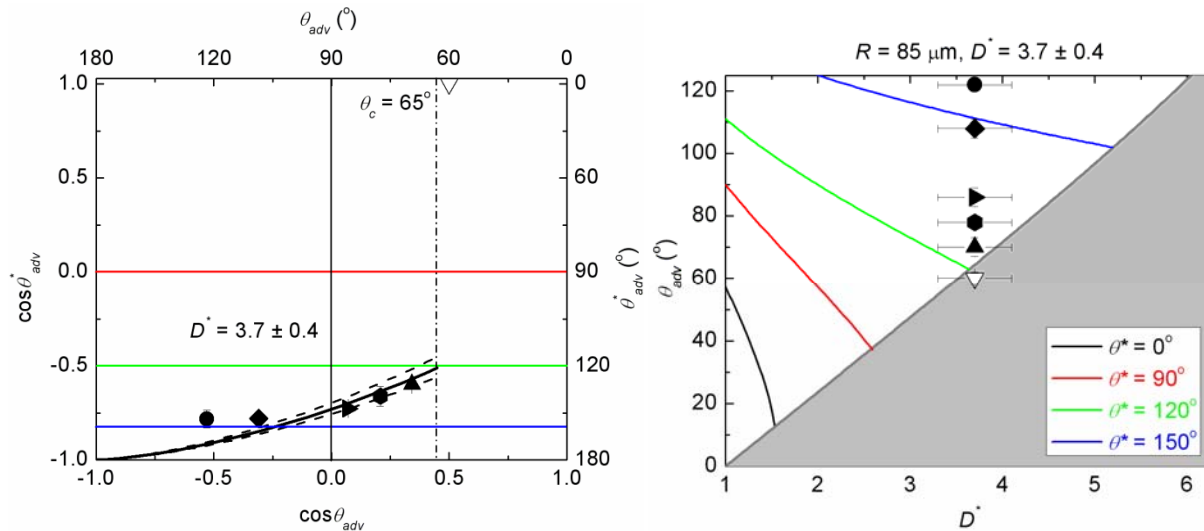
Figure 7-2. (a) Generalized wetting diagram and (b) the design chart for wettability for liquid droplets on 50% POSS – 50% Tecnoflon coated ECWCS fabrics. A wide range of probing liquids from water to dodecane form a robust composite interface on the dip-coated fabric surface whereas lower surface tension liquids like decane wet the fabric. The effective dimensionless spacing ratio (D*) and effective length scale (R) are extracted to be 3.7 ± 0.4 and 85 μm respectively.

Table 7-1. Apparent advancing (θ^*_{adv}) and receding contact angles (θ^*_{rec}) on 50% POSS – 50% Tecnoflon coated ECWCS fabric for liquid droplets with a wide range of surface tensions are listed in the following table.

Liquid	Surface tension γ_{lv} (mN/m)	Apparent advancing contact angle θ^*_{adv} (°)	Apparent receding contact angle θ^*_{rec} (°)
Water	72.1	142 ± 4	117 ± 7
Ethylene glycol	47.7	141 ± 3	118 ± 4
Rapeseed oil	35.5	137 ± 1	106 ± 2
Hexadecane	27.5	132 ± 4	94 ± 14
Dodecane	25.3	126 ± 2	86 ± 5
Decane	23.8	≈ 0	≈ 0

From the values of advancing contact angle on flat (θ_{adv}) and textured dip-coated fabric surface (θ^*_{adv}), the effective spacing ratio was found by regression to be $D^* = 3.7 \pm 0.4$ (Figure 7-2(a)).

The contours of the apparent contact angle (θ^*) for ($\theta^* = 0$ (——), 90 (——), 120 (——) and 150° (——)) are plotted on the design chart (Figure 7-2(b)) with the equilibrium contact angle on a chemically identical smooth surface (θ_E) and the spacing ratio (D^*) as the two axes. The dimensionless robustness factor (A^*) compares the ratio of the breakthrough pressure (P_b) to a reference pressure ($P_{ref} = 2\gamma_{lv} / \ell_{cap}$), where ℓ_{cap} is the capillary length ($\ell_{cap} = \sqrt{\gamma_{lv} / \rho g}$), γ_{lv} is the liquid surface tension and ρg is the specific weight. The reference pressure (P_{ref}) is close to the minimum pressure differential across a millimetric scale liquid droplet; therefore is a necessary condition for the existence of a robust composite interface. For an array of cylinders with radius R and inter-cylinder spacing $2D$, the robustness factor (A^*) can be calculated using the following expression[1, 2, 5] –

$$A^* = \frac{P_b}{P_{ref}} = \frac{\ell_{cap}}{R(D^* - 1)} \left[\frac{(1 - \cos\theta_E)}{(D^* - 1 + 2\sin\theta_E)} \right] \qquad (7\text{-}2)$$

The robustness factor is a function of the equilibrium contact angle on a chemically identical smooth surface (θ_E), the geometrical spacing ratio (D^*) introduced above, and the ratio of

capillary length (ℓ_{cap}) to the feature length-scale (R) of the solid's surface texture. Values of $A^* \leq$ 1 (grey shaded region in Figure 7-2(b)) indicate that a drop sitting on the composite fibrous surface will spontaneously transition to a fully-wetted interface.

7.2 Oleophobic Nomex / Kevlar / P-140 fabric

A similar procedure was repeated for the Kevlar / Nomex / P140 fabric and the contact angle results are summarized in Table 7-2. For the Kevlar Nomex fabric (shown in Figure 7-3), the spacing ratio was found to be $D^* = 4.5 \pm 0.4$ and the effective length scale, $R = 35$ μm. Therefore the period of the cylindrical texture L (= $2RD^*$) was found to be 315 ± 30 μm, which is consistent with the SEM micrograph shown in Figure 7-4(b).
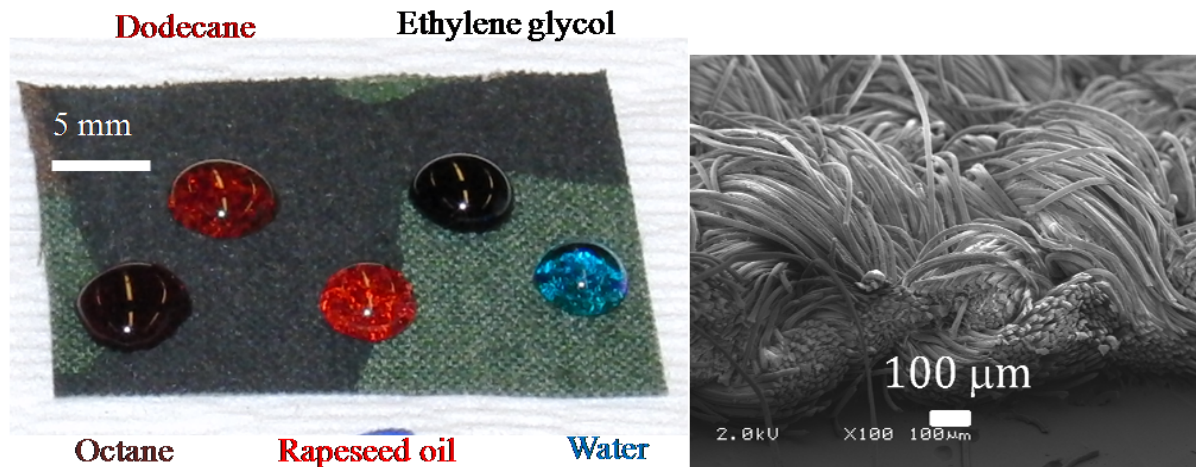
Figure 7-3. Droplets of water (γ_{lv} = 72.1 mN/m), ethylene glycol (γ_{lv} = 47.7 mN/m), rapeseed oil (γ_{lv} = 35.5 mN/m), dodecane (γ_{lv} = 25.3 mN/m), and octane (γ_{lv} = 21.6 mN/m) form robust composite interfaces on the ECWCS fabric dip-coated with 50% POSS – 50% Tecnoflon. (b) SEM micrograph of the uncoated 92% Nomex / 5% Kevlar / 3% P-140 fabric showing the bundles and individual fibers of the fabric.
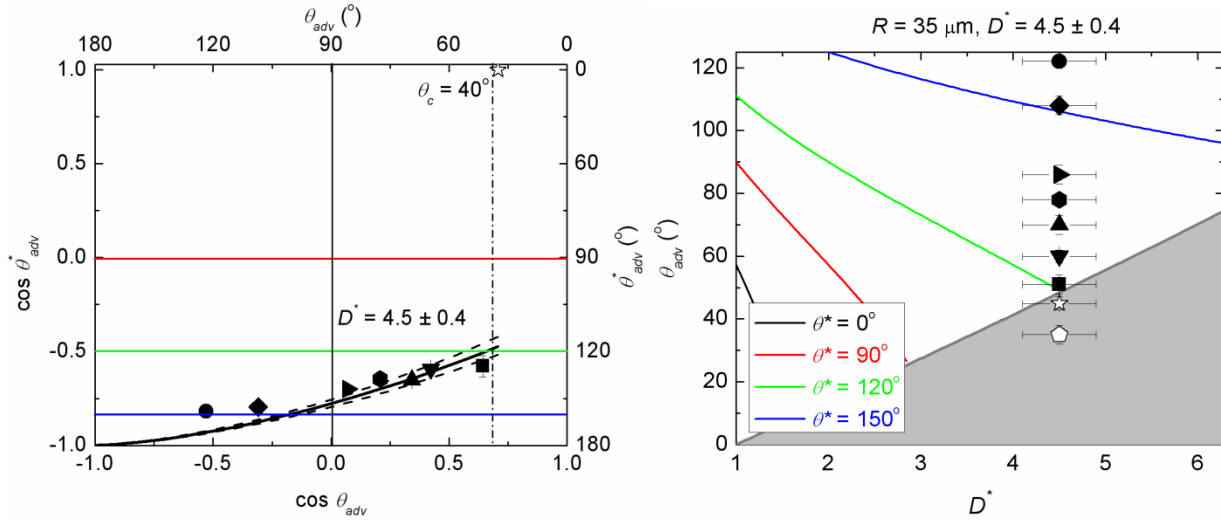
Figure 7-4. (a) Generalized wetting diagram and (b) the design chart for wettability for liquid droplets on 50% POSS – 50% Tecnoflon coated 92% Nomex / 5% Kevlar / 3% P-140 fabrics. A wide range of probing liquids from water to octane form a robust composite interface on the dip-coated fabric surface whereas lower surface tension liquids like heptane wet the fabric. The effective dimensionless spacing ratio (D^*) and effective length scale are extracted to be 4.5 ± 0.4 and 35 μm respectively.

Table 7-2. Apparent advancing (θ^*_{adv}) and receding contact angles (θ^*_{rec}) on 50% POSS – 50% Tecnoflon coated Nomex / Kevlar / P-140 fabric for liquid droplets with a wide range of surface tensions are listed in the following table.

Liquid	Surface tension γ_{lv} (mN/m)	Advancing contact angle θ^*_{adv} (°)	Receding contact angle θ^*_{rec} (°)
Water	72.1	145 ± 1	133 ± 6
Ethylene glycol	47.7	143 ± 3	122 ± 3
Rapeseed oil	35.5	137 ± 1	106 ± 2
Hexadecane	27.5	130 ± 3	110 ± 7
Dodecane	25.3	130 ± 1	96 ± 4
Decane	23.8	127 ± 2	96 ± 10
Octane	21.6	125 ± 4	76 ± 4
Heptane	20.1	≈ 0	≈ 0

Kawase et. al. proposed four new models to explain the wettability of woven meshes, namely (1) hole model, (2) cross model, (3) plane model, and (4) modified plane model.[7] The geometric illustration of these models is shown in Figure 7-6. The wettability of the above mentioned model textured surfaces can be understood by plotting corresponding design charts, where the

145

variation of θ^* in terms of θ_E and D^* is plotted. These design charts for hole, cross and plane model are plotted in Figure 7-7, Figure 7-8, and Figure 7-9 respectively.

7.3 Refinement of the 1D cylinder model
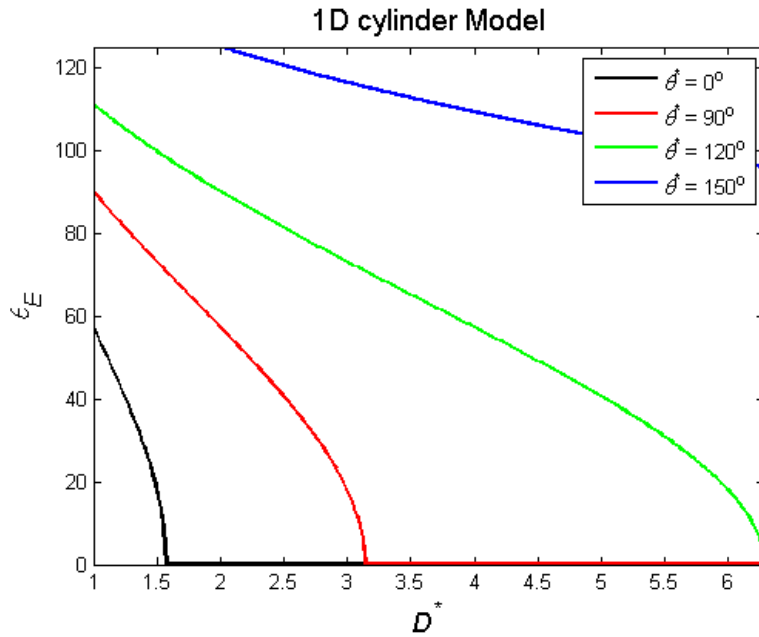
Figure 7-5. Variation of the apparent contact angle (θ^*) in terms of equilibrium contact angle (θ_E) and a spacing ratio (D^*) is plotted for a 1D cylinder model. The four contours are for apparent contact angles of 0, 90, 120, and 150° respectively.
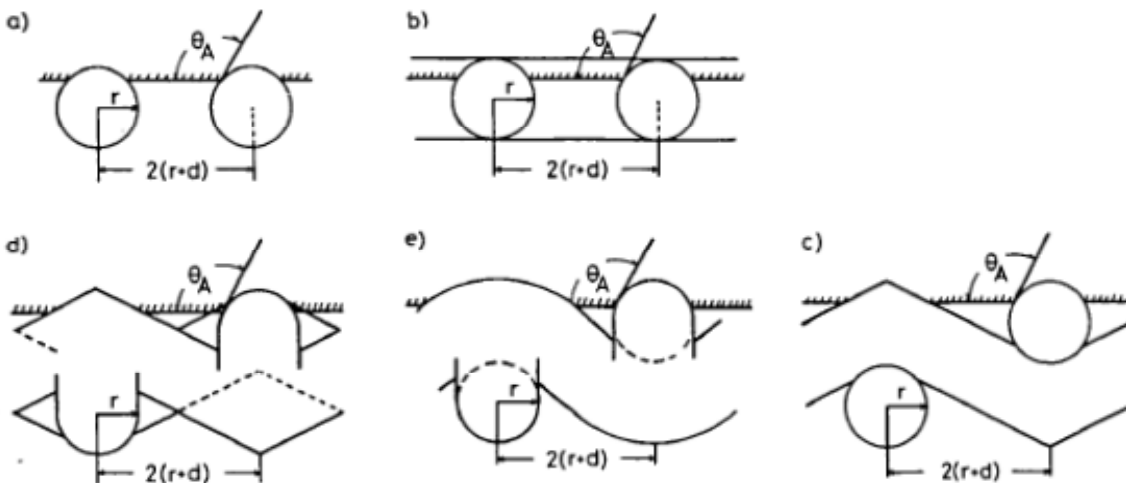
Figure 7-6. Schematic illustrations of proposed models for mesh screens: (a) Cassie-Baxter model, (b) hole model, (c) cross model, (d) plane model, and (e) modified plane model.[7]

146
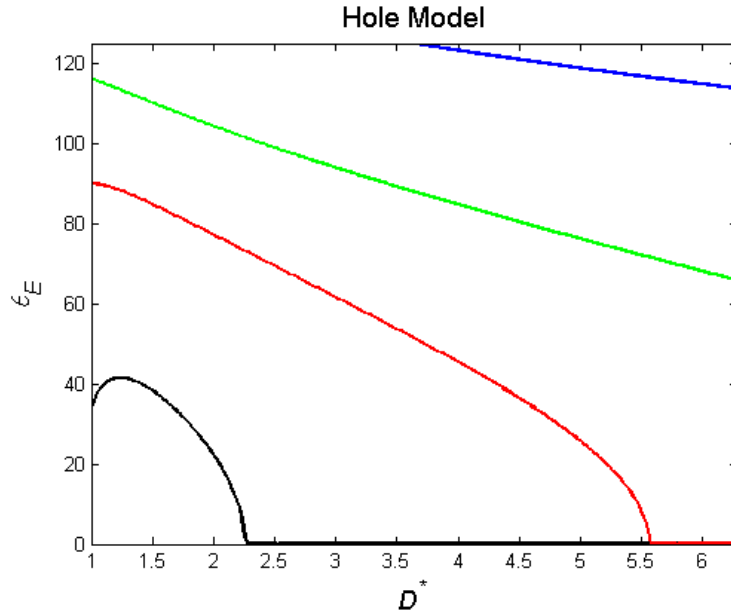
Figure 7-7. Variation of the apparent contact angle (θ^*) in terms of equilibrium contact angle (θ_E) and a spacing ratio (D^*) is plotted for a hole model. The four contours are for apparent contact angles of 0, 90, 120, and 150° respectively.
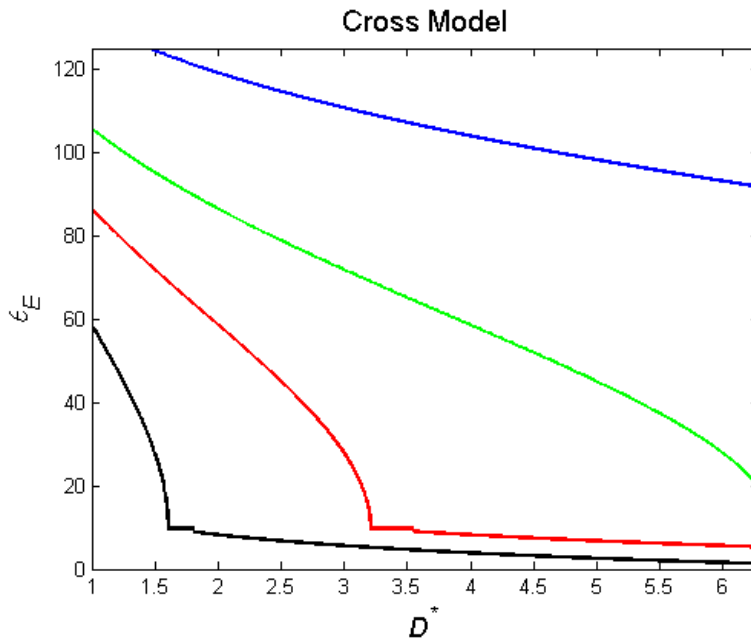
Figure 7-8. Variation of the apparent contact angle (θ^*) in terms of equilibrium contact angle (θ_E) and a spacing ratio (D^*) is plotted for a cross model. The four contours are for apparent contact angles of 0, 90, 120, and 150° respectively.

The legends in Figure 7-7, Figure 7-8, and Figure 7-9 are identical to the legend in Figure 7-5,

therefore they are omitted in the later figures. It is very clear that all four models show similar

147

qualitative dependence of θ^* on θ_E and D^*, *i.e.* the apparent contact angle (θ^*) increases as the equilibrium contact angle (θ_E) or the spacing ratio (D^*) increases. For the hole model (Figure 7-7), in the region of low θ_E and low D^*, the apparent contact angle (θ^*) seems to increase as the spacing ratio (D^*) decreases, which is an unphysical result. Finally, the apparent kinks in the contour lines are artifacts due to numerical technique employed to solve the implicit equations.
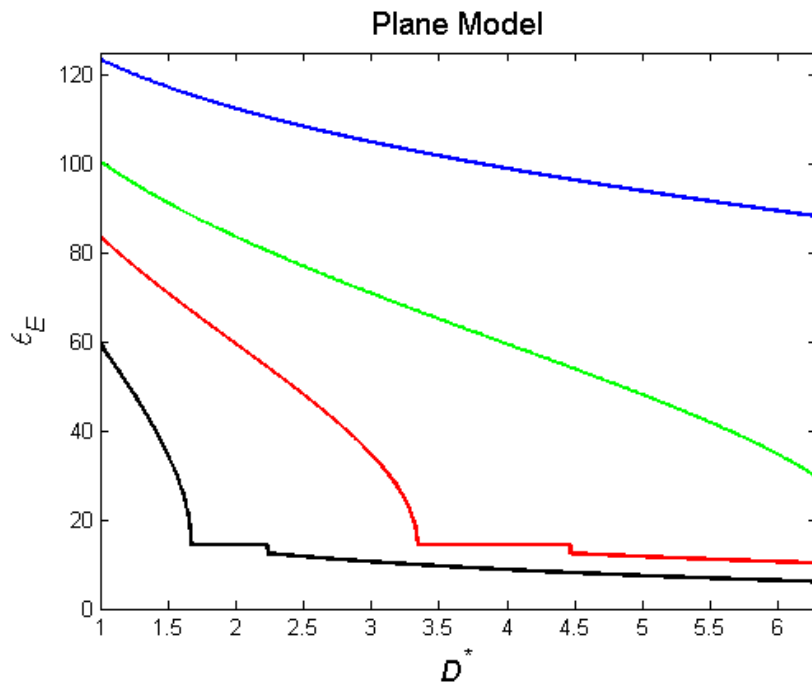
Figure 7-9. Variation of the apparent contact angle (θ^*) in terms of equilibrium contact angle (θ_E) and a spacing ratio (D^*) is plotted for a cross model. The four contours are for apparent contact angles of 0, 90, 120, and 150° respectively.

In the above figures, the variation of the apparent contact angles (θ^*) on some of the model textured surfaces is summarized. Qualitatively, all four models behave similarly in terms of the variation of the apparent contact angle. Therefore, the 1-D cylindrical model was retained as the preferred model for this analysis.

In this chapter, two Army Uniform Fabrics were dip-coated and rendered oleophobic. The design parameter helped to predict and quantify the non-wettability. A fabric with smaller characteristic

148

length scale (either bundle or individual fiber radius R), tight weave (small D*), coated with a non-wetting coating (high θ_{adv}) will lead to high apparent contact angles (θ^*) for droplets of low surface tension liquids.

7.4 References

1.   Chhatre, S. S.; Tuteja, A.; Choi, W.; Revaux, A.; Smith, D.; Mabry, J. M.; McKinley, G. H.; Cohen, R. E., Thermal annealing treatment to achieve switchable and reversible oleophobicity on fabrics. *Langmuir* **2009,** In Press.

2.   Choi, W.; Tuteja, A.; Chhatre, S.; Mabry, J. M.; Cohen, R. E.; McKinley, G. H., Fabrics with tunable oleophobicity. *Advanced Materials* **2009,** 21, (21), 2190-2195.

3.   Michielsen, S.; Lee, H. J., Design of a Superhydrophobic Surface Using Woven Structures. *Langmuir* **2007,** 23, (11), 6004-6010.

4.   Tuteja, A.; Choi, W.; Ma, M.; Mabry, J. M.; Mazzella, S. A.; Rutledge, G. C.; McKinley, G. H.; Cohen, R. E., Designing Superoleophobic Surfaces. *Science* **2007,** 318, (5856), 1618-1622.

5.   Tuteja, A.; Choi, W.; Mabry, J. M.; McKinley, G. H.; Cohen, R. E., Robust omniphobic surfaces. *Proceedings of the National Academy of Sciences, USA* **2008**, 18200-18205.

6.   Tuteja, A.; Choi, W.; McKinley, G. H.; Cohen, R. E.; Rubner, M. F., Design parameters for superhydrophobicity and superoleophobicity. *MRS Bulletin* **2008,** 33, (8), 752-758.

7.   Kawase, T.; Fujii, T.; Minagawa, M., Repellency of Textile Assemblies: Part I: Apparent Contact Angle of Wax-Coated Monofilament Mesh Screen. *Textile Research Journal* **1987,** 57, (4), 185-191.

8 A goniometric microscope to quantify feather structure, wettability, and robustness to liquid penetration

8.1 Introduction

Birds in the cormorant family routinely dive in water up to tens of meters for food and are known to subsequently dry their wings by spreading them in sunlight for extended periods of time. Noting this behavior, researchers have attempted to correlate the wing spread phenomena to the structure of bird feathers, with notable efforts for the cormorant and darter, but there is a lack of consensus.[1-3] Rijke correlated the two by reporting on the wing-spreading behaviors of cormorants and studying feather barbs and barbules, which he characterized by applying an idealized cylindrical model to feather texture. [1]

Bird feathers have cylindrically shaped barbs and barbules that emerge from the main shaft of the feather, as shown in Figure 8-3(a). Rijke employed optical microscopy and photography to measure barb spacing, *2D*, and diameter, *2R*, from which he calculated a spacing ratio $D^* = (R + D)/R$ for various bird species.[1] In previous literature, researchers have argued both in favor of and against a correlation between D^* for the feathers and diving, swimming, and wing-spreading behavior. [4-7] Past studies have relied on photographic and microscopic techniques in attempts to characterize feather structure and wettability.[1, 3-5, 8, 9]

Analysis of Feather structure using microscopy is complicated

An array of parallel cylinders is typically considered as a simplistic model of a bird feather. Even for such a simple model, accurate estimation of the cylinder radius and spacing is key for predicting feather wettability. However, feather structures are complicated and hierarchical, as shown in Figure 8-1 and Figure 8-2 for wing feathers of African Darter and Common Shelduck

respectively. Features generally contain a main shaft (rachis), barbs (ramus) that branch out of the main shaft and barbules that extend from the barbs and often form an interlocking microstructure. Barbules compose the majority of the surface area in these bird feathers. Due to such complex nature of the feather topography as viewed in photographed images it is difficult if not impossible to select appropriate representative values of spacing (2D) and diameter (2R) in order to apply the simple cylindrical model. SEM evaluations at different spots on the feathers and at different magnifications to determine R and D from images are time consuming and the inherent texture might get damaged due to long exposure to high energy electron beam.[4]
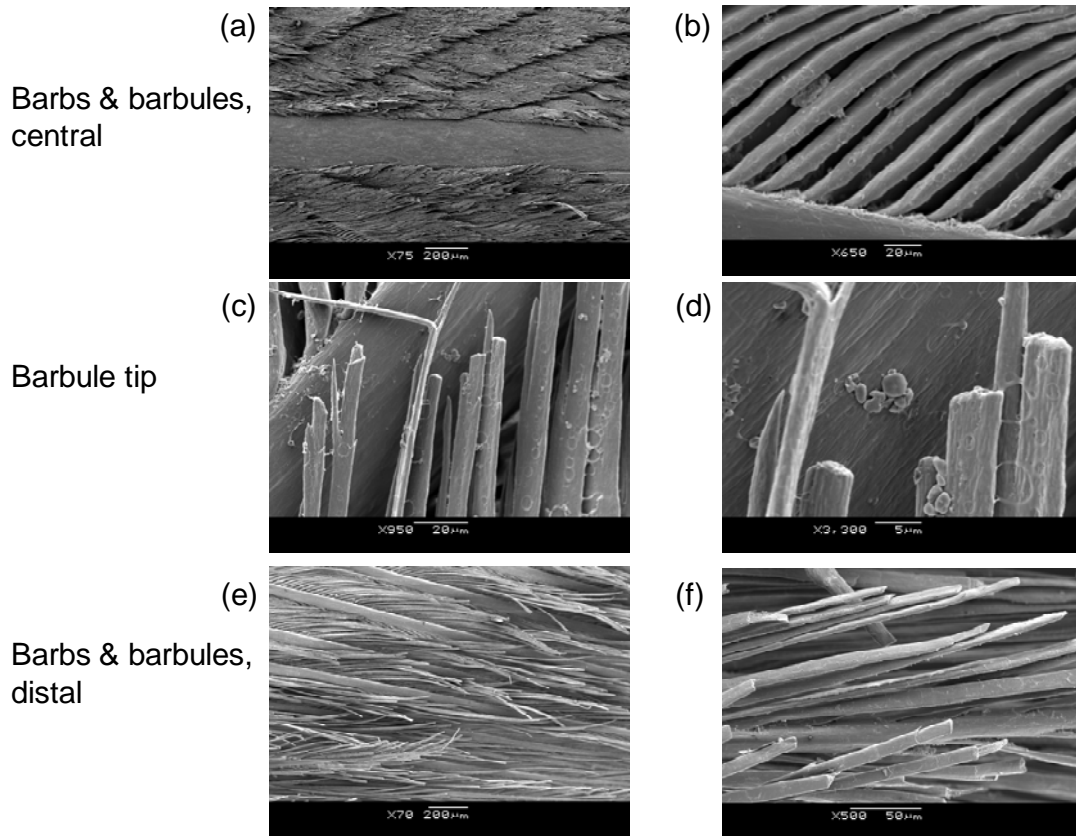
Figure 8-1. Scanning electron micrographs for the topography of a wing feather of an African Darter are shown. Pair of images at different magnifications for the central (a), (b), tip (c), (d) and distal part (e), (f) of the feather indicate the complexity and hierarchical nature of its texture.

(a) Barbs & barbules, central

(b)

(c) Barbule tip

(d)

(e) Barbs & barbules, distal

(f)
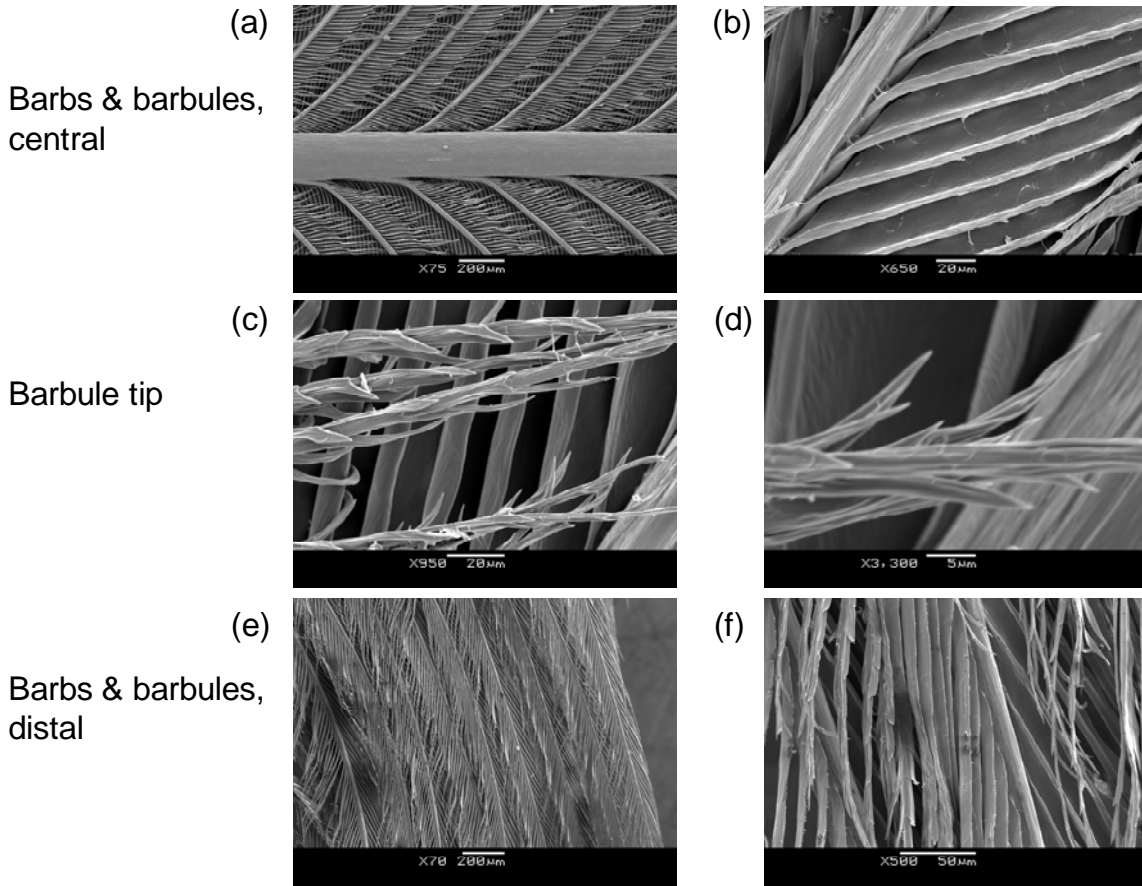
Figure 8-2. Scanning electron micrographs for the topography of a wing feather of Common Shelduck are shown. Pair of images at different magnifications for the central (a), (b), tip (c), (d) and distal part (e), (f) of the feather indicate the complexity and hierarchical nature of its texture.

A second complication arises due to imperfections or defect in feather topography. Even if a careful microscopic analysis is conducted, one might miss a defect on a feather, and this defect will trigger wetting of such feather. Therefore, microscopic analysis might lead to erroneous predictions for apparent contact angles (θ^*_{adv} and θ^*_{rec}) and breakthrough pressure. A third shortcoming is that SEM analysis is based on either a top view or a side view of a feather; therefore it is inherently two dimensional. But, wetting of a bird feather is a three dimensional phenomenon, as indicated by the shape of the contact line in Figure 8-3. Moreover, the location and curvature of the contact line changes as either the surface tension of the probing liquid (γ_{lv}) or the applied pressure differential across the air-liquid interface (ΔP) is altered.

(a)

(b) Water, $\Delta P = 0$ Pa

(e) Ethylene glycol, $\Delta P = 0$ Pa

(c) Water, $\Delta P = 80$ Pa

(f) Hexadecane, $\Delta P = 0$ Pa

(d) Water, $\Delta P = 160$ Pa

(g) Octane, $\Delta P = 0$ Pa
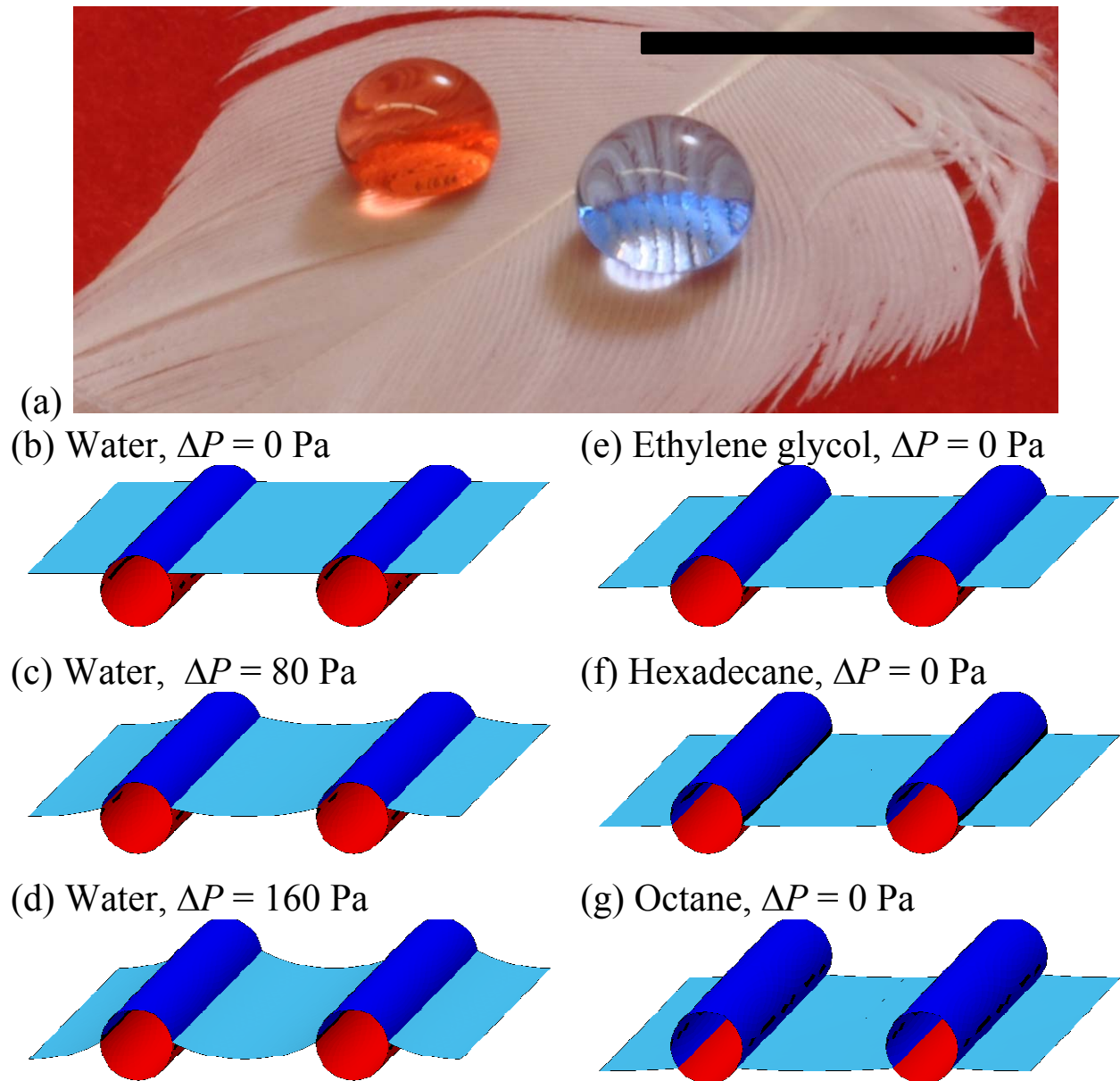
Figure 8-3. (a) A wing feather of a common shelduck after dip-coating in 50-50 fluorodecyl POSS/Tecnoflon solution is not wetted by water (γ_{lv} = 72.1 mN/m, colored blue), or rapeseed oil (γ_{lv} = 35.5 mN/m, colored red). The scale bar in the figure corresponds to 1 cm. A surface evolver simulation of the wetting phenomena of a bird feather by liquids is shown. As the pressure differential across the air-water interface increases from (b) zero, (c) 80 Pa, and (d) 160 Pa, higher and higher fraction of the solid texture is wetted by water. The response of the same feather in contact with (e) ethylene glycol (γ_{lv} = 44 mN/m, θ_{adv} = 100°), (f) hexadecane (γ_{lv} = 27.5 mN/m, θ_{adv} = 80°), and (g) octane droplet (γ_{lv} = 21.6 mN/m, θ_{adv} = 60°) with negligibly small pressure differential is depicted.

So, a single SEM image cannot be used to predict wetting both by water droplets and octane droplets or wetting as a function of diving depth. A method that can systematically probe feathers in a sequentially aggressive manner would be ideal for this purpose.

8.2 A wetting-based surface characterization of bird feathers

On a smooth, chemically homogeneous surface, a liquid droplet exhibits a contact angle at equilibrium (θ_E) given by Young's relation $\cos \theta_E = (\gamma_{sv} - \gamma_{sl})/\gamma_{lv}$, where γ is the pair wise interfacial tension between the solid (s), liquid (l) and vapor (v) phases.[10] The equilibrium contact angle (θ_E) depends strongly on the molecular architecture of the three phases and their mutual interactions. On rough surfaces, both surface chemistry and surface topography influence the wetting and the apparent contact angles (θ^*) that a liquid droplet manifests. On rough surfaces, liquid droplets can exhibit one of the following two states – (i) either a composite state (Cassie-Baxter state) where the droplets partially rest on the solid elements and partially on the trapped air pockets between the asperities (Figure 8-3(a)), or (ii) a fully-wetted state (Wenzel state) where the droplets wet and penetrate the topography of the surface.[11, 12] Therefore, the topographical details of the feathers are critical in determining whether a bird will be wetted by the water that it is diving into.[1, 3, 13]

The natural oils secreted from the uropygial glands of birds are typically hydrophobic. So a combination of an inherently hydrophobic surface with numerous packets of trapped air lead to water repellent feathers.[14] In a solid-liquid-air non-wetting composite state for a droplet on a feather, tiny air pockets are trapped within the barbules of bird feathers. These air pockets appear shiny when under a liquid and they are called a plastron (as shown in Figure 8-3(a) for water and oil droplets). Apart from decreasing the tendency to wet, a plastron layer around the plumage

provides insulation and ensures adequate thermoregulation. The air layer also provides additional buoyancy to aquatic birds. A plastron-like air layer is also used by aquatic insects to hide from predators, for mating, or for providing a safe habitat for their young.[15-22]

Water has a relatively higher surface tension (γ_{lv} = 72.1 mN/m); therefore, it has a high equilibrium contact angle on the coating chemistry of the bird feathers (θ_E ~ 60 – 115°).[1] As a result, water wets only a small portion at the top of the cylindrical elements of the feather texture, as shown in Figure 8-3(b). Consider a water droplet sitting on cylindrically textured surface in Figure 8-3(b). Here, the pressure differential across the air-liquid interface is negligible, so the interface is flat. At every location on the triple phase contact line, Young's relation is satisfied, and therefore the triple phase contact line is above the equator of the texture elements.

As more and more pressure is applied, a higher and higher fraction of the solid texture is wetted by water (shown in Figure 8-3(c) and (d) for ΔP = 80 and 160 Pa respectively). At high pressure differentials, the portion underneath the equator of the solid texture, *i.e.* the re-entrant texture, is also wetted.[23-27] Note that Young's relation is still valid, however, and the air-liquid interface assumes a curvature so as to support the pressure differential and therefore the location of the contact line changes. So, the same liquid probes the surface in a sequentially aggressive manner with increasing pressure differential. When a bird dives in water, its feathers are subjected to increasing pressures, and the response is expected to follow the sequence of images in Figure 8-3(b) to (d).

When the same feather is exposed to a droplet of lower surface tension liquids like ethylene glycol (γ_{lv} = 44 mN/m, Figure 8-3(e)), hexadecane (γ_{lv} = 27.5 mN/m, Figure 8-3(f)), or octane (γ_{lv}

= 21.6 mN/m, Figure 8-3(g)), the position of the triple phase contact line is much lower on the texture elements due to low equilibrium contact angles of these probing liquids. Even under a negligibly small pressure differential across the air-liquid interface, these liquids sit much lower on the texture and the propensity to sag and wet the underlying surface is much greater.[23, 24] A close correspondence between the two sets of images, i.e. probing the feather with water at increasing pressure and probing the feather with lower liquid surface tension, indicate that the feather behaves similarly under the two scenarios. Therefore, the wetting of a bird feather during diving can be characterized by probing it with a series of successively lower surface tension liquids. Direct experimental reports studying the effect of liquid surface tension on whole birds are scarce, and difficult to carry out.[28, 29] However, probing individual feathers with liquid droplets is a simple and effective alternate to dipping whole birds in pools of probing liquids.

In this work, we present an approach to quantitatively characterize bird feathers and other textured surfaces by performing contact angle measurements using a set of probing liquids. The main objectives of the work are (i) to quantify the wetting aspects of the hierarchical topography of a bird feather in terms of simple parameters, (ii) to predict whether a fully-wetted interface or a solid-liquid-air composite interface represents the global equilibrium state for liquid droplets on feathers, (iii) to predict the apparent contact angle (θ^*) for a liquid droplet, and (ii) the threshold pressure (or depth) at which the structure of the feather will be fully wetted by the surrounding liquid.

In this study, we focus primarily on wing feathers, as those are relevant during diving and wing spreading phenomena. We focus on contact angle measurements on single feathers that will potentially help us to screen bird species for whole plumage experiments. We propose a systematic approach to characterize bird feathers by measuring contact angles with a series of

probing liquids. As described in detail below, we employ a dip-coating technique to extent the range of liquid surface tension that does not wet the bird feathers. From these data, we extract an effective spacing ratio and effective length scale of the cylindrical texture, parameters that completely characterize the wetting aspects of the feather texture. Finally, we seek to elucidate the correlation between the details of feather texture and the behavioral response of these birds. Analysis of bird feather texture using visual techniques like photography and microscopy is tedious and subjective. Whereas, the method proposed here is based on apparent advancing contact angle measurements, which are expected to be less subjective than microscopy.

8.3 Experimental Procedure

Collection of bird feathers

The wing feathers studied in this work came from six different species of aquatic birds, three from the same *Phalacrocoracidae* family: the reed cormorant, the great cormorant, and the European shag. The remaining species each come from distinct families and were chosen because of their diving and feather-drying behavior. These three other species are: the African darter, the common shelduck, and the mallard. Feather samples from twelve birds from six species were furnished by the Natural History Museum (NHM), London, UK. No birds were sacrificed specifically for this study. After pruning, wing, breast, and belly feathers of these birds were available (shown in Figure 8-4). As a representative of the bird plumage, wing feathers were chosen for wettability characterization in this work.

Coating protocol

Fluorodecyl POSS (polyhedral oligomeric silsesquioxane) molecules consist of silsesquioxane cages surrounded by eight $1H,1H,2H,2H$-heptadecafluorodecyl groups.[30]

(a) Reed or long-tailed cormorant
(*Phalacrocorax africanus*)

(b) Great cormorant (*Phalacrocorax carbo*)

(c) European shag (*Phalacrocorax aristotelis*)

(d) African darter (*Anhinga rufa*)
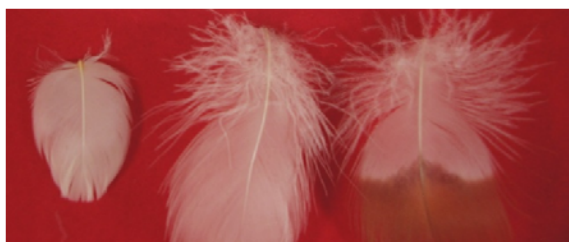
(c) Common shelduck (*Tadorna tadorna*)
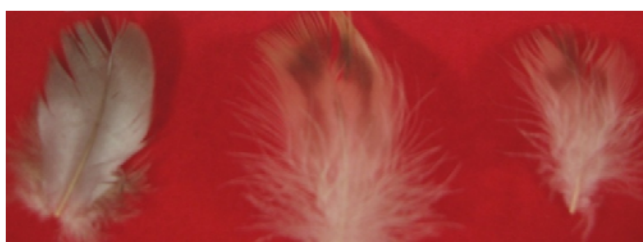
(f) Mallard / wild duck (*Anas platyrhynchos*)

Figure 8-4. Optical photographs of wing, breast, and belly feathers for the six bird species - **(a)** reed cormorant, **(b)** great cormorant, **(c)** European shag, **(d)** African darter, **(e)** common shelduck, and **(f)** mallard are shown respectively. Feathers are typically 2 to 3 cm in length and wing feathers (leftmost among the three feathers) are typically less fluffy than breast and belly feathers (middle and right feather respectively).

Due to the high density of perfluorinated carbon atoms present in the eight alkyl chains surrounding the silsesquioxane cages, a smooth fluorodecyl POSS surface has one of the lowest solid-surface energy values reported to date ($\gamma_{sv} \approx 10$ mN/m). Similar to our earlier experience with woven fabrics and meshes, we were able to confer the feathers with thin, uniform, flexible, and conformal coatings of fluorodecyl POSS mixed with a commercially available Tecnoflon® fluoroelastomer (BR 9151, Solvay Solexis, $\gamma_{sv} \approx 18$ mN/m). Asahiklin AK225 (Asahi Glass Company) was used as the solvent for fluorodecyl POSS and Tecnoflon. Silicon wafer substrates

were spin-coated with a POSS−Tecnoflon solution (50–50 by weight, total solids 10 mg/mL, γ_{sv} = 10.7 mN/m) at a rotation speed of 900 rpm for 30 s. The bird feathers were dip-coated in an identical POSS −Tecnoflon solution for 5 min. Later, the samples were removed and dried in air to ensure complete evaporation of the Asahiklin solvent.

Contact angle measurements

Contact angle measurements and sliding angle measurements were obtained with a Ramé-Hart 590-F1 goniometer. Advancing and receding contact angles were measured using ~5 μL (~ 2 to 3 mm diameter) droplets of various liquids (purchased from Aldrich and used as received). At least 6 contact angle measurements were performed with each liquid on each feather sample.

Microscopy

Scanning electron microscopy (SEM) was conducted for wing feathers using a JSM-JEOL 6060 microscope at an accelerating voltage of 5 kV, and a working distance of about 10 mm. Samples were cleaned in Asahiklin solvent and gold-coated with a thickness of ~ 5nm in preparation for microscopy. Micrographs were obtained at multiple magnifications to capture levels of structural hierarchy on the feather surfaces. SEM - EDX (Energy Dispersive X-ray) analysis was performed by first gold coating the samples and then using a XL30 FEG Environmental Scanning Electron Microscope (FEI/Philips) to confirm the nature of the coating.

8.4 Uniform and conformal nature of POSS / Tecnoflon coatings on bird feathers

Bird feathers typically have a waxy coating on their surface, and the exact chemistry of this coating can be different among various bird species or even within a given bird species. Therefore, to achieve uniform surface chemistry, the feather samples were dip-coated using a 50-50 wt% fluorodecyl POSS / Tecnoflon, as described here and in earlier papers from our group.[23-

[27, 31] An SEM micrograph of a Common Shelduck feather is shown in Figure 8-5(a) whereas the corresponding fluorine elemental map is shown in Figure 8-5(b). Fluorine is present only in the applied coating and therefore a close correspondence between the two images indicates the conformal nature of this coating, even at the scale of individual barbules.
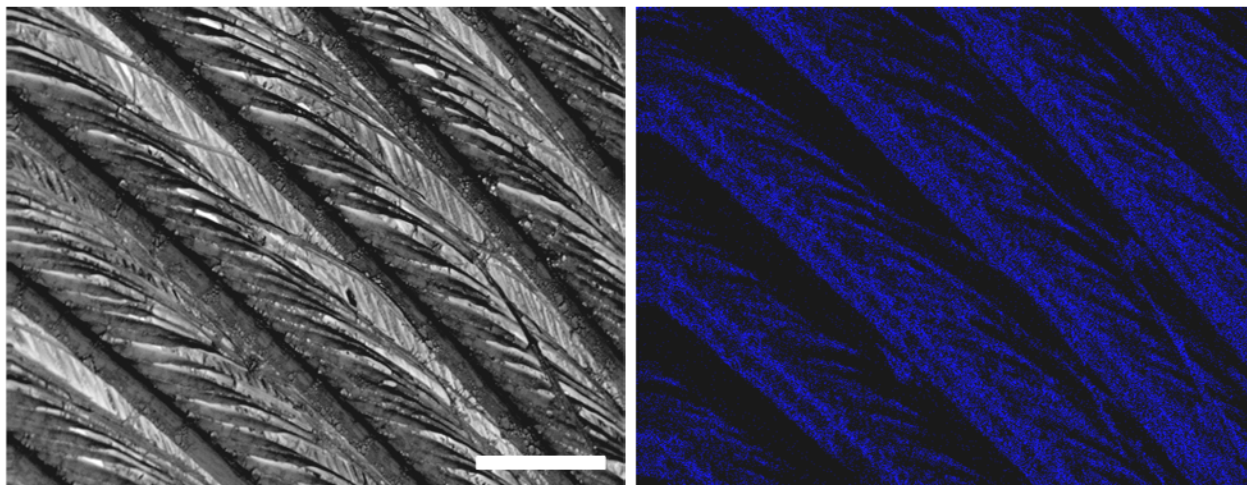
Figure 8-5. (a) SEM image of a bird feather (scale bar = 200 µm) and (b) the fluorine elemental map of the same area is shown. The close correspondence between the two images indicates that the intricacies of the feather texture are conformally coated with the POSS/Tecnoflon coating.

Coating the intricate texture of a bird feather with POSS/Tecnoflon has three main advantages. (1) POSS / Tecnoflon is inherently non-wetting due to its low solid surface energy (γ_{sv} = 10.7 mN/m), which makes the feathers more repellent to water and other probing liquids.[31] Liquids with a wider range of surface tension values (Figure 8-6) exhibit a robust solid-liquid-air composite interface, and therefore, feathers dip-coated with POSS/ Tecnoflon can be thoroughly probed. (2) The coating is thin (< 200 nm in thickness) and conformal and therefore the original topography of the feather is preserved after coating. (3) The chemistry and wetting characteristics of this coating are known, and they are constant across all feather samples. Therefore, contact angle data on different feathers with different liquid droplets can be compared objectively.

160

A wing feather of a common shelduck is moderately hydrophobic in the uncoated state and water droplets (γ_{lv} = 72.1 mN/m) have moderately high apparent contact angles (θ^{*}_{adv} = 134 ± 1°, ■ in Figure 8-6 and θ^{*}_{rec} = 129 ± 2°, □ in Figure 8-6). Moreover, this uncoated feather is not wetted by liquids like ethylene glycol and dimethyl sulfoxide that have moderate values of liquid surface tension. However, when probed with lower surface tension liquids like hexadecane or dodecane, the shelduck wing feather is instantaneously wetted.
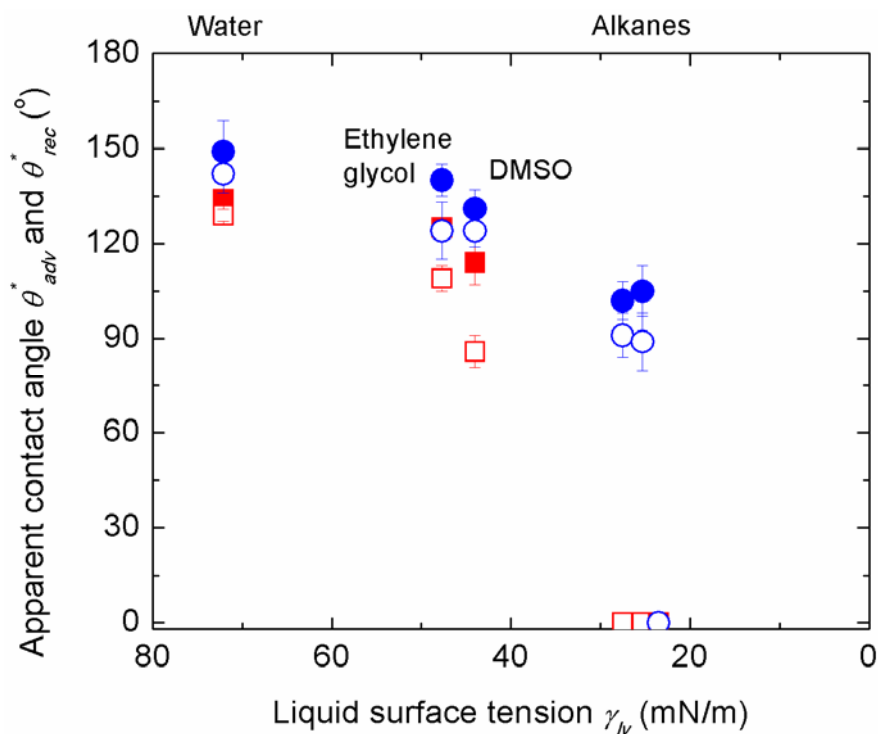
Figure 8-6. Apparent advancing (θ^{*}_{adv}, filled symbols) and receding contact angles (θ^{*}_{rec}, open symbols) on a wing feather of a common shelduck are plotted against the surface tension of the probing liquids. Red squares (■, □) represent contact angles on the feather in the uncoated state while blue circles (●, ○) indicate contact angles on the same feather after coating with 50% POSS – 50% Tecnoflon.

The same shelduck wing feather can be made non-wettable to low surface tension liquids like hexadecane and dodecane by coating it with a 50:50 mixture of POSS and Tecnoflon. Droplets of hexadecane (γ_{lv} = 27.5 mN/m, θ^{*}_{adv} = 102 ± 6° and θ^{*}_{rec} = 91 ± 7°) and dodecane (γ_{lv} = 25.3 mN/m, θ^{*}_{adv} = 105 ± 8° and θ^{*}_{rec} = 89 ± 9°) exist in a robustly metastable composite state on such coated feathers. The POSS coating is inherently non-wetting, so the contact angles of other liquid

droplets with higher surface tension also increase, as shown in Figure 8-6. From the contact angle data on a common shelduck feather, it is clear that the coated feather is not wetted by hexadecane whereas the same feather with the same inherent topography is completely wetted in the uncoated state.

8.5 Wetting behavior of dip-coated bird feathers

Contact angle measurements using liquids with a descending surface tension provides an ideal probing technique to test feathers for wettability. A water droplet (γ_{lv} = 72.1 mN/m) on a dip-coated common shelduck feather touches only the top hills of the feathers (as indicated by the region colored dark blue in Figure 8-3(b)). As the fraction of solid-liquid interface is small, relatively large apparent contact angles are observed. As we sequentially decrease liquid surface tension, from water (72.1, Figure 8-3(b)), to ethylene glycol (47.7, Figure 8-3(e)), down to alkanes like hexadecane (27.5, Figure 8-3(f)) and octane (21.6, Figure 8-3(g)), a higher fraction of the cylindrical texture is probed. For low surface tension liquids like alkanes, the portion underneath the equator of the feather (*i. e.* the re-entrant region) is probed. Note that this re-entrant region is necessary to achieve non-wettability by low surface tension liquids like alkanes with $\theta_E < 90°$.[23, 24, 32, 33] However, the re-entrant region cannot be directly seen in a top view during SEM imaging. This sequential probing method reveals the same amount of information as multiple SEM analyses followed by sequential etching would.

In this study, we use contact angle measurement to analyze feather topography and wettability. Millimetric scale liquid droplets are used for contact angle measurements and therefore, these droplets have a significant footprint on the feathers. These droplets probe an area much larger than any electron microscope can. As a result, imperfections and wide variety in texture parameters can be incorporated in this analysis. Liquid droplets in a composite state bead up on

dip-coated feathers and in this state, they act as lenses. Therefore, small air pockets (plastron) are magnified and can be easily spotted (as shown in Figure 8-3(a)).

Each dip-coated bird feather was probed using a series of liquids covering a range of surface tension from 72.1 to 23.5 mN/m. The apparent advancing and receding contact angles (θ^*_{adv} and θ^*_{rec}, respectively) on wing feathers of all six bird species are reported in Table 8-1. The advancing and receding contact angles (θ_{adv} and θ_{rec}) on a flat, fluorodecyl-POSS-coated surface are also provided for comparison in the last column of Table 8-1. Note that the uncertainties reported in the table correspond to the standard deviation in the contact angle data and at least six contact angles are measured for each combination of liquid and feather. Droplets of low surface tension liquids beaded up on coated feathers and the presence of air pockets underneath the liquid droplets indicated that the droplets were in a solid-liquid-air composite interface (as shown in Figure 8-3(a)). Apparent contact angles in the composite (Cassie-Baxter) state decreased with decreasing surface tension (γ_{lv}) and beyond a threshold liquid surface tension, the droplets irreversibly transitioned from a composite to a fully-wetted interface with low contact angle.

The non-wettability of these coated feathers can be viewed superficially by comparing the value of apparent contact angles for a particular liquid droplet or by comparing the lowest surface tension liquid that does not wet the particular feather. Hexadecane droplets (γ_{lv} = 27.5 mN/m) bead up on a dip-coated reed cormorant wing feather whereas rapeseed oil (γ_{lv} = 35.5 mN/m) is the lowest surface tension liquid that does not wet the dip-coated feather of a great cormorant. These criteria help us to rank order the feather surfaces in decreasing order of wettability, but it does not shed any light as to why a particular feather has a different wettability than a feather of another bird from the same family. Moreover, it does not provide any information about the structure and topography of these feathers. In our previous work on fabrics, we developed a more

quantitative assessment of the robustness of the nonwetting state.[23, 24, 26, 27, 31] We measured contact angles on the fabric and a chemically identical smooth surface using liquids with a wide range of surface tension values and we modeled the topography using a 1-D cylindrical model, for which the CB relation can be expressed as:

$$\cos\theta^*_{adv} = -1 + \frac{1}{D^*}\left[(\pi - \theta_{adv})\cos\theta_{adv} + \sin\theta_{adv}\right]$$ (1)

Fitting this model to the $\{\theta^*_{adv}, \theta_{adv}\}$ data provides a wetting-based quantification of D^*, an effective cylinder spacing ratio. Using this framework, the contact angle data were distilled into one dimensionless parameter that characterizes the topographical details.[25, 27] The advancing contact angles (θ_{adv}) were used in the previous study to characterize texture of a textile fabric.[25] Advancing represents the wetting of previously dry surfaces, and therefore the advancing contact angle is more relevant if we are concerned with the transition from a composite state to a fully-wetted state. The receding angle (θ_{rec}) represents the interaction of the liquid with the surface after liquid has already come into contact with the surface, and therefore it is more relevant in the estimation of solid-liquid adhesion.

8.6 Mesoscopic characterization of feathers using the contact angles and a spacing ratio

The cosine values of the apparent advancing contact angles (θ^*_{adv}) are plotted against the cosine of advancing contact angles (θ_{adv}) on chemically identical, but smooth spin-coated silicon wafer surfaces, as shown in Figure 8-7 for the six bird species under investigation. Using the Cassie-Baxter (CB) relation for cylindrical texture (equation 1), a non-linear regression was performed with D^* as the only regression parameter (the solid curve). A 95% confidence interval is used as a metric of uncertainty for the spacing ratio D^* (the area sandwiched between the two dashed lines in Figure 8-7, shown in Table 8-2).

Table 8-1. Apparent advancing and receding contact-angle data (θ^*_{adv} and θ^*_{rec}, in degrees (°)) for wing feathers of each species and for a chemically identical, spin-coated flat surface (θ_{adv} and θ_{rec}) with various liquids are summarized here. For each species, liquids are listed in order of decreasing surface tension (γ_{lv}), values of which are provided in parenthesis in column 1 in units of mN/m

Liquid / Bird species	Reed cormorant		Great cormorant		European shag		African darter		Mallard		Common shelduck		Flat spin-coated surface	
	Adv	Rec	Adv	Rec	Adv	Rec	Adv	Rec	Adv	Rec	Adv	Rec	Adv	Rec
Water (72.1)	125 ± 6	107 ± 5	142 ± 4	133 ± 5	140 ± 6	130 ± 6	137 ± 2	126 ± 2	141 ± 6	132 ± 3	149 ± 10	142 ± 6	122 ± 2	116 ± 2
Diiodome thane (50.8)	103 ± 4	90 ± 5	124 ± 2	109 ± 6	137 ± 7	115 ± 5	--	--	--	--	--	--	100 ± 2	79 ± 3
Ethylene glycol (47.7)	121 ± 9	96 ± 7	134 ± 5	120 ± 6	137 ± 4	120 ± 6	120 ± 3	104 ± 6	133 ± 3	115 ± 4	140 ± 5	124 ± 9	111 ± 2	87 ± 1
Dimethyl sulfoxide (44)	115 ± 3	101 ± 1	120 ± 5	104 ± 5	126 ± 8	114 ± 6	112 ± 2	103 ± 8	125 ± 7	107 ± 7	131 ± 6	124 ± 5	98 ± 2	80 ± 5
Rapeseed oil (35.5)	113 ± 8	89 ± 15	108 ± 10	90 ± 1	114 ± 9	100 ± 6	--	--	--	--	--	--	88 ± 3	66 ± 3
Hexadeca ne (27.5)	85 ± 13	78 ± 12	0	0	0	0	97 ± 5	82 ± 2	113 ± 6	92 ± 7	102 ± 6	91 ± 7	80 ± 1	61 ± 3
Dodecane (25.3)	0	0	0	0	0	0	0	0	108 ± 9	99 ± 5	105 ± 8	89 ± 9	75 ± 1	60 ± 4
Decane (23.5)	0	0	0	0	0	0	0	0	0	0	0	0	70 ± 2	44 ± 2

Table 8-2. Effective D^* values (D^*_{eff}) from this work are compared against $D^*_{microscopy}$ values from the literature in the second and the third column. In the last three columns, an effective length scale (R) from contact angle measurements and the corresponding error (δR) are also reported.

Bird species	D^*_{eff}	$D^*_{microscopy}$	References	R_{eff} (µm)	δR_{eff} (µm)	
					Up	Down
African darter	1.28 ± 0.1	~ 2–3, 4.5[*]	Elowson (The Auk, 1984), Rijke (The Auk, 1984), Rijke et. al. (J. African Ornithology, 1989)	2356	1711	791
Reed cormorant	1.24 ± 0.14	~ 3–4, 4.3[*]	Elowson (The Auk, 1984)	2798	4805	1234
Great cormorant	1.57 ± 0.15	4.8[*]	Rijke (J. Exp. Biol., 1968)	1193	691	381
Mallard	1.84 ± 0.13	~ 6–7, 5.9[*]	Elowson (The Auk, 1984)	544	188	131
European shag	1.91 ± 0.16	--	--	660	269	176
Common shelduck	1.89 ± 0.12	~ 9–10,	Elowson (The Auk, 1984)	510	151	110

[*] From breast feathers in Rijke's study (J. Exp. Biol., 1968)

The spacing ratio (D^*) was found to be significantly different for different birds, starting from as low as 1.28 for African darter to as high as 1.91 for the European shag (Table 8-2). Scanning electron micrographs obtained for the African darter ($D^* = 1.28 \pm 0.1$) and common shelduck ($D^* = 1.89 \pm 0.12$) showcase the complexity and diversity of feather topography (Figure 8-1 and Figure 8-2 respectively). The micrographs for the African Darter feather are qualitatively different from that of the Common Shelduck. However, a quantification of a geometric spacing ratio (D^*) using the SEM micrographs is difficult. Contact angle using a set of probing liquids can be accurately measured on these bird feathers. Therefore, these contact angle values provide an objective way to characterize the feather topography in a more quantitative manner. In evaluating our effective microscopy technique as applied to bird feathers, a comparison with literature values $D^* = (R + D)/R$ of obtained from microscopy (henceforth $D^*_{microscopy}$) is useful.
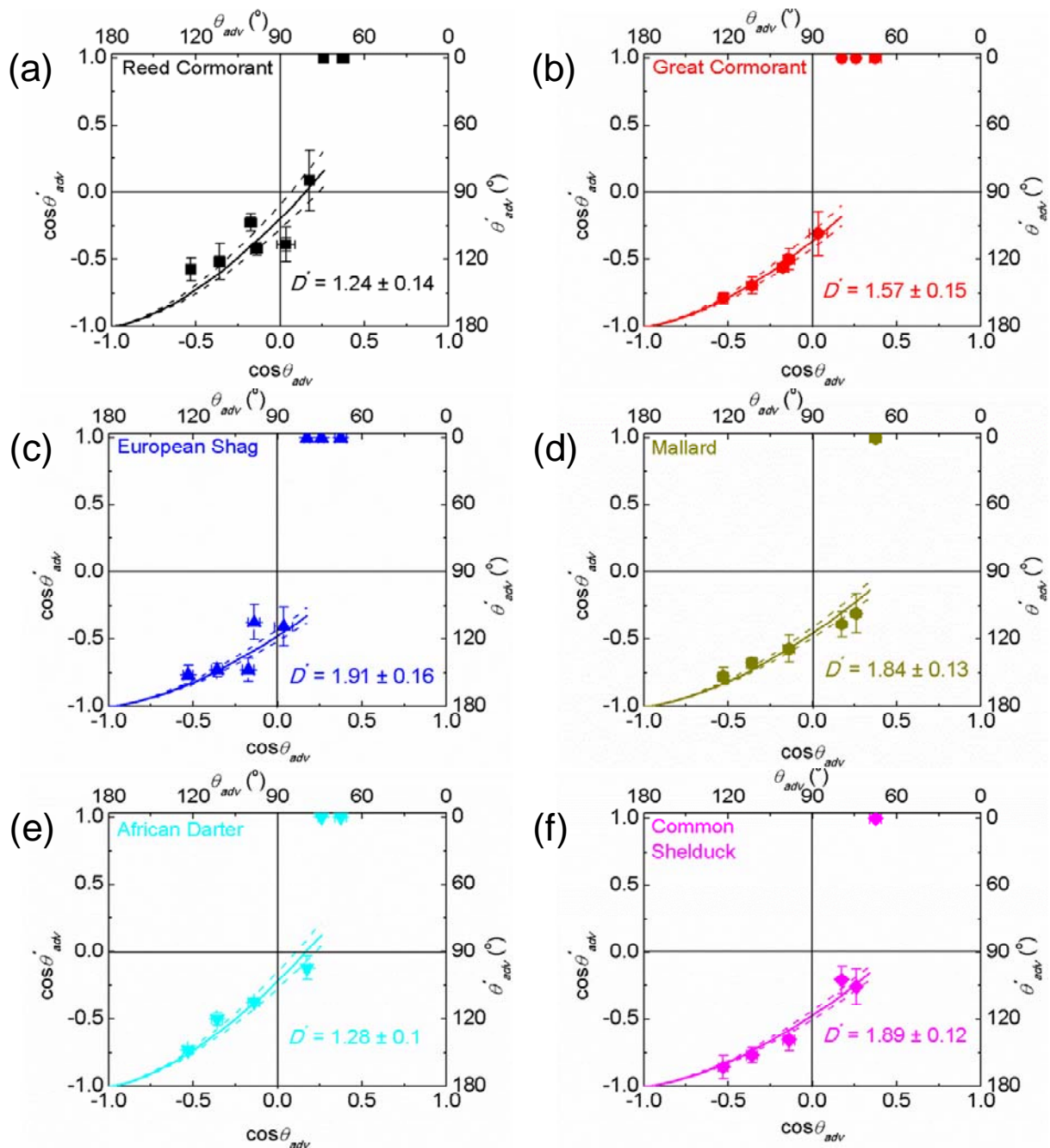
Figure 8-7. Apparent advancing contact angles (θ^*_{adv}) on fluorodecyl POSS / Tecnoflon coated feathers and on smooth silicon wafers spin-coated with the same coating (θ_{adv}) are plotted for the six bird species. Values of effective spacing ratio (D^*) extracted from a best fit Cassie-Baxter fit (solid lines) are also indicated, along with a 95% confidence interval (dashed lines).

Effective D^* values (D^*_{eff}) as obtained from the CB fits (Figure 8-7) are reproduced alongside

$D^*_{microscopy}$ values obtained from microscopy in Table 8-2. A comparison between the two

indicates that both follow the same general trend; however, there is lack of quantitative

167

agreement. Note that D^* measurements based on microscopy ($D^*_{microscopy}$) explore only a small portion of a surface at a time. Moreover, $D^*_{microscopy}$ characterizes the physical appearance in a top view, and not the wetting behavior. The re-entrant portion of the texture, (*i.e.* the portion below the top half of the structural features) is not visualized, and therefore is missed, by microscopic or visual techniques. The wetting-based technique of estimating an effective D^* is directly relevant to wettability and captures structural details otherwise missed.

8.7 Quantification of the resistance to wetting by pressure perturbations

The preceding structural analysis based on the CB relation is valid only for liquids that do not wet bird feather, and therefore in the previous section, we excluded the data collected using lower surface tension liquids that wet the dip-coated feathers. However, the contact angle data in a fully-wetted state also provide important information about the structure of these feathers. An air-liquid interface is curved to sustain a pressure differential across it. Such a curved air-liquid interface sags more and more severely as the surface tension of the probing liquid decreases (Figure 8-3(e) to (g)) and beyond a threshold, this sagged interface touches the underlying texture elements leading to irreversible wetting. This breakthrough phenomena was explained and quantified in terms of a dimensionless robustness factor (A^*) in our previous work.[23, 24] Here, we use the A^* framework in conjunction with contact angle data to predict the wetting of feathers.

In short, A^* is a dimensionless robustness factor and $A^* > 1$ is a necessary condition for the existence of a solid-liquid-air composite interface. Consider a cylindrically textured surface with a radius of cylinder as R, and inter-cylinder spacing of $2D$, with a droplet of surface tension γ_{lv}, density ρ and let g be the acceleration due to gravity. Let the equilibrium contact angle on a chemically identical smooth surface be θ_E, the capillary length be defined as $\ell_{cap} = \sqrt{\gamma_{lv}/\rho g}$, and

a reference pressure scale be $P_{ref} = 2\gamma_{lv}/\ell_{cap}$ Then the breakthrough pressure (P_b) for the

disruption of a composite interface and the robustness factor (A^*) is given as [24-27]

$$A^* = \frac{P_b}{P_{ref}} = \frac{\ell_{cap}}{R}\left(\frac{1}{D^*-1}\right)\left(\frac{1-\cos\theta_E}{D^*-1+2\sin\theta_E}\right)$$

(2)

From the expression for A^*, it is clear that the breakthrough pressure is inversely proportional to

the length scale of the texture (R), and therefore, the choice of R is critical. In a typical bird

feather, there are many length scales (R) corresponding to the barb, barbules, and tiny offshoots

from the barbules. Therefore, based on a microscopic examination, it is unclear whether to favor

one length scale and the corresponding spacing ratio over the other. Barbules occupy most of the

area fraction of the feather, and therefore the barbules length scale is expected to be the dominant

length scale. Unfortunately, barbules can have different diameters at different location on the

same feather, and they possess even finer features (ex. Figure 8-2(c)). Therefore, it is hard to

determine a unique value of the length scale (R) for a given feather from microscopy.

According to the formulation of the robustness factor, it is greater than unity ($A^* > 1$) for all

liquids that do not instantaneously wet a given feather, however, $A^* \leq 1$ holds when a liquid

droplet instantaneously wets the same feather. We have significant contact angle data on dip-

coated feathers using liquids with a wide range of surface tension values. Therefore, we can

bracket the range of surface tension value at which the robustness factor would have been equal

to unity. *E. g.* the wing feather of a common shelduck is not wetted by dodecane ($\gamma_{lv} = 25.3$

mN/m) or by any liquid with a higher surface tension. However, decane droplets ($\gamma_{lv} = 23.5$

mN/m) readily wet the same dip-coated feather. Therefore, we equate A^* to unity when the liquid

surface tension is the arithmetic mean of the lowest surface tension value that does not wet the

feather and the highest surface tension liquid that wets *i.e.* $\gamma_{lv} = 24.4$ mN/m. In the expression of

A^* (Equation 2), every physico-chemical parameter except the length scale R is known, so the effective length scale can be computed as –

$$R = \frac{\ell_{cap}}{A^*}\left(\frac{1}{D^*-1}\right)\left(\frac{1-\cos\theta_E}{D^*-1+2\sin\theta_E}\right)$$

(3)

In the above expression, we substitute mean values of liquid surface tension (γ_{lv}), contact angle (θ_E), and capillary length (ℓ_{cap}). Further, we use the best-fit spacing ratio (D^*) obtained from goniometric analysis of the same feather. From this analysis on a wing feather of a common shelduck, we found that the effective length scale, $R = 510$ μm when the robustness factor is equated to unity. The same exercise is repeated for the wing feathers of other five bird species and the results are summarized in the last three columns of Table 8-2 and in Figure 8-8.
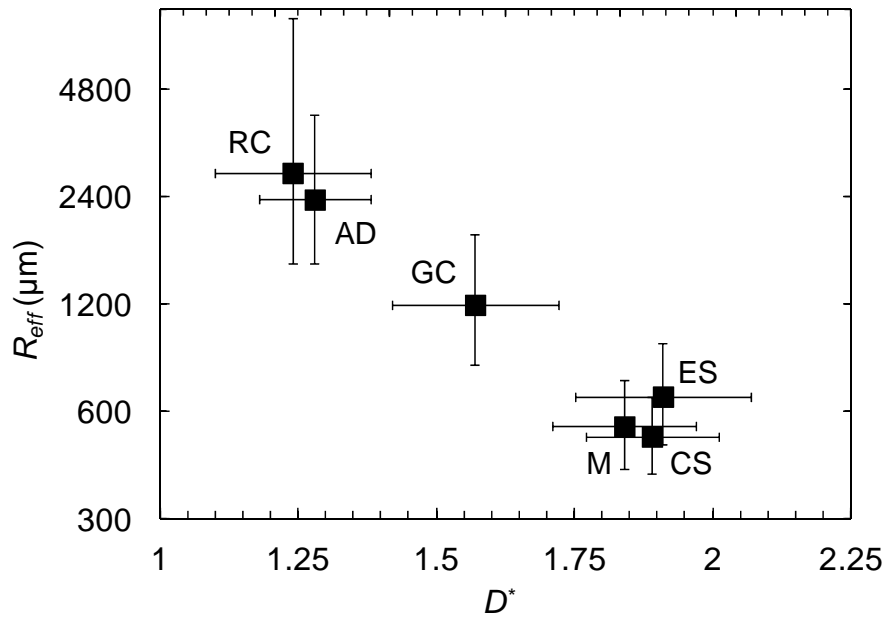
Figure 8-8. Wing feathers of six birds are characterized using contact angle measurements in terms of a spacing ratio (D^*) and an effective length scale (R). The six bird feathers characterized in this study are - African darter (AD), Reed cormorant (RC), Great cormorant (GC), Mallard (M), European shag (ES), and Common shelduck (CS). Error bars around D^* are 95% confidence intervals whereas error bars around R are computed by propagating the error in D^*, γ_{lv} and θ_{adv}.

In Figure 8-8, the effective length scale of a feather (R) is plotted against an effective spacing ratio (D^*) obtained from contact angle measurements. The uncertainty in the spacing ratio (δD^*)

170

is a 95% confidence interval obtained from the regression of CB curve through a set of contact

angle measurement. The procedure to estimate R and D^* might appear circular at a first glance,

however it is not. The D^* estimation is based on contact angle data for droplets with robust

composite interfaces. The Cassie-Baxter equation used in the fitting exercise is dimensionless

and therefore the choice of R is immaterial. On the contrary, determination of R is based on the

transition from a composite state to a fully-wetted state and the contact angle values do not

matter in this analysis. The only caveat is that we have used a model of A^* which requires prior

knowledge of D^* and therefore, the value of R strongly depends on the value of D^*.

Within the uncertainty of this framework, wing feathers of three bird species – Mallard (M),

European Shag (ES), and Common Shelduck (CS) have similar structural features *i.e.* similar

values of R and D^*. Great Cormorant (GC) is found to have intermediate values of R and D^*,

while the Reed Cormorant and African Darter species have the lowest D^* and highest R.

Values of the effective length scale (R) vary over a large range *i.e.* from about 500 μm for M,

CS, and ES, to about 3000 μm for RC. Note that this value of an effective length scale is much

larger than the barb or barbules length scale ($R >> R_b$), and there is no physical feature in the

feather that has the same length scale as that of R found through the goniometric procedure. This

value of R should be used to "translate" the wetting aspects of bird feathers with complicated

topography with multiple length scales into a 1-D cylindrical model with a single length scale.

As a result of this analysis, wetting behavior of the wing feathers of six bird species have been

characterized in terms of two parameters – (1) an effective length scale (R) and (2) an effective

spacing ratio (D^*). Therefore, the breakthrough pressure required to disrupt a composite interface

can be predicted using these parameters and a model for the robustness factor (A^*) for any liquid

droplet on feather surfaces. The breakthrough pressure estimates based on the contact angle data

and a model of cylindrical geometry (equation 2) are summarized in Table 8-3.

Table 8-3. Robustness factor (A^*), predicted breakthrough pressure for water droplets (
$P_b = A^* P_{ref}$) and corresponding breakthrough depth under a column of water (h_b) are compiled
for the POSS-coated wing feathers of the six bird species. The last three columns contain
empirically observed diving depth, diving speed and wing-spreading behavior for the same bird
species.

Bird species	Robustness factor, A^*_{water}	Breakthrough Pressure, P_b (Pa)	Breakthrough depth, h_b (mm)	Diving depth (m)	Diving speed (m s^{-1})	Wing-spreading
African darter	3.2	170	17	< 5	0.19 ± 0.16[†]	Y
Reed cormorant	2.7	143	15	5 – 6[*]	0.7 – 0.85	Y
Great cormorant	2.7	141	14	4.7, < 10[‡]	1.1-2.1	Y
Mallard	3.2	169	17	Dabbling	Dabbling	N
European shag	3.6	190	19	33 – 35	1.7-1.9	Y
Common shelduck	3.5	188	19	Dabbling	Dabbling	N

* from neutral buoyancy experiments, not natural observation; [†] horizontal traveling speed, not diving speed; [‡] usually < 10 m, but can dive to depths of 35 m;[34] Wing-spreading: Y = predictably, N = never; Dabbling = dabbling species, not primarily divers

The robustness factors for water droplets on POSS-coated bird feathers were found to be greater

than unity for all feathers. This result is expected since these bird feathers are not wetted by

carefully placed water droplets. However, if the same feathers are probed with water droplets

such that the pressure differential exceeds the corresponding breakthrough pressure (column 3 of

Table 8-3), the feather is expected to be wetted by water. Based on a single feather analysis, the

computed breakthrough depths were found to be less than 20 mm for all 6 species. This depth is

significantly smaller than a typical diving depth of a bird species that prey on fish. Therefore,

from a single feather analysis, it is expected that the individual bird feather will get wetted

during a typical dive. However, the feathers of these deep diving birds appear dry once the birds

come out of water. In order to explain the inconsistency between the physical observation and wetting predictions based on A^*, we look at the thermodynamics of wetting on textured surfaces.

8.8 Thermodynamics of wetting – binodal and spinodal

To test whether water droplets on a given bird feather are in a thermodynamically stable CB state, the contact angle on a smooth surface with identical chemistry (θ_E) and the spacing ratio (D^*) are needed. The D^* values for feathers are already known from the goniometric analysis, but the contact angle of water droplets on smooth surfaces with the chemistry of the inherent wax material (θ_{adv}, θ_{rec}) of the feather are unknown. However, apparent advancing contact angles for water droplets (θ_{adv}^*) on feathers without any POSS coating can be measured. Using the CB relation (Equation 1), and the values of θ_{adv}^* and D^*, θ_{adv} for water droplets on the inherent waxy coating of the feathers are estimated (outlined in the fourth column of Table 8-4). The POSS coating is thin (< 200 nm) and conformal, and therefore the effective spacing ratio (D^*) does not change on the application of this coating. Hence, the same value of D^* can be used for both POSS-coated and uncoated feathers.

The apparent contact angle (θ^*) for a droplet with solid-liquid-air composite interfaces is given by the CB relation (Equation 1), whereas, the apparent contact angle (θ^*) in a fully-wetted state is computed using the Wenzel relation $\cos\theta^* = r\cos\theta_E$, where θ_E is the equilibrium contact angle on a chemically identical smooth surface. The Wenzel roughness, r, is the ratio of actual solid-liquid interfacial area and the corresponding projected area. For the model geometry of 1-D cylinders, the Wenzel roughness is $r = 1 + \pi/D^*$.[27] On a wetting surface ($\theta_E < 90°$), the fully-wetted state represents the global equilibrium, whereas on a strongly non-wetting surface ($\theta_E >> 90°$), the composite state is the global equilibrium. The thermodynamic crossover

173

condition between the two states (the binodal (θ_c), dashed line in Figure 8-9, and third column of Table 8-4) can be found by equating the two expressions for apparent contact angles, given by –

$$D^* = \frac{\sin\theta_C - \theta_C\cos\theta_C}{1+\cos\theta_C}$$

(4)

Table 8-4. Critical angle for the Cassie-Baxter to Wenzel transition (θ_c) based on D^* values and estimated values of advancing contact angles on the inherent waxy coating (θ_{adv}) are summarized

Bird	D^*	θ_c (°)	θ_{adv} (°)
African darter	1.28 ± 0.10	96 ± 2	112 ± 2
Reed cormorant	1.24 ± 0.14	95 ± 3	118 ± 2
Great cormorant	1.57 ± 0.15	100 ± 2	117 ± 6
Mallard	1.84 ± 0.13	104 ± 2	105 ± 3
European shag	1.91 ± 0.16	105 ± 2	106 ± 3
Common shelduck	1.89 ± 0.12	104 ± 1	116 ± 2

* Uncertainty in θ_{adv} is computed using Monte Carlo simulation with 10,000 repeats and by sampling values of D^* and θ^* as random normal distributions.

Here, θ_c is the critical angle of crossover and if for a given D^*, the composite state is thermodynamically stable if $\theta_{adv} > \theta_c$ (region above the dashed line in Figure 8-9). When $\theta_{adv} < \theta_c$, the Wenzel state has a lower free energy than the CB state, however the liquid droplet can be trapped in a robustly metastable CB state. Liquid droplets in metastable CB states eventually transition into a more stable Wenzel state under pressure perturbations. This transition becomes spontaneous when the robustness factor approaches unity ($A^* \to 1^+$). This spontaneous transition is analogous to a spinodal, and the condition for the spinodal is given by equating the expression of A^* equal to unity. From Equation 2, the robustness factor (A^*) depends on the spacing ratio (D^*) and the length scale (R). As the six bird feathers were found to have a wide range of effective length scale, the exact location of the spinodal will be different for different birds. Therefore, the spinodal are not plotted for clarity in Figure 8-9. Unlike the spinodal, the condition for the binodal is independent of the length scale of surface texture (R). On comparing

the last two columns of Table 8-4, it is clear that for all six bird species, $\theta_{adv} > \theta_c$. Therefore, water droplets on the feathers of all six birds are in a thermodynamically stable CB state, as shown in Figure 8-9.
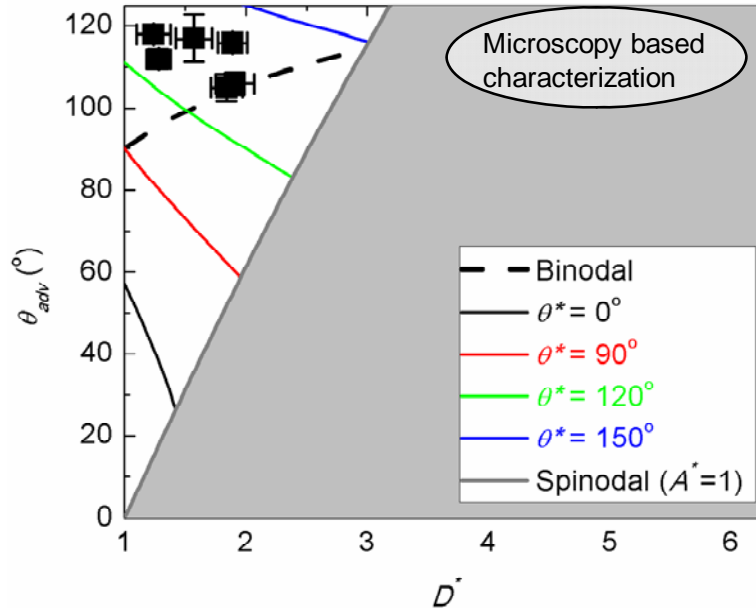
Figure 8-9. A phase diagram of surface wettability is plotted where advancing contact angles (θ_{adv}) are depicted on the y-axis and a regressed value of the effective spacing ratio (D^*) is plotted on the x-axis. Contact angle data for the 6 bird species under consideration lie above the dashed line, *i.e.* in a region where the composite interface is thermodynamically stable. Grey region of the chart is below the spinodal obtained by equating the robustness factor to unity for the Common Shelduck with $R = 510$ µm. SEM based characterization of the same feathers would erroneously place the feathers below the binodal (dashed line) in a region where the Wenzel state is thermodynamically stable.

Here, θ_c is the critical angle of crossover from non-wetting (Cassie-Baxter) to wetting (Wenzel) textures. If, for a given D^*, the composite state is thermodynamically stable, then $\theta_{adv} > \theta_c$ (region above the dashed line in Figure 8-9). When $\theta_{adv} < \theta_c$, the Wenzel state has a lower free energy than the CB state, and the texture should become wetted spontaneously, however the liquid droplet can be trapped in a robust metastable CB state beneath the binodal (between the dashed line and the grey region in Figure 8-9).

Liquid droplets in metastable CB states eventually transition into a more stable Wenzel state under pressure perturbations. This transition becomes spontaneous when the robustness factor approaches unity ($A^* \rightarrow 1^+$). This spontaneous transition is analogous to a spinodal (Figure 8-9), and the condition for the pseudo-spinodal is given by equating the expression of A^* equal to unity. From Equation 2, the robustness factor (A^*) depends on the spacing ratio (D^*) and the length scale (R). As the six bird feathers were found to have a wide range of effective length scale, the exact location of the spinodal will be different for different birds. A representative spinodal curve for the common shelduck ($R = 510$ μm) is plotted as the grey line in Figure 8-9.

Unlike the spinodal, the condition for the binodal is independent of the length scale of surface texture (R). On comparing the last two columns of Table 8-4, it is clear that for all six bird species, $\theta_{adv} > \theta_c$. Therefore, water droplets on the feathers of all six birds are in a thermodynamically stable CB state, as shown in Figure 8-9.

Natural waxy coating on bird feathers can be, at best, moderately hydrophobic ($\theta_{adv} \sim 105\text{-}118°$), and therefore a low value of effective spacing ratio ($1 < D^* < 2$) is necessary to push the feathers above the binodal in Figure 8-9. Therefore, the effective spacing ratio (D^*) is critical in determining whether the CB or Wenzel state is the global equilibrium. Based on goniometrically obtained D^* values, all 6 species are located in the top left corner of the plot, *i.e.* in a region where the solid-liquid-air composite state represents the global equilibrium. A fully-wetted (Wenzel) state can at best be a metastable state, and therefore, a dewetting transition from a fully-wetted state to a non-wetting composite state will be thermodynamically favored. This thermodynamic interpretation based on a goniometrically obtained D^* is consistent with the experimental observation that bird feather emerge dry when they are pulled out of water. The same feathers appear fully wetted when pulled out from a low surface tension liquid like

hexadecane or dodecane. The corresponding equilibrium contact angle $\theta_E < 90°$, and therefore, the fully-wetted state is the global equilibrium for such liquid droplets.

Microscopy-based estimations of the spacing ratio lead to much larger values of the spacing ratio ($D^* \approx 3 - 10$). Therefore, the feathers would be erroneously located in the top right corner of Figure 8-9, in a region where the fully-wetted state is the global equilibrium for water-feather interactions. From this observation, we conclude that microscopy-based values of structure parameters do not capture the wetting behavior of feathers whereas goniometrically-based values do.

8.9 Connection between wetting, thermodynamics and bird behavior

Based on the robustness factor framework, the predicted breakthrough pressure for feathers is significantly lower than hydrostatic pressure that the feathers are subjected to in a typical dive. With increasing hydrostatic pressure, the air between the asperities of the solid topography is gradually replaced by water as the air-water interface sags. Therefore, the individual feathers are expected to be wetted in a typical dive.

However, as the birds return to water surface, the wetted feather topography becomes energetically unfavorable as compared to solid-liquid-air composite state. Spontaneous de-wetting of the texture is expected, but this reversible behavior may be burdened by kinetic barriers that trap the water temporarily in the feather texture. Spreading of their wings possibly facilitates the transition from a fully-wetted to a non-wetting composite state. The spontaneity of the transition from a fully-wetted state to a composite state will depend on the geometry and wetting characteristic of the feather. However, for all 6 feathers under consideration, the non-wetting feather structure is thermodynamically favorable.

In this work we looked at whether or not a single feather will be spontaneously wetted by a liquid. However, the dynamics of the wetting process under pressure differential are not investigated. So at this point it is unclear whether the whole plumage of the bird with multiple layers of feathers will get wet during the time of a single dive. Complementary wettability experiments with higher-order structures of feathers, such as feather groups, feather coats, or whole birds would help to draw connections between the parameters quantified in this work and the bird behavior.

8.10 Conclusions about the bird feather wettability analysis

In this work, we extend and apply our understanding of wetting of textured surfaces to bird feathers. We demonstrate that feathers of aquatic bird species with thin, conformal coatings of POSS/Tecnoflon are not wetted by low surface tension liquids like hexadecane and dodecane. Such droplets have robustly non-wetting solid-liquid-air composite interfaces and high apparent contact angles on dip-coated bird feathers. From the apparent advancing contact angle data (θ_{adv}^*), we extract a dimensionless spacing ratio ($1 < D^* < 2$) and an effective length scale (500 μm < R < 2800 μm) for cylindrical texture. These two structural parameters capture the wetting aspects of complicated texture of bird feathers in terms of a simple 1-D cylindrical model. This approach provides a simpler and quantitative manner to investigate bird feathers, as compared to previous work based on microscopic or photographic evaluation.

Based on a robustness factor (A^*) analysis in conjunction with these two structural parameters (R and D^*), we predict that all six wing feathers will get wet at a shallow depth of about 2 cm, which is much smaller than the typical diving depth. From the effective spacing ratio (D^*) of these feathers, we conclude that a solid-liquid-air composite interface is the global equilibrium

state of water droplets on these feathers. Therefore, once the birds emerge out of water, the

dewetting transition is thermodynamically favorable. The wing spreading behavior might help

the drying of feathers by providing higher plumage area. Applying this framework to feathers of

other bird species will help to relate the structure of bird feathers with bird behavior.

8.11   References

1.   Rijke, A. M., *Journal of Experimental Biology* **1968,** 48, 185-189.
2.   Gremillet, D.; Chauvin, C.; Wilson, R. P.; Le Maho, Y.; Wanless, S., *Journal of Avian Biology* **2005,** 36, (1), 57-63.
3.   Rijke, A. M., *Journal of experimental biology* **1970,** 52, (2), 469-469.
4.   Elowson, A. M., *The Auk* **1984,** 101, (2), 371-383.
5.   Rijke, A. M., *The Auk* **1987,** 104, (1), 140-142.
6.   Rijke, A. M.; Jesser, W. A., *The Wilson Journal of Ornithology* **2010,** 122, (3), 563-568.
7.   Rijke, A. M.; Jesser, W. A., *The Condor* **2011,** 113, (2), 245-254.
8.   Rijke, A. M.; Jesser, W. A.; Mahoney, S. A., *Ostrich: Journal of African Ornithology* **1989,** 60, (3), 128-128.
9.   Rijke, A. M.; Jesser, W. A.; Evans, S. W.; Bouwman, H., *Ostrich* **2000,** 71, (1-2), 143-145.
10.   Young, T., *Philosophical Transactions of the Royal Society of London* **1805,** 95, 65-87.
11.   Wenzel, R. N., *Ind. Eng. Chem.* **1936,** 28, (8), 988-994.
12.   Cassie, A.; Baxter, S., *Transactions of the Faraday Society* **1944,** 40, 546-551.
13.   Bormashenko, E.; Bormashenko, Y.; Stein, T.; Whyman, G.; Bormashenko, E., *Journal of Colloid and Interface Science* **2007,** 311, (1), 212-216.
14.   Salibian, A.; Montalti, D., *Brazilian Journal of Biology* **2009,** 69, (2), 437-446.
15.   Schutz D., T. M., *Evolutionary Ecology Research* **2003,** 5, 105-117.
16.   Anderson, D. S., *Journal of Insect Physiology* **1960,** 5, (2), 120-128.
17.   Hebets, E. A.; F. Chapman, R., *Journal of Insect Physiology* **2000,** 46, (1), 13-19.
18.   Hinton, H. E., *Journal of Insect Physiology* **1960,** 4, (2), 176-183.
19.   Thorpe, W. H.; Crisp, D. J., *Journal of experimental biology* **1947,** 24, (3-4), 227-269.
20.   Thorpe, W. H.; Crisp, D. J., *Journal of experimental biology* **1947,** 24, (3-4), 270-303.
21.   Thorpe, W. H.; Crisp, D. J., *Journal of experimental biology* **1947,** 24, (3-4), 310-330.
22.   Hsu, S.-H.; Woan, K.; Sigmund, W., *Materials Science and Engineering: R: Reports* 72, (10), 189-201.
23.   Tuteja, A.; Choi, W.; Ma, M.; Mabry, J. M.; Mazzella, S. A.; Rutledge, G. C.; McKinley, G. H.; Cohen, R. E., *Science* **2007,** 318, (5856), 1618-1622.
24.   Tuteja, A.; Choi, W.; Mabry, J. M.; McKinley, G. H.; Cohen, R. E., *Proceedings of the National Academy of Sciences* **2008,** 105, (47), 18200-18205.
25.   Chhatre, S. S.; Tuteja, A.; Choi, W.; Revaux, A. l.; Smith, D.; Mabry, J. M.; McKinley, G. H.; Cohen, R. E., *Langmuir* **2009,** 25, (23), 13625-13632.
26.   Choi, W.; Tuteja, A.; Chhatre, S.; Mabry, J. M.; Cohen, R. E.; McKinley, G. H., *Advanced Materials* **2009,** 21, (21), 2190-2195.

27. Chhatre, S. S.; Choi, W.; Tuteja, A.; Park, K.-C.; Mabry, J. M.; McKinley, G. H.; Cohen, R. E., *Langmuir* **2010,** 26, (6), 4027-4035.
28. Stephenson, R., *Environmental Conservation* **1997,** 24, (02), 121-129.
29. Stephenson, R.; Andrews, C. A., *Canadian journal of zoology* **1997,** 75, (2), 288-294.
30. Mabry, J. M.; Vij, A.; Iacono, S. T.; Viers, B. D., *Angewandte Chemie (International Ed. in English)* **2008,** 47, (22), 4137-4140.
31. Chhatre, S. S.; Guardado, J. O.; Moore, B. M.; Haddad, T. S.; Mabry, J. M.; McKinley, G. H.; Cohen, R. E., *ACS Applied Materials & Interfaces* **2011,** 2, (12), 3544-3554.
32. Nosonovsky, M., *Langmuir* **2007,** 23, (6), 3157-3161.
33. Marmur, A., *Langmuir* **2008,** 24, (14), 7573-7579.
34. Hatch J. J.; Brown K. M.; Hogan G. G.; D., M. R., Great Cormorant (Phalacrocorax carbo), The Birds of North America Online (A. Poole, Ed.). Ithaca: Cornell Lab of Ornithology In 2000.

9 PhD-CEP Capstone chapter on the economics of fog collection

9.1 Summary

The final chapter of this thesis brings the business and management perspective of the MIT Sloan experience into conjunction with my research topic. This chapter discusses the feasibility of large scale deployment of woven mesh based fog harvesting devices to alleviate water shortage in Chile. The main conclusion of the economic analysis presented in this chapter is that over a wide range of assumptions, the break-even price of water is lower than water obtained from sea-water desalination.

The chapter models the daily fog collection rates in the coastal parts of the Atacama Desert as normal distribution with different means and standard deviations corresponding to the four seasons. Based on the model, a heuristic is developed to choose water tank size. Further, a demand response strategy with lower demand in summer and spring and a higher demand in winter and autumn is found to lower the tank size by a third. Later, the chapter discusses all the assumptions in the economic analysis of fog collection and a diversification strategy of combining fog collection with solar power generation is proposed. A risk-return framework is applied to this portfolio indicates that its volatility is minimum at a fractional weight of 0.28 on fog harvesting. Due to a negative correlation between the time series data for fog collection rates and solar insolation, a joint project has lower risk than two individual projects, thus a lower discount rate can be justified for such joint project. The chapter ends by presenting customer value proposition and competitive analysis based on Porter's framework.

Even though this chapter talks about deployment in Chile, most of the techno-economic challenges are similar in other parts of the world. Therefore, this chapter can serve as a good starting point for researchers engaged in fog harvesting in other parts of the world.

Scale of the water shortage problem, especially in arid parts of the world

Access to adequate supplies of clean drinking water is a major concern in some parts of the developing world. A large population living in the arid parts of such countries depends either on groundwater which is not suitable for drinking, or on water supplied by tankers which is expensive and intermittent. According to WHO statistics, less than 0.007% of all water on the earth is readily accessible for human consumption, about a billion people lack access to safe drinking water, more than 3.5 million people die every year due to water-related diseases, water insecurity is one of the leading causes for school dropouts, especially among girls, and more than 200 million working hours are spent (almost exclusively by women) daily for the collection of domestic water.[1]

The water crisis is worsened in arid parts of the world due to abuse of groundwater, water-intensive crop cultivation, rapid industrialization, and changing life style. However, in some dry regions, the appearance of fog in the early morning is common. Fog is a completely untapped water resource. Fog harvesting provides an opportunity to "produce" water locally for rural communities, which will reduce the stress on groundwater. In the north of Chile, due to its long and mountainous coastline, a persistent advection fog is observed. According to a rough estimate from the CDA (*Centro Del Desierto De Atacama*) group, 10 billion m^3 of fog water per year is available in Chile. Currently, water consumption in northern Chile is 391 million m^3 per year i.e.

only 4% of the total water content in the fog. Therefore, water collection from fog harvesting has a huge potential to locally satisfy the need for a pure and dependable supply of water in Chile.

9.2 Fog harvesting – a possible solution to alleviate water scarcity

Fog consists of tiny water droplets of 1 to 40 μm in diameter suspended in air. Fog droplets can be carried with wind over long distances from their source, even when the surrounding temperature is above the dew point. Water from fog can be collected by a direct impaction process. When a streamline in a fluid flow encounters a solid obstacle, it bends around the object due to the no flux boundary condition at the solid surface. However, water droplets carried with the streamline have higher inertia, as they are significantly denser than air ($\rho \approx 1000$ kg/m^3 for water vs. 1.2 kg/m^3 for air at room temperature and pressure). As a result, these droplets migrate across the fluid streamlines and impact the object, as schematically shown in Figure 9-1. Therefore, any solid object that intercepts the flow of fog should be able to collect at least some fog water. However, an impermeable solid surface completely blocks the wind and significantly slows down the wind flow in front of the solid obstacle leading to a stagnant region that is depleted of droplets. As a result, a suboptimal amount of fog is convected to the surface and renders the surface ineffective at collecting fog. Therefore, a fog harvesting surface has to be permeable to allow some wind flow and to maintain a steady flux of water droplets towards the surface. The ratio of inertia and viscous drag force on the droplets can be expressed in terms of a dimensionless group – the Stokes number (*St*). Previous theoretical studies indicate that for a cylindrical solid object, the efficiency of droplet collection increases with increasing Stokes number *i.e.* as inertia dominates viscous effects.[2, 3]

Woven or knitted meshes with a significant range of air permeability can be bought off the shelf. Moreover, they are inexpensive, mechanically robust and easy to manufacture. Meshes are available in a wide variety of fiber materials, patterns or kinds of weave. Fog-containing wind is slowed down around each of these fibers. But when the fibers are relatively close to each other, the regions of decreased velocity start to interact and overlap with each other.[4] Therefore, for a given spacing between two cylindrical fibers, different weaves will result in different fog harvesting efficiencies. The quantitative impact of these mesh weave patterns on fog collection efficiency is still an open question. A systematic theoretical study backed up by a set of parametric experiments will help us to choose the optimal mesh weave to maximize fog harvesting.
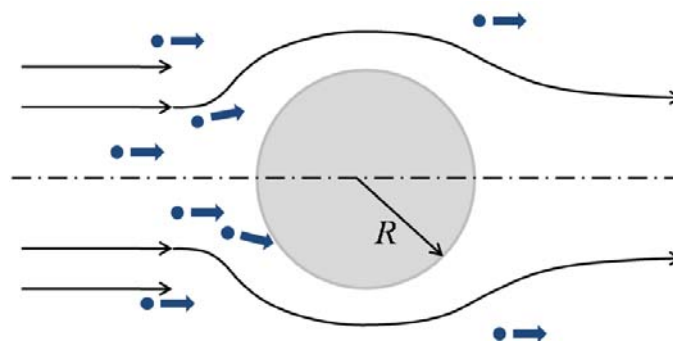
Figure 9-1. A schematic of streamlines that bend around an infinitely long cylindrical object of radius R is shown. Tiny fog droplets continue to travel along the original direction due to inertia and therefore get intercepted by the solid object.

9.2.1 Survey of fog harvesting work around the globe

Many research groups have assessed the potential to harvest fog in different parts of the world and many pilot projects to capture fog have been carried out.[1, 5-10] A woven mesh surface of $1m^2$ area, called a Standard Fog Collector (SFC) was typically used to quantify fog collection in these areas.[8] Water collection rates from as low as 0.1 L/m^2/day to as high as 70 L/m^2/day have been reported at various locations in these studies.[6] Generally, a Raschel mesh made of polypropylene is used as the active surface for fog harvesting. The duration, frequency and the water content in

184

fog cannot be accurately predicted. Moreover, a low collection ability of these mesh surfaces coupled with the uncertainty of fog occurrence made fog harvesting a questionable proposition for capital investment.

In the Atacama Desert in Northern Chile, a persistent and dense fog called "Camachancha" is observed between 600 to 1200 m above sea level. Cereceda and co-workers measured fog collection efficacy of 0.25 m^2 area fog collectors at two sites in this region over the period of 8 years.[5, 11] Between 1997 and 2005, the average fog collection rate was 7 L/m^2/day for the coastal site of *Alto Patache*. The annual average fog collection yield varied between 8.4 and 5.3 L/m^2/day, and there were no "dry years" with appreciably low fog collection.[11] They found that fog collection efficacy increased significantly with the altitude, and highest amount of water was collected at 850 m above sea level. Collection rates were higher around 15 – 17 L/m^2/day during the Chilean winter months of August – October, whereas in the summer months of January - March, the collection rates dipped to 2 – 3 L/m^2/day. Even though the amount of fog was significantly lower in summer, there were almost no dry months. In this work, a double layer Raschel mesh made of polyolefins, with a 35% shade coefficient was used to collect water.

9.2.2 Our contribution to the field of fog harvesting

We address the low efficiency of fog harvesting of these woven meshes by studying the influence of surface topography and surface wettability on the fog or mist harvesting ability of woven mesh surfaces. We investigate the influence of surface wettability characteristics, length scale, and weave density on the fog harvesting capability of meshes, by testing various meshes shown in Figure 9-2(a). We conformally coated these meshes to tune their solid surface energy over a large range, and then probed these coated meshes with artificially generated fog, as shown

in Figure 9-2(b). [12-14] The fog collection efficiency was enhanced by five-fold by appropriately choosing the solid surface chemistry and surface topography. Technical details of the coating protocol, modeling and experimental results can be found elsewhere.[15] Once a fundamental understanding was developed, we collaborated with Prof. Rivera, Prof. Cereceda and co-workers to apply our understanding to deploy large-scale fog harvesting meshes in Chile. Their expertise on fog harvesting and familiarity with the Chilean system complemented the Cohen/McKinley group's strength in understanding interfacial phenomena.[5, 16] Concurrent with the pilot plant deployment of 4 m2 of woven mesh surface, we quantified the economics of fog harvesting in Chile, which is the focus of the rest of the chapter.
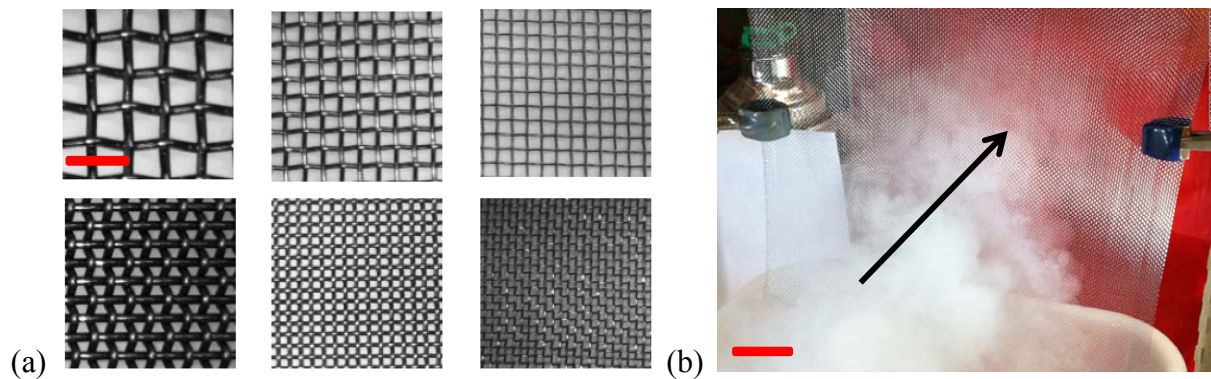
Figure 9-2. (a) Microscope image of various liquid-collecting permeable structures with different wire radii (R) and spacing ratio (D^*) [Image courtesy – Kenneth Park, MIT, (scale bar ~ 500 μm)], and (b) a prototype of a fog harvesting mesh being impinged by a column of air with tiny water droplets in the Cohen lab at MIT (scale bar ~ 1cm)

9.3 Business case on fog harvesting

Lack of water resources in the Atacama Desert - The Atacama Desert in Chile is one of the driest places on earth but it is home to one of the most water-intensive industry *i.e* the mining industry. According to a recent estimate by CORFO, the mining industry in Atacama represents about 45% of the regional GDP and consumes about 70% of the local water resources.[17] The Atacama area has rich deposits of copper and copper mining over the last few decades has put

significant stress on the groundwater resources in the area. The mining industry has been purchasing water rights from the farmers and therefore non-mining consumers of water are finding it increasingly hard to survive in this region.[18] There are about a million inhabitants in the region, mostly in fishing villages along the Pacific Coast. These inhabitants compete with mining for access to scarce water. Sources of surface and groundwater are under stress in this region and therefore, there is plenty of demand for water from other sources like fog.

Water – a tradable commodity in Chile - A second key enabler for the deployment of water technologies arises from the 1981 Water Code enacted in Chile. The code classifies Chilean water as a privately traded commodity and therefore, the market-based system (*laissez faire*) is incentivized to promote "higher value" uses of water.[19] The code allowed the transfer of agricultural water to industrial water, which led to a rapid proliferation of the mining industry by consuming water that was initially allotted for farming. However, the Chilean water utility company (Dirección General de Aguas: DGA) imposed restriction on transferring water rights across different geographic locations and across different end uses.[20] These restrictions forced the mining companies to look for alternate source of water. As the mining industry has proliferated, the incremental cost of a liter of water has skyrocketed, and this steeply upward sloping cost curve allows newer technologies to enter the Chilean market. In 2009, the weighted average prices of surface and ground water were $0.2/m^3 and $0.9/m^3 respectively in the Antofagasta Region of Chile.[20] Due to increasing population, changing lifestyle and further expansion of the mining sector is expected to push the price of water resources even higher.

Water utility companies also subsidized 25 – 85% of the water price for the first 15 m^3/ month of domestic use.[21] This subsidy was targeted towards low income families living in rural areas of

the country. The retail tariff price in Chile (before subsidy) was anywhere between $0.8 – 4.1/m³ depending on the location.

Rise of desalination - Desalination has emerged as the solution for producing water in the Atacama Desert on a scale relevant to the mining industry *i.e.* millions m³/day. Desalination has the potential to produce water at a relatively cheap price ($0.5-2/m³), but large capital investments, increased reliance on dwindling energy resources, shortage of local expertise in desalination and long project delays are some of the downsides of desalination. Moreover, most desalination plants are situated next to the Pacific Ocean, and after desalination, the water has to be pumped over long distances and high altitudes. For an altitude of 900 m above sea level, the pumping cost is expected to be about $2.5/m³.[20] Therefore, the total price of desalinated water on the edge of the Atacama Desert exceeds $3/m³.

Starting 2014, Antofagasta (pop. 360 k) and Mejillones (10 k) will be the first Latin America cities to completely depend on desalination for drinking water. Desalination provides a good price point for other technologies like fog harvesting. Desalination is more suitable for mining industry due to large capital costs and large volume of water involved. However, smaller consumers like village dwellers or small farmers may not have access to desalinated water, a niche that can be effectively fulfilled using fog harvesting. In general, it is hard to put up a price tag on water, but transferrable water rights in Chile have eased this task. A large part of the incremental water supply is expected to be in terms of desalinated water, and therefore desalination serves as a good comparison for marginal cost analysis.

For the purpose of the economic analysis, we will assume that people will sell their conventional water right as long as the price that they get does not outweigh the foregone utility from that

water (*i.e.* we will assume that people are economically rational). The confluence of many rare events, namely - the presence of the economically profitable and water intensive mining industry, market-based water laws and ever increasing demand for water offer the right entry point for a new enterprise that sells water. In the next section, we estimate the breakeven price of water obtained by fog collection.

9.4 Discounted cash flow analysis

There are a few key variables that dictate the feasibility of fog harvesting on a large scale (shown in Table 9-1). The annual revenue (R, $/y) is equal to the product of the price (*P*), quantity of water collected every day (*Q*), and the area of a fog collector (*A*). Using a discounted cash flow analysis for annuity for *t* years, the net present value of the project (NPV) is computed as a function of the key variables using the following relation –

$$NPV = \frac{(QAP - m)}{r}\left[1 - \frac{1}{(1+r)^t}\right] - \text{capex}$$

Table 9-1. A set of key variables along with the range of typical values are summarized

Variable	Symbol	Possible range
Capital cost ($)	Capex	$300 - $600
Amount of water collected (L/m^2/day)	Q	3 - 13 L/m^2/day
Area of a fog collector	A	30 m^2
Price of water ($/m^3)	P	1 – 4 $/m^3
Lifetime of the project (years)	t	5 – 20 years
Annual maintenance ($/year)	m	$25 - $75
Discount rate (%)	r	10 – 30%

The NPV is computed for a single mesh of area 30 m^2 along with required water collection and purification system. Here we assume that the annual revenue (*R* = *QAP*) starts after one year from installation, and it remains constant for *t* years. We further assume that all capital expenditure occurs today and the residual value of the system is negligible at the end of its

lifespan. Note that this analysis does not assume any subsidy or any other revenue stream apart from the proceeds obtained by selling the fog-water.

As shown in Table 9-1, the key variables span a large range, and therefore, many scenarios have to be considered to establish whether fog harvesting can be an economically sustainable enterprise. Initially, we assume a constant discount rate (r) of 20% to conduct the breakeven price analysis and later we revisit the assumptions behind choosing the discount rate. The analysis under a wide range of capital cost deployment and annual revenue are summarized in Table 9-2. From the table, it is clear that over a wide range of collection rates and capital costs, water can be collected at a reasonably low price. However, this analysis is sensitive to various parameters, and therefore, it is critical to examine the assumptions regarding every key variable in this analysis. $3/m^3$ is a ballpark price of water using thermal desalination and pumping, and according to the analysis, the breakeven price is lower than desalination price under some conditions (marked green).

Table 9-2. Scenario analysis for estimating the breakeven price of fog water, assuming a discount rate of 20%, collection area of 30 m2, annual maintenance expense of $50 every year and project lifetime of 10 years is summarized.

Breakeven price ($/m^3$)		Capex ($/30 m^2 mesh unit)			
		400	600	800	1000
Water collection rate (L/m^2/day)	3	4.4	5.9	7.3	8.8
	7	1.9	2.5	3.1	3.8
	10	1.3	1.8	2.2	2.6
	13	1.0	1.4	1.7	2.0

The preceding analysis projects a wide range of scenarios in terms of fog collection efficiency. The same framework is now used to estimate the breakeven price of water at a particular location in the Atacama Desert. Cereceda *et. al*. reported fog collection data over the period of 8 years at the *Alto Patache* site on the edge of the Atacama desert.[11] They collected 7 L/m^2/day (annual

average) of water and the collection varied between 8.4 and 5.3 L/m^2/day (annual average) over the course of these 8 years. For the purpose of the economic analysis, we will consider 3 scenarios – the mean (7), minimum annual rate (5.3) and maximum annual rate (8.4 L/m^2/day) and project the breakeven price of water. The estimated breakeven prices (plotted in Figure 9-3) indicate that water can be collected at a price < 3 $/m^3 over many scenarios of capital expense and fog collection rates.
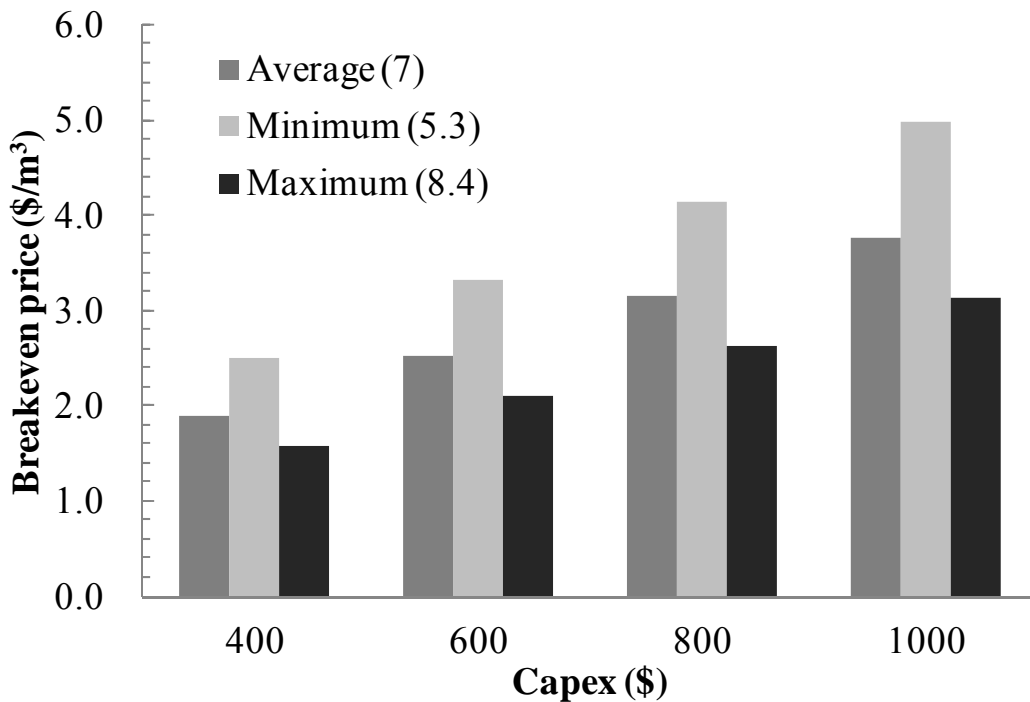
Figure 9-3. The breakeven prices of fog water are plotted for three scenarios based on the data collected by Cereceda et. al. at Alto Patache. The three scenarios represent an average collection rate (7 L/m2/day), along with a minimum rate of 5.3 and a maximum rate of 8.4 L/m2/day.

The above presented breakeven price calculations are based on annual average values and two representative cases - an optimistic and a pessimistic scenario each. However, the collected water will be distributed on a daily or a weakly time scale, and therefore the fog collection rates should be predicted with more granularity than annual averages. Such detailed predictions will help to capture the uncertainty in fog collection.

Cereceda *et. al* reported fog collection values at *Alto Patache* over the course of 7 years. They

report annual averages for 7 years, seasonal average for a year and monthly average over a

different year. By combining these data, we can estimate the variability in fog collection over

different timescales. Their data indicate that fog collection efficacy was highest in winter (July to

September), intermediate in spring (October to December) and autumn (April to June) and

lowest in summer (January – March). By combining the two sets of data over seasonal and

monthly averages, we estimated monthly and daily variations in fog harvesting rates (Table 9-3)

in the units of L/m^2/day. Here, we assume that daily fog occurrence can be modeled as a

normally distributed random variable with a specified mean and standard deviation. For normally

distributed random variables, we invoke the central limit theorem which postulates that the sum

of *n* normally distributed random variables with mean μ and standard deviation σ is a normal

distribution with mean μ and standard deviation $\sigma\sqrt{n}$.

Table 9-3. Mean and standard deviation in the fog collection rates in L/m2/day are estimated
from the data collected by Cereceda et. al. and the standard deviations are scaled to a weekly and
daily timescale by modeling fog occurrence as a normally distributed independent variable.

Season	Monthly		Weekly	Daily
	Average	Standard deviation (σ_m)		
Autumn	6	2.8	5.8	15.3
Winter	15	2.8	5.8	15.3
Spring	7.8	4.2	8.7	23.0
Summer	1.7	0.8	1.7	4.4

Using the data summarized in Table 9-3, daily and weekly averages of fog collection rates were

simulated, and the results of such a simulation are plotted in Figure 9-4(a) and (b) respectively.

The daily collection rates vary over a much larger range from 0 to 65 L/m^2/day whereas the

weekly average collection rates vary to a much smaller extent from 0 to 19 L/m^2/day. This

decrease in weakly averages is expected due to the assumption that individual fog appearances are random and there is no correlation in time. This assumption might be questionable in locations where weather patterns do not change daily; however it provides a starting point for the modeling exercise. As an artifact of the normal random distribution, several collection rates were found to be negative, which is an unphysical result. These negative values are not plotted in these figures, however those values are considered for the numerical analysis in order to preserve the normal distribution.

As shown in Figure 9-4(a) and (b), the supply of fog water has a large variation, but the water demand is expected to be relatively uniform throughout the year. Therefore, a large tank is needed to dampen out these large supply variations. The next section discusses how to choose water tanks with the correct size and some suggestions to lower the disparity between supply and demand of water.
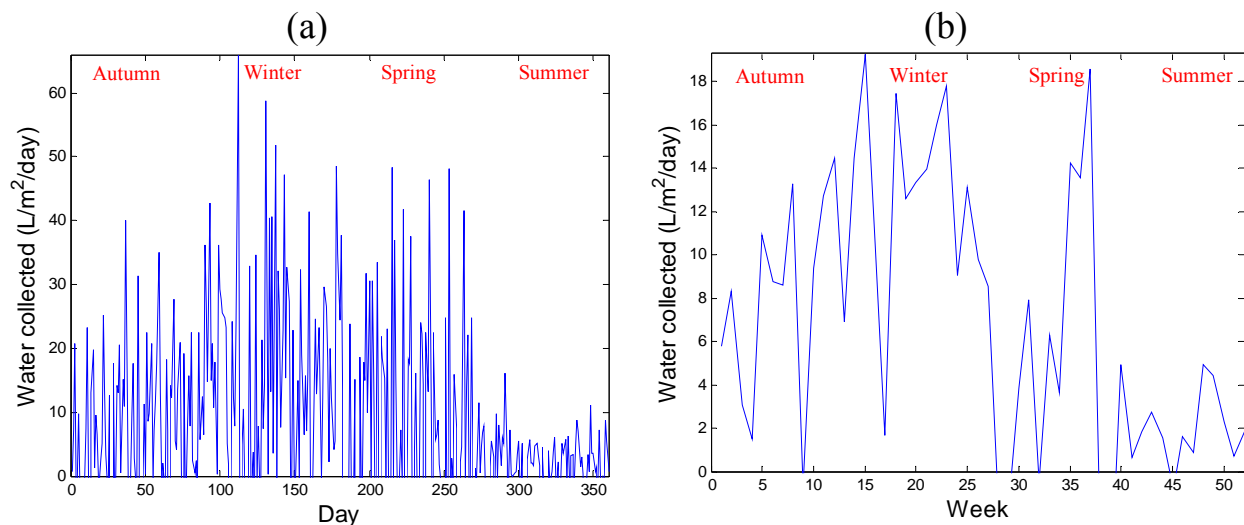
Figure 9-4. Simulated variation in daily and weekly fog collection rates (L/m2/day) are plotted in (a) and (b) respectively, assuming that fog occurrence is a normally distributed random variable.

9.4.1 Modeling the accumulation and consumption of water

Ideally the final consumers would like the system of fog collectors along with the storage and purification system to supply water of clean quality, without any supply interruptions, and at a

193

reasonably low price. However these three requirements coupled with uncertainty of fog events impose conflicting constraint on the system, and this section suggests some strategies to minimize these conflicts.

Consider a system with a fog collector of 30 m^2 area coupled with a large storage tank. The mesh surface collects on average 7 L/m^2/day or ~1.5 m^3 of water every week. We assume that water is being drawn from the attached tank at the average rate of collection and monitor the amount of water in the tank against time in Figure 9-5 (red circles). In this simulation, the tank runs out of water for 3 weeks at the end of autumn, whereas the tank contains about 28 m^3 of water at the end of spring. Note that in this simulation we assumed that the tank has 1 month's supply of water in week zero. If a fog collector system is run with a constant supply, then a large tank (> 28 m^3) will be required and this tank will be less than half full during autumn and winter. Also, for an average collection rate of about 1.5 m^3/week, a tank of say 30 m^3 will be needed, so the tank would be large enough to collect 20 weeks of water supply.

(a)

(b)
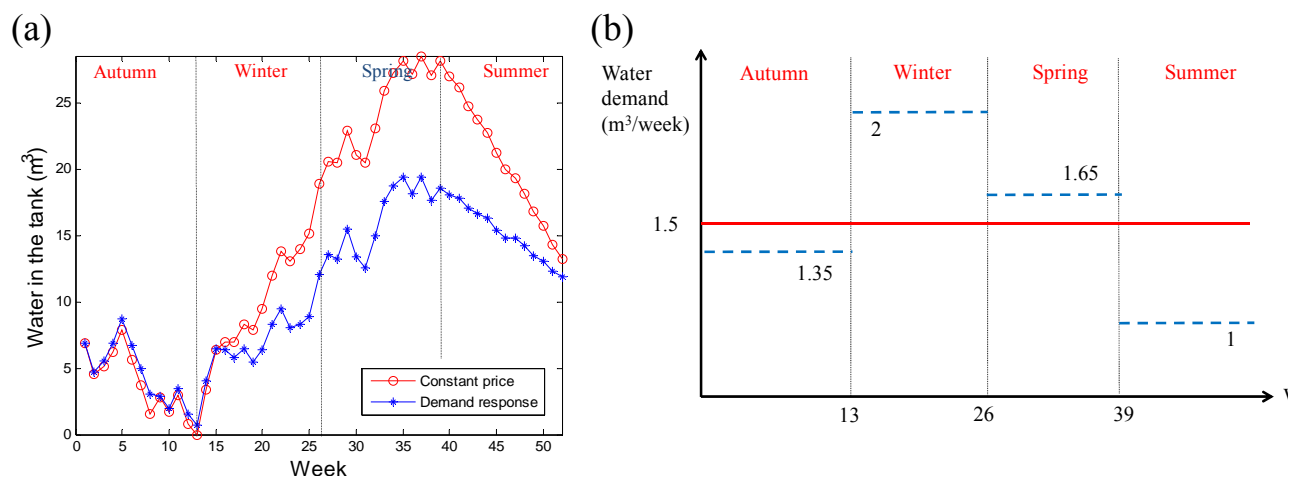
Figure 9-5(a). Accumulation of water in the storage tank is plotted against time for two cases – (i) constant demand for water at 1.5 m3/week (red circles), or (ii) an adaptive demand of 1.35 m3/week in autumn, 2 m3/week in winter, 1.65 m3/week in spring and 1 m3/week in the summer (blue stars). (b) The demand response strategy is plotted against time.

If the end user critically depends upon this water, then the large capital and operating cost associated with a large tank might be justified. However, if the user's demand is elastic i.e. he/she can change the amount of water they demand based on the price, a more efficient strategy might be considered. In the base case scenario in Figure 9-5(a), it is clear that the water is most abundant at the end of spring and most scarce at the end of autumn. Therefore, the price of water should be set so as to incentivize lower consumption in summer and autumn and higher consumption in winter and spring. One particular demand response strategy (plotted in Figure 9-5(b)) is implemented in the simulation and the results are plotted as blue stars in Figure 9-5(a).

In the simulated profile with demand response strategy, the tank runs out for 2 weeks at the end of autumn, and the peak water collection is only about 19 m^3 instead of 28 m^3 without demand response. Therefore, the tank size could be reduced by about 33% without disrupting the water supply. The demand response behavior like the one outlined in Figure 9-5(b) can be achieved by changing the unit price of water ($\$/m^3$) for different seasons based on the predicted demand curve for water.

The preceding analysis assumes that there is a single fog collector connected to a storage tank. The presence of multiple fog harvesting meshes in the vicinity will help decrease piping and storage cost. However, the amount of fog collected by different mesh units in the same area is expected to be highly correlated. Therefore, as a first approximation, the analysis for a single fog collector can be used for multiple fog collectors just by using a correct multiplication factor.

9.5 Testing the assumptions in the economic analysis

- **Capital cost (Capex)** – The main contribution to the capital cost comes from the fog nets, support structure, water storage tanks, water purification equipment and installation cost. The

195

capital cost per 30 m^2 mesh installation will go down due to the economies of scale, as shown

in Figure 9-6. The biggest scale advantage will be achieved in the water storage, purification

and installation costs. The capital cost is expected to decrease from about $900 / unit for a

single installation to about $ 600/ unit when there are about 10 units installed at a site.

In this analysis, the price of the fog net is assumed to go down by about 10% ($100 to $90

per unit of 30 m^2 area) due to a better negotiation position due to bulk purchase. Storage and

purification cost are expected to decrease significantly as a central, more efficient unit could

be used to hold and purify water. Although the total cost of such units is higher, it will be

distributed over 10 mesh units, making each unit cheaper. Installation cost included about

half a day of labor cost for a skilled worker per mesh unit. Therefore, a 50% reduction in

installation cost is assumed as a result of more efficient transport of the material to the

installation site and lower wages per installed mesh.
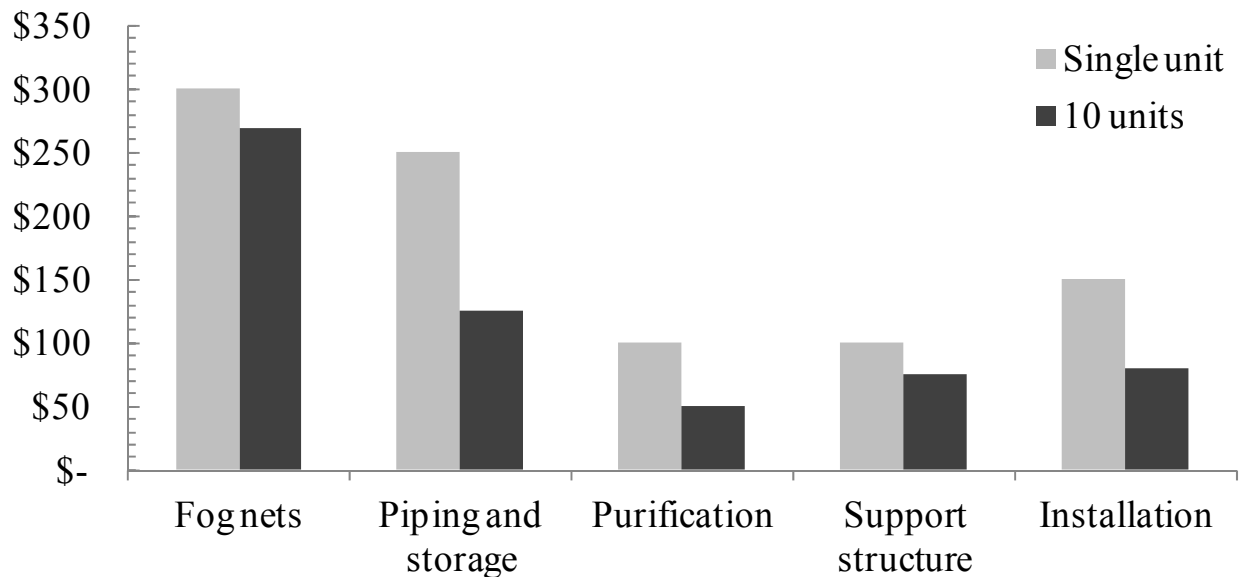
Figure 9-6. Influence of the economy of scale on the capital cost for deploying a fog harvesting mesh is depicted. The light grey bars represent a standalone installation whereas dark grey bars represent costs for a battery of 10 adjacent units. Total capital cost is expected to decrease from $900/unit to about $600/unit as a result of the scale effects.

- **Average amount of water collected (Q)** – A wide range of water collection rate from 1 to 70 L/m^2/day has been reported at various locations.[6] Here, we use a conservative range from 5 to 25 L/m^2/day for water collection from fog. We believe that a combination of appropriate surface chemistry and surface topography would help us capture more water than previously obtained, so this range is clearly conservative. From the analysis presented in Table 9-2, it is clear that breakeven price is inversely proportional to water collection rate. In northern Chile, wind speeds are typically higher around 8 m/s, and droplet radius is also higher around 6 μm. Due to such relatively inertial conditions of droplet impact, the water collection efficiency is expected to be higher and the 5 to 25 L/m^2/day range seems attainable.

  The next three key variables determine the annual revenue from a fog harvesting mesh. The product of number of foggy days and the average amount of water collected estimates how much total water we are able to harvest from fog.

- **Number of foggy days (n)** – This is a variable dictated by the location of the fog collector. Typically, there is a different amount and duration of fog every day of the year, and the amount of liquid water content is also different. Moreover, fog has a wide range of droplet size distribution specific to the microclimate of the location. From the point of view of fog harvesting, one would like to have fog with plenty of larger droplets that are travelling at high velocity. Meteorologists quantify fog in terms of the longest distance that one can see *i.e.* a fog with 100 m visibility is thinker/denser than a fog with 500 m visibility. The liquid water content in the fog (LWC) is negatively correlated with visibility in the fog; however a universal relationship between the two is not established. Therefore, it is not a trivial task whether to count given climate conditions as foggy or not. A pilot scale study will help chose the appropriate location for the installation of large area fog collection meshes. For the

purpose of this analysis, annual average fog harvesting rates are considered, therefore

number of foggy days do not directly enter the expression for NPV.

- **Area of a fog collector (A)** – In the literature, two different sizes, 30 and 48 m^2 have been

   used in fog harvesting pilot experiments. Two other smaller sizes, namely quarter fog

   collector (QFC, 0.25 m^2) and standard fog collector (SFC, 1 m^2) are used mainly to evaluate

   a site before placing a full-scale fog collector. In this chapter, I have fixed the size of fog

   collectors to 30 m^2, but a simple algebraic exercise would, at least in theory, allow

   researchers to translate the data to compare with other sizes. When comparing data over

   widely different areas of meshes, one has to be careful. A previous report indicated that data

   for water collected in $L/m^2/day$ was consistent between 1 and 30 m^2, but not in between 0.25

   and 1 m^2. When the area of a fog collector is small, the edge effects start to dominate

   collection efficiency, which might be the reason for the above reported mismatch.

- **Price of water ($/m³)** – Estimation of the retail price of drinking water in remote areas of

   Chile is a difficult exercise. However, there are some relevant numbers to consider, like the

   opportunity cost of scouting for and carrying water, or the price of water from the cheapest

   available alternate source. Thermal and/or membrane desalination has emerged as a

   promising technology with good economy of scale. A ballpark price of \$2 - 3/m^3 is taken as a

   reference price for water from thermal desalination. However, there are considerable

   variation in this price depending on the location, temperature, salinity of the ocean and

   distance/height over which pumping is required.

- **Lifetime of the project (years)** – According to the Chilean manufacturers, the polyolefin

   meshes are supposed to last for about 10 years. However, strong wind storms and sand

   abrasion can degrade the mesh quickly and the mesh might need to be replaced. Additional

capital cost to purchase and install meshes will dent the profitability of the enterprise, and therefore care needs to be taken to maintain these meshes. Previously, a few pilot projects in Chile have suffered due to the lack of maintenance, and therefore some incentive should be provided to local villagers / stakeholders to maintain the mesh structures. Automatic mechanisms to fold the whole mesh assembly in the event of very strong winds or sandstorm are also being investigated.

9.6 Discount rate and diversification strategies

In a valuation exercise, the discount rate should be commensurate with the riskiness and the duration of the cash flows. Traditionally, one would look at comparable companies or projects to estimate a discount rate. However, there is no reasonable comparable in case of a fog harvesting enterprise. The cash flow is subjected to a weather risk due to intermittent occurrence of fog, as well technological risk as this technology is not well established. In the preceding analysis, we used a 20% discount rate, which is typical for high risk projects. A large change in the discount rate will change the profitability and the breakeven price of water, as summarized in Figure 9-7. In Figure 9-7, the discount rate is changed by 10% and the breakeven price of water is computed. A higher discount rate of 30% depresses the value of future cash flow, and therefore water has to be sold at higher price (dark grey bars) to maintain the feasibility of this project.

A thorough pilot project at the desired location will help to narrow the range of uncertainty in the key variables. Consequently, the whole project can be structured as a combination of a risky but inexpensive pilot deployment followed by a series of successively larger but safer capital investments. The discount rate for a project is based on the anticipated risk, which is the sum of systematic risk and idiosyncratic risk. Systematic risk to a fog harvesting project originates from broad factors like climate change, long-term changes in fog patterns, seasonal weather patterns

and technology related risks. Idiosyncratic risk arises due to project-specific events like a sandstorm that might destroy a woven mesh collector. The idiosyncratic component of the risk can be diversified by operating in multiple fog collectors spread over a large area. However, even such a "diversified" fog collector portfolio is deemed risky, and therefore a high discount rate (say 20%) is expected.
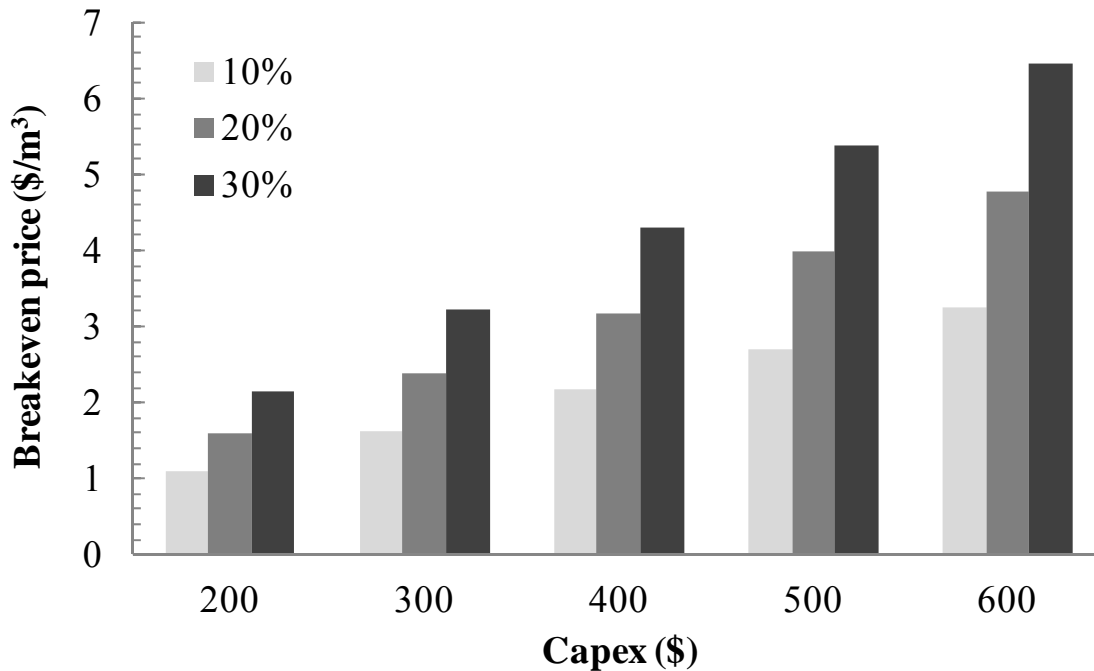
Figure 9-7. Breakeven price of water from fog collection ($/m3) is plotted as a function of the initial capital investment for three different discount rates for future cash flows assuming 10 year duration for the project and 10 m3 of water is collected annually using a 30 m2 mesh.

A second level of diversification can be achieved by investing in fog collection and another enterprise whose cash flows have negative correlation with those of fog collection. A joint investment in such a portfolio will be less risky than individual investments in each of these ventures. Either photovoltaic or solar thermal energy seems to be a good choice of investment along with fog collection due to following reasons. (1) The Atacama Desert receives one of the highest solar insolation (about 6.4 kWh/m^2/day).[22] (2) The insolation is maximum in summer (November – January), which coincides with the period of minimum of fog occurrence. (3)

Collected solar energy can be used to pump water in order to supplement fog collection. In order

to quantify the correlation between fog collection and solar insolation, monthly average data for

fog[11] and solar radiation[22] was normalized with respect to its maximum, and the results are

summarized in Table 9-4. Monthly variation in fog collection rates at Alto Patache and solar

insolation in Northern Chile are tabulated and normalized with respect to corresponding

maximum values

Month	Fog collection		Solar insolation	
	L/m2/day	Normalized	kWh/m2/day	Normalized
January	2.5	0.139	8	1.000
February	1.5	0.083	7.5	0.938
March	1	0.056	6.5	0.813
April	3.5	0.194	5.5	0.688
May	5.5	0.306	4.75	0.594
June	9	0.500	4.5	0.563
July	12.5	0.694	4.75	0.594
August	14.5	0.806	5.5	0.688
September	18	1.000	6.5	0.813
October	12.5	0.694	7	0.875
November	6.5	0.361	8	1.000
December	4.5	0.250	8	1.000
Average		0.424		0.797
Std. dev.		0.311		0.168

 and Figure 9-8. The correlation between the two was found to be –0.34, and therefore a portfolio

with a combination of these two ventures is less risky than either fog collection or solar power

generation by itself.

Table 9-4. Monthly variation in fog collection rates at Alto Patache and solar insolation in
Northern Chile are tabulated and normalized with respect to corresponding maximum values

Month	Fog collection		Solar insolation	
	L/m^2/day	Normalized	kWh/m^2/day	Normalized
January	2.5	0.139	8	1.000
February	1.5	0.083	7.5	0.938

March	1	0.056	6.5	0.813
April	3.5	0.194	5.5	0.688
May	5.5	0.306	4.75	0.594
June	9	0.500	4.5	0.563
July	12.5	0.694	4.75	0.594
August	14.5	0.806	5.5	0.688
September	18	1.000	6.5	0.813
October	12.5	0.694	7	0.875
November	6.5	0.361	8	1.000
December	4.5	0.250	8	1.000
Average		0.424		0.797
Std. dev.		0.311		0.168

All linear combinations with positive weights of fog and solar energy (no shorting allowed) are plotted as the portfolio frontier on the risk-return diagram in Figure 9-8(b). The variance minimizing portfolio consists of 28% relative weight on fog collection and 72% weight on solar energy. This portfolio represents the tangent portfolio or the market portfolio in a fictitious world where only these two investment vehicles exist. A green dotted line between this market portfolio and a risk-free investment is called the Capital Market Line. The risk free rate r_f= 3.5% is chosen based on a 10 year Chilean government bond (taken from Bloomberg). Chile has an A^+ bond rating (Standard and Poor's) therefore it is a good proxy for a risk-free asset.
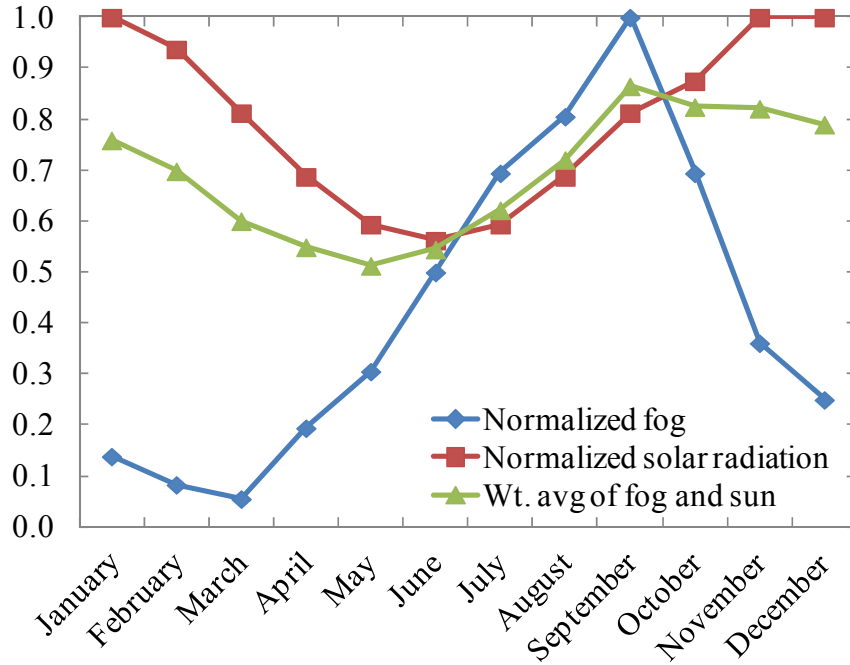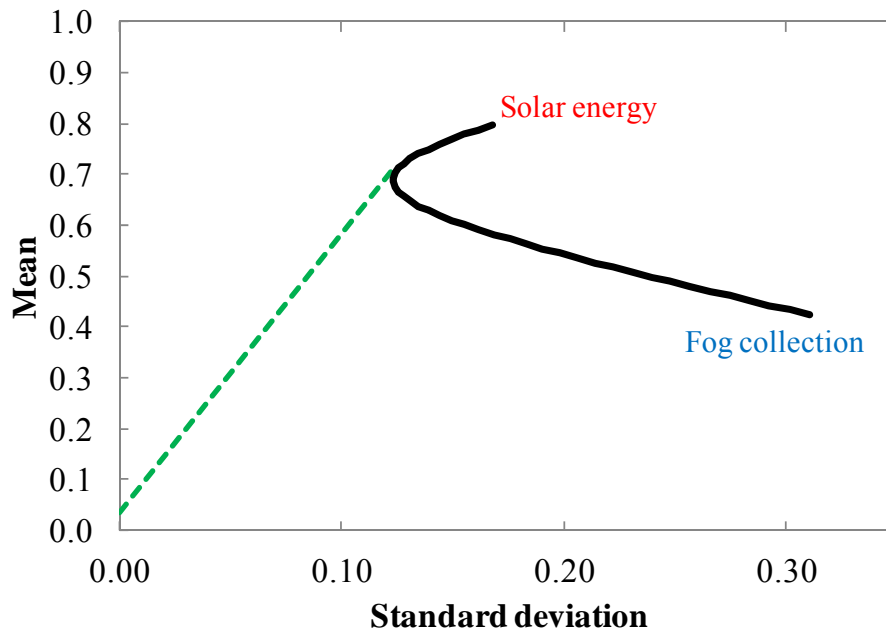
Figure 9-8. (a) Normalized fog collection rates and solar radiation are plotted against the month of the year. A portfolio with 28% weight of fog and remaining 72% weight on solar energy represents minimum variance over the course of the year. (b) Solar energy, fog harvesting and all linear combinations of the two are plotted on the risk-return diagram, and the variance minimizing 28% fog – 72% solar portfolio is identified.

The market portfolio has an expected return of 0.7 at a standard deviation of 0.123. The portfolio has a lower return than pure solar energy, which has a higher standard deviation of 0.168, due to the diurnal motion of the sun. Fog collection rates have an even higher variation as represented

by a standard deviation of 0.311. The maximum of solar radiation coincides with the minimum fog occurrence in November – January. However, the maximum fog occurs in September, which is a couple of month offset from the minimum in solar energy in June. A portfolio with 28% weight on fog and 72% on solar energy has a much lower variation throughout the year. A lower standard deviation in the expected cash flows of such a portfolio leads to lower risk, and therefore, a lower discount rate.

Fog collection has a lower mean return and a higher volatility in returns due to the nature of the fog resource. Still, a combination of solar power and fog collection leads to a better risk-return profile. Therefore, new technologies should not be ignored just due to high volatility of the resources that it plans to exploit. If a new technology can create returns on non-sunny and non-foggy days, then it will act as insurance and smoothen out the cash flows over the course of the year. Such analysis can be generalized to include other technologies. A detailed resource assessment will help quantify the variability over time and correlations with returns on existing investments.

9.7 Identifying customers and understanding the customer value proposition

Previously developed fog harvesting projects in the Atacama region of Chile provided drinking water for local communities and for Aloe Vera farming in the desert. Few fishermen from the Caletas community living in the coastal area of the Atacama Desert have showed that fog collection can be a reliable source of water for drinking and irrigation for farming. Using 6 fog catching nets, they could collect $> 1 \text{ m}^3$ of water/day and irrigate a greenhouse to grow Aloe Vera and Tomatoes. Their expertise should be shared with other communities in the area and with local municipalities and the mining industry.

There is plenty of land for Aloe Vera plantation, so the water demand for irrigation is large. Herbal medicines based on Aloe Vera are used to cure skin rashes, sunburn, insect bite/cuts, and aging/wrinkling of skin. Therefore, local farmers can sell their Aloe Vera output to local processing facilities and pharmaceutical companies for a high price. Farmers might be willing to pay more for the water in order to grow the cash crop of Aloe Vera. The quality standard for drinking water is more stringent than irrigation water. Therefore, we believe that a fog harvesting enterprise should concentrate on selling the fog-water to local farmers, at least in the initial period.

In parallel with fog water collection and distribution to farmers, a thorough water quality analysis should be conducted to check whether the water fulfills WHO standard for human and/or animal consumption. Based on the results of these tests, subsequent purification strategies should be implemented before supplying drinking water.

Typically, the tolerance for impurities goes down from agriculture water, to water for animal, and finally to human consumption. Therefore, after agriculture, the next likely market segment would be farmers with animal feedstock. Once the consumer trusts fog-water as animal feed, he/she is more likely to consider it for human consumption.

 It is important to recognize the difference between actual quality and perceived quality of water. If we start providing water for farming and animals, then people might believe that the water is not suitable to human consumption. Therefore, once we decide to cater to the drinking water demand, a strict demarcation should be made between water quality for different end uses.

Water quality, ease of access and price are the three main metrics that a customer will use to evaluate a water related project. Fog collection is a local source of generation, and with

appropriate storage, the access to water becomes simple. Water quality, both perceived and actual, matters a lot, so a fog collection venture will have to maintain the water quality and communicate the results through local media. Price of water is intricately coupled to both access and quality, but price should not be thought of as the main tool in establishing a fog collection system.

9.7.1 The Porter five force framework for fog harvesting

Factor	Source	Strategy
Bargaining power of suppliers	Suppliers of woven meshes, storage tanks, pipes and water filters	1. Place large orders and negotiate volume discounts 2. Place orders when construction demand is low
Bargaining power of customers	Geographic isolation of fog harvesting systems	1. Encourage local stakeholders to form co-operatives and own a part of the venture 2. Participate in the local water market at the spot price
Threat of new entrants	Groundwater, desalination plant, rainwater harvesting	1. Compete based on the quality of fog-water and high costs of pumping water from the sea level 2. Atacama Desert has low levels of groundwater and negligible rain
Threat of substitute products		
Rivalry within the industry	Local duplication of the fog harvesting technology	1. Encourage people to work together and share best practices rather than compete on price 2. Create goodwill by employing local people and supplying free water to schools

9.7.2 Identifying the stakeholders to mitigate risk

The fog harvesting project has three main types of risks – (1) weather related risks, (2) competition, and (3) social acceptance, and the three risk categories are discussed below.

Rain and fog are natural phenomena and therefore, there is considerable uncertainty about their occurrence and persistence. Water storage will smooth out some of these short term supply shocks. However, prolonged periods of no fog and no rain will eventually lead to interruption in water distribution and revenue collection. Moreover, customers might get annoyed if such disturbances occur frequently. Weather risk can be diluted by diversification *i.e.* by having a

206

portfolio of water resources including ground water, many fog harvesting de vices, and solar powered pumping facility. In the absence of these resources, the storage and distribution infrastructure can still be used to equitably distribute water supplied by the government. Once the venture becomes large enough, then sophisticated hedging strategies can be employed. Either weather-based futures or dynamic pricing will help eliminate some of the weather risk.

The other risk categories can be mitigated by establishing cordial relations with the local community. Vandalism of rare assets is a hard problem to solve. Some physical barriers and active policing will be needed during the time when the fog nets are not producing water. Crime and backlash tends to be highest against an activity when it does not provide any useful service to people. Again, educating women and school children will cut down vandalism. Some insurance on the assets might be needed during the first few years of operation.

A new venture like fog collection based water generation should not disrupt the social practices of customers. Typically, water collection tends to be a daily activity, and the water reservoir provides a place for people to socialize. Therefore, in designing a distribution system, such factors should not be ignored. If people want convenience, they should get a door-to-door distribution system, but otherwise, a centrally located distribution center might suffice.

Also, it will take some time, and advertising to ensure that people feel confident about drinking water collected from fog. Some early adaptors should be incentivized to popularize this concept of water. Endorsement from a national soccer player will help to push this initial campaigning.

9.8 The team involved in the pilot scale studies in Chile

Table 9-5. An interdisciplinary team in Chile and at MIT working on various aspects of fog harvesting

Name	Affiliation	Specialty

Prof. Juan de Dios Rivera	Mechanical and Metallurgical Engineering, PUC[*]	Droplet capture, water collection and fluid mechanics
Magdalena Walczak		Materials
Pilar Cereceda	Institute of Geography, PUC	Fog and fog collection
Luis Gurovich	Enology and Fruticulture, PUC	Water quality and water uses
Robert Holmes	School of Design, PUC	Biomimetics design
Diego López-García	Structural and Geotechnical Engineering, PUC	Innovative structural systems
Richard LeBoeuf	School of Engineering and Applied Sciences, Universidad de los Andes	Instrumentation, fluid dynamics, systems engineering, and project management
Prof. Gareth H. McKinley	MechE, MIT	Fluid mechanics, rheology, optical diagnostics and instrumentation, interfacial phenomena
Prof. Robert E. Cohen	ChemE, MIT	Polymer physics, specialty coatings, and interfacial phenomena
Kenneth Park	MechE, MIT	Fluid mechanics, photolithography
Shreerang S. Chhatre	ChemE / Sloan, MIT	Materials, interfacial phenomena, technology entrepreneurship

*PUC = Pontificia Universidad Católica de Chile, ChemE = Chemical Engineering, MechE = Mechanical Engineering, Sloan = Sloan School of Management

Assembling people with the right set of expertise, and experience is probably the hardest challenge in setting up a new venture. Thankfully, fog harvesting has been practiced in Chile for many decades, and there is considerable hands-on experience in the deployment of this technology. Currently, an interdisciplinary team with a wide range of expertise (Table 9-5) is working on the fog collection problem.

A photograph of the pilot scale deployment of our fog harvesting wire mesh in *Pena Blanca* in Northern Chile is shown in Figure 9-9. Fog water will be collected for next few years at this location, and based on the results; appropriate scale-up will begin.
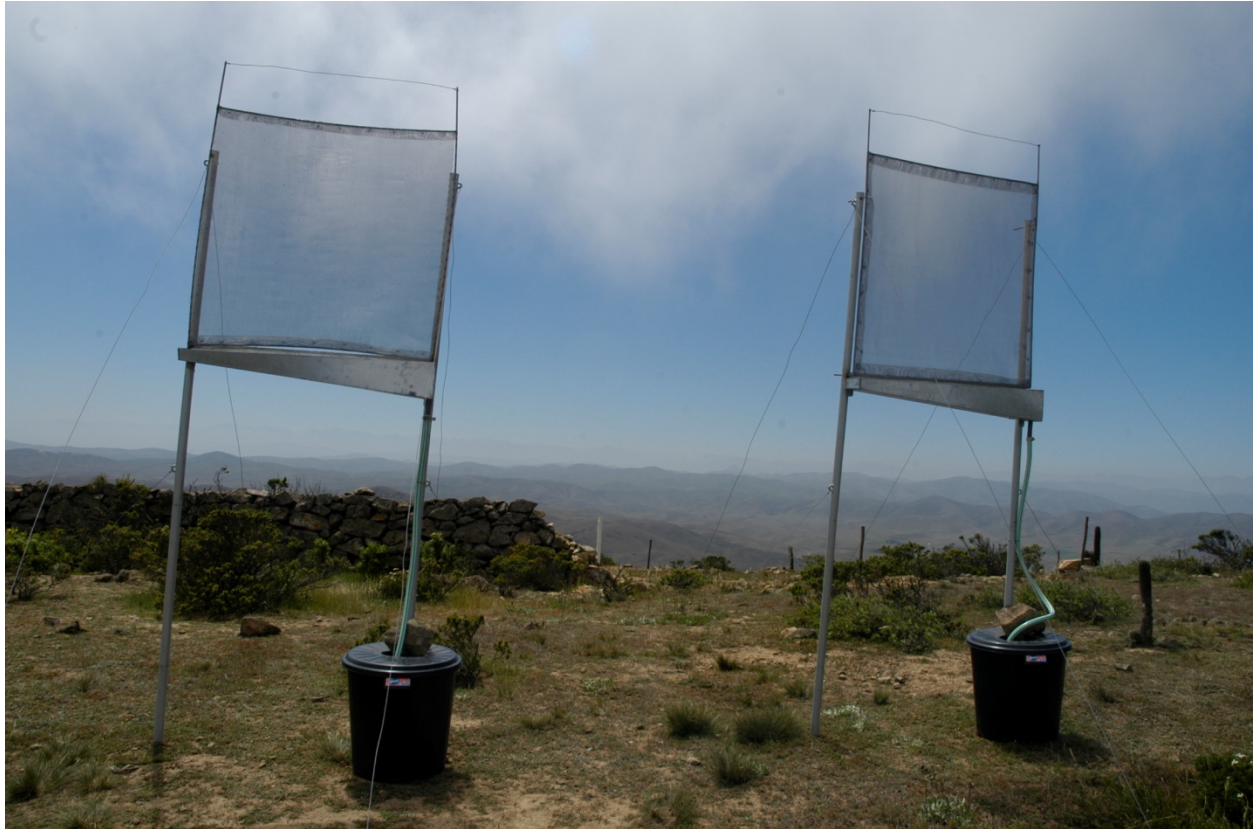
Figure 9-9. Pilot scale deployment of fog harvesting woven meshes at *Pena Blanca* in Chile (Image courtesy – Prof. Pilar Cereceda)

9.9 References

1. Abdul-Wahab, S. A.; Lea, V., *International Journal of Environmental Studies* **2008,** 65, (3), 485-498.
2. Langmuir, I.; Blodgett, K. B. *A mathematical investigation of water droplet trajectories* US Air Force Tech. Rep. No. 5418: 1946; p 68.
3. McComber, P.; Touzot, G., *Journal of the Atmospheric Sciences* **1981,** 38, (5), 1027-1036.
4. Bresci, E., *Atmospheric Research* **2002,** 64, 217-225.
5. Cereceda, P.; Larrain, H.; Osses, P.; Faras, M.; Egana, I., *Atmospheric Research* **2008,** 87, (3-4), 301-311.
6. Klemm, O.; Schemenauer, R.; Lummerich, A.; Cereceda, P.; Marzol, V.; Corell, D.; van Heerden, J.; Reinhard, D.; Gherezghiher, T.; Olivier, J.; Osses, P.; Sarsour, J.; Frost, E.; Estrela, M.; Valiente, J.; Fessehaye, G., *AMBIO: A Journal of the Human Environment* **2012,** 41, (3), 221-234.

7. Rivera, J. D., *Atmospheric Research* **2011,** 102, 335-342.
8. Schemenauer, R. E., *Journal of Applied Meteorology* **1994,** 33, (11).
9. Schemenauer, R. S., *Water International* **1994,** 19, 70-76.
10. Schemenauer, R. S.; Joe, P. I., *Atmospheric Research* **1989,** 24, 53-69.
11. Cereceda, P.; Larrain, H.; Osses, P.; Faras, M.; Egana, I., *Atmospheric Research* **2008,** 87, (3-4), 312-323.
12. Das, S. R., Water good idea. Biomimicry: An improved way to harvest drinking water from fog in remote areas takes its inspiration from an African beetle *The Economist* 2011.
13. Dizikes, P., A Vision Through Fog. *Technology Review* 2011.
14. Sutter, J. D., Can new tech improve 'fog harvesting'? *CNN* 04/26/2011, 2011.
15. Park, K.; Chhatre, S. S.; Srinivasan, S.; Cohen, R. E.; McKinley, G. H., *Proceedings of the Natural Academy of Science* **2012,** Submitted.
16. Westbeld, A.; Klemm, O.; Griebaum, F.; Stater, E.; Larrain, H.; Osses, P.; Creceda, P., *Annales Geophysicae* **2009,** 27, 3571-3576.
17. Mining Cluster in Chile, by Invest Chile - CORFO (Chilean Economic Development Agenecy). http://www.unido.it/americalat/Mining%20Cluster%20in%20Chile%5B1%5D.pdf
18. *Current issues in the Chilean mining sector, by Sustainable Development Strategies Group (http://www.sdsg.org/wp-content/uploads/2010/02/10-10-08-CHILE-REPORT.pdf);* 2008.
19. Bauer, C. J., *Siren Song: Chilean Water Law As Model For International Reform*. Washington, DC, 2004.
20. Edwards, G.; Cristi, O.; Diaz, C., *EconPapers* **2012,** 421.
21. Carranza;, C.; Vega;, A.; Vega, H. Mexico Quarterly Water Report http://www.lgaconsulting.com/water/IE-MexicoWaterReport-2011Winter-ChileanWaterSegmentOverview.html
22. Larrain, T.; Escobar, R., *Renewable Energy* 41, 123-133.

9.10 Supplementary information

Opportunity cost of desalination

Most of the thermal desalination capacity under construction in Chile will use coal as the primary fuel. In this section, we estimate the revenue obtained by producing electricity instead of water from this coal.

Assume:

(1) Price of coal = $2.4 /MMBTU (+ 205 lb of CO_2 /MMBTU of coal, CO_2 price = $25/ton)

(2) Energy input in thermal desalination of seawater = 280 MJt/m3 of water

(3) Thermal to electric efficiency = 30%

(4) 1 kWhr = 3.6 MJ = 0.003 MMBTU

(5) Desalinated water price = $2/m3

(6) Electricity transfer price at transmission = $0.15/kWhr

Sources: http://www.eia.gov/forecasts/steo/report/prices.cfm,
http://www.aneel.gov.br/arquivos/PDF/Hugh%20Rudnick_Jun09_AneelSeminar.pdf,
http://www.uspowerpartners.org/Topics/SECTION1Topic-NaturalGas.htm,

Based on these assumptions, about 280 MJ of thermal energy is used to produce 1 m^3 of desalinated water. The coal cost is expected to be about $0.64, with an additional $0.62 of CO_2 emissions tariff. The same amount of coal will produce 84 MJ of electricity which is worth $3.5 against the 1 m^3 of water which is worth about $2. Therefore, the available coal should be used to produce electricity rather than being used for desalination; and the opportunity cost of desalinated water should be taken as $3.5/m^3.

Two business models – selling water Vs. selling fog collection devices

	Sell devices	Sell water
Immediate cash flow	Proceeds from the sale	None
Long term cash flow	None	Revenue by selling water
Need for financing	Short term	Long term
Control	Almost none	Complete control
Chance to understand customer behavior	Limited	Large
Target market	More informed buyer with access to capital	Retail buyer
Risk	Duplication, bad reviews	Cash flow risk, weather risk

10 Summary and Recommendations for future work

10.1 Summary

The main aim of this thesis was to develop rules for systematically designing liquid repellent surfaces and applying those to commercial textile surfaces. In Chapter 3, a design chart framework was developed which provides an easy appreciation of the importance of surface chemistry (in terms of the equilibrium contact angle θ_E) and surface texture (in terms of a dimensionless spacing ratio D^*) on the apparent contact angles (θ^*) observed on textured surfaces. Moreover, the importance of the length scale (R) on the existence and robustness of composite interfaces against external pressure perturbations is clearly demonstrated. A set of woven meshes with a wide range of wire radii (R), spacing ratios (D^*) and coatings (γ_{sv}) were probed using contact angle measurements by liquids with a broad range of surface tension (γ_{lv}).[1] These experiments substantiate the robustness parameter framework and also illustrate the utility of the design chart approach.

In Chapter 4 and Chapter 5, this theoretical framework was applied to a commercial polyester fabric (Anticon 100). A broad range of liquids from water (γ_{lv} = 72.1 mN/m) to dodecane (γ_{lv} = 25.3) formed a robust composite interface with high apparent contact angles on the fabric when dip-coated with fluorodecyl POSS along with a polymeric binder. The 10% POSS – 90% poly (ethyl methacrylate) (PEMA) coated fabric displayed reversibly switchable wettability for hexadecane (γ_{lv} = 27.5) and dodecane (γ_{lv} = 25.3) droplets when annealed in water or dry air at 90 °C for three hours. This behavior was linked with the change in the molecular constitution of the 10% POSS – 90% PEMA coating using XPS studies. Further, a method to characterize the

complex topography of the fabric in terms of a single dimensionless geometric factor (D^*) was established.[2]

In Chapter 5, the wettability of the commercial polyester fabric dip-coated with 50% POSS – 50% Tecnoflon was tuned and reversibly switched using biaxial strain as a stimulus. For droplets with composite interfaces on the dip-coated fabric, the apparent contact angle increases with increasing strain. However, as the air pockets get larger, the extent of sagging of the air-liquid interface increases and the robustness degreases and beyond a threshold composite interfaces cannot be sustained. Inspired by this understanding, the dip-coated fabric was used to demonstrate strain induced sequential wetting for four alkane droplets with small difference in liquid surface tensions ($\Delta\gamma_{lv} \approx 2$ mN/m).[3]

Chapters 3, 4, and 5 illustrated the importance of re-entrant texture, the length scale and relative spacing of the topography on its wettability. However, the apparent contact angle (θ^*) and the robustness (A^*) can be increased by lowering the solid surface energy of the coating (γ_{sv}) or increasing the equilibrium contact angles (θ_E). Water droplets form highest contact angles ($\theta_{adv} = 122$ and $\theta_{adv} = 116°$) on a flat surface spin-coated with fluorodecyl POSS. In Chapter 6, wettability of molecules similar to fluorodecyl POSS is investigated using contact angle measurements by liquids with a broad range of surface tension (γ_{lv}) and polarity. Girifalco-Good method was used to quantify the dispersion (γ_{sv}^d), hydrogen bond donating (γ_{sv}^+), hydrogen bond accepting components (γ_{sv}^-) of the surface free energy. Out of the molecules tested so far, fluorodecyl POSS had the lowest solid surface energy ($\gamma_{sv} = 9.3$ mN/m) and the lowest increment in solid surface energy ($\Delta\gamma_{sv} = 7$ mN/m) due to surface reorganization in contact with probing liquids. The summary of first five chapters is schematically presented in Figure 10-1.
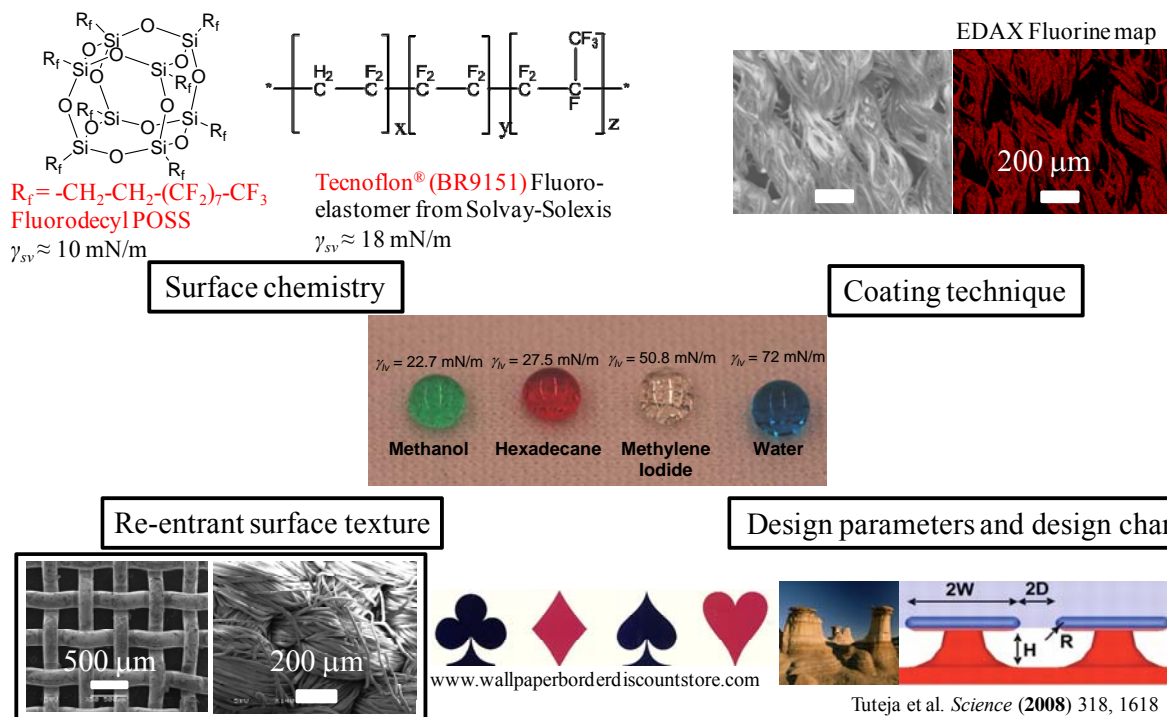
Figure 10-1. Four important aspects of this thesis dealing with the surface chemistry of the coatings, technique to achieve conformal coatings, re-entrant surface topography and design charts to explain the wettability of textured surfaces are summarized.

In the next three chapters of this thesis, the understanding about the influence of surface texture and surface chemistry on wettability was applied towards diverse applications. In Chapter 7, the design parameter framework is applied to army uniform fabrics to estimate the apparent contact angles (θ^*) and breakthrough pressure (P_b) for these surfaces. A 50% POSS – 50% Tecnoflon coated fabric was not wetted even by octane ($\gamma_{lv} = 21.6$ mN/m). Further, these fabric topographies were characterized in terms of a length scale (R) and an effective spacing ratio (D^*).

In Chapter 8, this robustness framework was extended and applied to wing feathers of aquatic birds. The wetting aspects of the bird feather texture were quantified using contact angle measurements with a set of probing liquids. Based on this analysis, wetting behavior of these feathers with complicated and hierarchical texture could be simplified to a 1-dimensional

cylindrical model. Using this model, thermodynamics of wetting and influence of pressure perturbation on wetting could be *apriori* predicted.

Finally in the Capstone Chapter (Chapter 9), economic aspects of fog collection using woven meshes are investigated. The break-even price of fog water was found to be comparable to the price of desalinated water. The volatility of fog could be partially offset by water storage, dynamic pricing strategies and a water back-up system. Combining fog harvesting with solar energy would help reduce the volatility of the combined resource, both in terms of cash flows and amount of water available for consumption.

10.2 Publications

Accepted publications:

1.   Choi, W. *et. al*. *Advanced Materials* **2009,** 21, 2190-2195

2.   Chhatre, S. S. *et. al*. *Langmuir* **2009,** 25, 13625-13632

3.   Chhatre, S. S. *et. al*. *Langmuir* **2010,** 26, 4027-4035

4.   Chhatre, S. S. *et. al*. *ACS Applied Materials and Interfaces* **2010**, 2, 3544-3554

5.   Meuler A. J. *et. al*. *Soft Matter* **2011,** 7, 10122-10134

6.   Srinivasan S. et. al., *Polymer* **2011**, 52, 3209-3218

In preparation:

1.   Chhatre S. S. *et. al*., *Proceedings of the Royal Society B* (wetting of bird feathers)

2.   Park K. *et. al*., *Proceedings of the National Academy of Sciences USA* (fog harvesting)

3.   Srinivasan S. *et. al*., *Phys. Fluids* (hydrodynamic drag reduction)

Conference presentations / posters:

1.   Chhatre, S.S. *et. al*. Materials Research Society (MRS) Fall 2009 Meeting, Boston, MA, December 2009.

2.   McKinley, G. H. *et. al.* 62nd Annual Meeting of the APS Division of Fluid Dynamics, Minneapolis, MN, November 2009.

3.   Chhatre S. S. *et. al*. Chemical and Biological Defense Science and Technology Conference, Dallas, November 2009.

4.   Chhatre, S. S. *et. al;., Symposium on Contact angle, Wettability and Adhesion*, Danbury CT, June 2010.

5.   Chhatre S. S. *et. al*. *ACS Fall 2010 Meeting*, Boston MA, August 2010.

10.3 Future work

a. Most of the work outlines in this thesis is based on goniometric measurements of advancing and receding contact angles on smooth and rough surfaces. Probing surfaces using a dynamic tensiometer will provide more information about the dynamics and rearrangements that might take place as the solid surface comes in contact with liquids. Also, contact angle hysteresis can be more accurately quantified using tensiometry.

b. Mechanical robustness of the coating to the substrate is a key parameter in the commercialization of a lot of applications. In the current work, the low surface energy coatings adhere to the substrate purely based on Van der Walls interactions. Chemically cross-linking the coatings to the substrate and various polymers might increase the mechanical robustness.

11 Appendices

11.1 Matlab Programs

Program used for plotting the design chart

```matlab
function cos_thetastar
%This function illustrates the inter-relation between cos(theta*),
%cos(theta) and D*
%written by - Shreerang Chhatre
n = 250;                  %number of points
theta = linspace(0,pi,n);
costheta = cos(theta);
ymin = 1; ymax = 4*pi;        % range on Dstar
Dstar = linspace(ymin,ymax,n);
costhetastar = zeros(n,n);

for i=1:n                  %cassie baxter
    for j=1:n
        costhetastar(i,j) = -1+(sqrt(1-costheta(i)^2)+(pi-theta(i))*costheta(i))/Dstar(j);
    end;
end;

% figure; [C,h] = contour(Dstar, costheta, (180/pi)*acos(costhetastar),9);
% set(h,'ShowText','on','TextStep',get(h,'LevelStep'))
% axis([ymin ymax -1 1]);
% ylabel('cos(\theta)','fontsize',14); xlabel('D*','fontsize',14); zlabel('cos(\theta^*)','fontsize',14); hold off;
%========================================================================

%now solve the equation cos(theta*) = 0 to get cos(theta) for various D*
costheta0 = cos(pi/4)*ones(4,1);  %some initial guess
xmin = 1; xmax = 10;
Dstar = linspace(xmin, xmax, n);
costheta_root = zeros(n,4);
options = optimset('Display','none','TolFun',1e-8);
for i=1:n
    costheta_root(i,1) = fsolve(@(x)myfun(x,Dstar(i)), costheta0(1),options);     %theta* = 0
    costheta0(1) = costheta_root(i,1);
    costheta_root(i,2) = fsolve(@(x)myfun1(x,Dstar(i)), costheta0(2),options);    %theta* = 90
    costheta0(2) = costheta_root(i,2);
    costheta_root(i,3) = fsolve(@(x)myfun5(x,Dstar(i)), costheta0(3),options);    %theta* = 120
    costheta0(3) = costheta_root(i,3);
    costheta_root(i,4) = fsolve(@(x)myfun4(x,Dstar(i)), costheta0(4),options);    %theta* = 150
    costheta0(4) = costheta_root(i,4);
end;
Dstar_crit = [1.55; 2.4; 3.2; 4.25];   %values of D* at which A* = 1 for angles 0, 90, 150 and 120
index = zeros(4,1);                 %stores the index of transition values
for i=1:n
    for j=1:4
        if (Dstar(i)<Dstar_crit(j))
            index(j) = i;
        end;
    end;
```

```matlab
end;
%==============================================================================

%now attempting to solve dual scale cassie baxter equation.
costheta0 = cos(pi/4)*ones(4,1);  %some initial guess
xmin = 1; xmax = 10;
D2star = linspace(xmin, xmax, n);
D1star = 3;          %spacing ratio on individual fiber scale, kept fixed for time being
costheta_dual_root = zeros(n,4);
for i=1:n
    costheta_dual_root(i,1) = fsolve(@(x)myfun_dual(x,D2star(i),D1star), costheta0(1));    %theta** = 0
    costheta0(1) = costheta_dual_root(i,1);
    costheta_dual_root(i,2) = fsolve(@(x)myfun1_dual(x,D2star(i),D1star), costheta0(2));   %theta** = 90
    costheta0(2) = costheta_dual_root(i,2);
    costheta_dual_root(i,3) = fsolve(@(x)myfun5_dual(x,D2star(i),D1star), costheta0(3));   %theta** = 120
    costheta0(3) = costheta_dual_root(i,3);
    costheta_dual_root(i,4) = fsolve(@(x)myfun4_dual(x,D2star(i),D1star), costheta0(4));   %theta** = 150
    costheta0(4) = costheta_dual_root(i,4);
end;

%==============================================================================

% Now solving for theta at which A* = 1, as a function of D (or D*)
%lcap = 2e-3;
lcap = 1.85e-3;    % for dodecane

%lcap = 1.98e-3;   %for rapeseed oil
%lcap = 1.587e-3;   %for pentane
%lcap = 1.854e-3;  %for hexadecane
%lcap = 1.25e-3;    %diiodo

R = 2750e-6;         %for e-spun, R_max = 5e-7; polyester fabric = 1.5e-4
D_max = 2.5*pi*R;    %for e-spun, D_max = 1e-5; polyester fabric = 6e-4
D_min = 0;
D_var = linspace(D_min, D_max, n);
theta1 = zeros(n,1);
theta2 = zeros(n,1);
Dstar_new = zeros(n,1);
x0_1 = 1;
x0_2 = 1;

 for i=1:n
    theta1(i) = acos(fsolve(@(x)myfun2(x,D_var(i),R,lcap), x0_1,options));
    x0_1 = cos(theta1(i));   %improving the initial guess for the next point
    theta2(i) = acos(fsolve(@(x)myfun3(x,D_var(i),R,lcap), x0_2,options));
    x0_2 = cos(theta2(i));
    Dstar_new(i) = (R + D_var(i))/R;
end;
%==============================================================================

%Now putting in the limit of metastability on the chart
theta_crit = linspace(pi/2,5*pi/6,n);
Dstar_crit = zeros(n,1);

for i=1:n
    Dstar_crit(i) = (sin(theta_crit(i))-theta_crit(i)*cos(theta_crit(i)))/(1+cos(theta_crit(i)));
```

```matlab
end;

%======================================================================
figure;
colormap summer; whitebg('w')
plot(Dstar, (180/pi)*acos(costheta_root),'LineWidth',2); hold on;
area(Dstar_new, theta1*180/pi); hold on;            %....single scale
plot(Dstar_crit, theta_crit'*180/pi,'--','LineWidth',2); hold on; %metastability

plot(Dstar_new, theta2*180/pi,'k--'); hold on;      % A* = 2
plot(D2star, (180/pi)*acos(costheta_dual_root), 'o'); hold on; %....dual scale

axis([xmin 2*pi 0 125]);
title(['\it{R} =  ',num2str(1e6*R),' {\mu}m'],'fontsize',14);
xlabel('\it{D^*}','fontsize',14); ylabel('\it{\theta_E}','fontsize',14); hold on;
legend ('\it{\theta^*}= 0^o','\it{\theta^*}= 90^o','\it{\theta^*}= 120^o','\it{\theta^*}= 150^o',...
   '\it{A^*} < 1','Binodal','Location','SouthEast');
%legend ('\theta^*= 0^o','\theta^*= 90^o','\theta^*=120^o','\theta^*= 150^o','Location','SouthEast');
hold off;
%index

%dummy = 2*pi*ones(length(theta1));

% figure; colormap summer; whitebg('w')
% plot(costheta_root,Dstar,'LineWidth',2); hold on;
% %area(cos(theta1),dummy); hold on;
% plot(cos(theta1),Dstar_new,'LineWidth',3); hold on;

% plot(cos(theta_crit),Dstar_crit,'--','LineWidth',2); hold on;  %metastability
% axis([-1 1 1 2*pi]); title(['\it{R} =  ',num2str(1e6*R),' {\mu}m'],'fontsize',14);
% ylabel('\it{D^*}','fontsize',14); xlabel('cos\it{\theta_E}','fontsize',14);
% legend ('\it{\theta^*}= 0^o','\it{\theta^*}= 90^o','\it{\theta^*}= 120^o','\it{\theta^*}= 150^o',...
%    '\it{A^*} < 1','Binodal','Location','NorthEast');
% hold off;

M = [Dstar', real((180/pi)*acos(costheta_root))];
xlswrite('matrix_out.xls', M, 1);
N = [Dstar_new, theta1*180/pi]; %data for A* = 1
xlswrite('matrix_out.xls', N, 2);
%O = [Dstar_crit, theta_crit'*180/pi];
%xlswrite('matrix_out.xls', O, 4);
%P = [D2star', real(acos(costheta_dual_root)*180/pi)]; %data for A* = 1
%xlswrite('matrix_out.xls', P, 3);
return;
%======================================================================

%Now writing the individual functions called from f-solve
function F = myfun(x,Dstar)
F = -1+(sqrt(1-x^2)+(pi-acos(x))*x)/Dstar -1;          %0 degrees
F = 1e6*F;
return;

function F = myfun1(x,Dstar)
F = -1+(sqrt(1-x^2)+(pi-acos(x))*x)/Dstar;              %90 degrees
F = 1e6*F;
return;
```

```
function F = myfun4(x,Dstar)
F = -1+(sqrt(1-x^2)+(pi-acos(x))*x)/Dstar -cos(5*pi/6);     %150 degrees
F = 1e6*F;
return;

function F = myfun5(x,Dstar)
F = -1+(sqrt(1-x^2)+(pi-acos(x))*x)/Dstar -cos(4*pi/6);     %120 degrees
F = 1e6*F;
return;

function F = myfun2(x,D,R,lcap)
F = 1e0 - (R*lcap/D^2)*(1-x)/(1+2*(R/D)*sqrt(1-x^2));
F = 1e6*F;
return;

function F = myfun3(x,D,R,lcap)
F = 2 - (R*lcap/D^2)*(cos(pi/6)-x)/(1+2*(R/D)*sqrt(1-x^2));    %B* ==1
return;
%===============================================================
% %writing functions for the dual part now
%
function F = myfun_dual(x,D2star,D1star)
z = -1+(sqrt(1-x^2)+(pi-acos(x))*x)/D1star;          %cos(theta*)... inner angle

F = -1+(sqrt(1-z^2)+(pi-acos(z))*z)/D2star -1;        %0 degrees
return;

function F = myfun1_dual(x,D2star,D1star)
z = -1+(sqrt(1-x^2)+(pi-acos(x))*x)/D1star;          %cos(theta*)... inner angle

F = -1+(sqrt(1-z^2)+(pi-acos(z))*z)/D2star -0;        %90 degrees
return;

function F = myfun4_dual(x,D2star,D1star)
z = -1+(sqrt(1-x^2)+(pi-acos(x))*x)/D1star;          %cos(theta*)... inner angle

F = -1+(sqrt(1-z^2)+(pi-acos(z))*z)/D2star -cos(5*pi/6); %150 degrees
return;

function F = myfun5_dual(x,D2star,D1star)
z = -1+(sqrt(1-x^2)+(pi-acos(x))*x)/D1star;          %cos(theta*)... inner angle

F = -1+(sqrt(1-z^2)+(pi-acos(z))*z)/D2star -cos(4*pi/6); %120 degrees
return;
%===============================================================
```

Program used for creating the video which illustrates the impact of length scale (R) on the robustness factor (A^*)

```
function cos_thetastar_3D
%This function illustrates the inter-relation between cos(theta*), %cos(theta) and D*
%written by - Shreerang Chhatre
n = 25;               %number of points on the theta axis
theta = linspace(0,pi,n);
```

```matlab
costheta = cos(theta);
xmin = 1; xmax = 2*pi;          % range of Dstar
Dstar = linspace(xmin,xmax,n);
costhetastar = zeros(n,n);

for i=1:n                    %Cassie-Baxter
    for j=1:n
        costhetastar(i,j) = -1+(sqrt(1-costheta(i)^2)+(pi-theta(i))*costheta(i))/Dstar(j);
    end;
end;
%====================================================================

%now solve the Cassie-Baxter equation to get contours of theta* for various D*
costheta0 = cos(pi/4);  %some initial guess
costheta_root = zeros(n,4);
for i=1:n
    costheta_root(i,1) = fsolve(@(x)myfun(x,Dstar(i)), costheta0);    %theta* = 0
    costheta_root(i,2) = fsolve(@(x)myfun1(x,Dstar(i)), costheta0);   %theta* = 90
    costheta_root(i,3) = fsolve(@(x)myfun5(x,Dstar(i)), costheta0);   %theta* = 120
    costheta_root(i,4) = fsolve(@(x)myfun4(x,Dstar(i)), costheta0);   %theta* = 150
end;
theta_root = (180/pi)*real(acos(costheta_root));       % is a n by 4 matrix
%====================================================================

% Now solving for theta at which A* = 1, as a function of D (or D*)
m = 81;              %number of 'R' valus chosen for the video = # of video frames
R = logspace(-6,-2,m); %defining range of R

D_max = zeros(m,1);
D_min = zeros(m,1);
D_var = zeros(m,n);

for i=1:m
    D_max(i) = (xmax-1)*R(i);       %related D to D* and R
    D_var(i,:) = linspace(D_min(i), D_max(i), n);
end;

theta1 = zeros(m,n);
Dstar_new = zeros(m,n);
x0 = 1;
lcap = 1.91e-3;                 %liquid physical propert
theta2 = zeros(m,n,4);

%now getting the curve which defines A* = 1
for i=1:m
    for j=1:n
        theta1(i,j) = acos(fsolve(@(x)myfun2(x,D_var(i,j),R(i),lcap), x0));
        Dstar_new(i,j) = (R(i) + D_var(i,j))/R(i);
    end;
    theta2(i,:,:) = theta_root(:,:);        %contours
end;
theta = (180/pi)*real(theta1);       % is a m by n matrix

%====================================================================

fig=figure;
```

```matlab
colormap summer;
set(gcf,'Color',[1,1,1]);
aviobj = avifile('video_for_MRS.avi','fps',2,'quality',100, 'compression','None')
for i=1:m
    plot(Dstar, theta_root(:,1),'k','LineWidth',2); hold on;      %....single scale
    plot(Dstar, theta_root(:,2),'r','LineWidth',2); hold on;
    plot(Dstar, theta_root(:,3),'g','LineWidth',2); hold on;
    plot(Dstar, theta_root(:,4),'b','LineWidth',2); hold on;

    area(Dstar, theta(i,:),'FaceColor',[.7 0.7 0.7]); hold on;                %....available and prohibited region
    title(['\it{R} = ',num2str(floor(1e6*R(i))),' \it{\mu}m'],'fontsize',14)
    axis([xmin xmax 0 125]); xlabel('\it{D^*}','fontsize',14); ylabel('\it{\theta_E}','fontsize',14);
    legend ('\it{\theta*}= 0^o','\it{\theta*}= 90^o','\it{\theta*}= 120^o','\it{\theta*}=
150^o','\it{A*}<1','Location','SouthEast');
    F = getframe(fig);
    aviobj = addframe(aviobj,F);
end;
close(fig);
aviobj = close(aviobj);
return;
%===========================================================================

%Now writing the individual functions called from f-solve
function F = myfun(x,Dstar)
F = -1+(sqrt(1-x^2)+(pi-acos(x))*x)/Dstar -1;            %0 degrees
return;

function F = myfun1(x,Dstar)
F = -1+(sqrt(1-x^2)+(pi-acos(x))*x)/Dstar;               %90 degrees
return;

function F = myfun4(x,Dstar)
F = -1+(sqrt(1-x^2)+(pi-acos(x))*x)/Dstar -cos(5*pi/6);    %150 degrees
return;

function F = myfun5(x,Dstar)
F = -1+(sqrt(1-x^2)+(pi-acos(x))*x)/Dstar -cos(4*pi/6);   %120 degrees
return;

function F = myfun2(x,D,R,lcap)
F = 1 - (R*lcap/D^2)*(1-x)/(1+2*(R/D)*sqrt(1-x^2));       %for A* = 1
return;
%===========================================================================
```

Program used for fitting an effective spacing ratio (D^*) to a data of $\cos\theta_{adv}$ and $\cos\theta^*_{adv}$

```matlab
function estimate_Dstar
%This function reads the contact angle data from an excel spreadsheet and
%fits the cylindrical cassie-baxter equation to estimate D*.
%written by Shreerang Chhatre
global cos_theta;
%first read the data from ACU fabric Dstar calculation.xls
contact_angle = xlsread('Dstar.xls', 3, 'I2:J13');
cos_contact_angle = cos(contact_angle*pi/180);
```

222

```
cos_thetastar = cos_contact_angle(:,1);    %the 'y' datapoints
cos_theta = cos_contact_angle(:,2);        %the 'x' datapoints
Dstar0 = 2;                    %initial gues for ACU fabric
%actual function
[Dstar,r,J,SIGMA,mse] = nlinfit(cos_theta,cos_thetastar,@fun,Dstar0);
Dstar
mse
ci = nlparci(Dstar,r,'covar',SIGMA);
delta = (ci(2)-ci(1))/2

%Now plotting the datapoints along with the fitted CB relation
n = 100;
xx = linspace(-1,1,n);

figure; plot(xx, fun(Dstar,xx), xx, fun(Dstar+delta,xx), xx, fun(Dstar-delta,xx)); hold on;
plot(cos_theta,cos_thetastar, 'o'); hold on;
axis([-1 1 -1 1]);
legend('D^* from regression','D^*+\delta','D^*-\delta'); xlabel('cos\theta_E'); ylabel('cos\theta^*');
hold off;
return;

function y = fun(D,x)
y  = -1 + (1/D)*(sin(acos(x))+(pi-acos(x)).*x);     %the function
return;
%=====================================================================
```

Program used for plotting different models with cylindrical texture

```
function cos_thetastar_cross
%This function illustrates the inter-relation between cos(theta*), cos(theta) and D* for the cross model from Kawase
et al.
%written by - Shreerang Chhatre
n = 2000;                   %number of points
theta = linspace(0,pi,n);
costheta = cos(theta);
ymin = 1; ymax = 2*pi;          % range on Dstar
Dstar = linspace(ymin,ymax,n);
costhetastar = zeros(n,n);

for i=1:n                    %cassie baxter
    for j=1:n
        costhetastar(i,j) = -1+(sqrt(1-costheta(i)^2)+(pi-theta(i))*costheta(i))/Dstar(j);
    end;
end;

% figure; [C,h] = contour(Dstar, costheta, (180/pi)*acos(costhetastar),9);
% set(h,'ShowText','on','TextStep',get(h,'LevelStep'))
% axis([ymin ymax -1 1]);
% ylabel('cos(\theta)','fontsize',14); xlabel('D*','fontsize',14); zlabel('cos(\theta^*)','fontsize',14); hold off;
%=====================================================================

%now solve the equation cos(theta*) = 0 to get cos(theta) for various D*
costheta0 = cos(pi/4)*ones(4,1);  %some initial guess
xmin = 1; xmax = 2*pi;
Dstar = linspace(xmin, xmax, n);
```

```matlab
costheta_root = zeros(n,4);
options = optimset('Display','none','TolFun',1e-8);
for i=1:n
    costheta_root(i,1) = fsolve(@(x)myfun(x,Dstar(i)), costheta0(1),options);    %theta* = 0
    costheta0(1) = costheta_root(i,1);
    costheta_root(i,2) = fsolve(@(x)myfun1(x,Dstar(i)), costheta0(2),options);   %theta* = 90
    costheta0(2) = costheta_root(i,2);
    costheta_root(i,3) = fsolve(@(x)myfun5(x,Dstar(i)), costheta0(3),options);   %theta* = 120
    costheta0(3) = costheta_root(i,3);
    costheta_root(i,4) = fsolve(@(x)myfun4(x,Dstar(i)), costheta0(4),options);   %theta* = 150
    costheta0(4) = costheta_root(i,4);
end;

figure;
colormap summer; whitebg('w')
plot(Dstar, (180/pi)*acos(costheta_root(:,1)),'k','LineWidth',2); hold on;
plot(Dstar, (180/pi)*acos(costheta_root(:,2)),'r','LineWidth',2); hold on;
plot(Dstar, (180/pi)*acos(costheta_root(:,4)),'g','LineWidth',2); hold on;
plot(Dstar, (180/pi)*acos(costheta_root(:,3)),'b','LineWidth',2); hold on;
axis([xmin 2*pi 0 125]);
title('Cross Model','fontsize',14);
xlabel('\it{D^*}','fontsize',14); ylabel('\it{\theta_E}','fontsize',14);
hold off;
return;
%======================================================================

%Now writing the individual functions called from f-solve
function F = myfun(x,Dstar)                          %0 degrees

F = (x/(2*Dstar))*((pi-acos(x))*(1+x)+sqrt(1-x^2)) - (1-(sqrt(1-x^2)/Dstar)*(0.5+pi*(1+x)/8)) -1; %Cross model

F = 1e6*F;
return;

function F = myfun1(x,Dstar)                         %90 degrees
F = (x/(2*Dstar))*((pi-acos(x))*(1+x)+sqrt(1-x^2)) - (1-(sqrt(1-x^2)/Dstar)*(0.5+pi*(1+x)/8));
F = 1e6*F;
return;

function F = myfun4(x,Dstar)                         %120 degrees
F = (x/(2*Dstar))*((pi-acos(x))*(1+x)+sqrt(1-x^2)) - (1-(sqrt(1-x^2)/Dstar)*(0.5+pi*(1+x)/8)) -cos(4*pi/6);
F = 1e6*F;
return;

function F = myfun5(x,Dstar)                         %150 degrees
F = (x/(2*Dstar))*((pi-acos(x))*(1+x)+sqrt(1-x^2)) - (1-(sqrt(1-x^2)/Dstar)*(0.5+pi*(1+x)/8)) -cos(5*pi/6);
F = 1e6*F;
return;
%======================================================================
```

11.2　Preliminary results on fog harvesting under inertial fog conditions

This section summarizes the data collected by Hongzhi Deng in the summer of 2010 in inertial fog conditions developed in the lab.

Experimental plan

We used a fog machine called the Fogmaster junior (shown in Figure 11-1) to simulate fog inside our lab. This machine is capable of delivering fog droplets of various sizes with a maximum flow rate of 300 L/min. Woven meshes with a wide range of physic-chemical properties (R, D^*, and γ_{sv}) were used to model the actual fog collection condition. Our aim is to find the optimal length scale (R), texture spacing (D^*) and coating (γ_{sv}) to maximize the fog collection.

(a)　　　　　　　　　　　　　　　　(b)
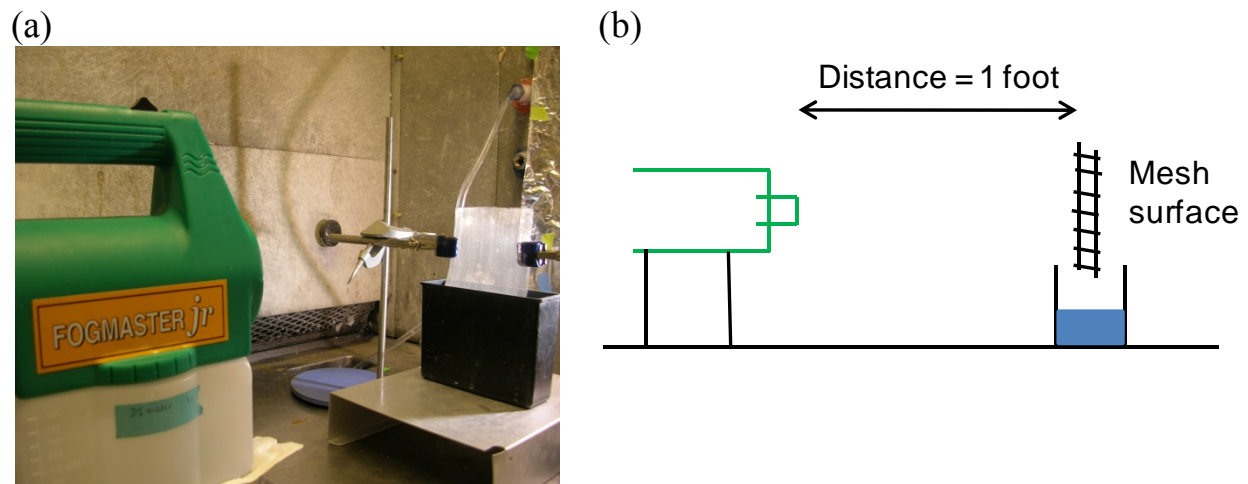
Figure 11-1. Picture of the fog harvesting setup in the lab is shown. The Fogmaster junior machine, a mesh used for fog collection along with a collection vessel is shown.

Observation / results

In a typical fog collection experiment, we measured the initial ($V_1 = 800$ ml) and final (V_2) volume of water in the tank of the fog machine, the amount of water collected by the mesh (V_c). The efficiency of fog water collection was computed as $\eta = V_c/(V_1 - V_2)$. The other parameters

for the experiments (and their default values) were duration of one experimental run (5 minutes),

distance between the mesh and the fog machine (1 foot). Table 11-1 summarizes the results for

the experimental runs performed in the lab.

Table 11-1. Amount of water collected and percent efficiency for woven meshes with a wide
range of texture (R µm, D^*), and chemistry of the coating (θ_E) is summarized.

Mesh number	Distance between mesh and the machine (feet)	Radius (R) µm, D^*	Coating	Water collected (ml)	Efficiency (%)
6	1	254, 8.33	None	11.667	9.5
6	0.5	254, 8.33	None	21	19
6	2	254, 8.33	None	3.667	4.1
12	1	254, 4.17	None	74.333	22.8
12	0.5	254, 4.17	None	28.333	24.5
12	2	254, 4.17	None	6.333	6.3
12	1	254, 4.17	PVA	67	21
12	1	254, 4.17	Poss	65.667	21
15	1	127, 6.67	None	50.333	15.4
15	0.5	127, 6.67	None	14.333	17.3
15	2	127, 6.67	None	0	0
18	1	254, 2.78	None	79.667	24.9
18	2	254, 2.78	None	13	12
18	0.5	254, 2.78	None	38.333	31.6
20	1	254, 2.50	None	77.333	25.7
20	2	254, 2.50	None	12.667	10.9
20	0.5	254, 2.50	None	43.333	30.3
28	1	127, 3.57	None	82.667	25.7
28	0.5	127, 3.57	None	25.333	28.5
28	2	127, 3.57	None	2.667	3.9
28	1	127, 3.57	PVA	73	23.1
28	1	127, 3.57	Poss	61.333	19.2
35	1	127, 2.86	None	74.667	23.5
35	0.5	127, 2.86	None	35.333	31.5
40	1	127, 2.50	None	83.667	25.8
40	2	127, 2.50	None	3.667	4.4
40	0.5	127, 2.50	None	42.667	31.6
40	1	127, 2.50	PVA	70.667	22.1
40	1	127, 2.50	Poss	58.667	18.1
42	1	70, 4.33	None	83.667	25.9
42	2	70, 4.33	None	0	0

42	0.5	70, 4.33	None	23.667	26.4
42	1	70, 4.33	Poss with PVA spots 1cm apart	68.333	21.6
42	1	70, 4.33	Poss with PVA spots 0.5cm apart	73.333	23.4
44	1	70, 4.13	None	50.667	25
44	1	70, 4.13	PVA	77.333	23.5
44	1	70, 4.13	PMMA	76	23.5
50	1	70, 3.64	None	84.333	25.8
50	2	70, 3.64	None	0.333	0.4
50	0.5	70, 3.64	None	118.67	37.5
52	1	70, 3.50	None	33.667	20.9
54	0.5	70, 3.37	None	16.667	23.9
54	2	70, 3.37	None	0.667	0.8
80	1	70, 2.27	None	77.667	23.6
80	1	70, 2.27	PVA	76.667	24
80	1	70, 2.27	PMMA	73.667	22.8
80	1	70, 2.27	Poss	56	17.2
80	1	70, 2.27	Poss with PVA spots 1cm apart	62.667	20.3
80	1	70, 2.27	Poss with PVA spots 0.5cm apart	73.667	22.8
90	1	70, 2.02	None	26.667	20.9
90	2	70, 2.02	None	3	3.4
90	0.5	70, 2.02	None	19.333	26.6

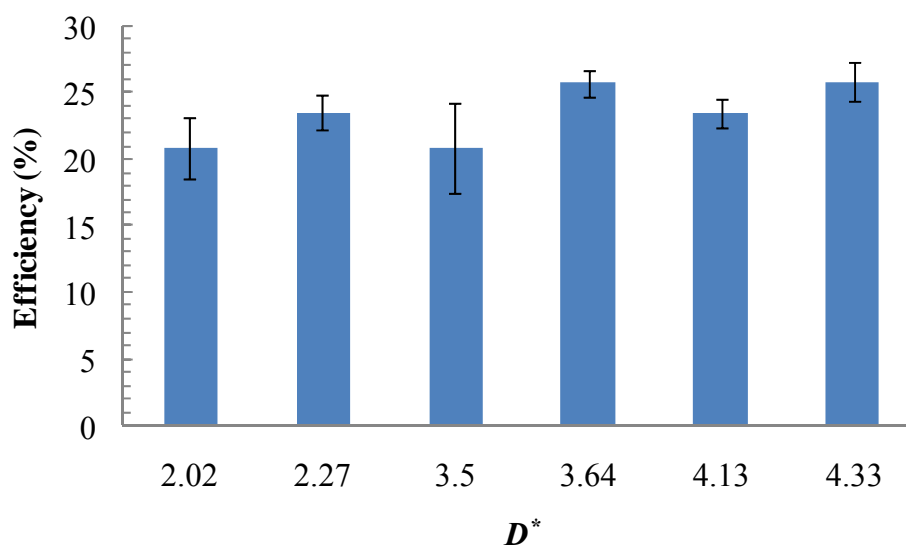(PVA = poly(vinyl alcohol), PMMA = poly(methyl methacrylate), POSS = fluorodecyl POSS)

Figure 11-2. A bar chart of the efficiency of fog collection for various meshes with a constant wire radius, $R = 70$ μm is plotted as a function of the spacing ratio (D^*)
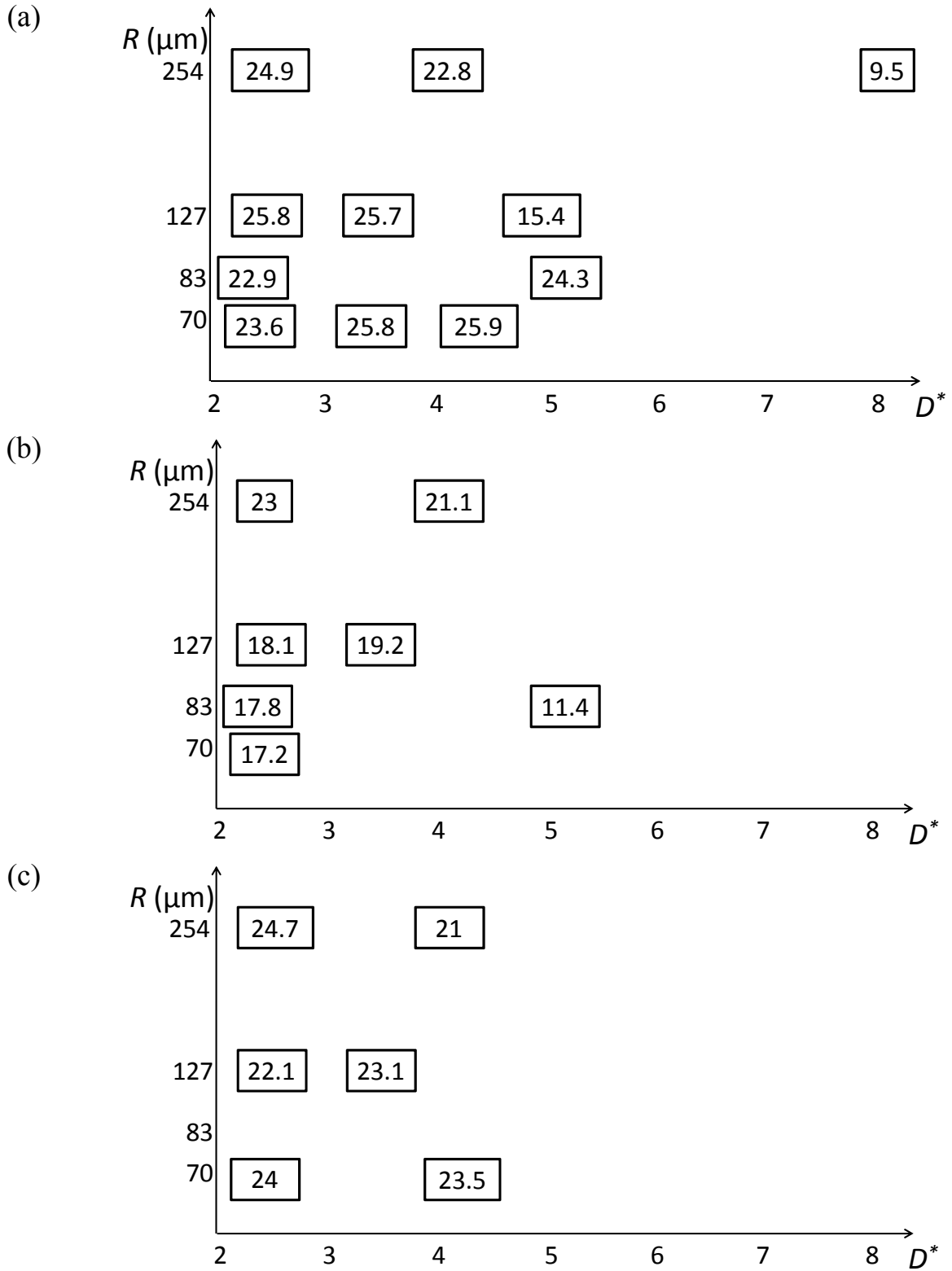
Figure 11-3. Fog collection efficiency for (a) uncoated (b) 50% POSS − 50% Tecnoflon coated, and (c) PVA coated wire meshes are plotted as a function of the spacing ratio (D^*) and radius of the wire (R)
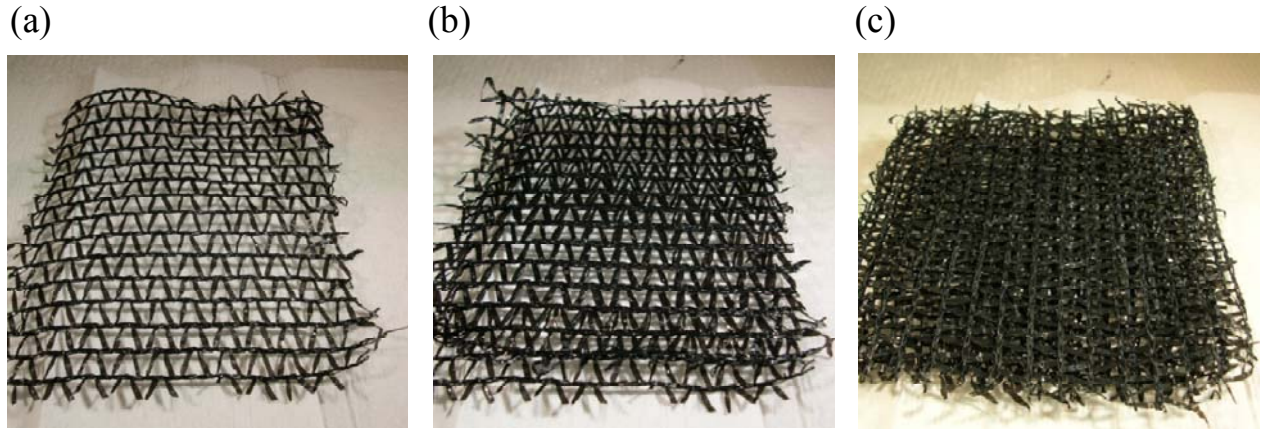
Figure 11-4. (a) Single, (b) double, and (c) quadruple Raschel meshes used for the fog collection experiments are shown
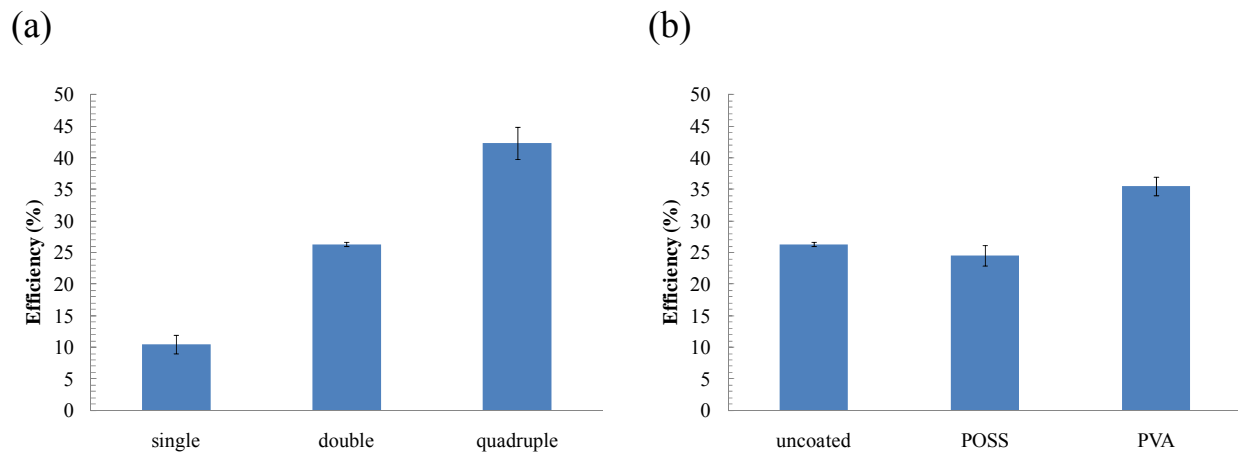

Figure 11-5. Efficiency of fog collection for (a) uncoated meshes and (b) coated double meshes are shown

11.3 Tensiometry of bird feathers

Contact angle measurements or goniometry is the main characterization technique used to quantify the surface / interfacial energies. However, sessile drop contact angle measurements do not simulate the condition of immersion of a solid surface inside a pool of liquid. On the contrary, a Wilhelmly plate setup involves dipping of a solid plate inside liquid and tracking the force as a function of vertical displacement. Therefore, a dynamic tensiometry (Wilhelmly plate like, Figure 11-6(a)) experiments were performed to quantify the wettability of dip-coated bird feathers.
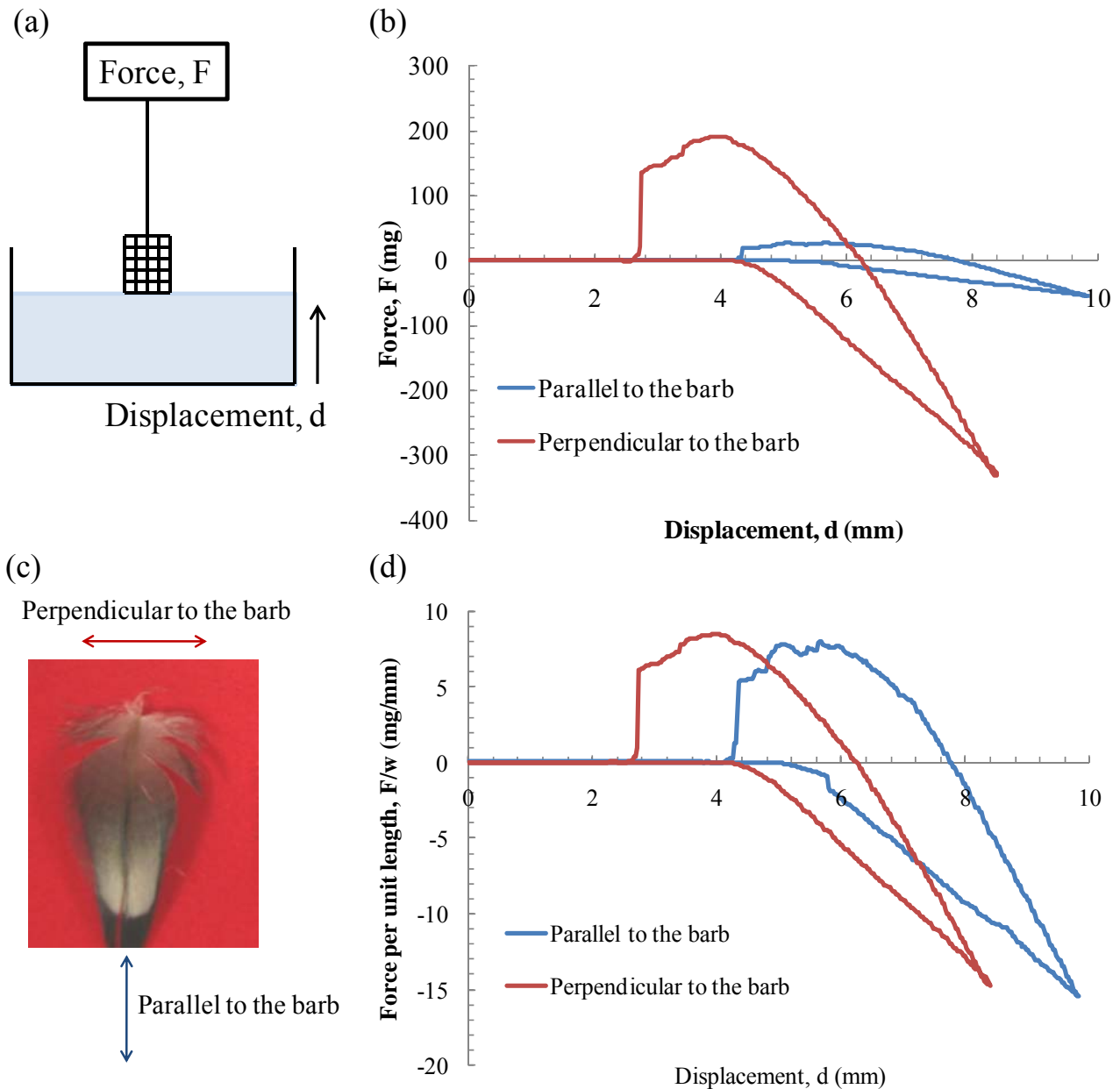
Figure 11-6.(a) Schematic of the Wilhelmly plate like tensiometer setup. (b) Tensiograms showing the variation in force in mg versus vertical displacement for the cormorant feather dip-coated with 50% POSS – 50% Tecnoflon. (c) Picture of the reed cormorant wing feather on which tensiometry was done along and perpendicular to its barb. (d) Tensiograms in part (b) are replotted after scaling the force with the width of the feather.

These experiments were performed using a tensiometer at the Cambridge Polymer Group. The advancing and receding speed was chosen to be $U \approx 60$ μm/s, which is small enough so that the corresponding Capillary number, $Ca = U\eta/\gamma_{lv}$ (where $\eta = 10^{-3}$ Pas, and $\gamma_{lv} = 72.1$ mN/m for water) is very small ($\sim 10^{-6}$), and the dynamic effects due to viscous dissipation can be

ignored.Two tensiometry experiments were performed on the wing feather of a reed cormorant, one where the feather is dipped parallel to its barb and the other one where the feather is dipped almost normal to its barb (as shown in Figure 11-6(b) and (c)). On a tensiogram, the observed force (F, mg) is plotted on the y-axis against the vertical displacement (d, mm) on the x-axis. The force experienced in the two cases was found to be different as the solid-liquid interfacial area for the feather is different along the two directions. Therefore, the observed forces were scaled by the average width of the feather (0.4 cm for the parallel and 2.25 cm for the perpendicular case) and force per unit length is plotted in Figure 11-6(d). In these scaled tensiograms, the size, shape and peak force (~15 mg/mm) was observed to be similar for the experiments.